

# **Analysis of Options and Experimental Examination of Fuels for Water Cooled Reactors with Increased Accident Tolerance (ACTOF)**

*Final Report of a Coordinated Research Project*



**IAEA**

International Atomic Energy Agency

ANALYSIS OF OPTIONS AND  
EXPERIMENTAL EXAMINATION  
OF FUELS FOR WATER COOLED  
REACTORS WITH INCREASED  
ACCIDENT TOLERANCE (ACTOF)

The following States are Members of the International Atomic Energy Agency:

|                                     |                                     |  |
|-------------------------------------|-------------------------------------|--|
| AFGHANISTAN                         | GERMANY                             | PAKISTAN   |
| ALBANIA                             | GHANA                               | PALAU  |
| ALGERIA                             | GREECE                              | PANAMA   |
| ANGOLA                              | GRENADA                             | PAPUA NEW GUINEA   |
| ANTIGUA AND BARBUDA                 | GUATEMALA                           | PARAGUAY   |
| ARGENTINA                           | GUYANA                              | PERU   |
| ARMENIA                             | HAITI                               | PHILIPPINES  |
| AUSTRALIA                           | HOLY SEE                            | POLAND   |
| AUSTRIA                             | HONDURAS                            | PORTUGAL   |
| AZERBAIJAN                          | HUNGARY                             | QATAR  |
| BAHAMAS                             | ICELAND                             | REPUBLIC OF MOLDOVA  |
| BAHRAIN                             | INDIA                               | ROMANIA  |
| BANGLADESH                          | INDONESIA                           | RUSSIAN FEDERATION   |
| BARBADOS                            | IRAN, ISLAMIC REPUBLIC OF           | RWANDA   |
| BELARUS                             | IRAQ                                | SAINT LUCIA  |
| BELGIUM                             | IRELAND                             | SAINT VINCENT AND<br>THE GRENADINES                        |
| BELIZE                              | ISRAEL                              | SAN MARINO   |
| BENIN                               | ITALY                               | SAUDI ARABIA   |
| BOLIVIA, PLURINATIONAL<br>STATE OF  | JAMAICA                             | SENEGAL  |
| BOSNIA AND HERZEGOVINA              | JAPAN                               | SERBIA   |
| BOTSWANA                            | JORDAN                              | SEYCHELLES   |
| BRAZIL                              | KAZAKHSTAN                          | SIERRA LEONE   |
| BRUNEI DARUSSALAM                   | KENYA                               | SINGAPORE  |
| BULGARIA                            | KOREA, REPUBLIC OF                  | SLOVAKIA   |
| BURKINA FASO                        | KUWAIT                              | SLOVENIA   |
| BURUNDI                             | KYRGYZSTAN                          | SOUTH AFRICA   |
| CAMBODIA                            | LAO PEOPLE'S DEMOCRATIC<br>REPUBLIC | SPAIN  |
| CAMEROON                            | LATVIA                              | SRI LANKA  |
| CANADA                              | LEBANON                             | SUDAN  |
| CENTRAL AFRICAN<br>REPUBLIC         | LESOTHO                             | SWEDEN   |
| CHAD                                | LIBERIA                             | SWITZERLAND  |
| CHILE                               | LIBYA                               | SYRIAN ARAB REPUBLIC                                       |
| CHINA                               | LIECHTENSTEIN                       | TAJIKISTAN   |
| COLOMBIA                            | LITHUANIA                           | THAILAND   |
| CONGO                               | LUXEMBOURG                          | TOGO   |
| COSTA RICA                          | MADAGASCAR                          | TRINIDAD AND TOBAGO  |
| CÔTE D'IVOIRE                       | MALAWI                              | TUNISIA  |
| CROATIA                             | MALAYSIA                            | TURKEY   |
| CUBA                                | MALI                                | TURKMENISTAN   |
| CYPRUS                              | MALTA                               | UGANDA   |
| CZECH REPUBLIC                      | MARSHALL ISLANDS                    | UKRAINE  |
| DEMOCRATIC REPUBLIC<br>OF THE CONGO | MAURITANIA                          | UNITED ARAB EMIRATES                                       |
| DENMARK                             | MAURITIUS                           | UNITED KINGDOM OF<br>GREAT BRITAIN AND<br>NORTHERN IRELAND |
| DJIBOUTI                            | MEXICO                              | UNITED REPUBLIC<br>OF TANZANIA                             |
| DOMINICA                            | MONACO                              | UNITED STATES OF AMERICA                                   |
| DOMINICAN REPUBLIC                  | MONGOLIA                            | URUGUAY  |
| ECUADOR                             | MONTENEGRO                          | UZBEKISTAN   |
| EGYPT                               | MOROCCO                             | VANUATU  |
| EL SALVADOR                         | MOZAMBIQUE                          | VENEZUELA, BOLIVARIAN<br>REPUBLIC OF                       |
| ERITREA                             | MYANMAR                             | VIET NAM   |
| ESTONIA                             | NAMIBIA                             | YEMEN  |
| ESWATINI                            | NEPAL                               | ZAMBIA   |
| ETHIOPIA                            | NETHERLANDS                         | ZIMBABWE   |
| FIJI                                | NEW ZEALAND                         |  |
| FINLAND                             | NICARAGUA                           |  |
| FRANCE                              | NIGER                               |  |
| GABON                               | NIGERIA                             |  |
| GEORGIA                             | NORTH MACEDONIA                     |  |
|                                     | NORWAY                              |  |
|                                     | OMAN                                |  |

The Agency's Statute was approved on 23 October 1956 by the Conference on the Statute of the IAEA held at United Nations Headquarters, New York; it entered into force on 29 July 1957. The Headquarters of the Agency are situated in Vienna. Its principal objective is "to accelerate and enlarge the contribution of atomic energy to peace, health and prosperity throughout the world".

IAEA-TECDOC-1921

ANALYSIS OF OPTIONS AND  
EXPERIMENTAL EXAMINATION  
OF FUELS FOR WATER COOLED  
REACTORS WITH INCREASED  
ACCIDENT TOLERANCE (ACTOF)

FINAL REPORT OF A COORDINATED RESEARCH PROJECT

INTERNATIONAL ATOMIC ENERGY AGENCY  
VIENNA, 2020

## COPYRIGHT NOTICE

All IAEA scientific and technical publications are protected by the terms of the Universal Copyright Convention as adopted in 1952 (Berne) and as revised in 1972 (Paris). The copyright has since been extended by the World Intellectual Property Organization (Geneva) to include electronic and virtual intellectual property. Permission to use whole or parts of texts contained in IAEA publications in printed or electronic form must be obtained and is usually subject to royalty agreements. Proposals for non-commercial reproductions and translations are welcomed and considered on a case-by-case basis. Enquiries should be addressed to the IAEA Publishing Section at:

Marketing and Sales Unit, Publishing Section  
International Atomic Energy Agency  
Vienna International Centre  
PO Box 100  
1400 Vienna, Austria  
fax: +43 1 26007 22529  
tel.: +43 1 2600 22417  
email: [sales.publications@iaea.org](mailto:sales.publications@iaea.org)  
[www.iaea.org/publications](http://www.iaea.org/publications)

For further information on this publication, please contact:

Nuclear Fuel Cycle and Materials Section  
International Atomic Energy Agency  
Vienna International Centre  
PO Box 100  
1400 Vienna, Austria  
Email: [Official.Mail@iaea.org](mailto:Official.Mail@iaea.org)

© IAEA, 2020  
Printed by the IAEA in Austria  
July 2020

### IAEA Library Cataloguing in Publication Data

Names: International Atomic Energy Agency.  
Title: Analysis of options and experimental examination of fuels for water cooled reactors with increased accident tolerance (ACTOF) / International Atomic Energy Agency.  
Description: Vienna : International Atomic Energy Agency, 2020. | Series: IAEA TECDOC series, ISSN 1011-4289 ; no. 1921 | Includes bibliographical references.  
Identifiers: IAEAL 20-01339 | ISBN 978-92-0-114120-0 (paperback : alk. paper) | ISBN 978-92-0-114220-7 (pdf)  
Subjects: LCSH: Nuclear fuels. | Water cooled reactors. | Nuclear reactors — Safety measures..

## FOREWORD

Nuclear power has proven to be a reliable, environmentally sustainable and cost effective source of large scale electricity. In the interest of continued technological improvement, further improvements in operational reliability, economics and safety under normal and transient conditions are being pursued worldwide. Most existing nuclear power plants utilize light water reactors with uranium dioxide pellets and zirconium alloy cladding. Decades of research combined with continued operation have produced steady advancement in technology and yielded an extensive data, experience and knowledge base on the performance of light water reactor fuel during normal operation and accident conditions. Particular attention has been given to the development of fuels with higher burnup to minimize waste, and to increasing power density for power upgrades and fuel reliability. The events at the Fukushima Daiichi nuclear power plant, along with progress in the development of advanced materials, have provided the motivation to improve nuclear performance and safety, thereby mitigating the effects of severe accidents. This was in line with the recommendations from the IAEA International Experts Meeting Strengthening Research and Development Effectiveness in the Light of the Accident at the Fukushima Daiichi Nuclear Power Plant, held in Vienna in 2015. Those recommendations, which reflected the experts' views on the need for further R&D activities and international cooperative efforts, were further refined at the Technical Meeting on Post-Fukushima Research and Development Strategies and Priorities in December 2015.

Among the new technologies under development is accident tolerant fuel, which has the potential to enhance safety at nuclear power plants by offering better performance in normal operation, transient conditions and accident scenarios. These new fuels and cladding need to be licensed before being deployed industrially; therefore, research is being undertaken to assess their behaviour in normal operation and accident conditions.

The development and verification of computer codes to model nuclear fuel behaviour in different conditions requires extensive and reliable experimental data collected through durable and expensive studies. This is why international cooperation in this area is highly desirable. The IAEA traditionally supports interested Member States in their efforts to enhance the capacities of their computer codes used for prediction of fuel behaviour. The coordinated research project (CRP) entitled Analysis of Options and Experimental Examination of Fuels for Water Cooled Reactors with Increased Accident Tolerance (ACTOF) complemented these efforts by considering the modelling and development of advanced fuel concepts, supporting the collection of the experimental data that will be needed to allow implementation of such fuels in commercial reactors. The CRP was a continuation of the IAEA Action Plan on Nuclear Safety and followed a Technical Meeting on Accident Tolerant Fuel Concepts for Light Water Reactors held in the United States of America in 2014.

ACTOF was made possible as a result of the support and dedication of many organizations and individuals. The IAEA would like to thank the Technical Working Group on Fuel Performance and Technology (TWG-FPT) for suggesting and supporting the CRP. The IAEA would also like to thank all those who prepared the intermediate working material and the final report. The IAEA officer responsible for this publication was M. Veshchunov of the Division of Nuclear Fuel Cycle and Waste Technology.

#### *EDITORIAL NOTE*

*This publication has been prepared from the original material as submitted by the contributors and has not been edited by the editorial staff of the IAEA. The views expressed remain the responsibility of the contributors and do not necessarily represent the views of the IAEA or its Member States.*

*Neither the IAEA nor its Member States assume any responsibility for consequences which may arise from the use of this publication. This publication does not address questions of responsibility, legal or otherwise, for acts or omissions on the part of any person.*

*The use of particular designations of countries or territories does not imply any judgement by the publisher, the IAEA, as to the legal status of such countries or territories, of their authorities and institutions or of the delimitation of their boundaries.*

*The mention of names of specific companies or products (whether or not indicated as registered) does not imply any intention to infringe proprietary rights, nor should it be construed as an endorsement or recommendation on the part of the IAEA.*

*The authors are responsible for having obtained the necessary permission for the IAEA to reproduce, translate or use material from sources already protected by copyrights.*

*The IAEA has no responsibility for the persistence or accuracy of URLs for external or third party Internet web sites referred to in this publication and does not guarantee that any content on such web sites is, or will remain, accurate or appropriate.*

# CONTENTS

|        |   |    |
|--------|---|----|
| 1.     | INTRODUCTION .....                                      | 1  |
| 1.1.   | Background.....   | 1  |
| 1.2.   | Objectives.....   | 1  |
| 1.3.   | Scope .....   | 1  |
| 1.4.   | Structure .....   | 2  |
| 2.     | MATERIALS PROPERTIES .....                              | 3  |
| 2.1.   | FeCrAl cladding .....                                   | 3  |
| 2.1.1. | Thermophysical properties .....                         | 3  |
| 2.1.2. | Mechanical properties .....                             | 5  |
| 2.1.3. | Thermal and irradiation creep .....                     | 6  |
| 2.1.4. | Swelling .....  | 6  |
| 2.1.5. | Oxidation.....  | 6  |
| 2.1.6. | Burst failure criterion .....                           | 7  |
| 2.2.   | U <sub>3</sub> Si <sub>2</sub> fuel .....               | 7  |
| 2.2.1. | Specific heat .....                                     | 8  |
| 2.2.2. | Thermal conductivity .....                              | 8  |
| 2.2.3. | Thermal diffusivity.....                                | 9  |
| 2.2.4. | Coefficient of thermal expansion .....                  | 9  |
| 2.2.5. | Young's modulus and Poisson's ratio .....               | 9  |
| 2.2.6. | Swelling .....  | 9  |
| 2.3.   | SiC cladding .....                                      | 10 |
| 2.3.1. | Specific Heat .....                                     | 10 |
| 2.3.2. | Thermal conductivity .....                              | 10 |
| 2.3.3. | Emissivity.....   | 11 |
| 2.3.4. | Volumetric thermal expansion .....                      | 12 |
| 2.3.5. | Elastic constant.....                                   | 12 |
| 2.3.6. | Creep .....   | 13 |
| 2.3.7. | Yield strength.....                                     | 13 |
| 2.3.8. | Irradiation swelling .....                              | 13 |
| 2.3.9. | Oxidation.....  | 14 |
| 2.4.   | Alloy 348.....  | 15 |
| 3.     | ROUND ROBIN TEST REPORT IN THE FRAMEWORK OF ACTOF ..... | 16 |
| 3.1.   | Round robin test: objectives and motivation .....       | 16 |
| 3.2.   | Sample production.....                                  | 17 |
| 3.2.1. | USP Brazil: AISI 348 SS .....                           | 17 |
| 3.2.2. | CTU/UJP Czech Republic: Cr PVD coatings .....           | 18 |
| 3.2.3. | KIT Germany: MAX phase PVD coatings.....                | 19 |
| 3.2.4. | INCT Poland: ZrSi-Cr PVD Coatings.....                  | 20 |
| 3.3.   | Long term corrosion .....                               | 23 |
| 3.4.   | Facility, conditions, and experimental methods .....    | 23 |
| 3.4.1. | CTU/UJP .....   | 24 |
| 3.4.2. | VTT.....  | 25 |
| 3.4.3. | INCT .....  | 25 |
| 3.5.   | Results: CTU/UJP .....                                  | 29 |
| 3.6.   | Results: VTT .....                                      | 33 |
| 3.6.1. | Uncoated Zr-based alloys: reference samples .....       | 33 |
| 3.6.2. | Cr PVD coated Zry-2 .....                               | 37 |

|        |   |     |
|--------|---|-----|
| 3.6.3. | Cr/Cr <sub>2</sub> AlC/Cr (MAX phase) PVD coated Zry-4.....             | 41  |
| 3.6.4. | ZrSi-Cr PVD coated Zry-2.....   | 47  |
| 3.6.5. | AISI 348 SS.....  | 49  |
| 3.7.   | Results: INCT.....  | 51  |
| 3.7.1. | Uncoated Zr-based alloys: reference samples.....                        | 51  |
| 3.7.2. | PVD Cr coated Zry-2.....  | 54  |
| 3.7.3. | PVD Cr/Cr <sub>2</sub> AlC/Cr (MAX phase) coated Zry-4.....             | 56  |
| 3.7.4. | ZrSi-Cr PVD coated Zry-2.....   | 57  |
| 3.7.5. | AISI 348 SS.....  | 59  |
| 3.8.   | Discussion.....   | 61  |
| 4.     | HIGH TEMPERATURE OXIDATION.....   | 64  |
| 4.1.   | Experimental procedures and setups.....                                 | 65  |
| 4.1.1. | CTU/UJP.....  | 65  |
| 4.1.2. | VTT.....  | 67  |
| 4.1.3. | KIT.....  | 68  |
| 4.1.4. | MTA EK.....   | 69  |
| 4.2.   | Results: CTU/UJP.....   | 71  |
| 4.3.   | Results: VTT.....   | 84  |
| 4.3.1. | Cr coated Zry-2.....  | 84  |
| 4.3.2. | Cr/Cr <sub>2</sub> AlC/Cr (MAX phase) PVD coated Zry-4.....             | 88  |
| 4.3.3. | AISI 348 SS.....  | 94  |
| 4.4.   | Results: KIT.....   | 99  |
| 4.4.1. | PVD Cr Coated Zry-2.....  | 99  |
| 4.4.2. | PVD MAX Phase Coated Zry-4.....   | 101 |
| 4.4.3. | PVD ZrSi-Cr Coated Zry-2.....   | 103 |
| 4.4.4. | AISI 348 SS.....  | 104 |
| 4.5.   | Results: MTA EK.....  | 106 |
| 4.5.1. | Steam oxidation: PVD Cr coated Zr1%Nb.....                              | 106 |
| 4.5.2. | Air oxidation test for PVD Cr coated Zr1%Nb.....                        | 108 |
| 4.5.3. | Ring compression test.....  | 109 |
| 4.5.4. | SEM investigations.....   | 113 |
| 4.5.5. | Metallography and Microhardness.....                                    | 115 |
| 4.6.   | Discussion.....   | 117 |
| 5.     | MODELLING BENCHMARK FOR FECRAL CLADDING.....                            | 119 |
| 5.1.   | Introduction.....   | 119 |
| 5.2.   | Specifications for the benchmark calculations.....                      | 120 |
| 5.2.1. | Normal operating conditions cases.....                                  | 120 |
| 5.2.2. | Loss of coolant conditions cases.....                                   | 121 |
| 5.3.   | Description of fuel performance codes.....                              | 122 |
| 5.3.1. | BISON.....  | 122 |
| 5.3.2. | TRANSURANUS.....  | 123 |
| 5.3.3. | FEMAXI.....   | 125 |
| 5.3.4. | FRAPCON-USP.....  | 126 |
| 5.3.5. | BACO.....   | 126 |
| 5.4.   | Benchmark results for normal operating conditions.....                  | 127 |
| 5.4.1. | Reference calculations for Zircaloy-4 cladding.....                     | 128 |
| 5.4.2. | Comparisons of calculation results for FeCrAl cladding.....             | 131 |
| 5.5.   | Benchmark results for loss of coolant conditions.....                   | 136 |
| 5.5.1. | Time-dependent hoop strain predictions for FeCrAl.....                  | 136 |
| 5.5.2. | Burst failure predictions for FeCrAl and comparisons to Zircaloy-4..... | 137 |

|  |     |
|--|-----|
| 5.6. Conclusions and recommendations .....   | 139 |
| 6. BENCHMARK ON THE QUENCH-19 BUNDLE TEST WITH ATHLET-CD<br>AND SOCRAT CODES ..... | 141 |
| 6.1. Introduction .....  | 141 |
| 6.2. Temperature history of QUENCH-19 for different bundle elevations .....        | 142 |
| 6.3. Hydrogen release during QUENCH-19 .....                                       | 145 |
| 6.4. Conclusions .....   | 148 |
| CONCLUSIONS AND FUTURE WORK .....  | 149 |
| REFERENCES .....   | 151 |
| ANNEX .....  | 159 |
| ABBREVIATIONS .....  | 161 |
| LIST OF CHIEF SCIENTIFIC INVESTIGATORS .....                                       | 163 |
| CONTRIBUTORS TO DRAFTING AND REVIEW .....  | 165 |



## 1. INTRODUCTION

### 1.1. BACKGROUND

Nuclear fuel for water cooled reactors (both Light Water Reactors (LWRs) and Pressurized Heavy Water Reactors (PHWRs)) is manufactured based on a design of uranium dioxide pellets contained in a cladding of zirconium base alloy. Since the first use of this fuel type in the 1960s and 1970s there have been many incremental improvements made to both fuel pellets and cladding, and fuel now routinely reaches burnup in excess of 60 MWd/kgU in LWRs, around three times the burnup of the early fuel designs. Increased fuel burnup and long operating experience have been accompanied by significant improvements in the fuel safety, that is why fuel failures under normal operation or transient conditions are currently rare.

However, the experience of the Fukushima accident in Japan highlighted the vulnerability of zirconium - cladding to severe accident conditions. In this accident, cooling was lost for many days and the overheating cladding reacted with steam to produce hydrogen. This induced fuel melting and hydrogen explosion as temperatures rose. In response to this event it is considered important to investigate other fuel designs that would be more resistant to such severe accidents, whilst retaining the reliability and burnup potential of current fuel designs. Many Member States are now considering new fuel types that range from using an oxidation resistant coating on zirconium based cladding to alternate fuel and cladding materials.

These new fuels/claddings under development must be licensed before being deployed industrially and therefore research is undertaken to assess their behaviour in various conditions.

Development and verification of computer codes to model nuclear fuel behaviour are possible only on the basis of good experimental data that requires very durable and expensive studies. That is why international cooperation in this area is highly desirable, and the IAEA traditionally supports interested Member States in their efforts to enhance capacities of their computer codes used for prediction of fuel behaviour.

### 1.2. OBJECTIVES

The objectives and scope of the IAEA CRP on Analysis of Options and Experimental Examination of Fuels for Water Cooled Reactors with Increased Accident Tolerance (ACTOF) (2015–2019) were the acquisition of data through experiments on new fuel types and cladding materials, development of modelling capacity to predict the behaviour of the components and the integral performance of accident tolerant fuel designs under normal and transient conditions and to demonstrate improvements under severe accident conditions. The goal was to provide information to Member States on the choices available to improve the safety of Nuclear Power Plants under normal and accident conditions.

The licensing of novel ATF materials requires series of testing and safety evaluations that involve different industrial and regulatory experts. This necessitates the coordinated efforts on new materials testing, evaluation, and modelling. This is why the CRP ACTOF focused on the following two important areas for ATF:

- Collecting good quality test data for candidate ATF materials which can be used for performance and safety evaluation and to develop materials models in fuel performance codes;
- Revising and improving computer codes with inputs from testing and literature to model and predict ATF behaviour in core.

### 1.3. SCOPE

Various ATF options were analysed within the CRP resulting in improved understanding of ATF's behaviours and developments of ATF technologies in Member States. For example, several coated cladding materials were produced, tested, characterized and analysed in round robin tests. The feedbacks are important for Member States to improve their ATF concepts and development activities.

Fuel performance codes from participating organizations were significantly extended to the analysis of several ATF concepts (including FeCrAl and SiC claddings, coated Zircaloy claddings, and U<sub>3</sub>Si<sub>2</sub> fuel). Furthermore, a benchmark was carried out where the extended codes were compared for the analysis of fuel rod behaviour under both normal operation and design-basis accident conditions. Besides, integral codes

(ATHLET-CD and SOCRAT) were applied and benchmarked against the severe-accident bundle test QUENCH-19 with FeCrAl claddings of fuel rod simulators.

#### 1.4. STRUCTURE

This publication summarizes the finding and conclusions of the CRP ACTOF within a work plan jointly agreed on by 17 participating organizations from 13 Member States. A list of chief scientific investigators from the participating organizations are provided at the end of this publication.

This publication consists of six sections. Material properties of fuel claddings studied in the CRP are summarized in Section 2. Round robin tests carried out in the framework of the CRP including sample production and their long-term corrosion testing are presented in Section 3, whereas results of high-temperature oxidation of different samples are compared in Section 4. Results of benchmark exercises for FeCrAl cladding behaviour under normal operation and design basis accident (LOCA) conditions using several fuel performance codes extended to analysis of advanced cladding materials, are presented in Section 5. A benchmark exercise on the bundle test QUENCH-19 with the integral codes ATHLET-CD and SOCRAT is described in Section 6.

TECDOC individual contributions submitted by the participants are compiled in the Annex of this report.

## 2. MATERIALS PROPERTIES

### 2.1. FeCrAl cladding

One of the most significant issues in the Fukushima Daiichi accident was zircaloy oxidation leading to a large production of hydrogen within the core. Oxidation resistant FeCrAl alloys have been proposed as cladding materials for LWR fuel rods with improved accident tolerance. Oxidation rates of FeCrAl are one to three orders of magnitude lower than zircaloy [1–4]. Moreover, the stiffness of FeCrAl is approximately twice that of zircaloy [1], and the yield stress is a factor of four higher [4]. The melting point of FeCrAl alloys is within 1525–1540°C [5]. While the oxidation resistance of FeCrAl is beneficial in terms of accident tolerance, the thermal neutron absorption cross section is about ten times that of zircaloy. This neutronic penalty can be partially compensated by reducing the thickness of the cladding. This allows for a slightly larger pellet radius with the same pellet-to-cladding gap. However, in addition to the slight increase in pellet radius, enriching the fuel beyond the current 5% limit appears to be necessary to compensate for the neutronic penalty [6]. Current estimates indicate that this will imply an increase in fuel cost of 15–35% [1, 4]. Furthermore, a larger tritium release to the coolant is anticipated because the permeability of hydrogen in FeCrAl is about 100 times higher than in zircaloy [7]. Finally, radiation induced hardening and embrittlement of FeCrAl still need to be fully characterized experimentally [8].

FeCrAl alloys for application as nuclear fuel cladding material are currently under development and characterization. Material property data are still limited and mostly from out-of-pile tests. However, recently, work has been performed at Oak Ridge National Laboratory (ORNL) to develop FeCrAl alloys specifically for nuclear applications [3, 9–12]. This work has ultimately led to the development and characterization of the laboratory optimized FeCrAl alloy known as C35M [9]. This alloy (or similar) is a leading contender to be included in a lead test rod or assembly in a commercial reactor in 2022 as irradiation testing has been performed in the Halden Reactor [11] and is underway in the Advanced Test Reactor (ATR) at INL [13]. The ORNL FeCrAl alloy C35M is Fe-13Cr-4.5Al + Y with minor alloying additions of molybdenum and silicon. Alloy composition is given in Table 1.

Based on the experimental data from tests performed at ORNL and at the Halden Reactor, researchers at ORNL and INL have developed empirical models for C35M properties and behaviour [3, 9–11, 14]. Specifically, models have been developed for thermophysical properties as a function of temperature, thermal and irradiation creep, volumetric swelling, and oxidation. Furthermore, a failure criterion for FeCrAl during loss-of-coolant accident (LOCA) conditions has been developed [14]. Models and properties developed at ORNL and INL have been published in recent years [3, 9–11, 14].

Based on this work, a set of material properties and models for FeCrAl C35M was constructed. For areas where C35M experimental data is non-existent, data from the commercial alloy Kanthal APMT were used [14]. Although this collection of properties may be extended and updated in the future, it is sufficiently complete to allow for fuel performance calculations with FeCrAl cladding. This information was provided to the participants in the FeCrAl modelling benchmark organized in ACTOF [15]. This set of material properties and models for FeCrAl C35M is overviewed in the following subsections.

TABLE 1. NOMINAL COMPOSITION OF THE ORNL FeCrAl ALLOY C35M [9].

| Fe    | Cr | Al  | Y    | Mo | Si  | Remarks            |
|-------|----|-----|------|----|-----|--------------------|
| 80.15 | 13 | 4.5 | 0.15 | 2  | 0.2 | Arc-melt + hot-rol |

#### 2.1.1. Thermophysical properties

The thermal conductivity and specific heat of Kanthal APMT (used in the absence of thermal property data of C35M) were obtained from [16]. The values are shown in Table 2 and Table 3, respectively. Piecewise linear interpolation was used in [14]. The thermal expansion coefficient (TEC) values as a function of temperature were also obtained from [16]. The mean TEC values for different temperature ranges are given in Table 4. To obtain the instantaneous thermal expansion coefficient as a function of the temperature, the methodology of Niffenegger and Reichlin [17] was employed in [14].

TABLE 2. THERMAL CONDUCTIVITY OF KANTHAL APMT [16]

| Temperature (K) | Thermal conductivity (W/m·K) |
|-----------------|------------------------------|
| 323             | 11                           |
| 873             | 21                           |
| 1073            | 23                           |
| 1273            | 27                           |
| 1473            | 29                           |

TABLE 3. SPECIFIC HEAT OF KANTHAL APMT [16]

| Temperature (K) | Specific heat (J/kg·K) |
|-----------------|------------------------|
| 293             | 480                    |
| 173             | 560                    |
| 673             | 640                    |
| 873             | 710                    |
| 1073            | 670                    |
| 1273            | 690                    |
| 1473            | 700                    |

TABLE 4. COEFFICIENT OF THERMAL EXPANSION (CTE) OF KANTHAL APMT [16]

| Temperature range (K) | CTE ( $\mu\text{m}/\text{m}\cdot\text{K}$ ) |
|-----------------------|---|
| 293–523               | 12.4  |
| 293–773               | 13.1  |
| 293–1023              | 13.6  |
| 293–1273              | 14.7  |
| 293–1473              | 15.4  |

### 2.1.2. Mechanical properties

The temperature dependent Young's modulus and Poisson's ratio of C35M were obtained from Thompson et al. [10] as a function of temperature:

$$E = -5.46 \times 10^{-5} T^2 - 3.85 \times 10^{-2} T + 1.99 \times 10^2 \quad (1)$$

$$\nu = 3.85 \times 10^{-5} T - 2.68 \times 10^{-1} \quad (2)$$

where

- $E$  Young's modulus (GPa);
- $\nu$  Poisson's ratio;
- $T$  temperature (°C).

These equations are valid for temperatures ranging from 25–850°C.

Data for the yield stress (YS) and ultimate tensile strength (UTS) of C35M as a function of temperature were given by Yamamoto et al. [9] and are shown in Table 5 and Table 6, respectively. Piecewise linear interpolation of the data was used in [14]. According to the observations on other ferritic and martensitic steels [18], the UTS continuously reduces to zero at the melting point. On this basis, a data point of UTS of zero was added at the melting point of C35M (1773 K) for linear interpolation [14]. Considering that the YS approaches the UTS at the mid-range temperatures, a YS of zero at the melting point was also set.

TABLE 5. YIELD STRESS OF FeCrAl ALLOY C35M [9, 14]

| Temperature (K) | Yield stress (MPa) |
|-----------------|--------------------|
| 291             | 447                |
| 546             | 314                |
| 640             | 296                |
| 825             | 226                |
| 1007            | 67                 |
| 1773            | 0                  |

TABLE 6. ULTIMATE TENSILE STRENGTH OF FeCrAl ALLOY C35M [9, 14]

| Temperature (K) | Ultimate tensile strength (MPa) |
|-----------------|---------------------------------|
| 295             | 569                             |
| 551             | 543                             |
| 644             | 527                             |
| 830             | 289                             |
| 1012            | 65                              |
| 1773            | 0                               |

### 2.1.3. Thermal and irradiation creep

Models for thermal and irradiation creep of FeCrAl C35M are given in [11] and are based on experimental data from in-pile and out-of-pile creep tests carried out at Halden and at ORNL. The thermal creep correlation takes the form of the Norton power law

$$\dot{\epsilon} = 2.89 \times 10^{-36} \sigma^{5.5} \exp\left(\frac{-297}{T}\right) \quad (3)$$

at temperatures below 873 K. Above 873 K, the correlation from Saunders et al. [19] is used

$$\dot{\epsilon} = 5.96 \times 10^{-2} \sigma^{5.5} \exp\left(\frac{-47136}{T}\right) \quad (4)$$

where

- $\dot{\epsilon}$  creep rate ( $s^{-1}$ );
- $\sigma$  effective (von Mises) stress (Pa);
- $T$  temperature (K).

For irradiation creep, a creep coefficient  $5 \times 10^{-6}$  per MPa per dpa is recommended in [11]. Using a conversion factor of  $1 \times 10^{25}$  neutrons·m<sup>-2</sup> = 0.9 dpa [20], the following correlation for irradiation creep is derived [14]

$$\dot{\epsilon} = 4.5 \times 10^{-31} \sigma \varphi \quad (5)$$

where

- $\sigma$  effective stress (MPa);
- $\varphi$  fast neutron flux (neutrons·m<sup>-2</sup>·s<sup>-1</sup>).

### 2.1.4. Swelling

To model the swelling of C35M, a preliminary approach has been proposed in [14] whereby an upper bound swelling rate from Terrani et al. [11] of 0.05% per dpa is used. Considering the same conversion factor as for irradiation creep, i.e.  $1 \times 10^{25}$  neutrons/m<sup>-2</sup> = 0.9 dpa [20], integration over time results in the following correlation for the volumetric swelling strain

$$\epsilon = 4.5 \times 10^{-29} \Phi \quad (6)$$

where  $\Phi$  is the fast neutron fluence (neutrons·m<sup>-2</sup>).

### 2.1.5. Oxidation

Waterside oxidation of FeCrAl at normal operating temperatures was investigated through autoclave experiments by Terrani et al. [3]. The experiments were conducted at temperatures 330°C for PWR conditions and 290°C for BWR conditions. The oxidation kinetics is governed by a parabolic law for the growth of the chromium rich chromite (FeCr<sub>2</sub>O<sub>4</sub>) layer

$$w = k\sqrt{t} \quad (7)$$

where

- $k$  parabolic oxidation rate constant (mg·cm<sup>-2</sup>·h<sup>-1/2</sup>);
- $t$  time (h).

Then, thickness of the chromite layer is given by

$$\delta = w/\rho_{ox} \quad (8)$$

where  $\rho_{ox}$  is the density of oxygen in chromite (1440 kg/m<sup>3</sup>) [3].

The parabolic rate constants given in [3] are  $3.96 \times 10^{-3}$  for PWR and  $4.51 \times 10^{-4}$  mg·cm<sup>-2</sup>·h<sup>-1/2</sup> for BWR-NWC (normal water chemistry) coolant conditions. These rate constants correspond to a FeCrAl alloy with composition

of Fe-13Cr-4Al, which among the alloys investigated in [3] is the one that represents C35M most closely. Note that these parameters are independent of temperature. New data will be necessary in order to be able to account for the temperature dependence of the oxidation rate. However, the current model is representative of FeCrAl behaviour under normal operating conditions. Also note that besides the formation of an oxide scale, additional metal will dissolve in the water, resulting in a further reduction of the overall cladding thickness [3]. This dissolution process does not occur in zirconium based claddings.

### 2.1.6. Burst failure criterion

A failure model for FeCrAl under loss of coolant accident (LOCA) conditions was developed at INL [14]. The model consists of an overstress criterion, which establishes that cladding failure occurs when the local hoop stress exceeds a limiting burst stress. This concept is analogous to overstress criteria used for burst failure of zircaloy under loss-of-coolant conditions [21]. The burst stress varies as a function of temperature and was derived on the basis of the failure data from recent out-of-pile FeCrAl cladding burst tests completed at ORNL by Massey et al. [12]. To the best of our knowledge, Massey et al.'s are the only experimental data available on burst failure behaviour of FeCrAl claddings under LOCA conditions at this time. From the measured tube pressures, data were given in [12] in terms of hoop stress according to temperature at burst failure. Using a least squares method, a best fit to the data was performed in [14] to obtain a correlation for burst (hoop) stress as an exponential function of temperature. It was also noted that at low temperatures the UTS provided a conservative failure criterion. Therefore, the developed correlation for the burst stress  $\sigma_{burst}$  (in MPa) is given by [14]:

$$\sigma_{burst} = \begin{cases} \text{UTS} & \text{for } T \leq 797 \text{ K} \\ 28441 \exp(-0.005588 T) & \text{for } T > 797 \text{ K} \end{cases} \quad (9)$$

where

UTS Ultimate Tensile Strength (in MPa);

$T$  temperature (in K).

The exponential decay of the burst stress with increasing temperature matches the functional form of Erbacher et al. for zircaloy claddings [21] (without consideration of the oxygen content effect). Note that the experimental burst data from [12], upon which the criterion is based, were obtained from tests of ORNL first-generation FeCrAl cladding tubes, whereas C35M is a second generation alloy. The first generation alloys are expected to be less resistant than C35M [9]. In the absence of specific data for the burst behaviour of C35M, however, the burst criterion described above is expected to provide conservative LOCA burst failure predictions for C35M.

## 2.2. $\text{U}_3\text{Si}_2$ fuel

The main advantage of  $\text{U}_3\text{Si}_2$  over  $\text{UO}_2$  fuel is the higher thermal conductivity. Thermal conductivity of  $\text{UO}_2$  is  $\sim 2\text{--}5 \text{ W}\cdot\text{m}^{-1}\cdot\text{K}^{-1}$  whereas the thermal conductivity of  $\text{U}_3\text{Si}_2$  is  $\sim 15\text{--}30 \text{ W}\cdot\text{m}^{-1}\cdot\text{K}^{-1}$ . This large difference results in lower fuel centreline temperatures and lower temperature gradients in the fuel pellet. This in turn can reduce pellet cracking and fission gas release from fuel. Also, the high uranium density of  $\text{U}_3\text{Si}_2$  ( $11.3 \text{ gU}/\text{cm}^3$  versus  $9.7 \text{ gU}/\text{cm}^3$  for  $\text{UO}_2$  [22]) is economically attractive since it may enable higher burnup and longer cycle length.

Work to date indicates that  $\text{U}_3\text{Si}_2$  is more susceptible to chemical reaction than is  $\text{UO}_2$ . For example, Harp et al. [23] reported a "layered structure of corrosion products" on the surface of  $\text{U}_3\text{Si}_2$  subjected to contact with water at  $300^\circ\text{C}$  for up to 24 hours. Furthermore, the authors reported interdiffusion of  $\text{U}_3\text{Si}_2$  and zircaloy when tested at  $800^\circ\text{C}$  for 100 hours. Fe and Cr phases formed at the interface, with  $\text{ZrSi}_2$  and U-rich areas in zircaloy also present. The authors indicated that further studies are needed, but it is clear that  $\text{U}_3\text{Si}_2$  is more active than  $\text{UO}_2$ .

Oxidation of  $\text{U}_3\text{Si}_2$  has been investigated, e.g. in [24–26]. In particular, Wood et al. [24] explored the possibility to increase the oxidation resistance of  $\text{U}_3\text{Si}_2$  and showed that oxidation in air at  $400^\circ\text{C}$  improved with the addition of aluminum. However, any alloying element decreases the uranium content per volume, diminishing the high uranium density advantage of the fuel.

Other potential disadvantages of  $\text{U}_3\text{Si}_2$  as a fuel material include its lower melting temperature ( $\sim 1938 \text{ K}$ ) and possible large amount of gaseous swelling. Finlay et al. [27] reported significant swelling of  $\text{U}_3\text{Si}_2$  under

irradiation. However, they attributed the high swelling to a change from a crystalline to an amorphous state. This change may not occur at power reactor temperatures, and therefore the swelling may be considerably lower than originally assumed. The micrographs of  $U_3Si_2$  irradiated under power reactor temperatures in 1965 from Shimizu [28] showed that the material maintained a polycrystalline structure. From the micrographs, a large amount of gaseous swelling of the order of 10% at a burnup of 6 GWd/tU could be estimated [29], which is consistent with the fuel density variation measurements reported in the original experiment report [28].

However, the recent experimental irradiation in the Advanced Test Reactor (ATR) at Idaho National Laboratory has indicated that very low gaseous swelling and fission gas release occurred, at least at the low burnup reached to date (<20 GWd/tU) [30]. Formation of fission gas bubbles resolvable with optical microscopy occurred from the fuel pellet center outward to approximately 60% of the pellet radius. Other post irradiation examination results from this recent experiment include limited cracking in comparison with the expected behaviour of  $UO_2$  at the same power level. In addition, gamma scanning data did not reveal migration of fission products. Minor homogeneous hardening along the pellet radius due to accumulation of fission products and radiation damage was measured [30]. Scaling up the process to enable fueling whole assemblies and reactors remains to be done, with challenges still to be met [26].

In this Section, we give a brief account of fundamental material properties from  $U_3Si_2$  obtained from the existing literature, including thermophysical properties, mechanical properties and swelling. A more comprehensive review is given in [31].

### 2.2.1. Specific heat

For the specific heat of  $U_3Si_2$ , based on White's data [22] as well as data from Knacke et al. [32], the following empirical fit has been reported in [31]:

$$c_p = 141 + 0.02582 \times 10^{-2} T \quad (10)$$

where

$$\begin{aligned} c_p & \text{ specific heat capacity (J}\cdot\text{mol}^{-1}\cdot\text{K}^{-1}\text{);} \\ T & \text{ temperature (K).} \end{aligned}$$

### 2.2.2. Thermal conductivity

An empirical thermal conductivity model for  $U_3Si_2$  based upon experiments by White et al. [33] is

$$k = 4.996 + 0.0118 T \quad (11)$$

where

$$\begin{aligned} k & \text{ thermal conductivity (W/m}\cdot\text{K);} \\ T & \text{ temperature (K).} \end{aligned}$$

This model is valid for  $300 < T < 1773$  K.

Alternatively, based on the experimental data from White [22], Shimizu [28], Mohamad [34] and Antonio [35], the following empirical polynomial fit for the thermal conductivity of  $U_3Si_2$  has been reported in [31]:

$$\begin{aligned} k = & 9.029 \times 10^{-15} T^5 - 4.609 \times 10^{-11} T^4 + 8.676 \times 10^{-8} T^3 \\ & - 7.485 \times 10^{-5} T^2 + 4.166 \times 10^{-2} T + 0.5211 \end{aligned} \quad (12)$$

Equation (12) is applicable for  $13 < T < 1500$  K [31].

### 2.2.3. Thermal diffusivity

Based on the data from White et al. [22] and Mohamad [34], the following fit for the thermal diffusivity of  $U_3Si_2$  has been reported in [31]:

$$\alpha = -9.899 \times 10^{-7} T^2 + 5.797 \times 10^{-3} T + 1.603 \quad (13)$$

where  $\alpha$  is the thermal diffusivity ( $mm^2/s$ ).

### 2.2.4. Coefficient of thermal expansion

The linear thermal expansion coefficient of  $U_3Si_2$  is reported in multiple locations within the literature. We refer here to the work of White et al. [22], who determined the properties on sintered compacts under inert atmospheres in a dilatometer from 273 to 1673 K and reported for the coefficient of thermal expansion a constant value of  $16.1 \times 10^{-6} \pm 1.3 \times 10^{-6} K^{-1}$ .

### 2.2.5. Young's modulus and Poisson's ratio

Shimizu studied the Young's modulus of  $U_3Si_2$  on arc-cast specimens using compression testing and determined an average value of  $96 \text{ GPa} \pm 40 \text{ GPa}$  [28]. Taylor and McMurtry [36] determined a value of  $125 \text{ GPa} \pm 4 \text{ GPa}$  on sintered bars of  $U_3Si_2$  using a sonic method. This is consistent with Shimizu's value, but with a significantly higher error. These data were reported in [31].

Values for the Poisson's ratio of  $U_3Si_2$  have also been reported on sintered pellets to be  $0.183 \pm 0.003$  [37] and on spark plasma sintered pellets at  $0.2 \pm 0.1$  [34]. General agreement is observed between all values, but 0.184 was recommended in [31].

### 2.2.6. Swelling

An initial empirical model for swelling of  $U_3Si_2$  was derived in [38]. The swelling of fuel particles was calculated by Finlay et al. [27] using the results of miniplate irradiation tests. To convert Finlay's data (fission density) to FIMA, a value of  $10.735 \text{ g/cm}^3$  was used as the heavy metal density, equivalent to 95% theoretical heavy metal density. Based on Finlay's data the volumetric swelling strain can be written as a function of burnup:

$$\frac{\Delta V}{V} = 3.8808 \times bu^2 + 0.79811 \times bu \quad (14)$$

where

$$\frac{\Delta V}{V} \quad \text{volumetric strain (dimensionless);}$$

bu burnup (FIMA).

The quadratic equation for the total volumetric strain is then decoupled into its solid and gaseous components. Based on Hofman [39] and the same conversion procedure from fission density to burnup, the solid swelling correlation is:

$$\left(\frac{\Delta V}{V}\right)_{solid} = 0.34392 \times bu \quad (15)$$

Equation (15) subtracted from Eq. (14) results in a gaseous swelling contribution given by the following quadratic function of burnup:

$$\left(\frac{\Delta V}{V}\right)_{gaseous} = 3.8808 \times bu^2 + 0.45419 \times bu \quad (16)$$

Recently, physical models for gaseous swelling and fission gas release in  $U_3Si_2$  based on rate theory and multiscale approaches have been developed [29, 40]. There is, however, a need for experimental data of fission gas bubble characteristics, swelling and release in order to further develop and validate fission gas models for  $U_3Si_2$ .

Among the other current data needs for  $U_3Si_2$  fuel, we mention in-pile densification and thermal and irradiation creep.

### 2.3. SiC cladding

To analyze the SiC cladding behavior, the following properties are of most importance to consider: thermal conductivity, elastic modulus, shear modulus, Poisson's ratio, hardness, thermal expansion, creep, swelling, fracture strength, emissivity, corrosion, crud accumulation, density, decomposition temperature etc. These properties are closely influenced by the manufacturing and architecture of the SiC Ceramic Matrix Composite. Based on the available data, the material hand books for SiC and the three technical reports from CNPRI, CIAE and NPIC, a summary of the SiC properties is provided below.

#### 2.3.1. Specific Heat

The specific heat of SiC<sub>f</sub>/SiC highly depends on temperature and has negligible sensitivity on neutron irradiation. At temperature above 200 K, the specific heat increases slowly with temperature and the relationship ranging from 200 to 2400 K can be expressed as follows based on the CIAE's report:

$$C_p = 925.65 + 0.3772T - 7.9259 \times 10^{-5}T^3 - 3.1946 \times 10^{-7}T^2 \quad (17)$$

(200 < T < 2400 K)

where

$C_p$  specific heat (J/kg·K);

$T$  temperature (K).

The uncertainties recommended are  $\pm 7\%$  (200  $\leq T \leq$  1000 K) and  $\pm 4\%$  (1000  $\leq T \leq$  2400 K).

#### 2.3.2. Thermal conductivity

The thermal conductivity of SiC composite is affected by temperature and fast fluence. The temperature dependence of SiC was based on the measured data of SiC composites and the displacement damage (measured in dpa, using the conversion factor  $1 \times 10^{25}$  neutrons/m<sup>2</sup> = 1 dpa) [179–181]. An empirical relation of thermal conductivity as a function of temperature and dpa was developed [177],

$$k_{clad} = k_{sat} \left( \frac{(d+d_0)}{d_{sat}} \right)^{-0.4} \quad (18)$$

where

$d$  cumulative cladding dpa;

$d_0$  effective dpa for  $k(T) > k_{sat}$ ,

which is the cladding thermal conductivity after reaching the saturation dpa. Regardless of temperature, it is supposed that the thermal conductivity saturates after 1 dpa at 4 W/m·K in this model. The effective dpa factor should take into account the temperature effect,

$$d_0 = d_{sat} \left( \frac{k_{sat}}{k(T)} \right)^{2.5} \quad (19)$$

Before reaching the radiation saturation, the temperature dependence of the cladding follows the relation,

$$k(T) = 8 \times 10^{-6}T_{clad}^2 - 0.02T_{clad} + (k_{rt} + 46.4) \quad (20)$$

where

$k_{rt}$  is the cladding thermal conductivity at room temperature (300 K) and 0 dpa;

$T$  is the cladding temperature at the current geometric mesh point (K).

During the irradiation progresses, the thermal conductivity changes slightly with temperature. This suggested that the saturation conductivity is a constant value after reaching the saturation dpa.

A different reference and formula were used by CIAE. The thermal conductivity of SiC<sub>f</sub>/SiC can be summarized as the harmonic average of non irradiated thermal conductivity  $K_{non-irr}$  and the reciprocal of thermal defect resistance  $1/K_{rd}$ . The non irradiated thermal conductivity is theoretically expressed as a function of

$[A+BT]^{-1}$  with constants  $A$  and  $B$ . The thermal defect resistance reflects the linear relationship in the low range of fast neutron dose and saturation in after a threshold neutron fluence, therefore, the expression can be expressed in a similar form (with respect to dose) [175].

$$\frac{1}{K_{irr}} = \frac{1}{K_{non-i}} + \frac{1}{K_{rd}} \quad (21)$$

$$\begin{cases} \frac{1}{K_{non-irr}} = 36.262 \times 10^{-3} + 15.256 \times 10^{-6}T \\ \frac{1}{K_{rd}} = 52.632 \times 10^{-3} + 35.582 \times 10^{-3}D \end{cases} \quad (22)$$

where

$K_{irr}$  is the thermal conductivity ( $\text{W}\cdot\text{m}^{-1}\cdot\text{K}^{-1}$ );

$T$  is the temperature (K);

$D$  is displacement damage (dpa), related to the neutron fluence with the conversion factor  $1 \times 10^{25}$  neutrons/ $\text{m}^2 = 1$  dpa [179–181].

NPIC use the following equation for thermal conductivity as a function of temperature

$$k_{SiC} = \frac{17885}{T} + 2 \quad (23)$$

### 2.3.3. Emissivity

Based on the available data on composites, a constant value of the cladding emissivity 0.8 ( $\varepsilon = 0.8$ ) was obtained from the individual report from CNPRI.

CIAE used a different reference for surface emissivity as a function of temperature. The surface emissivity of SiCf nearly not change with the neutron fluence and is linearly interpolated between 0.82 at 1400 K and 0.92 at 1100 K, it is expressed as,

$$E_{mit} = \begin{cases} 0.92, & T < 1100\text{K} \\ 1.287 - 0.333 \times 10^{-3}T, & 1100 \leq T \leq 1400\text{K} \\ 0.82, & T > 1400\text{K} \end{cases} \quad (24)$$

where

$E_{mit}$  emissivity (dimensionless);

$T$  temperature (K).

NPIC use a different thermal conductivity model for the SiC layer and SiC matrix due to the differences in the fabrication and chemical component. In addition, Si and C exhibit similar electronegative property; thus, SiC is mainly combined by C and Si with the covalent bond according to Principle of Electro negativity. The thermal resistance of SiC can be simplified as the equation below by neglecting the contribution to the electron to the thermal conductivity at high temperatures.

$$\frac{1}{k} = R_m + R_{gb} + R_u + R_{id} \quad (25)$$

where

$k$  thermal conductivity ( $\text{W}\cdot\text{m}^{-1}\cdot\text{K}^{-1}$ );

$R$  thermal resistance (K/W);

and  $m, gb, u, id$  stand for matrix, grain boundary, phonon scattering and irradiation, respectively.

Matrix, grain boundary and phonon scattering is irrelevant to irradiation but dependent on the temperature. Accordingly, the equation can be simplified further as below:

$$\frac{1}{k} = R_0 + R_{irr} \quad (26)$$

where  $R_0$  and  $R_{irr}$  are the thermal resistance (K/W) of the prior- and post irradiated SiC, respectively.

The thermal resistance ( $R_0$ ) of prior-irradiated SiC matrix is expressed as below:

$$R = \frac{1}{-3.7 \times 10^{-8}T^3 + 1.54 \times 10^{-4}T^2 - 0.214T + 153.1} \quad (27)$$

The thermal resistance induced by the irradiation ( $R_{irr}$ ) is expressed as follows:

$$R_{irr} = \frac{1}{6.08 \cdot S} \quad (28)$$

#### 2.3.4. Volumetric thermal expansion

According to the published data, compared to the pure SiC, the linear thermal expansion coefficient for SiC composites has weaker temperature dependence, and is generally between  $2 \times 10^{-6}$  and  $5 \times 10^{-6} \text{ K}^{-1}$ . It is not clear whether there is a significant difference between swelling parallel and perpendicular to the fiber axis, so it was supposed that the expansion coefficient is identical in each direction. In addition, because of the lack of data on variation with temperature, a constant value was used. The thermal expansion coefficient for SiC cladding is set to  $4 \times 10^{-6} \text{ K}^{-1}$  per CNPRI's report (see Annex).

CIAE used a different reference for linear thermal expansion as a function of temperature (see Annex). The thermal expansion is expressed as a function of temperature range from 293 to 1273 K and irradiation has little influence on it.

$$\alpha_L = -0.7765 + 1.435 \times 10^2 T - 1.2209 \times 10^5 T^2 + 3.8289 \times 10^9 T^3 \quad (29)$$

$(293 \text{ K} < T < 1273 \text{ K})$

where

$\alpha_L$  linear thermal expansion coefficient ( $\text{K}^{-1}$ );

$T$  is the temperature (K).

NPIC used the following equation for linear thermal expansion coefficient for SiC as a function of temperature (see Annex):

$$\alpha_L (\times 10^{-6}) = \begin{cases} -1.8267 + 0.0178T - 1.5544 \times 10^{-5} T^2, & T > 1273 \text{ K} \\ 5.0 & + 4.5246 \times 10^{-9} T^3, & T < 1273 \text{ K} \end{cases} \quad (30)$$

where

$\alpha_L$  linear thermal expansion coefficient of SiC ( $\text{K}^{-1}$ );

$T$  temperature (K);

$E_{SiC}$  elastic modulus of SiC (Pa);

$k_{SiC}$  thermal conductivity of SiC ( $\text{W} \cdot \text{m}^{-1} \cdot \text{K}^{-1}$ ).

#### 2.3.5. Elastic constant

Young's modulus as a function of temperature was specified using a linear relation per CNPRI's report,

$$E(T) = 4.6 \times 10^5 - 40 T \exp\left(\frac{-962}{T}\right) \quad (31)$$

where  $T$  is given in K, and  $E$  is in MPa, which is expected to be valid for composites around the typical cladding temperature of 600 K.

It is also expected that the modulus may decrease slightly with irradiation. Using a conservative average for the behaviour, it is supposed that the Young's modulus decreases exponentially, and saturates at 40% of the unirradiated value after 20 dpa. The relation based on this assumption gives

$$E(T, f) = E(T) \left(1 - 0.4 \left(1 - \exp\left(-\frac{3f}{20}\right)\right)\right) \quad (32)$$

Poisson's ratio used for SiC/SiC is  $\nu = 0.13$ .

The shear modulus is calculated as

$$G = \frac{E}{2(1+\nu)} \quad (33)$$

where

$G$  shear modulus;

$E$  Young's modulus;

$\nu$  Poisson's ratio.

CIAE used a different reference for elastic modulus for composites. The composites exhibited excellent irradiation resistance, 15–20% degradation in elastic modulus from the unirradiated state to 12 dpa at 750°C. According to the reference, Young's modulus reduces 35% from the room temperature to 1400°C. With these data, it can be expressed by

$$E_0 = 212 \times (-1.7578 \times 10^{-7}T^2 + 1.7676 \times 10^{-4}T + 1.0) \quad (34)$$

$$E_{irr} = E_0 \left( 0.7158 + \frac{1}{D+3.5322} \right) \quad (35)$$

where

$E_0$  non-irradiated elastic modulus (GPa);

$E_{irr}$  irradiated elastic modulus (GPa);

$T$  temperature (K);

$D$  displacement damage measured in dpa, related to the neutron fluence with the conversion factor  $1 \times 10^{25}$  neutrons/m<sup>2</sup> = 1 dpa [179–181].

NPIC used another reference for elastic modulus. The properties SiC layer, SiC matrix and compact PyC materials are taken into accounts in the computation. The elastic modulus of the PyC layer is anisotropic, and can be calculated by the following equation:

$$E_{PyC} = 25.5(0.384 + 0.000324\rho_{PyC})(0.481 + 0.519 \cdot \text{BAF}) \times (1 + 0.23\Phi)(0.9560275 + 0.00015T) \quad (36)$$

where:

$\Phi$  fast neutron flux;

BAF anisotropy parameter (dimensionless);

$T$  temperature.

The elastic modulus of SiC layer is expressed using the following equations:

$$E_{SiC} = 460 - 0.04T \exp\left(-\frac{962}{T}\right) \quad (37)$$

### 2.3.6. Creep

SiC experiences negligible creep below 1000 K according to the CNPRI's report.

### 2.3.7. Yield strength

The yield strength of SiC/SiC depends on both temperature and fast fluence. CNPRI reported that the yield strength of SiC composites versus temperature was modeled as

$$\sigma_u(T) = 2.66 \times 10^4 T + 2 \times 10^8 \quad (38)$$

where  $T$  is given in Kelvin and  $\sigma_u$  in MPa. For brittle materials, the yield strength is very close to the ultimate strength because they experience little plastic deformation before fracturing. For simplicity, the cladding ultimate strength is set to be the same as the yield strength. In addition, the strains at yield and at failure are defined using Young's modulus and the yield and ultimate strengths, respectively.

Combined with irradiation effect, the model incorporates an exponential function that saturates at a 40% reduction in the temperature dependent ultimate tensile and strengths,

$$\sigma_u(T, f) = \sigma_u(T) \left[ 1 - 0.4 \left( 1 - \exp\left(-\frac{3f}{20}\right) \right) \right] \quad (39)$$

where  $f$  is given in dpa.

### 2.3.8. Irradiation swelling

With the limited available information on SiC composites utilizing Hi-Nicalon Type-S fibers, it is assumed to swell with irradiation, exponentially approaching a saturation value of 2  $v/o$ . Based on this model, the swelling

has reached 95% of its saturated value after 1 dpa. Furthermore, it is assumed this swelling show the same behaviour in the plane and through the thickness of the composite, and the maximum linear strain due to irradiation is 0.67%. This linear strain is then given as following equation per CNPRI's report [177],

$$c(f) = 0.67(1 - \exp(-3f)) \quad (40)$$

where  $f$  is given in dpa.

Different from zircaloy, SiC retains its strength and does not creep up to 1300°C, and it is stable under irradiation.

The swelling model of the SiC matrix and SiC cladding was relevant to the temperature and fast neutron flux, which can be written as follows:

$$S = k_s \gamma^{-1/3} \exp\left(-\frac{\gamma}{\gamma_{sc}}\right) \quad (41)$$

where

$S$  swelling rate (%);

$k_s$  coefficient of the swelling rate ( $\text{dpa}^{-2/3}$ );

$\gamma$  neutron dose (dpa);

$\gamma_{sc}$  characteristic dose for swelling saturation by the negative feedback mechanism (dpa).

The swelling of SiC can be obtained from the time integration of the equation below.

$$S = S_s \left[1 - \exp\left(-\frac{\gamma}{\gamma_{sc}}\right)\right]^{2/3} \quad (42)$$

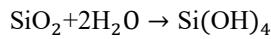
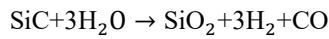
where  $S_s$  and  $\gamma_{sc}$  are function of the temperature, and can be expressed as be below:

$$S_s(T) = 0.05837 - 1.0089 \times 10^{-4}T + 6.9368 \times 10^{-8}T^2 - 1.8152 \times 10^{-11}T^3 \quad (43)$$

$$\gamma_{sc}(\text{dpa}) = -0.4603 + 2.6674 \times 10^{-3}T - 4.3176 \times 10^{-6}T^2 + 2.3803 \times 10^{-9}T^3 \quad (44)$$

### 2.3.9. Oxidation

When SiC exposures to steam, the following two chemical reactions are concerned,



Potential heat of the reactions is set to be 360 kJ/mol and 40 kJ/mol, respectively. The oxidation product of SiC is SiO<sub>2</sub>. The thickness of SiO<sub>2</sub> is described as following equation [176],

$$\frac{dx}{dt} = \frac{\alpha^2 k_p}{2\rho^2 x} - \frac{k_l}{\rho} \quad (45)$$

where

$\alpha$   $\text{MSiO}_2/(\text{MO}_2 - \text{MC}) = 60/(32 - 12) = 3$ ;

$\rho$  density of SiO<sub>2</sub> ( $\text{kg}/\text{m}^3$ );

$k_p$  parabolic rate constant ( $\text{kg} \cdot \text{m}^{-2} \cdot \text{s}^{-1}$ );

$k_l$  linear rate constant ( $\text{kg} \cdot \text{m}^{-2} \cdot \text{s}^{-1}$ ).

The increase of oxide layer describes by the parabolic kinetic model and the recession of oxide layer describes by the linear kinetic model. The net weight change ( $\text{kg}/\text{m}^2$ ) of oxide layer per surface unit is:

$$\Delta w_{\text{net}} = \frac{\alpha k_p}{2k_l} \left[1 + W\left(-\exp\left(\frac{-2k_l^2 t}{\alpha^2 k_p}\right) - 1\right)\right] - k_l t \quad (46)$$

On the right side of the equation, the first term is the increment due to oxidation; the second term is the weight loss due to reaction of SiO<sub>2</sub> and steam.  $W$  represents the Lambert W function.

In order to eliminate the uncertainty caused by the standard error in the fit, we chose the points from published data [178] to make a fitting again, with  $R=8.314 \text{ J}/(\text{mol}\cdot\text{k})$  and unit conversion, the following equations were obtained

$$k_p = 8.6008 \times 10^{-8} \exp\left(-\frac{238000}{8.314}\right) P \quad (47)$$

$$k_1 = 4.5728 \times 10^{-13} \exp\left(-\frac{159000}{8.314T}\right) P^{1.74} v^{0.69} \quad (48)$$

where

- $P$  pressure (Pa);
- $v$  velocity of steam flow (m/s);
- $T$  cladding temperature (K).

#### 2.4. ALLOY 348

Correlations for AISI 348 material properties are presented in the Table 7.

TABLE 7. MATERIAL PROPERTIES OF AISI 348

| Property   | AISI 348 Correlation/Value   |
|--|--|
| Density ( $10^3 \text{ kg}/\text{m}^3$ )                   | 7.94   |
| Melting point ( $^{\circ}\text{C}$ )                       | 1.400  |
| Specific heat ( $\text{J}/\text{g}\cdot\text{K}$ )         | $0.4424 + 0.0001482 T(\text{K})$   |
| Emissivity   | 0.8  |
| Thermal expansion (GPa)                                    | $221049 - 72.9 T(\text{K})$  |
| Thermal conductivity ( $\text{W}/\text{mm}\cdot\text{K}$ ) | $(9.419 + 0.01538 T(\text{K})) \times 10^{-3}$   |
| Poisson's ratio  | $0.2616 + 7.2 \times 10^{-5} T(\text{K})$  |
| Tensile strength at yield (MPa)                            | $268.9 - 0.16 T(\text{K})$   |
| Ultimate strength (MPa)                                    | $-1.3152 T(^{\circ}\text{C}) + 954.3$ if $T(^{\circ}\text{C}) < 200^{\circ}\text{C}$<br>$-0.258 T(^{\circ}\text{C}) + 738.5$ if $200^{\circ}\text{C} < T(^{\circ}\text{C}) < 470^{\circ}\text{C}$<br>$-0.9192 T(^{\circ}\text{C}) + 1050.9$ if $T(^{\circ}\text{C}) > 470^{\circ}\text{C}$ |

### 3. ROUND ROBIN TEST REPORT IN THE FRAMEWORK OF ACTOF

The motivation behind the development work on ATF claddings is based on specific limitations associated with zirconium alloys under design basis and beyond design basis accident scenarios. Zirconium cladding currently used in all LWRs provides adequate material performance while being relatively transparent to neutrons produced in a reactor core. However, high temperature interaction of Zr with steam producing a large volume of heat accompanied by hydrogen release is one of the main contributors to severe core damage and fission product release in nuclear reactor design extension conditions (DEC).

Several potential solutions have been proposed as replacements for the current zirconium based cladding materials, such as improved Zr-based alloys, FeCrAl alloy, Mo-based alloys, SiC composites, various coatings, and modified fuel pellets [1, 42–47]. In the development of new cladding materials, the understanding of their damage mechanisms in both normal operation and accidental conditions is crucial, i.e. the oxidation behaviour and mechanical properties in normal operating conditions and in loss of coolant scenarios and in high temperature steam environments.

During past few decades there have been standard methods and procedures for testing Zr-alloys. However, these methods and standards might not be applicable to the advanced ATF candidate materials. For this reason, a round robin test has been proposed for the ATF candidate cladding materials during the 2nd RCM of the CRP ACTOF. The main objectives were to:

- Test four different ATF cladding candidate materials from four different institutes;
- Study corrosion behaviour of the ATF cladding materials at representative LWR conditions;
- Study high temperature steam oxidation resistance in LOCA-related conditions;
- Compare the methods, procedures and standards used in different laboratories;
- Validate the current testing methods for ATF materials;
- Evaluate the ATF cladding candidate materials based on the two fundamental tests performed.

#### 3.1. ROUND ROBIN TEST: OBJECTIVES AND MOTIVATION

The tested materials include three coated cladding concepts and an AISI stainless steel. There were two fundamental tests defined – high temperature steam oxidation test and long term corrosion test. The high temperature steam oxidation test should study and quantify the behaviour of the ATF candidate materials in accidental conditions while the long term corrosion test focuses on the normal operation of LWRs. The participants of the RRT are: Czech Technical University/UJP Praha (CTU), Karlsruhe Institute of Technology (KIT), Institute of Nuclear Chemistry and Technology (INCT), VTT Technical Research Centre of Finland (VTT), University of São Paulo (USP) and Hungarian Academy of Sciences Centre for Energy Research (MTA EK). The RRT activity can be subdivided into three sub tasks:

- ATF cladding sample production;
- Long term corrosion test in WWER or PWR chemistry;
- High temperature oxidation.

The involvement of the parties in particular subtasks of the RRT activity is summarized in Table 8.

TABLE 8. INVOLVEMENT OF THE CRP PARTICIPANTS IN THE RRT SUBTASKS

|                            | CTU | KIT | INCT | VTT | USP | MTA EK |
|----------------------------|-----|-----|------|-----|-----|--------|
| Sample production          | X   | X   | X    | —   | X   | —      |
| Long term corrosion        | X   | —   | X    | X   | —   | —      |
| High temperature oxidation | X   | X   | —    | X   | —   | X      |

As can be seen from Table 8, there were four different types of ATF cladding samples produced by four institutes. Three institutes performed the long term corrosion test in PWR or WWER chemistry and four institutes performed the high temperature oxidation test.

The following ATF candidate cladding materials were provided:

- PVD MAX phase coated Zry-4 by KIT (layer thicknesses of 1.5 $\mu$ m (Cr), 4.5  $\mu$ m (Cr<sub>2</sub>AlC), and 0.5  $\mu$ m (Cr));
- PVD Cr coated Zry-2 and Zr1%Nb by CTU (~26  $\mu$ m and ~15  $\mu$ m thickness);
- PVD ZrSi-Cr coated Zry-2 by INCT (~2.5  $\mu$ m);
- Advanced stainless steel (AISI 348) by USP.

The nominal compositions of substrate materials and AISI 348 SS are as following (in weight-%):

- Zry-2 LK3 (1.5Sn; 0.12Fe; 0.1Cr; 0.12O; 0.05Ni);
- Zry-4 (1.5Sn; 0.20Fe; 0.1Cr; 0.09-0.13O);
- AISI 348 SS (17.5Cr; 11Ni; 1.7Mn; 0.41Si; 0.85Nb).

The tested specimens were prepared in different geometries based on the requirements of participants. As be seen, all of the three coated cladding concepts utilized different coating materials with different thicknesses. It should be noted that, some tests that were originally planned were not completed due to the time and material constraints.

### 3.2. SAMPLE PRODUCTION

Coated cladding concepts as ATF are expected to withstand loss of coolant during a nuclear accident for considerably longer than uncoated zirconium alloy cladding. In the current CRP Zircaloy-2 was used as a substrate for Cr and ZrSi-Cr coatings deposited using a PVD technique. Zircaloy-4 (Zry-4) was used as the substrate for the MAX phase (Cr/Cr<sub>2</sub>AlC/Cr) coated claddings deposited using a PVD technique. Besides, the AISI 348 stainless steel produced and provided by the Brazilian University of Sao Paulo was studied. The production of the ATF cladding candidate samples is described further in this chapter as well as in the Annex.

#### 3.2.1. USP Brazil: AISI 348 SS

There were two different geometries of austenitic stainless steel (AISI 348) samples supplied: tubes and plates. The composition and properties of both materials (tubes and plates) were the same and shown below:

- Chemical composition: Fe-balance, C-0.055%, Mn-1.70%, P-0.017%, S-0.003%, Si-0.41%, Cr-17.5%, Ni-11%, Nb-0.85%, N-0.0018%, Co-0.021%, Ta<0.005%, B-0.0008%;
- Micro-hardness: 150–200 HV;
- Surface roughness:  $\leq 0.7 \mu$ m Ra;
- Mechanical properties at 20°C: tensile strength — 640 MPa, yield strength — 330 MPa, elongation of a 50 mm specimen — 47%;
- Mechanical properties at 370°C: tensile strength — 455 MPa, yield strength — 260 MPa, elongation of a 50 mm specimen — 26%;
- Non metallic inclusions (ASTM E45, [48]):  $\leq 1$ ;
- Niobium carbides evaluation (ASTM E407 [49]): continuous non stabilized areas < than 0.05 mm of equivalent diameter;
- Intergranular corrosion (ASTM A262, Practice A [50]): material does not present intergranular cracks (magnification in the range 5 $\times$  to 20 $\times$ ).

The average grain size number (according to ASTM E112 classification [51]) was between 8 and 9 in tube samples, and lower than 7 in plate samples. Plate samples were prepared from AISI 348 bars with a diameter of 22 mm. After machining, each plate sample was polished, labelled, and cleaned. Tubular samples were prepared by cutting long tubes of AISI 348 tubes with a diameter of 9.8 mm and thickness of 0.6 mm. After cutting, each tube sample was labelled and cleaned.

### 3.2.2. CTU/UJP Czech Republic: Cr PVD coatings

Standard Zircaloy-2 (Zry-2) LK3 sheets (Sn-1.3 wt%; Fe+Cr+Ni-0.26-0.38 wt%; Zr-balance) and Zry-2 tubes were used as substrate and reference materials. Small coupons 2×2 cm were machined, cleaned and coated with pure Cr and prepared as originally planned (see Fig. 1.). Later, 1×2 cm Cr coated coupons were prepared based on VTT's requirements in the second Cr deposition batch. The samples provided to other RRT participants are summarized in Table 9. The schematics of the originally defined geometry is shown in Fig. 1.(left), the machined and polished Zry-2 coupons before PVD deposition at CTU are shown in Fig. 1.(right). Additionally, tubular samples were tested. Only two participants (CTU/UJP and MTA EK) tested tubular samples. Mainly Zr1%Nb alloy provided by UJP Praha was used as the substrate in these tests and pure Cr coating was applied on its surface by the same technique.

TABLE 9. SAMPLES PROVIDED TO ACTOFORM ROUND ROBIN PARTICIPANTS BY CTU

| Long term corrosion VTT                               | Long term corrosion ICHTJ                                     | High temperature oxidation – KIT                              | High temperature oxidation – VTT   | Long term corrosion CTU/UJP                                   | High temperature oxidation – CTU/UJP  | High temperature oxidation – MTA                    |
|---|---|---|--|---|---|---|
| 3 - 2×2 cm Cr coated Zry-2 plates; 1 - uncoated Zry-2 | 3 - 2×2 cm Cr coated Zry-2 coupons; 1 - 2×2 cm uncoated Zry-2 | 3 - 2×2 cm Cr coated Zry-2 coupons; 1 - 2×2 cm uncoated Zry-2 | 3 - 2×2 cm Cr coated Zry-2 coupons; 2 - 2×2 cm uncoated Zry-2; 4 - 2×1cm Cr coated Zry-2 | 3 - 2×2 cm Cr coated Zry-2 coupons; 1 - 2×2 cm uncoated Zry-2 | 3 - 2×2 cm Cr coated Zry-2 plates; 1 - uncoated 2×2 cm Zry-2; 3 – Zry-2 Cr coated tubes; 1 – Zry-2 uncoated | 6 – 6 cm long Cr coated Zr1%Nb; 2 – Zr1%Nb uncoated |

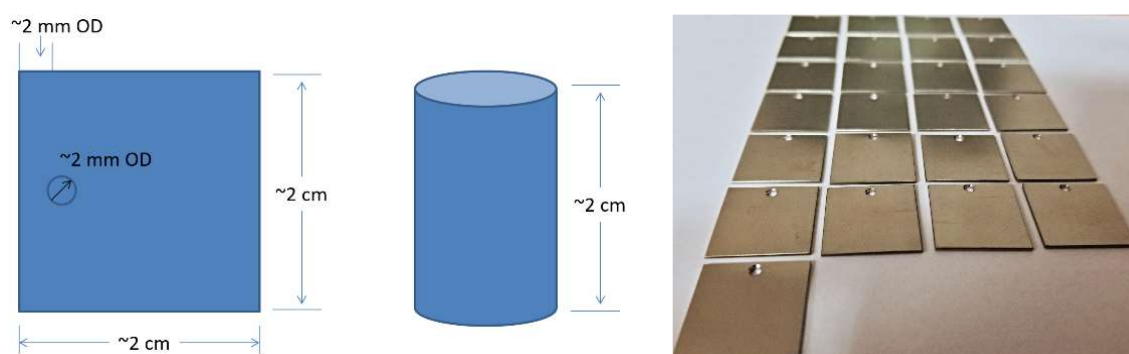


FIG. 1. Original sample geometry of exchanged samples within RRT (left); as-cut and polished Zry-2 coupons before PVD deposition (right).

Zr samples were Cr coated in two batches using unbalanced magnetron (UBM) sputtering in a Hauzer Flexicoat 850 industrial system. UBM is a special type of sputtering with extended and increased plasma density using coils in an unbalanced closed magnetic field. The images of the system, deposition chamber and rotating sample holders with Cr target are shown in Fig. 2 Before deposition, the Zr samples were ultrasonically cleaned in acetone and dried with a blower. The samples were placed into a vacuum chamber on rotation table with 3-axis rotating holders and the table rotation speed was set up on 2 rpm. Then the surfaces were cleaned by ion etching in argon plasma for approximately 20 minutes to remove thin oxide surface film and other impurities.



FIG. 2. Images of the Hauser Flexicoat 850 at CTU in Prague. Overview of the system (left); Deposition chamber (centre); Rotating sample holders with Cr target in the back (right) (Reproduced courtesy of Elsevier[182]).

The sputtering was made in DC mode using two cathodes with Cr (99.6 %) targets. Cathodes were powered at 6 or 3 kW depending on the stage of the process. Negative DC bias 75 V was applied on the samples. The working pressure was 0.2 Pa, deposition temperature 250°C and current 2 A on the external UBM coils. The coatings were deposited in a metal mode using the gas flow 90 sccm Ar (99.999 %) for about 18 hours. The thickness of the coatings was measured with a Calotest (CSM, Switzerland) and was found to be  $26 \pm 0.1 \mu\text{m}$  in the first batch and  $16 \pm 0.1 \mu\text{m}$  in the second batch. The results of the Calotest with Cr coating from the second batch are shown in Fig. 3. More details about the fabrication process of the Cr PVD coatings on Zr-based substrates are given in the CTU TECDOC report as well as in [52, 54, 55].

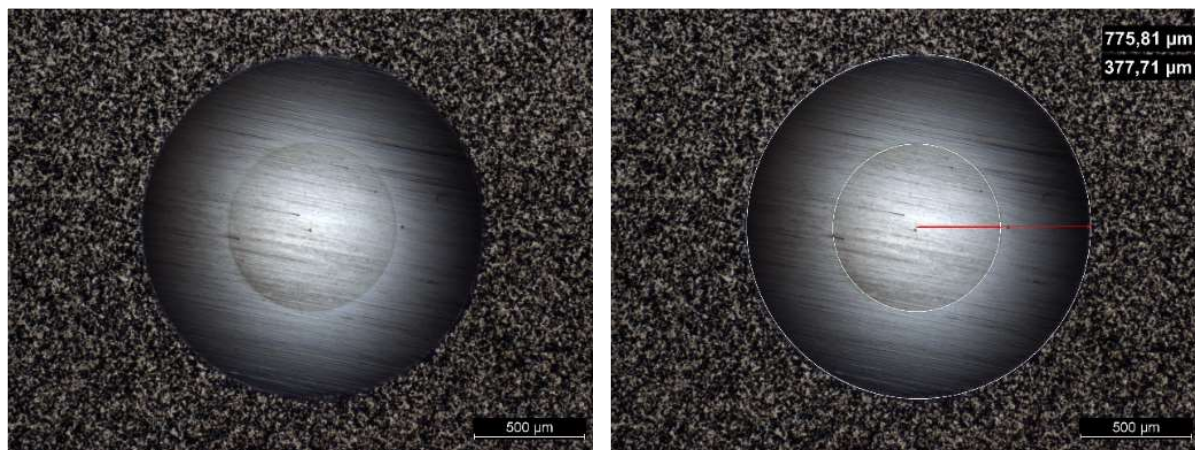


FIG. 3. Calotest of the Cr coating from the second batch.

### 3.2.3. KIT Germany: MAX phase PVD coatings

$\text{Cr}_2\text{AlC}$  MAX phase coated Zry-4 was produced at the Karlsruhe Institute of Technology, Institute for Applied Materials for the ACTOF round robin tests. The coatings were synthesized via a two-step process. Figure 4 shows the schemes of the design of the as-deposited coatings on Zry-4 substrates and the arrangement of the targets and substrates during deposition. To achieve the Cr/Cr-C-Al/Cr multilayer design of the coatings in Zry-4 substrate as shown in Fig. 4(a), the substrates were coated with pure Cr layer with power only on Cr target while off for two other targets. The PVD equipment run in a stop-and-go mode, i.e. the sample holder rotated from one target position to another one and stayed for various holding times at each individual target position (Fig. 4 (b)). A shutter was installed between the target and the substrate holder to only allow the deposition of one element at each position. The thicknesses of each elemental layer are around 8 nm for chromium, 2 nm for carbon and 4 nm for aluminium, calculated according to the stoichiometric ratio of these three elements (2:1:1) in  $\text{Cr}_2\text{AlC}$  and considering their theoretical densities. The thickness of each elemental layer was controlled by adjusting the dwell time at each target position. The periodical stacks have been repeated until a total film thickness of about 5  $\mu\text{m}$ . A 1.5  $\mu\text{m}$  Cr layer was finally deposited on top by only switching on the power on Cr target and without rotation of the substrate sample holder. Furthermore, the substrates were not heated and no bias applied during deposition.

After deposition, the coated Zry-4 specimens were ex-situ annealed in pure argon at atmospheric pressure using a commercial thermal balance to facilitate the growth of MAX phases by solid reaction of the nanoscale elemental multilayers. The heating and the cooling rates were fixed at 10 K/min and the isothermal holding time was 10 min. The annealing temperature was selected at 550°C. Cr<sub>2</sub>AlC MAX phase was successfully obtained while no significant diffusion between the Cr and Cr<sub>2</sub>AlC layer has confirmed at such conditions.

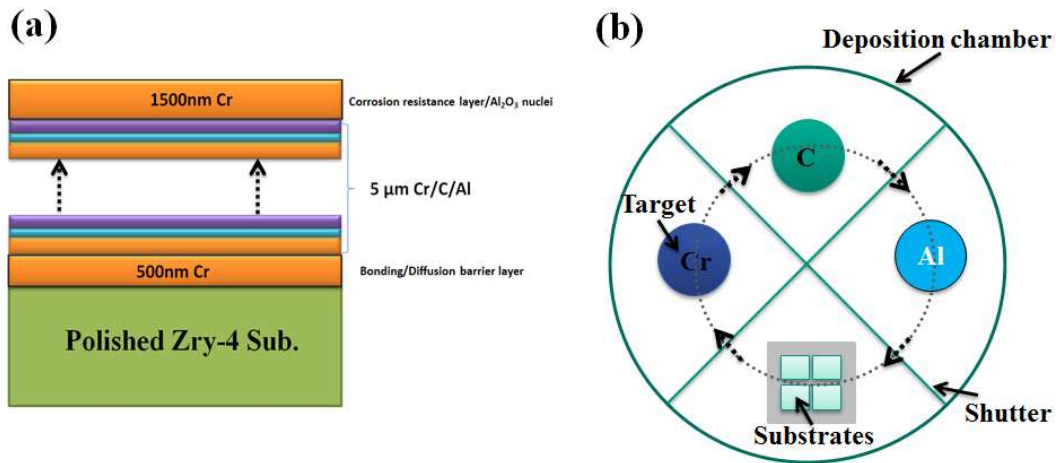


FIG. 4. Schematic representation of (a) the design of the as-deposited coatings on Zircaloy-4 substrates, and (b) arrangement of the targets and substrates during deposition.

More details about the fabrication process of the Cr<sub>2</sub>AlC MAX phase coatings on Zry-4 substrates are given in the KIT TECDOC report as well as in [56, 57].

### 3.2.4. INCT Poland: ZrSi-Cr PVD Coatings

The bulk substrate material was Zry-2) provided by Westinghouse Electric Company. It was received in the form of plates (12×12 cm) and tubes (8 cm in length). Samples for investigations were cut from the plates according to the scheme decided earlier. Tubular samples were not coated. Processes of coatings formation were carried out in the Institute for Sustainable Technologies ITS (Radom, Poland). Technological processes of coatings deposition were carried out using the Balzers system facility (Fig. 5.). The system contains three magnetrons plasma sources, three power and control panels. It allows to deposit materials from separate targets and to obtain multi elemental coatings. Two magnetrons with separate, flat, circular targets with composition: ZrSi<sub>2</sub> and Cr were used. Coatings Zr<sub>40</sub>Si<sub>24</sub>Cr<sub>36</sub> were obtained. Coupon samples were coated on both sides.

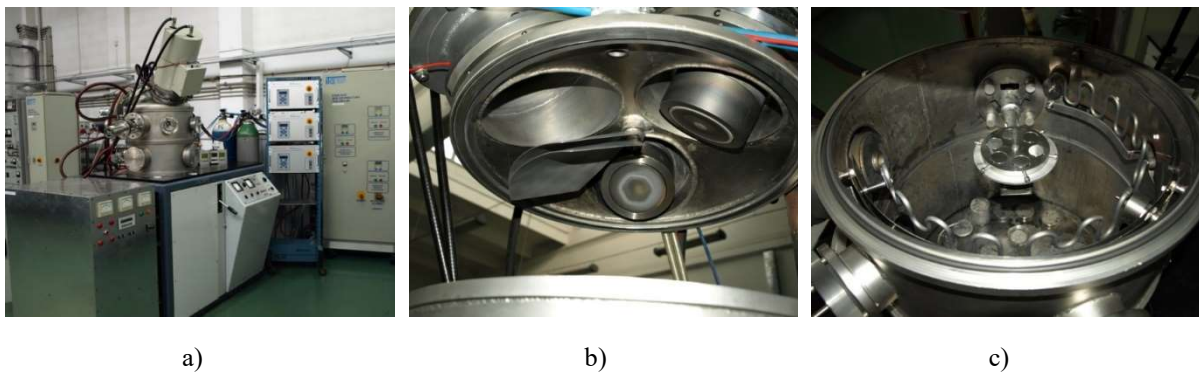


FIG. 5. Balzers system facility: a) general view, b) position of flat, circular magnetrons, c) chamber view.

Fourteen coated samples were prepared for long term corrosion test at CTU, VTT and INCT, as well as HT oxidation at KIT. Surfaces of modified samples were similar when comparing both sides. Dark contours were visible mainly close to the edges (Fig. 6). Dimensions of the initial material did not change.

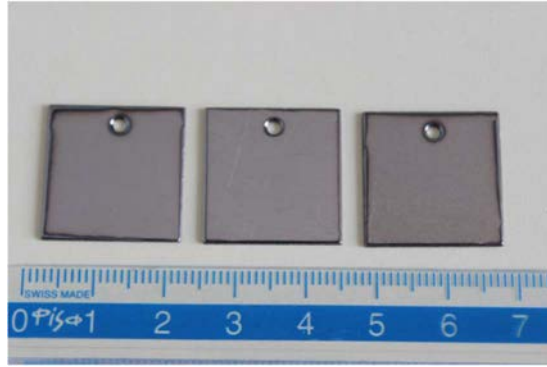


FIG. 6. General view of the PVD coated Zry-2 samples.

More surface details were observed using Scanning Electron Microscopy (SEM). Visible orientation was the result of initial material surface morphology (which related to material production). This fact means that the obtained layer was thin, and the surface morphology of initial material was mapped (Figs 7 (a, b)). Agglomerates of deposited material were visible on the surfaces. Grain boundaries can be distinguished. Cracks of the modified deposited layer were visible (Figs 7 (c, d)).

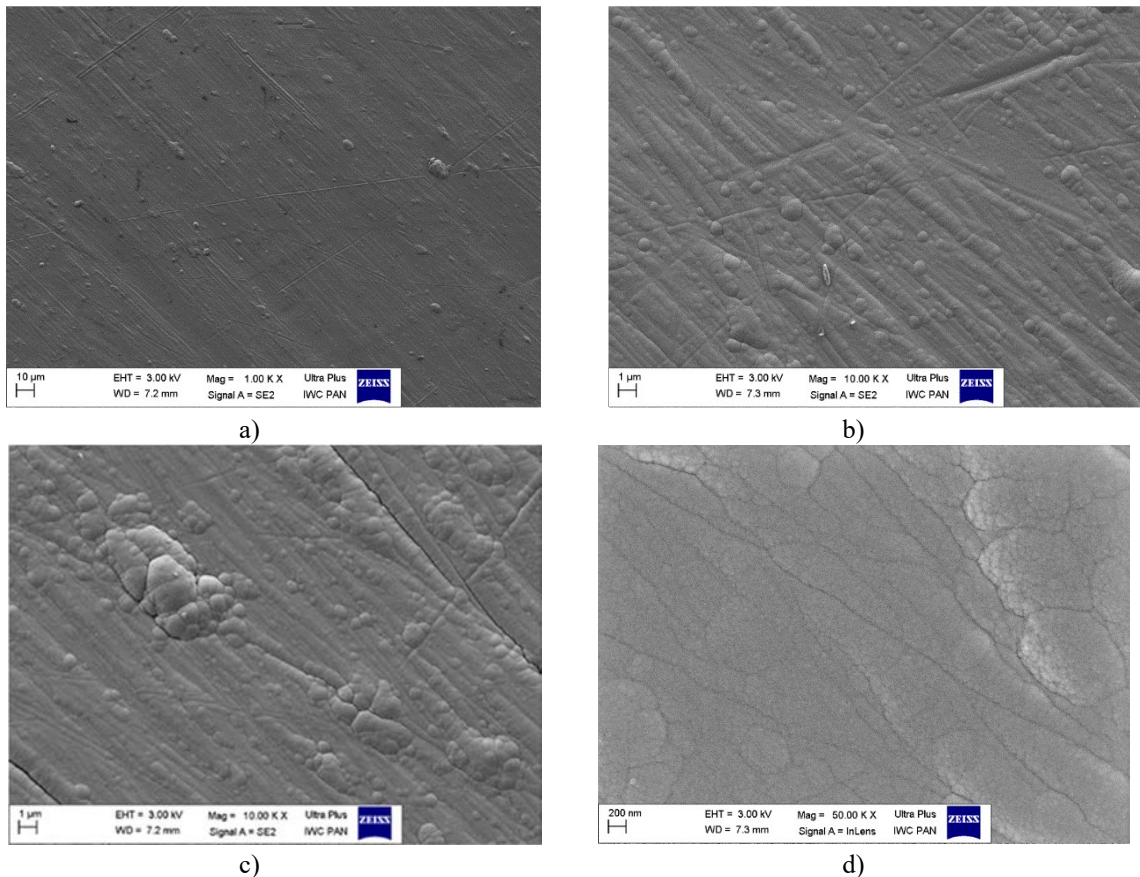


FIG. 7. SEM images of PVD modified surfaces of Zry-2: a) Mag. - 1000, b) and c) Mag. - 10 000, d) Mag. - 50 000.

The results of the elemental composition of the produced coating as measured by EDS are presented in Table 10. Presence of Zr, Si and Cr were confirmed.

TABLE 10. ELEMENTAL COMPOSITION OF THE Zry-2 PVD MODIFIED SURFACE

|       | Si    | Cr    | Zr    |
|-------|-------|-------|-------|
| at. % | 43.30 | 34.80 | 21.90 |
| wt %  | 24.20 | 36.00 | 39.80 |

Metallographic cross section was prepared according to the procedure defined at INCT for Zr samples preparation. Two areas can be clearly distinguished: substrate material and deposited coating (Fig. 8).

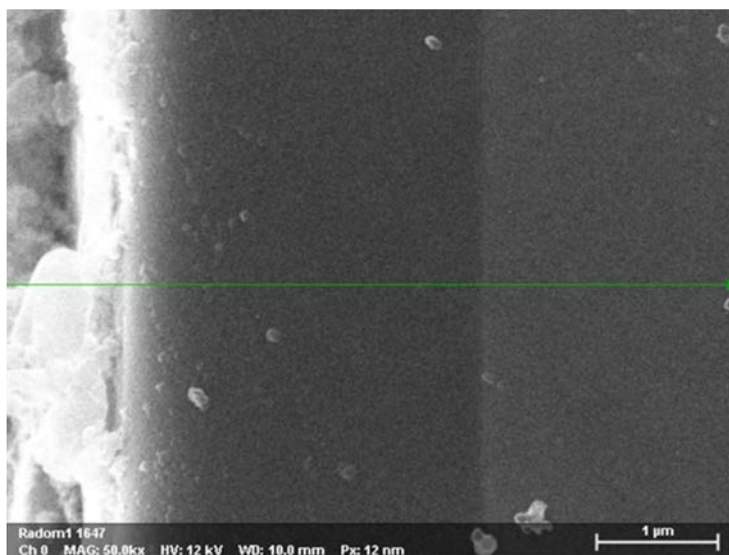


FIG. 8. Results of cross section investigations of PVD coated Zry-2: metallographic cross-section.

Elemental analysis confirmed the presence of Zr, Si and Cr in the deposited layer. The defined level of identified elements and the whole thickness of deposited layer was confirmed (mass %): Zr – 40, Si – 24, Cr – 36. There was only Zr detected in the base material. In summary, Zry-2 samples with homogeneous  $Zr_{40}Si_{24}Cr_{36}$  coatings with a thickness of 2.5 µm were produced as can be seen in Fig. 9

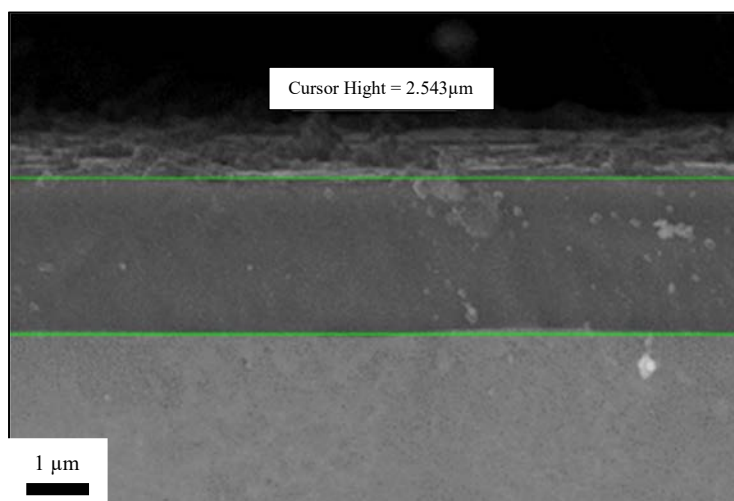


FIG. 9. Results of cross section investigations of PVD modified Zry-2 - the thickness of the modified layer measurements.

### 3.3. LONG TERM CORROSION

Three different institutes joined the long term corrosion test as one of the RTT subtasks. The experimental setups and procedures are described later in the report. More details can be found in the separate papers attached. The long term corrosion tests were done in two LWR chemistries – PWR (VTT, INCT) and WWER (CTU). The single period of 21 days was defined with a goal of 3 minimal periods (63 cumulative days). Destructive testing was performed after 63 days. If there was enough material left, then the tests continued for a longer exposure. The long term corrosion tests are summarized in Table 11.

TABLE 11. LONG TERM CORROSION TESTS PERFORMED BY INDIVIDUAL PARTICIPANTS WITH MAXIMAL LENGTH OF THE CUMULATIVE EXPOSITION FOR EACH ATF MATERIAL TYPE

| CTU — Czech Republic   |   |
|------------------------|---|
| Cladding material      | Long term corrosion<br>(WWER chemistry) |
| AISI 348               | 164 days                                |
| Cr coated Zry-2        | 164 days                                |
| MAX phase coated Zry-4 | 147 days                                |
| ZrSi-Cr coated Zry-2   | 101 days                                |
| E110 ref.              | 164 days                                |
| Cr coated E110         | 164 days                                |
| VTT — Finland          |   |
| Cladding material      | Long term corrosion<br>(PWR chemistry)  |
| AISI 348               | 63 days                                 |
| Zry-4 ref.             | 63 days                                 |
| Cr coated Zry-2        | 63 days                                 |
| MAX phase coated Zry-4 | 63 days                                 |
| ZrSi-Cr coated Zry-2   | 16.5 days                               |
| INCT — Poland          |   |
| Cladding material      | Long term corrosion<br>(PWR chemistry)  |
| AISI 348               | 63 days                                 |
| Zry-4 ref.             | 63 days                                 |
| Cr coated Zry-2        | 63 days                                 |
| MAX phase coated Zry-4 | 63 days                                 |
| ZrSi-Cr coated Zry-2   | 63 days                                 |
| Zry-2 ref.             | 63 days                                 |

### 3.4. FACILITY, CONDITIONS, AND EXPERIMENTAL METHODS

The experimental procedures vary depending on the available setups and standard procedures used at the institutes. For example, CTU/UJP uses 360°C, 19.4 MPa, 4 dm<sup>3</sup> static autoclave. VTT used standard operational PWR parameters with recirculation loop and online chemistry control whereas INCT used 360°C, 19.5 MPa, 1 dm<sup>3</sup> static autoclave.

The samples were characterized before, during and after testing by non destructive as well as destructive methods. The characterization techniques include visual inspections, SEM, X-ray Power Diffraction (XRD), Energy Dispersive Spectroscopy (EDS), metallography, weight changes or hydrogen measurements. The details about experimental setups and procedures can be found in the individual TECDOC reports.

### 3.4.1. CTU/UJP

Static autoclave with an active volume of 4 dm<sup>3</sup> was used. Standard WWER chemistry (1050 ppm B, 15.9 ppm K, and 1 ppm Li), the temperature of 360°C, and pressure 19.4 MPa were set. The predefined period was 21 days with evaluations that followed (visual, weight gain, hydrogen, microstructure analysis). Destructive characterizations were performed at the end of planned tests. The picture of the static autoclave used for the test is shown in Fig. 10.



FIG. 10. Static autoclave used in the test.

The summary of tested materials is shown in Table 12. The test with ZrSi-Cr coated Zry-2 started at a later time due to the sample availability. The MAX phase coated samples were removed after 7 periods from the test. The eighth period was only 17 days long as shown in Table 12.

TABLE 12. TEST MATRIX FOR CORROSION TEST IN WWER CONDITIONS OF THE PLATE SAMPLES

| Specimen ID | Material           | No. of periods | Cumulative oxidation time [days] |
|-------------|--------------------|----------------|----------------------------------|
| Zry2-1      | Reference Zry-2    | 8              | 164                              |
| Zry2-2      | Reference Zry-2    | 3              | 63                               |
| 3Cr3-01     | Zry-2 + Cr-coating | 8              | 164                              |
| 3Cr3-02     | Zry-2 + Cr-coating | 8              | 164                              |
| 3Cr3-03     | Zry-2 + Cr-coating | 3              | 63                               |
| KIT-21      | Zry-4 + MAX phase  | 7              | 147                              |
| KIT-22      | Zry-4 + MAX phase  | 7              | 147                              |
| KIT-23      | Zry-4 + MAX phase  | 3              | 63                               |
| SS-PS-13    | AISI 348           | 8              | 164                              |

TABLE 12. TEST MATRIX FOR CORROSION TEST IN WWER CONDITIONS OF THE PLATE SAMPLES (cont.)

| Specimen ID | Material        | No. of periods | Cumulative oxidation time [days] |
|-------------|-----------------|----------------|----------------------------------|
| SS-PS-14    | AISI 348        | 8              | 164                              |
| SS-PS-15    | AISI 348        | 3              | 63                               |
| INCT51      | Zry-2 + ZrSi-Cr | 3              | 63                               |
| INCT52      | Zry-2 + ZrSi-Cr | 5              | 101                              |
| INCT53      | Zry-2 + ZrSi-Cr | 5              | 101                              |

### 3.4.2. VTT

The autoclave tests in PWR water were performed in VTT's autoclave laboratory. The autoclave is connected to a water recirculation loop and standard PWR chemistry at 360°C with  $[Li] = 2\text{--}2.2$  ppm,  $[B] = 600\text{--}1000$  ppm, and  $[H_2] = 3$  ppm is controlled. The loop consists of low and high pressure sections. The low pressure section consists of a make-up water tank equipped with nitrogen, hydrogen and mixed gas gasification systems, a low pressure re-circulation pump, a mixed bed ion exchanger used for water purification before the test solution is prepared, and water chemistry measurement instrumentation for on-line monitoring of conductivity, pH, dissolved oxygen, and dissolved hydrogen. Water chemistry monitoring instruments can be switched either to measure autoclave inlet or outlet water. The autoclave used in this test campaign is presented in Fig. 11. A more detailed description can be found in individual VTT's report.



FIG. 11. Schematic structure of the water recirculation loop including autoclave (top) and a photograph of the used autoclave in this test campaign (bottom).

### 3.4.3. INCT

The equipment used for long term corrosion tests was an autoclave Parr 4653 with the active volume of 1 dm<sup>3</sup>. Samples were mounted on a sample holder (Fig. 12 (a) and (b)) and placed inside the autoclave. Standard PWR chemistry was used. Parameters were: 360°C; 19.5 MPa in 0.5 dm<sup>3</sup> PWR water. The schematic diagram of the experimental procedure is presented in Fig. 13. Analysis of the samples was done after 21, 42 and 63 days and the water chemistry was analyzed after 21 and 42 days.

The water used for the experiments was highly deionized water from the Millipore system that was treated to simulate PWR chemistry. The standard conditions are:  $[Li] = 2\text{--}2.2$  ppm and  $[B] = 600\text{--}1000$  ppm [58]. The procedure of involved two steps: addition of boric acid ( $H_3BO_3$ ) to get concentration  $[B] = 800$  ppm and then addition of lithium hydroxide (LiOH) to get concentration  $[Li] = 2.1$  ppm.  $H_3BO_3$  powder (99%, extra pure from

ACROS ORGANICS) and  $\text{LiOH}\cdot\text{H}_2\text{O}$  from POCH were used. ICP-MS method was used to determine the concentration of ions in the water. Other measurements have been done with multifunctional laboratory pH-meter ProLab2500 to measure pH, Total Dissolved Oxygen (TDO) and conductivity ( $\sigma$ ). The average results from 2 measurements are presented in Table 13.

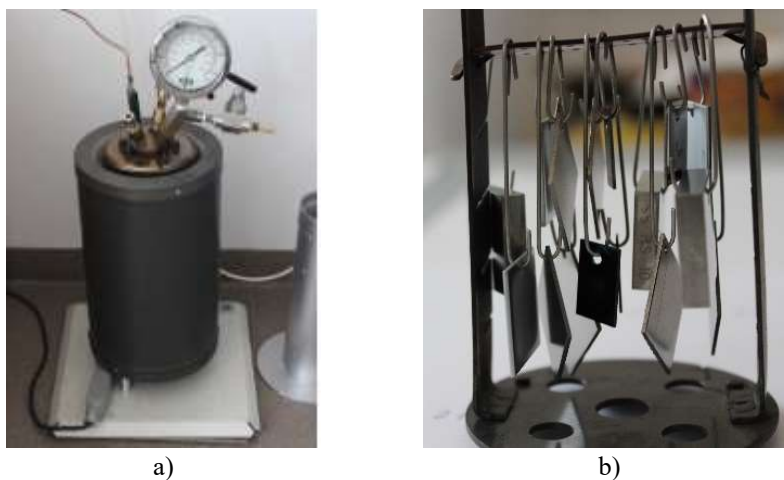


*FIG. 12. The equipment used for long term oxidation tests: a) autoclave Parr 4653 and b) sample holder.*

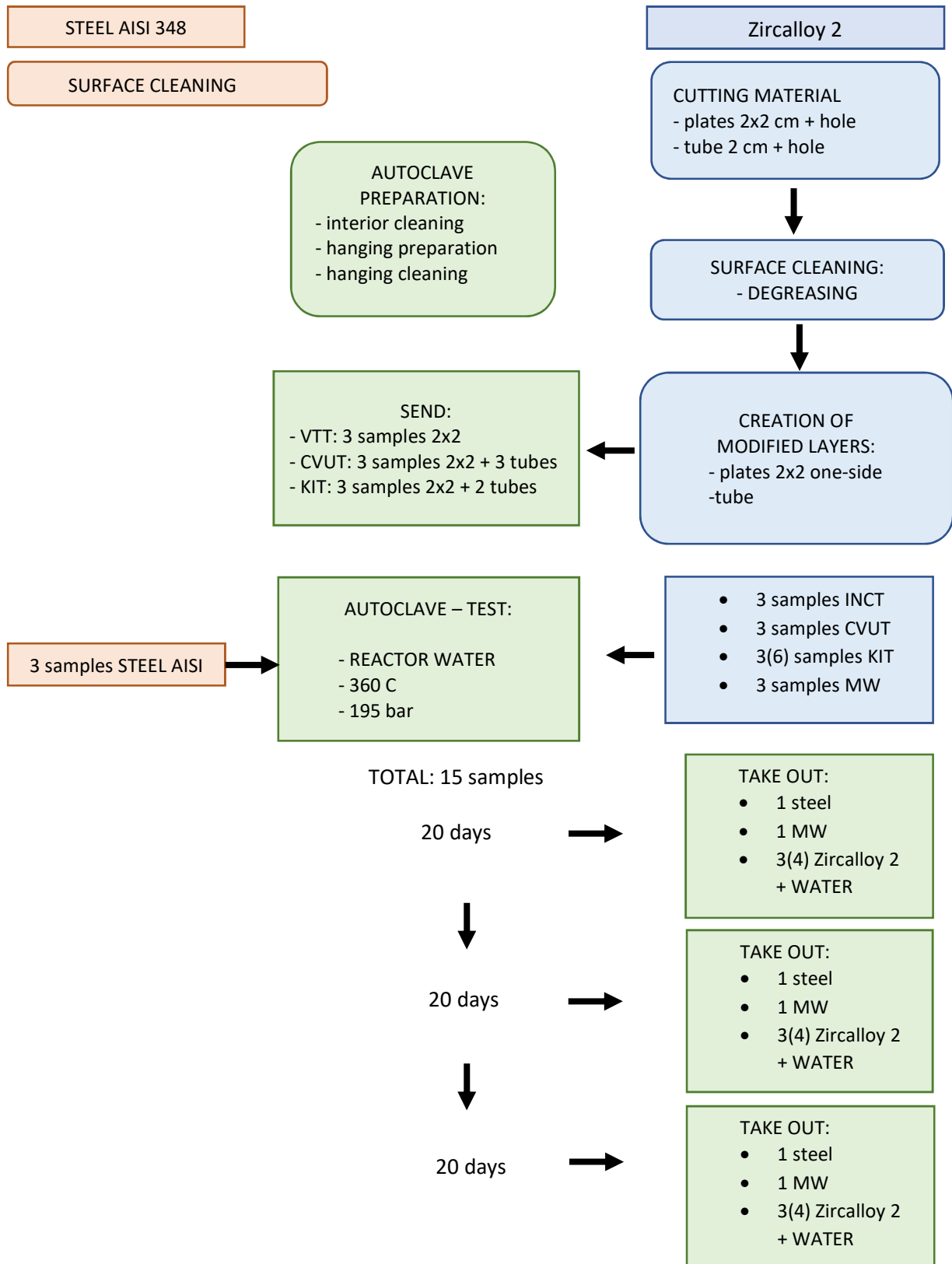


FIG. 13. Schematic diagram of the Round Robin Test procedures carried out at INCT.

Table 13 shows that the pH and TDO were similar in primary water and at the beginning of the test. The water conductivity was about 6 times higher after 21 and 42 days, which can be a result of higher ions concentration in water coming from coating dissolution. The concentration of all analyzed ions except Na<sup>+</sup> was significantly higher after 21 days. Interestingly, the concentrations were a bit lower after the next 21 days.

TABLE 13. CHEMICAL COMPOSITION AND PHYSICAL CHARACTERISTICS OF WATER USED IN THE AUTOCLAVE CORROSION TESTS

|                               | Primary water [mg/l] | 0 days [mg/l] | 21 days [mg/l] | 42 days [mg/l] |
|-------------------------------|----------------------|---------------|----------------|----------------|
| Cl <sup>-</sup>               | 0.053                | 0.45          | 7.03           | 2.16           |
| NO <sub>3</sub> <sup>-</sup>  | 0.093                | 0.037         | 1.46           | 0.183          |
| SO <sub>4</sub> <sup>2-</sup> | 0.305                | 0.438         | 9.79           | 5.37           |
| Na <sup>+</sup>               | 0.062                | 4.3           | 3.09           | 2.18           |
| K <sup>+</sup>                | 0.012                | 0.95          | —              | 0.96           |
| Ca <sup>2+</sup>              | 0.094                | 2.3           | 6.98           | 5.08           |
| Li <sup>+</sup>               | —                    | 0.4           | 2.09           | 1.65           |
| Mg <sup>2+</sup>              | —                    | 0.35          | 0.25           | 0.35           |
| TDO                           | 8.48                 | 8.64          | 7.41           | 7.32           |
| pH                            | 6.38                 | 6.75          | 5.68           | 6.51           |
| σ [μS/cm]                     | 1.45                 | 10.81         | 62.3           | 66.1           |

There were 6 different types of samples tested:

- Cr PVD coated Zry-2; CTU, coating thickness 26 μm;
- Cr/Cr<sub>2</sub>AlC/Cr (MAX phase) PVD coated Zry-4; KIT, coating thickness 6 μm;
- Zr<sub>40</sub>Si<sub>24</sub>Cr<sub>36</sub> PVD coated Zry-2; INCT, coating thickness 2.5 μm;
- AISI 348 SS; USP Brazil;
- Reference uncoated Zry-2;
- Reference uncoated Zry-4.

The as-received materials before the autoclave test are shown in Fig. 14.

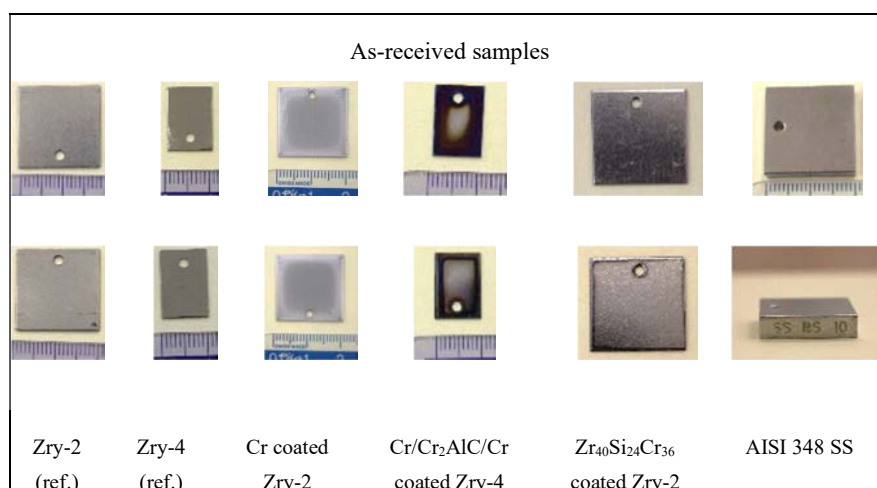


FIG. 14. General overview of the as-received samples (both sides).

Characterization of the samples during and after testing includes non-destructive and destructive techniques. The following methods were used:

- Surface morphology observations;
  - Light optical microscope OM with Bresser Science ADL-601 P (Bresser);
  - Scanning electron microscope SEM with DSM 942 (Zeiss) and high resolution HR-SEM ULTRA plus (Zeiss);
- Elemental analysis with EDS system with Quantax 400 (Bruker);
- Phase analysis with X-ray diffraction Advanced 8 (Bruker);
- Cross section investigations with HR-SEM, EDS;
- Mass changes with METTLER TOLEDO EXCELLENCE XS 105.

### 3.5. RESULTS: CTU/UJP

The dimensions and weights of the as-prepared and cleaned samples before testing were measured and the surface that corroded in the autoclave was calculated.

The visual evaluation of the samples during the test at each of the period up to the sixth period is shown in Table 15. The visual evaluation shows significant spallation and dissolution of the MAX phase coating. Due to the spallation, the weight loss is not a fully representative parameter when evaluating corrosion kinetics. However, even after several periods the surface still shows residuals of underlying parts of the coating system.

The as received Cr-coated samples showed a different color in the central region compared to areas close to edges. This was caused by the geometry of the sample and the orientation of the growth of crystals. The growth of crystals is different in the areas near the edges which causes a change of reflectivity of the material. A similar effect is not visible for tubular geometry.

The summary of the resulting weight changes evaluated after each period up to 8 periods is shown in Table 14. Some of the samples were tested up to 8 periods (164 days) and some were removed after 3 periods (63 days) for destructive testing. The results are plotted in Fig. 15. The results show very low (almost negligible) weight gains for Cr coated samples and AISI 348 SS. There is a steady weight loss for KIT MAX phase coated sample and a large weight gain for the ZrSi-Cr coated sample at the beginning of the test. The weight loss or gain rate then decreased. Except for the KIT specimens that had coating spallation and one sample with a damaged coating (ZrSi-Cr) possibly due to handling (INCT 51), the results show very good agreement and minimal measurement scattering (three samples were measured for each ATF cladding type). Standard kinetics for Zry-2 was confirmed with kinetics transition between 126 and 147 days that validates the procedure used in this test.

TABLE 14. WEIGHT GAINS OF SPECIMENS DURING THE AUTOCLAVE CORROSION EXPERIMENT.

| Material                | ID       | No. period / Exposure time: Weight gain [mg/dm <sup>2</sup> ] |        |        |        |        |         |        |        |
|-------------------------|----------|---|--------|--------|--------|--------|---------|--------|--------|
|                         |          | 1/21d   | 2/42d  | 3/63d  | 4/84d  | 5/105d | 6/126d  | 7/147d | 8/164d |
| Zry-2                   | Zry2-1   | 22.2  | 26.8   | 29.0   | 31.4   | 32.5   | 33.6    | 38.8   | 47.1   |
| REF.                    | Zry2-2   | 22.1  | 25.9   | 28.2   |        |        | Removed |        |        |
| Cr PVD coated<br>Zry-2  | 3Cr3-01  | 1.3   | 1.9    | 1.7    | 1.7    | 2.1    | 1.8     | 1.6    | 2.3    |
|                         | 3Cr3-02  | 1.0   | 1.7    | 1.2    | 1.6    | 1.4    | 1.4     | 1.5    | 2.1    |
|                         | 3Cr3-03  | 1.5   | 1.9    | 1.6    |        |        | Removed |        |        |
| MAX phase<br>PVD coated | KIT-21   | -142.1  | -211.7 | -225.7 | -237.3 | -246.4 | -252.8  | -256.4 | —      |
|                         | KIT-22   | -46.8   | -80.3  | -103.5 | -122.4 | -163.3 | -172.7  | -181.5 | —      |
| Zry-4                   | KIT-23   | -56.3   | -75.6  | -84.2  |        |        | Removed |        |        |
| AISI 348                | SS-PS-13 | -0.2  | 0.0    | -0.1   | 0.0    | 0.2    | 0.0     | -0.1   | 0.2    |
|                         | SS-PS-14 | 0.1   | 0.2    | -0.2   | 0.2    | 0.2    | 0.1     | 0.3    | 0.5    |
|                         | SS-PS-15 | 0.5   | 0.4    | 0.0    |        |        | Removed |        |        |
| ZrSi-Cr<br>PVD coated   | INCT51   | 28.8  | 46.5   | 33.6   |        |        | Removed |        |        |
|                         | INCT52   | 30.8  | 46.7   | 46.7   | 48.1   | 50.1   | —       | —      | —      |
| Zry-2                   | INCT53   | 31.3  | 48.8   | 48.1   | 49.7   | 46.0   | —       | —      | —      |

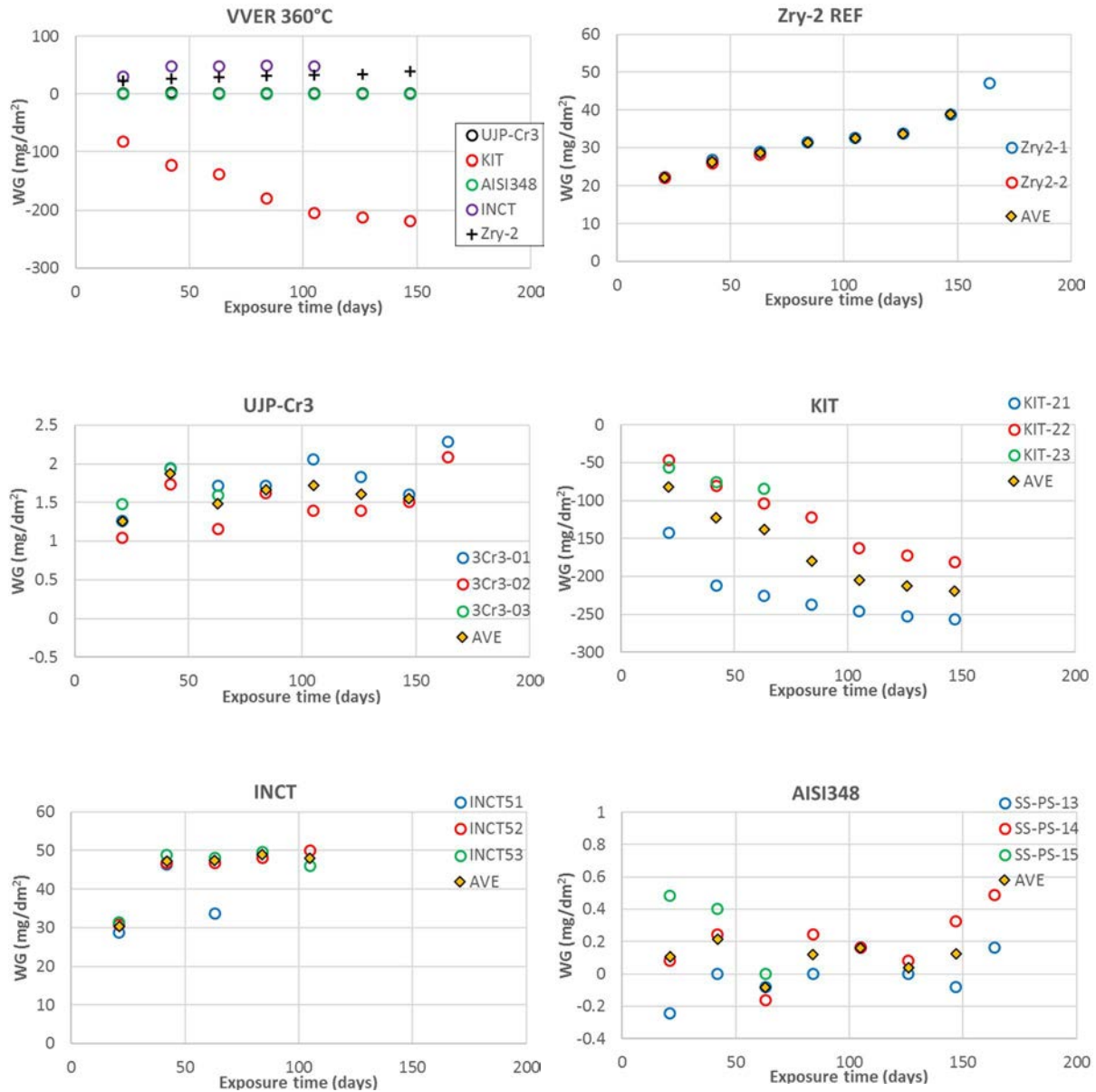


FIG. 15. Weight gains during long term corrosion experiment in WVER chemistry at 360°C (reference Zry-2, Cr PVD coated, MAX phase coated, AISI 348 and ZrSi-Cr coated).

The metallography evaluation of the ATF cladding samples is shown in Table 16 after cumulative exposure of 63 days. The visual inspection confirms negligible oxidation of AISI 348 SS and Cr coated sample, spallation of the MAX phase coated sample and oxidation of the Zr substrate under the ZrSi-Cr coating.

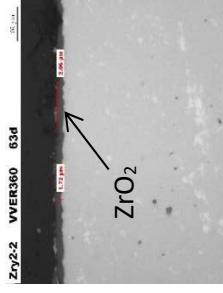
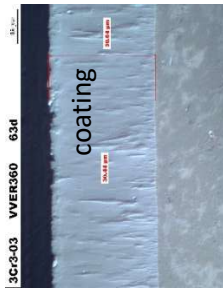
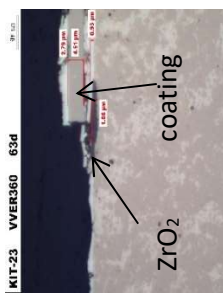
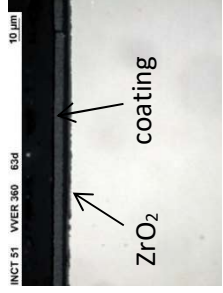
TABLE 15. VISUAL EVALUATION OF THE SAMPLES DURING AND AFTER LONG TERM CORROSION TEST IN WWER CHEMISTRY

| Time<br>days | REF     |             | Cr PVD coated |             | MAX phase PVD coated |             | ZrSi-Cr PVD coated |             |          |             |
|--------------|---------|-------------|---------------|-------------|----------------------|-------------|--------------------|-------------|----------|-------------|
|              | Zry2-1a | VVER360 21d | 3C3-01a       | VVER360 21d | MT-21a               | VVER360 21d | 55-PS-13a          | VVER360 21d | INCT-51a | VVER360 21d |
| 21           |         |             |               |             |                      |             |                    |             |          |             |
| 42           |         |             |               |             |                      |             |                    |             |          |             |
| 63           |         |             |               |             |                      |             |                    |             |          |             |
| 84           |         |             |               |             |                      |             |                    |             |          |             |

TABLE 15. VISUAL EVALUATION OF THE SAMPLES DURING AND AFTER LONG TERM CORROSION TEST IN WWER CHEMISTRY (cont.)

| Time days | REF<br>Uncoated Zry-2-1  | Cr PVD coated<br>Zry-2-Cr3-01   | MAX phase PVD coated<br>KIT-21  | AISI 348<br>SS-PS-13   | ZrSi-Cr PVD coated<br>INCT51 |
|-----------|--|---|---|--|------------------------------|
| 105       | Zry2-1a VVER360 84d   | 3Cr3-01a VVER360 105d  | KIT-21a VVER360 84d   | 55-PS-13a VVER360 84d   | —                            |
| 126       | Zry2-1a VVER360 126d  | 3Cr3-01a VVER360 126d  | KIT-21a VVER360 126d  | 55-PS-13a VVER360 126d  | —                            |

TABLE 16. MICROSTRUCTURE EVALUATION OF THE SAMPLES AFTER 63 DAYS OF CORROSION TEST IN WWER CHEMISTRY

| Time days | REF<br>Uncoated Zry-2-1  | Cr PVD coated<br>Zry-2-Cr3-01   | MAX phase PVD coated<br>KIT-21  | AISI 348<br>SS-PS-13   | ZrSi-Cr PVD coated Zry-2<br>INCT51  |
|-----------|--|---|---|--|---|
| 63        | Zry2-2 VVER360 63d  | 3Cr3-03 VVER360 63d  | KIT-23 VVER360 63d  | SS-PS-15 VVER360 63d  | INCT 51 VVER360 63d  |

The hydrogen content was analysed using the destructive Inert Gas Fusion (IGF) technique (G8 Galileo - Bruker) after 63 days. The results of the measured hydrogen content inside the samples after 63-day exposition are shown in Table 17. As can be seen, a very high H-content value was observed for Zry-2 ZrSi-Cr coated sample. The hydrides distribution and orientation in the ZrSi-Cr coated sample (INCT 51) are shown on the metallographic cross section sample in Fig. 16. It should be also noted that Cr coated sample shows similar hydrogen concentration in the sample as the uncoated one. The hydrogen produced in both cases is, however, considerably different, which implies that the H-pickup of Cr coated samples is much higher than uncoated Zr alloys.

TABLE 17. HYDROGEN CONTENT AFTER 63 DAYS OF AUTOCLAVE CORROSION EXPERIMENT.

| Material        | REF<br>Uncoated Zry2-1 | Cr PVD coated<br>Zry-2-Cr3-01 | MAX phase PVD coated<br>Zry-4<br>KIT-21 | AISI 348<br>SS-PS-13 | ZrSi-Cr PVD<br>coated Zry-2<br>INCT51 |
|-----------------|------------------------|-------------------------------|---|----------------------|---------------------------------------|
| ID              | Zry-2-2                | 3Cr3-03                       | KIT-23                                  | SS-PS-15             | INCT53                                |
| 63 days: H, ppm | 14.2                   | 15.0                          | 30.4                                    | 1.3, 1.4             | 191.8; 191.2                          |

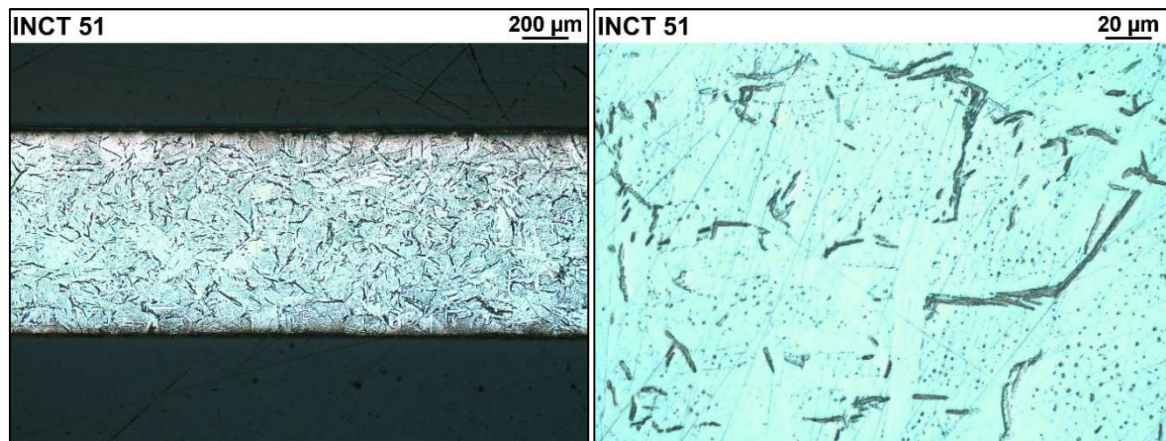


FIG. 16. Microstructure evaluation of the INCT 51 ZrSi-Cr coated sample (H content: 191.6 ppm) after 63 days of corrosion test in WWER chemistry. Hydrides distribution.

### 3.6. RESULTS: VTT

#### 3.6.1. Uncoated Zr-based alloys: reference samples

An overview and the detailed secondary electron (SE) images of Zircaloy-2 uncoated reference specimen, which was exposed up to 63 days (by using one coupon specimen same as in the case of Zry-4 reference specimen), are shown in Fig. 17. The oxide layer thickness ranges from 1  $\mu\text{m}$  to 10  $\mu\text{m}$ . The layer was continuous, however, it was slightly porous and several through the oxide layer cracks were formed.

SEM-EDS maps of O, Zr, Sn and Ni, where the oxide layer is on the left side, are shown in Fig. 18. SEM-EDS Selected Area (SA) analyses are shown in Fig. 19.

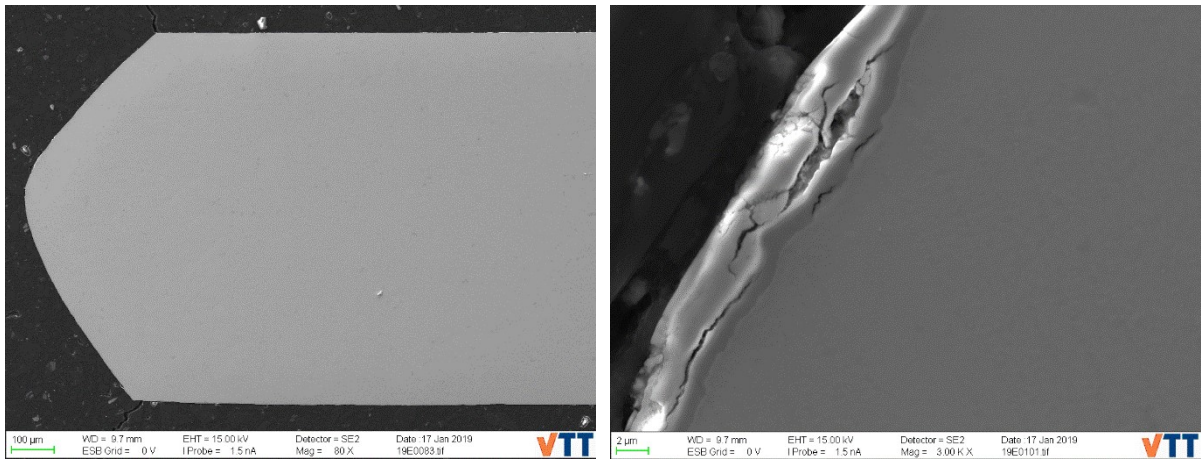


FIG. 17. SE images of Zry-2 reference CTU specimen (63-day exposure in PWR chemistry).

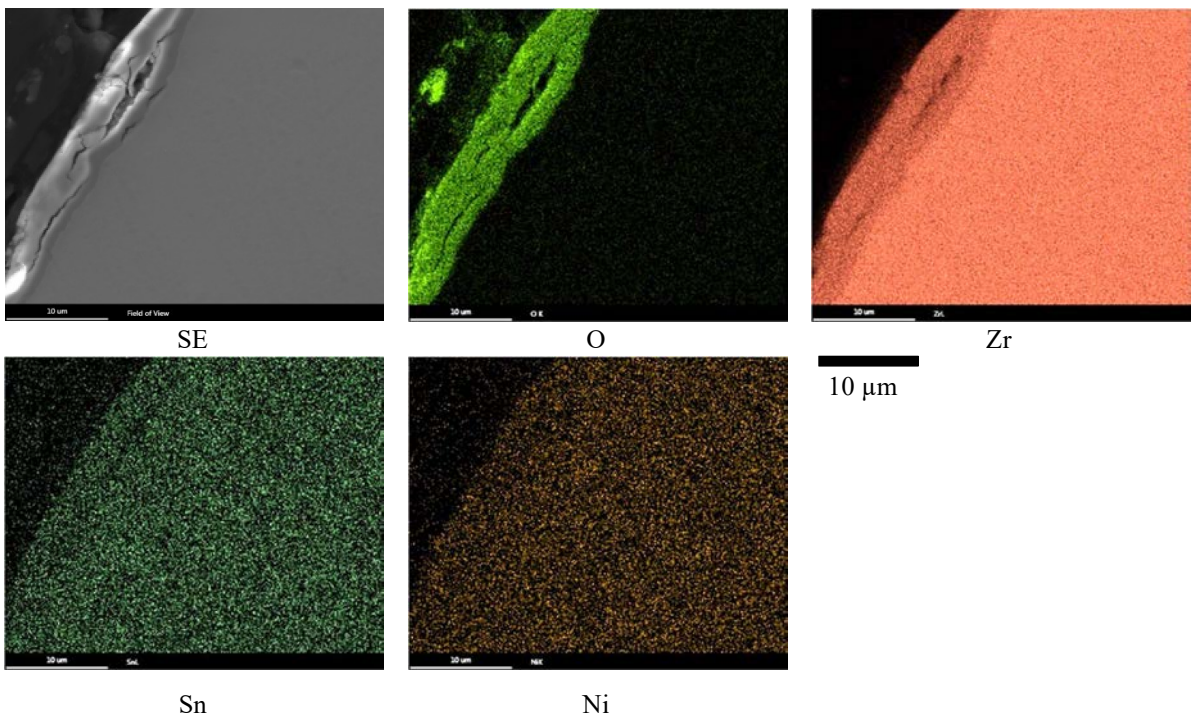
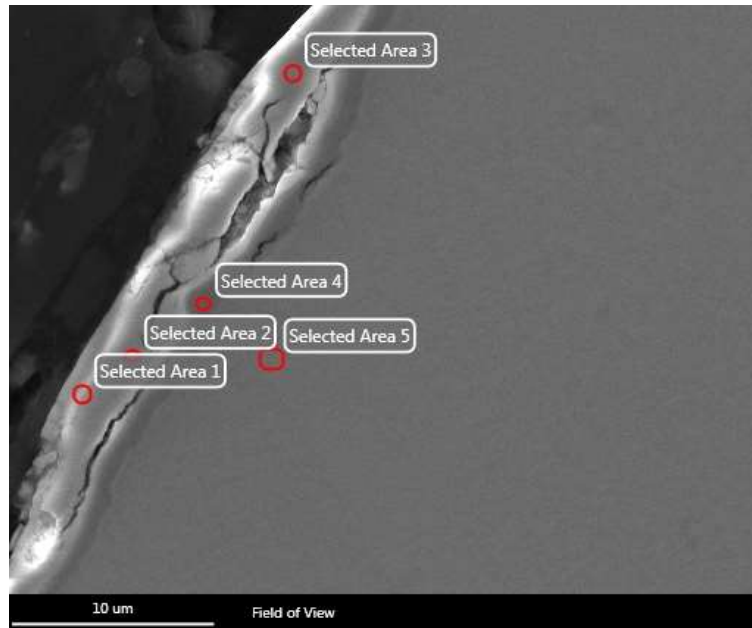


FIG. 18. SEM-EDS maps showing the distribution of O, Zr, Sn and Ni of the Zry-2 reference CTU specimen (63-day exposure).



|                 | O K  | Ni L | Zr L | Sn L | Fe K |
|-----------------|------|------|------|------|------|
| Selected Area 1 | 29.3 | 0.5  | 68.6 | 0.9  | 0.8  |
| Selected Area 2 | 28.4 | 0.2  | 70.1 | 0.6  | 0.8  |
| Selected Area 3 | 29.0 | 0.4  | 69.1 | 0.8  | 0.8  |
| Selected Area 4 | 25.7 | 0.8  | 71.6 | 1.1  | 0.9  |
| Selected Area 5 | 1.9  | 0.2  | 96.4 | 0.7  | 0.8  |

FIG. 19. SEM-EDS chemical composition (wt%) SA analyses of Zry-2 reference CTU specimen (63-day exposure). K and L X-ray emission lines were used for quantification.

Morphology of Zry-4 reference uncoated specimen, which was exposed for 63 days, is shown in Fig. 20. The reference specimen was exposed so that the same specimen was removed from the autoclave after each exposure period (21, 42, and 63 days) and then it was inserted back to the autoclave after photographing and weight change measurements. A cross section sample was prepared after the final exposure. The oxide layer thickness on the specimen surface ranged typically from 1 μm to 10 μm. The layer was continuous although slightly porous and several cracks through the oxide layer were observed.

SEM-EDS mapping is shown in Fig. 21. Selected Area analyses are shown in Fig. 22. A few microns thick darker layer can be seen between the outer oxide layer and the substrate in the SE image. Based on the Selected Area analyses, this layer is oxide with slightly elevated Cr and Fe content. Some Cr/Fe-rich particles are also observed in the oxide layer (see Cr/Fe-mapping in Fig. 21).

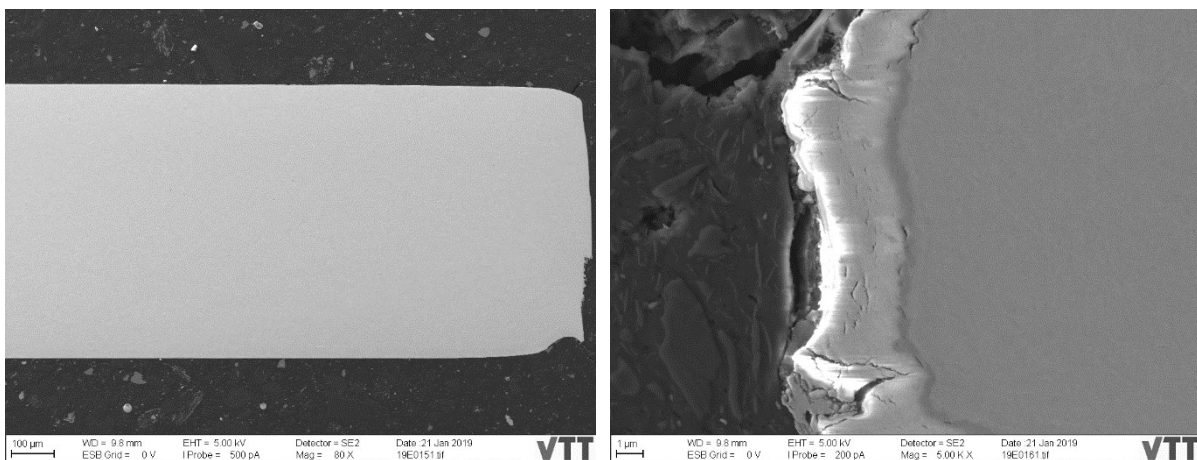


FIG. 20. SE images of Zry-4 reference uncoated specimen (63 days in PWR chemistry).

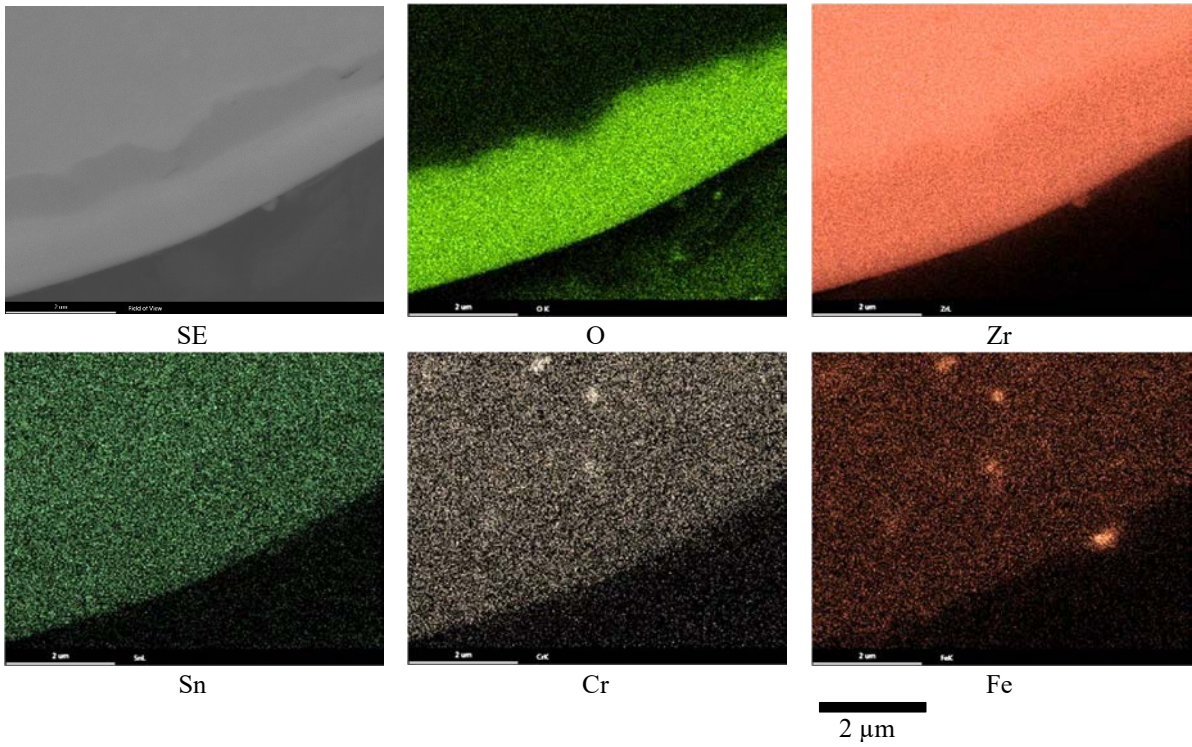
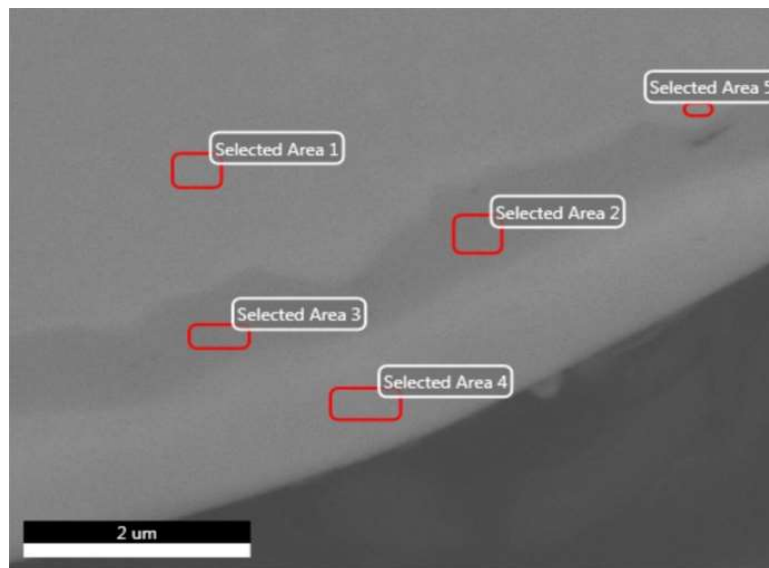


FIG. 21. SEM-EDS mapping showing the distribution of O, Zr, Sn, Cr and Fe of the Zry-4 reference KIT specimen (63 days).



|                 | O K  | Zr L | Sn L | Cr K | Fe L | Ni K |
|-----------------|------|------|------|------|------|------|
| Selected Area 1 | 1.8  | 95.8 | 1.4  | —    | 0.5  | 0.5  |
| Selected Area 2 | 24.7 | 72.6 | 1.2  | 0.4  | 0.8  | 0.3  |
| Selected Area 3 | 24.2 | 73.0 | 1.1  | 0.4  | 1.0  | 0.4  |
| Selected Area 4 | 25.9 | 71.8 | 1.1  | —    | 0.6  | 0.6  |
| Selected Area 5 | 12.6 | 85.0 | 1.4  | —    | 0.6  | 0.5  |

FIG. 22. SEM-EDS chemical composition (wt%) for Zry-4 reference specimen from KIT after 63 days of exposure. K and L X-ray emission lines were used for quantification.

### 3.6.2. Cr PVD coated Zry-2

Morphology of the PVD Cr coated Zry-2 CTU specimen, which was exposed for 21 days, is shown in Fig. 23. The coating thickness ranged from about 20  $\mu\text{m}$  to 30  $\mu\text{m}$ . The coating was continuous but some through the coating cracks and cracks between the coating and the substrate were found.

SEM-EDS mapping of O, Zr, Sn and Ni, where the coating is on the top, are shown in Fig. 24. SEM-EDS Selected Area analyses are shown in Fig. 25. No evident oxidation of the Zr substrate under the coating can be seen.

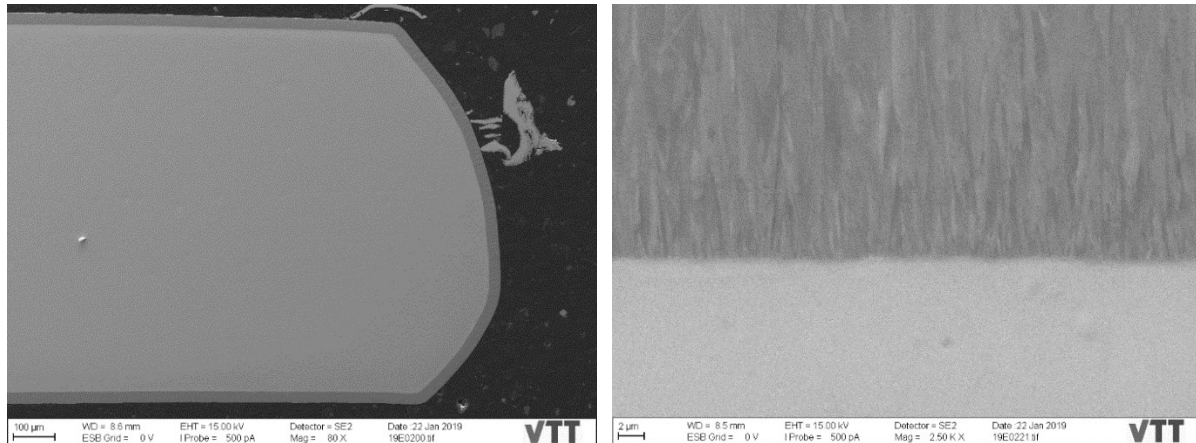


FIG. 23. SE images of Cr coated Zry-2 CTU specimen (21-day exposure).

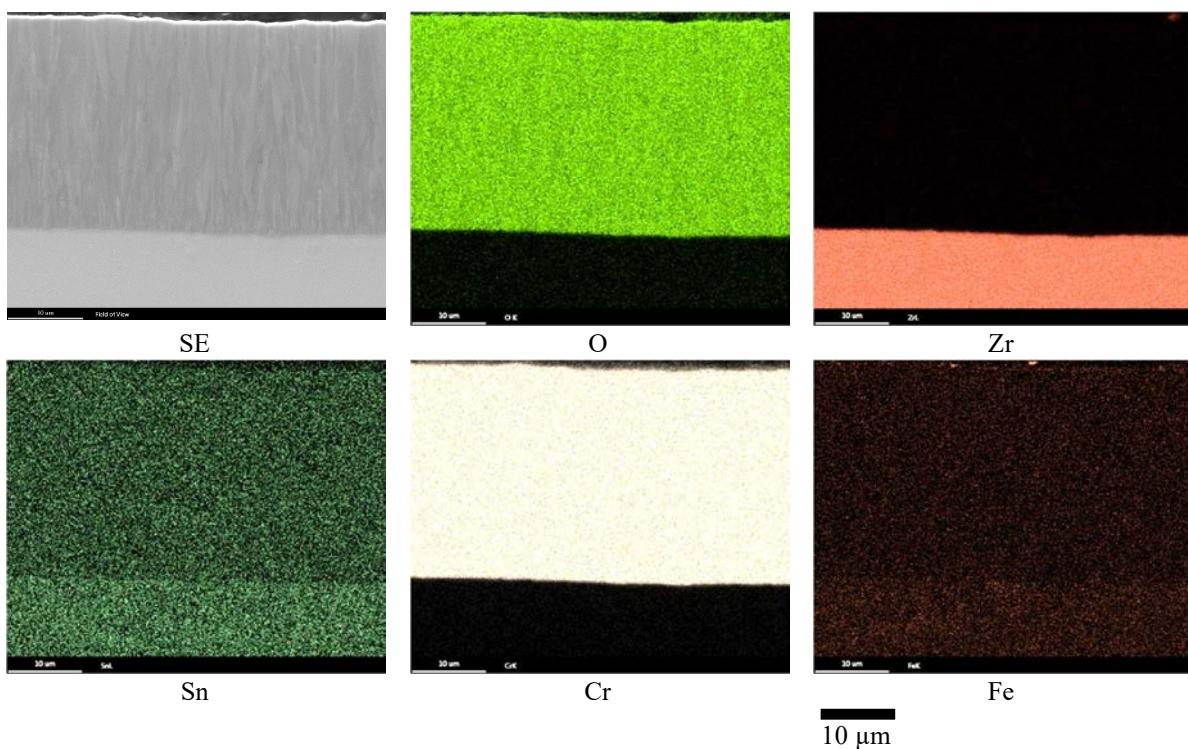
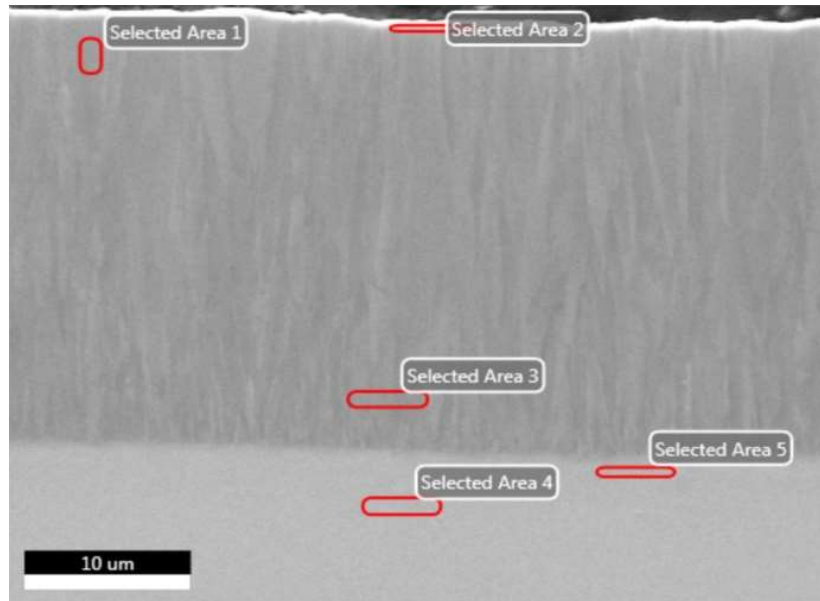


FIG. 24. SEM-EDS maps showing the distribution of O, Zr, Sn, Cr and Fe of the Cr coated Zry-2 CTU specimen (21-day exposure).



|                 | O K | Al K | Si K | Zr L | Sn L | Ti K | Cr K | Fe K | Ni K |
|-----------------|-----|------|------|------|------|------|------|------|------|
| Selected Area 1 | 3.2 | —    | —    | —    | 0.1  | —    | 95.7 | 0.6  | 0.4  |
| Selected Area 2 | 6.6 | 0.1  | 0.2  | —    | 0.2  | —    | 67.7 | 1.3  | 0.5  |
| Selected Area 3 | 3.4 | —    | 0.2  | —    | 0.1  | 0.2  | 95.4 | 0.4  | 0.4  |
| Selected Area 4 | 2.0 | —    | —    | 93.5 | 1.5  | —    | 1.3  | 0.9  | 0.8  |
| Selected Area 5 | 1.9 | —    | —    | 92.7 | 1.4  | —    | 2.6  | 0.9  | 0.6  |

FIG. 25. SEM-EDS chemical composition (wt%) SA analyses of Cr coated Zry-2 CTU (21-day exposure). K and L X-ray emission lines were used for quantification.

The morphology of Cr coated Zry-4 CTU specimen, which was exposed for 42 days, is shown in Fig. 26. The coating thickness ranged from about 20 µm to 30 µm. The coating was continuous but some the through coating cracks and the cracks between the coating and the substrate were found.

The SEM-EDS mapping of O, Zr, Sn, Cr and Fe, where the coating is on the top, is shown in Fig. 27. The SEM-EDS Selected Area analyses are shown in Fig. 28 (note: the image is upside down when compared to the images in Fig. 27 and Fig. 28). A crack through the coating can be seen. However, it did not result in oxidation of the underlying Zr substrate.

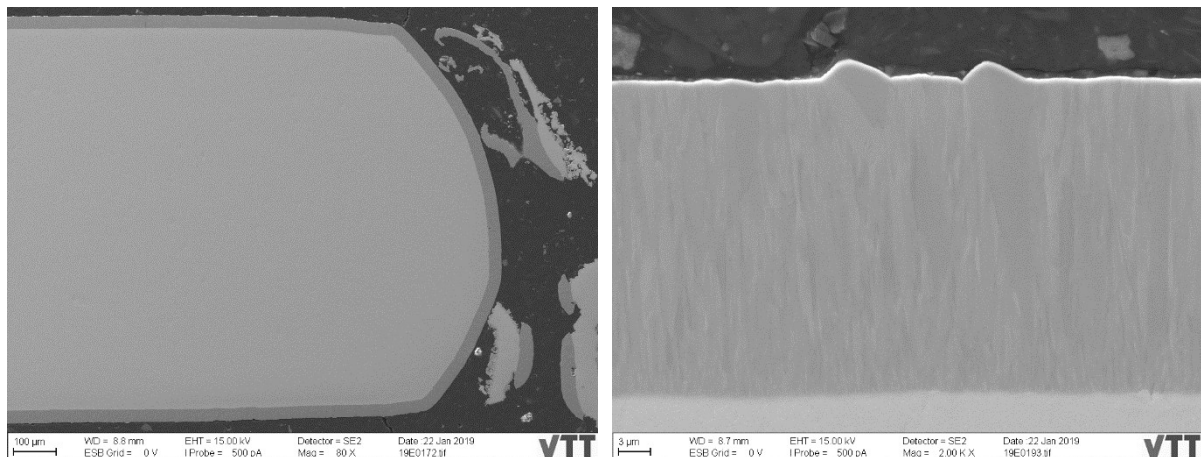


FIG. 26. SE images of Cr coated Zry-2 CTU specimen (42 day exposure).

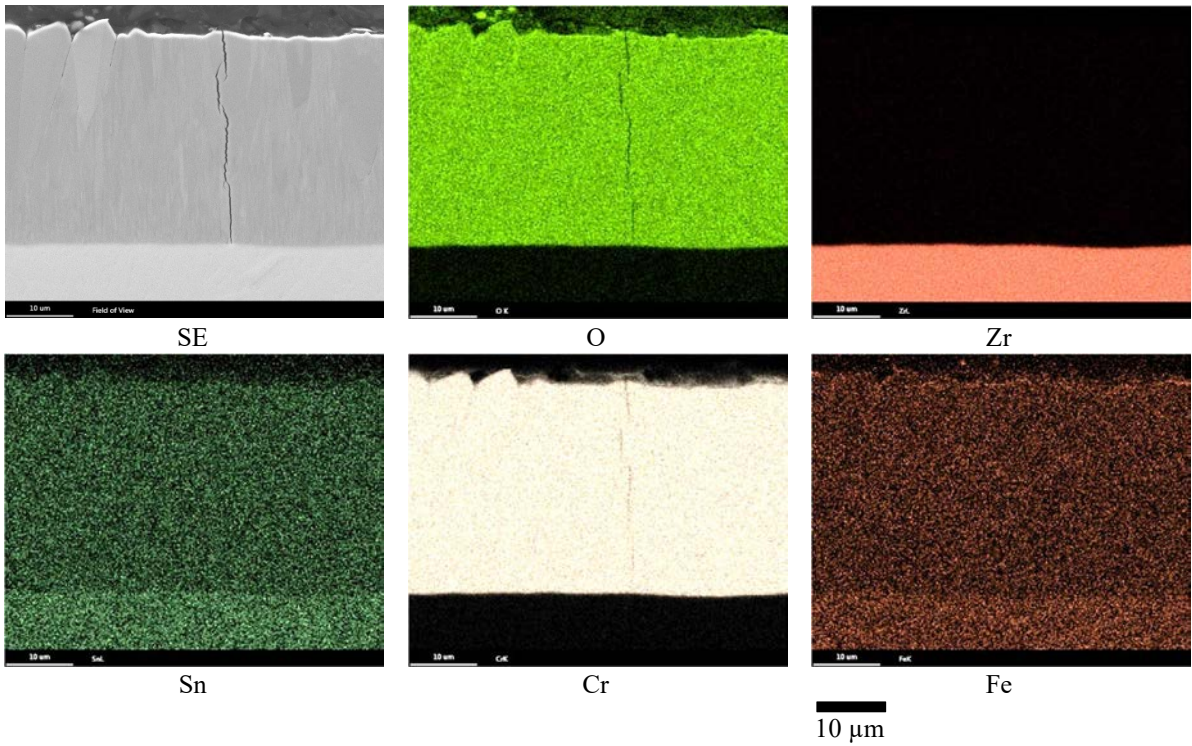
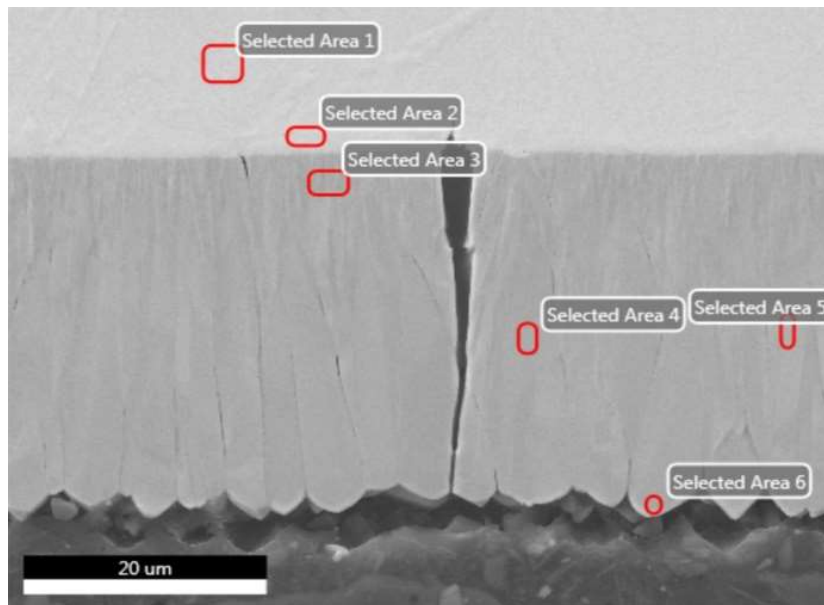


FIG. 27. SEM-EDS maps showing the distribution of O, Zr, Sn, Cr and Fe of the Cr coated Zry-2 CTU specimen (42-day exposure).



|                 | O K | Si K | Zr L | Sn L | Ti K | Cr K | Fe K | Ni K |
|-----------------|-----|------|------|------|------|------|------|------|
| Selected Area 1 | 2.2 | —    | 94.9 | 1.5  | —    | 0.5  | 0.5  | 0.4  |
| Selected Area 2 | 1.9 | —    | 93.8 | 1.3  | —    | 1.8  | 0.6  | 0.5  |
| Selected Area 3 | 3.3 | —    | —    | 0.1  | 0.2  | 95.6 | 0.5  | 0.3  |
| Selected Area 4 | 3.0 | —    | —    | 0.1  | —    | 96.5 | 0.5  | —    |
| Selected Area 5 | 3.1 | —    | —    | 0.1  | —    | 95.9 | 0.5  | 0.3  |
| Selected Area 6 | 3.0 | 0.1  | —    | 0.1  | —    | 96.0 | 0.6  | 0.2  |

FIG. 28. SEM-EDS chemical composition (wt%) SA analyses of Cr coated Zry-2 CTU specimen (42 days). K and L X-ray emission lines were used for quantification.

The morphology of the Cr coated Zry-2 CTU specimen, which was exposed for 63 days, is shown in Fig. 29. The coating thickness ranged from about 20  $\mu\text{m}$  to 30  $\mu\text{m}$ . The coating was continuous but some the through the coating cracks and the cracks between the coating and the substrate were found mainly on the sharper edges.

The SEM-EDS mapping of O, Zr, Sn, Cr and Fe is shown in Fig. 30. The SEM-EDS Selected Area analyses are shown in Fig. 31.

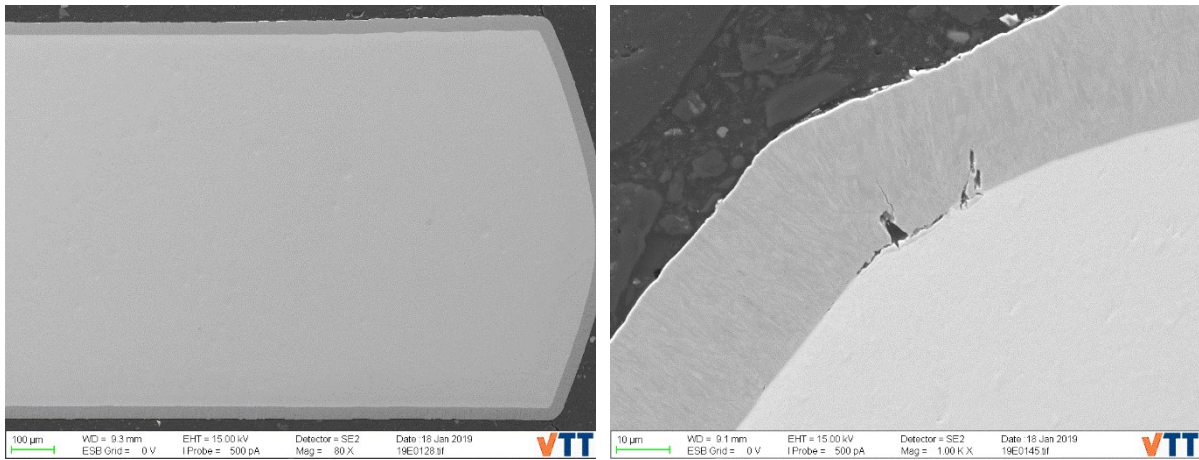


FIG. 29. SE images of Cr coated Zry-2 CTU specimen (63 day exposure).

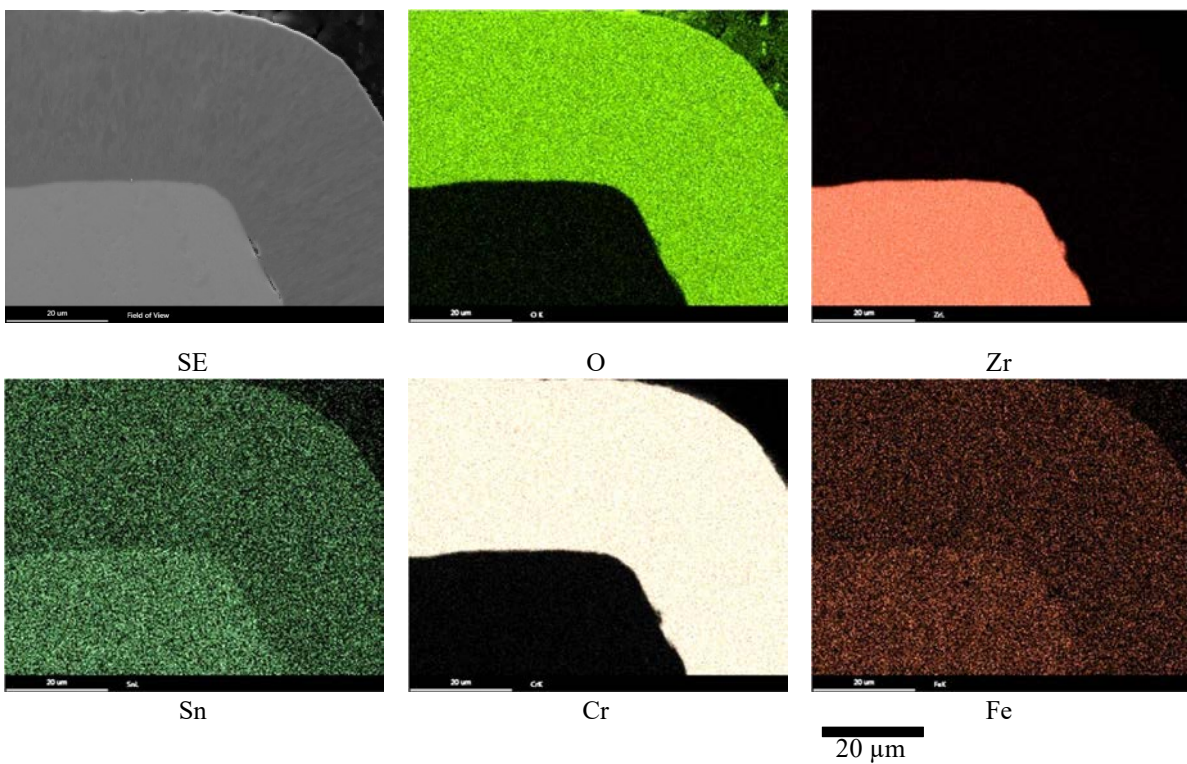
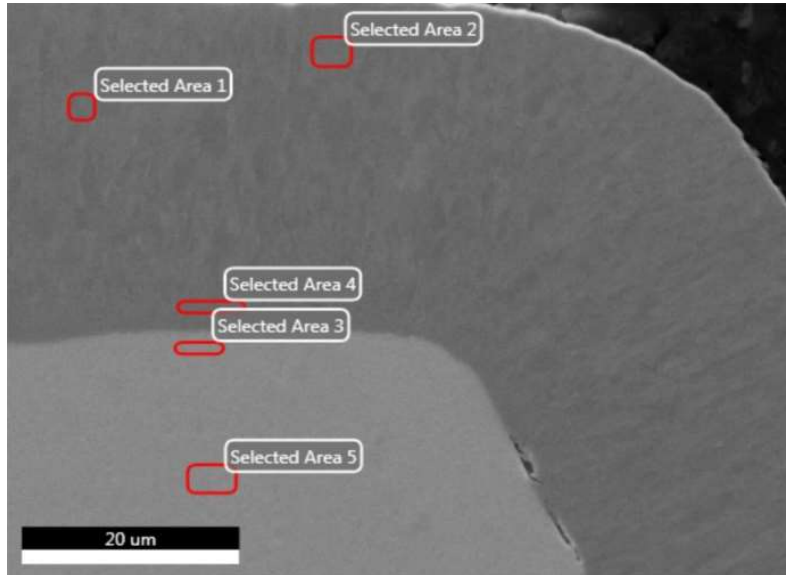


FIG. 30. SEM-EDS maps showing the distribution of O, Zr, Sn, Cr and Fe of the Cr coated Zry-2 CTU specimen (63 day exposure).



|                 | O K | Ni L | Si K | Zr L | Sn L | Cr K | Fe K |
|-----------------|-----|------|------|------|------|------|------|
| Selected Area 1 | 3.1 | 0.1  | 0.1  | —    | 0.2  | 96.0 | 0.5  |
| Selected Area 2 | 3.1 | 0.2  | 0.1  | —    | 0.1  | 96.0 | 0.5  |
| Selected Area 3 | 1.7 | 0.5  | —    | 94.6 | 1.5  | 1.8  | —    |
| Selected Area 4 | 3.1 | 0.3  | 0.2  | —    | 0.2  | 96.0 | 0.3  |
| Selected Area 5 | 1.9 | 0.3  | —    | 95.9 | 0.7  | 0.5  | 0.7  |

FIG. 31. SEM-EDS chemical composition (wt%) SA analyses of Cr coated Zry-2 CTU specimen (63-day exposure). K and L X-ray emission lines were used for quantification.

### 3.6.3. Cr/Cr<sub>2</sub>AlC/Cr (MAX phase) PVD coated Zry-4

The morphology of the MAX phase (Cr<sub>2</sub>AlC) coated Zry-4 specimen, which was exposed for 21 days, are shown in Fig. 32. The coating thickness ranged from about 0.5 μm to 5 μm. The coating was not continuous and parts of it have come loose during the sample preparation. Through the coating cracks and the cracks between the coating and the substrate were found.

SEM-EDS mapping of O, Al, Si, Zr, Sn, Cr, Fe and Ni, where the oxide layer is on the left side, is shown in Fig. 33. The SEM-EDS Selected Area analyses are shown in Fig. 34. There is no coating near the edges and the exposed Zr was oxidized. For the area covered by the coating, it was protected from oxidation.

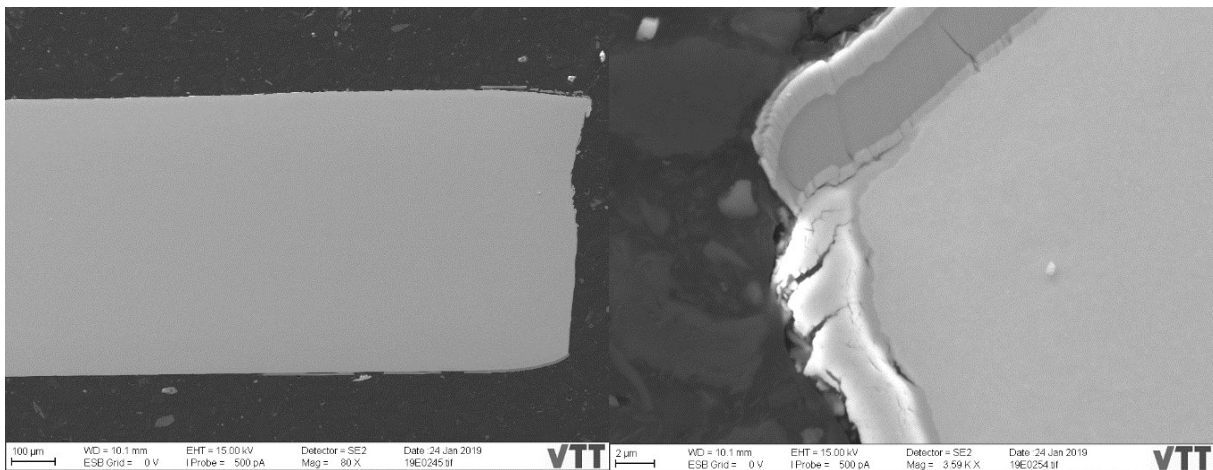


FIG. 32. SE images of MAX phase (Cr<sub>2</sub>AlC) coated Zry-4 KIT specimen (21-day exposure).

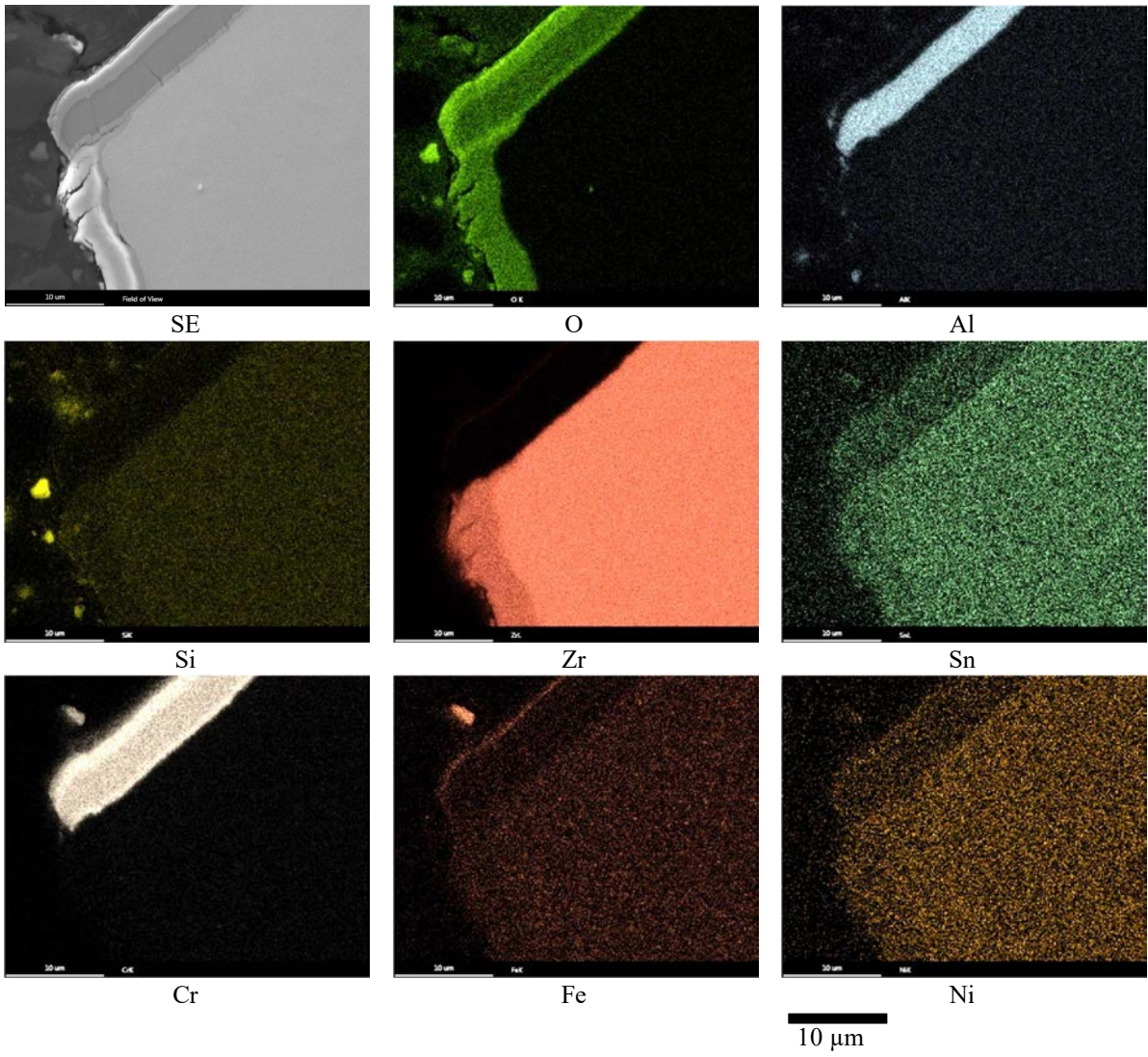
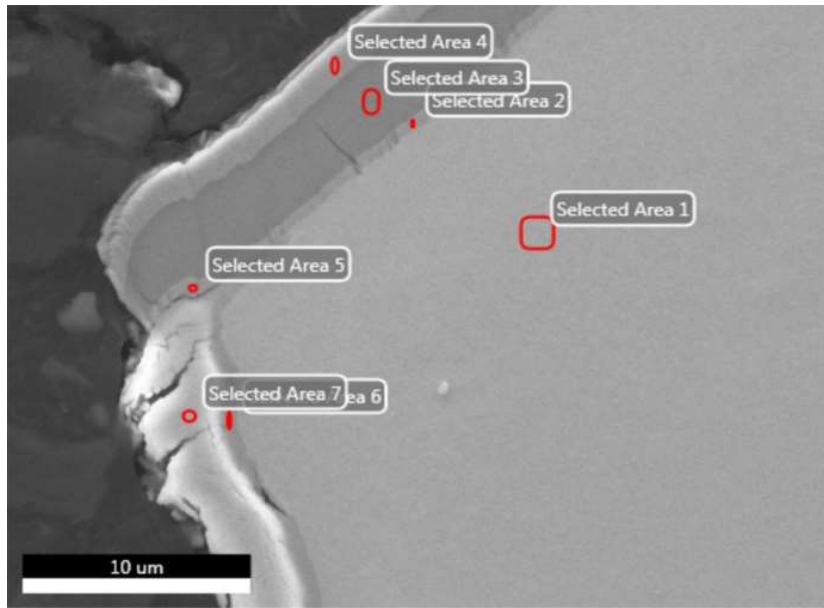


FIG. 33. SEM-EDS maps showing the distribution of O, Al, Si, Zr, Sn, Cr, Fe and Ni of the MAX phase ( $Cr_2AlC$ ) coated Zry-4 KIT specimen (21-day exposure).



|                 | O K  | Al K | Si K | Zr L | Sn L | Cr K | Fe K | Ni K |
|-----------------|------|------|------|------|------|------|------|------|
| Selected Area 1 | 1.8  | —    | —    | 94.1 | 1.7  | 1.2  | 1.3  | —    |
| Selected Area 2 | 2.8  | 8.0  | —    | 1.7  | 0.2  | 86.5 | 0.6  | —    |
| Selected Area 3 | 2.4  | 18.6 | —    | —    | 0.2  | 78.1 | 0.4  | —    |
| Selected Area 4 | 4.2  | 0.2  | —    | 0.3  | 0.2  | 94.1 | 0.8  | —    |
| Selected Area 5 | 4.1  | 2.8  | 0.3  | 1.9  | 0.3  | 89.9 | 0.7  | —    |
| Selected Area 6 | 25.4 | —    | —    | 71.0 | —    | 0.7  | 0.9  | 0.8  |
| Selected Area 7 | 27.3 | —    | —    | 70.1 | 1.1  | 0.6  | 1.0  | —    |

FIG. 34. SEM-EDS chemical composition (wt%) SA analyses of MAX phase ( $\text{Cr}_2\text{AlC}$ ) coated Zry-4 KIT specimen (21-day exposure). K and L X-ray emission lines were used for quantification.

The morphology of the MAX phase ( $\text{Cr}_2\text{AlC}$ ) coated Zry-4 specimen, which was exposed for 42 days, is shown in Fig. 35. The coating thickness ranged from about 3  $\mu\text{m}$  to 10  $\mu\text{m}$ . Similar to previous ones, the coating was not continuous and parts of it have come loose during the sample preparation. Through the coating cracks and the cracks between the coating and the substrate were found.

The SEM-EDS mapping of O, Al, Si, Zr, Sn, Cr, Fe and Ni, where the oxide layer is on the left side, is shown in Fig. 36. The SEM-EDS Selected Area analyses are shown in Fig. 37. On the short side of the specimen, the oxidation has progressed through the coating to the Zr substrate.

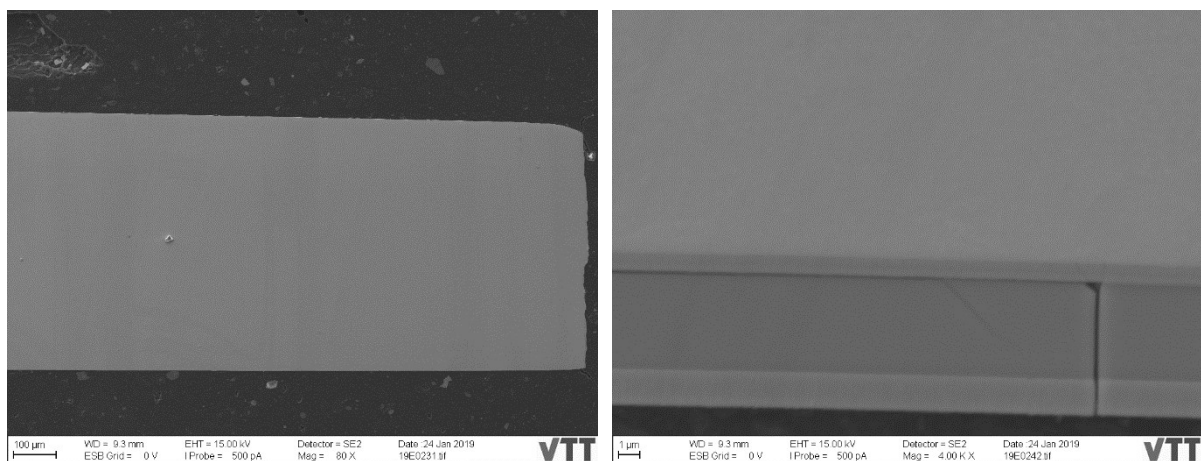


FIG. 35. SE images of MAX phase ( $\text{Cr}_2\text{AlC}$ ) coated Zry-4 KIT specimen (42-day exposure).

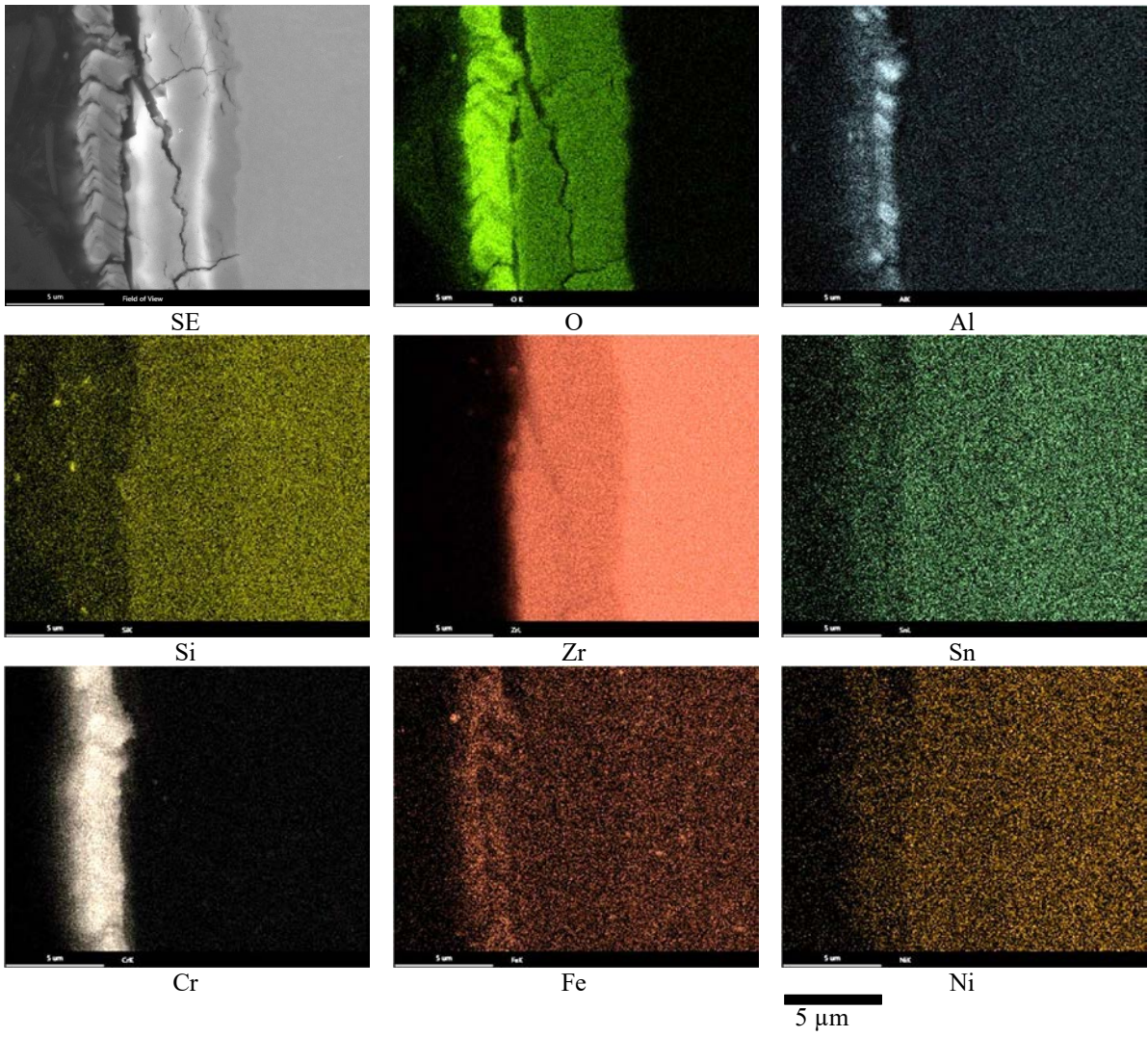
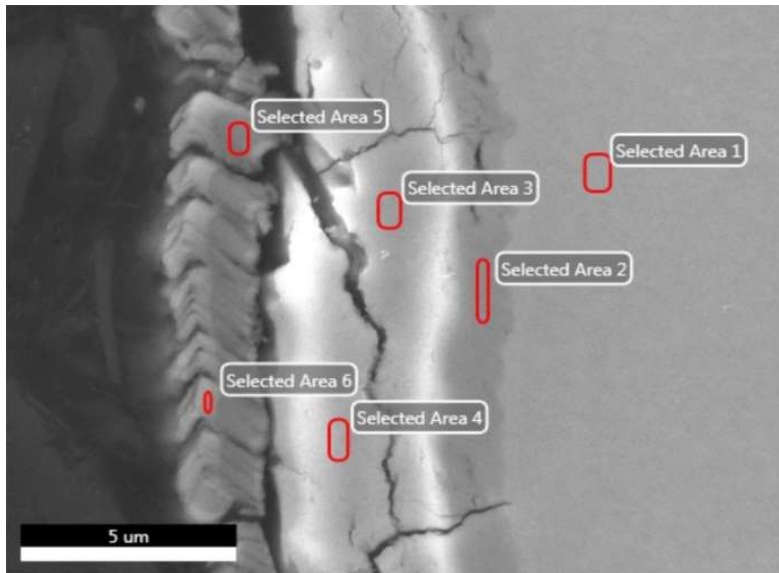


FIG. 36. The SEM-EDS mapping showing the distribution of O, Al, Si, Zr, Sn, Cr, Fe and Ni of the Max phase ( $Cr_2AlC$ ) coated Zry-4 KIT specimen (42-day exposure).



|                 | O K  | Al K | Si K | Zr L | Sn L | Cr K | Fe K | Ni K |
|-----------------|------|------|------|------|------|------|------|------|
| Selected Area 1 | 1.9  | —    | —    | 95.0 | 1.8  | —    | 1.4  | —    |
| Selected Area 2 | 24.7 | —    | —    | 70.7 | 1.3  | 0.9  | 1.4  | 1.0  |
| Selected Area 3 | 26.4 | —    | —    | 69.7 | 1.4  | 1.1  | 1.5  | —    |
| Selected Area 4 | 26.1 | —    | —    | 68.7 | 1.5  | 1.2  | 1.5  | 1.1  |
| Selected Area 5 | 9.5  | 12.0 | 0.4  | —    | 0.1  | 75.6 | 1.7  | 0.5  |
| Selected Area 6 | 13.6 | 1.9  | 0.3  | —    | 0.2  | 71.7 | 2.3  | 0.8  |

FIG. 37. SEM-EDS chemical composition (wt%) SA analyses of Max phase ( $Cr_2AlC$ ) coated Zry-4 KIT specimen (42-day exposure). K and L X-ray emission lines were used for quantification.

The morphology of the MAX phase ( $Cr_2AlC$ ) coated Zry-4 specimen, which was exposed for 63 days, is shown in Fig. 38. The coating thickness ranged from about 2  $\mu m$  to 40  $\mu m$ . The coating was not continuous and parts of it had come loose during the sample preparation. Through the coating cracks and the cracks between the coating and the substrate were found. When comparing 63 days to 21 days the remaining amount of coating is smaller in the specimen that was exposed for 63 days.

The SEM-EDS mapping of O, Al, Si, Zr, Sn, Cr, Fe and Ni is shown in Fig. 39. The SEM-EDS Selected Area analyses are shown in Fig. 40. During the exposure, majority of the coating peeled off from the specimen surface, and the exposed substrate was oxidized consequently as shown in Figs 39 and 40.

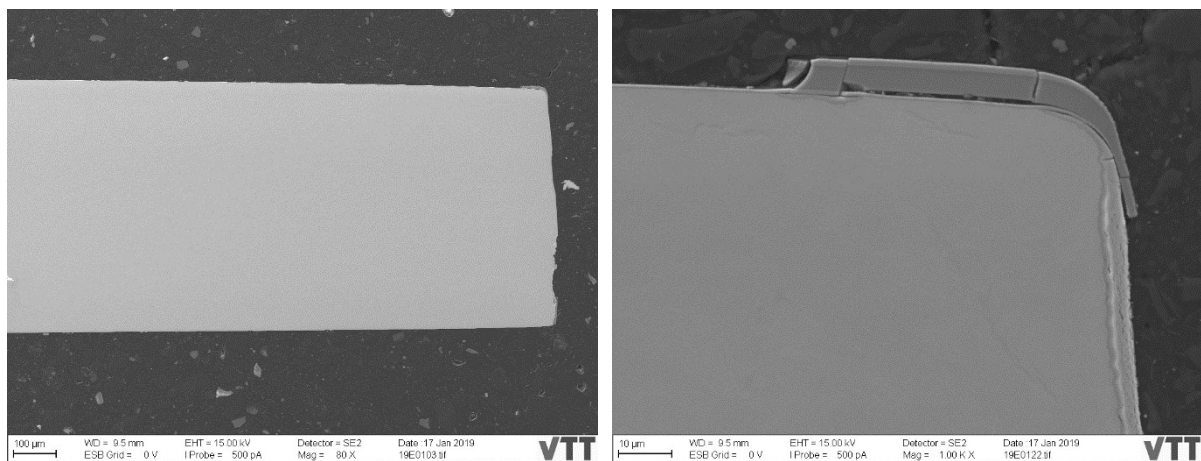


FIG. 38. SE images of MAX phase ( $Cr_2AlC$ ) coated Zry-4 KIT specimen (63 days).

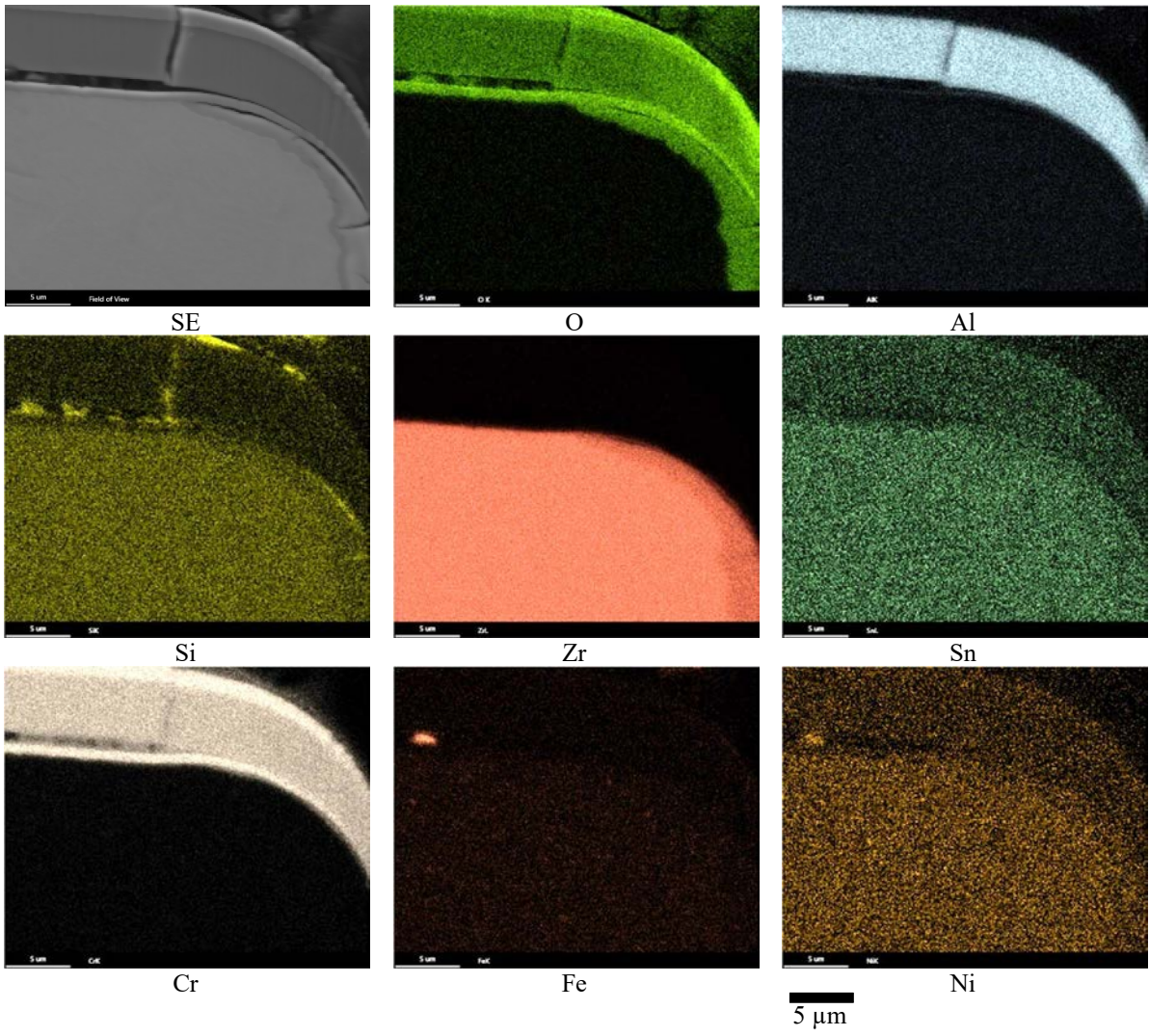
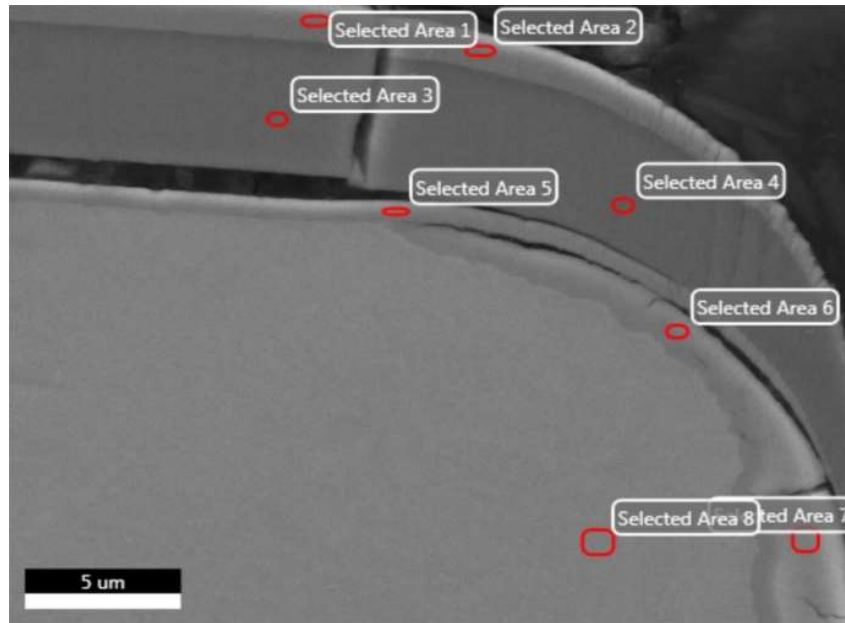


FIG. 39. SEM-EDS maps showing the distribution of O, Al, Si, Zr, Sn, Cr, Fe and Ni of the Max phase ( $Cr_2AlC$ ) coated Zry-4 KIT specimen (63-day exposure).



|                 | O K  | Ni L | Al K | Si K | Zr L | Sn L | Cr K | Fe K |
|-----------------|------|------|------|------|------|------|------|------|
| Selected Area 1 | 3.2  | 0.3  | 0.4  | 0.5  | —    | 0.1  | 95.2 | 0.4  |
| Selected Area 2 | 4.1  | 0.2  | 0.3  | 0.9  | —    | 0.2  | 93.9 | 0.4  |
| Selected Area 3 | 2.2  | 0.2  | 20.8 | 0.3  | —    | 0.2  | 76.1 | 0.2  |
| Selected Area 4 | 4.8  | 0.1  | 21.3 | 0.4  | 0.4  | 0.1  | 72.7 | 0.2  |
| Selected Area 5 | 4.0  | 0.2  | 0.9  | 0.5  | 2.2  | 0.1  | 91.9 | 0.3  |
| Selected Area 6 | 25.1 | 0.1  | 0.1  | —    | 68.7 | 1.1  | 3.8  | 1.1  |
| Selected Area 7 | 26.2 | 0.5  | —    | —    | 71.3 | 1.0  | 0.6  | 0.4  |
| Selected Area 8 | 1.9  | 0.4  | —    | —    | 95.6 | 1.5  | —    | 0.6  |

FIG. 40. SEM-EDS chemical composition (wt%) SA analyses of the MAX phase ( $Cr_2AlC$ ) coated Zry-4 KIT (63-day exposure). K and L X-ray emission lines were used for quantification.

### 3.6.4. ZrSi-Cr PVD coated Zry-2

The morphology of the ZrSi-Cr coated Zry-2 INCT specimen, which was exposed for 16.5 days, is shown in Fig. 41. The oxide layer thickness ranged from about 2  $\mu m$  to 10  $\mu m$ . The layer was not continuous and parts of it had come loose during the sample preparation. Through the oxide layer cracks and the cracks between the oxide layer and the substrate were found.

The SEM-EDS mapping of O, Al, Si, Zr, Sn, Cr, Fe and Ni, where the oxide layer is on the left side, is shown in Fig. 42. The SEM-EDS Selected Area analyses are shown in Fig. 43. The oxide layer is clearly damaged, which is shown in the O and Zr mapping in Fig. 42. Under the oxide layer the oxygen content in the zirconium substrate increased.

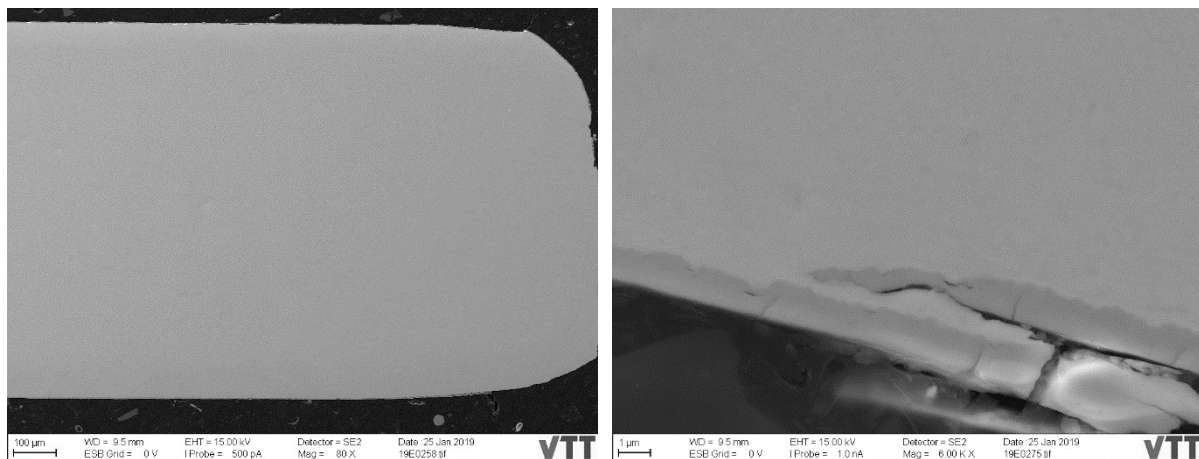


FIG. 41. SE images of ZrSi-Cr coated Zry-2 INCT specimen (16.5-day exposure).

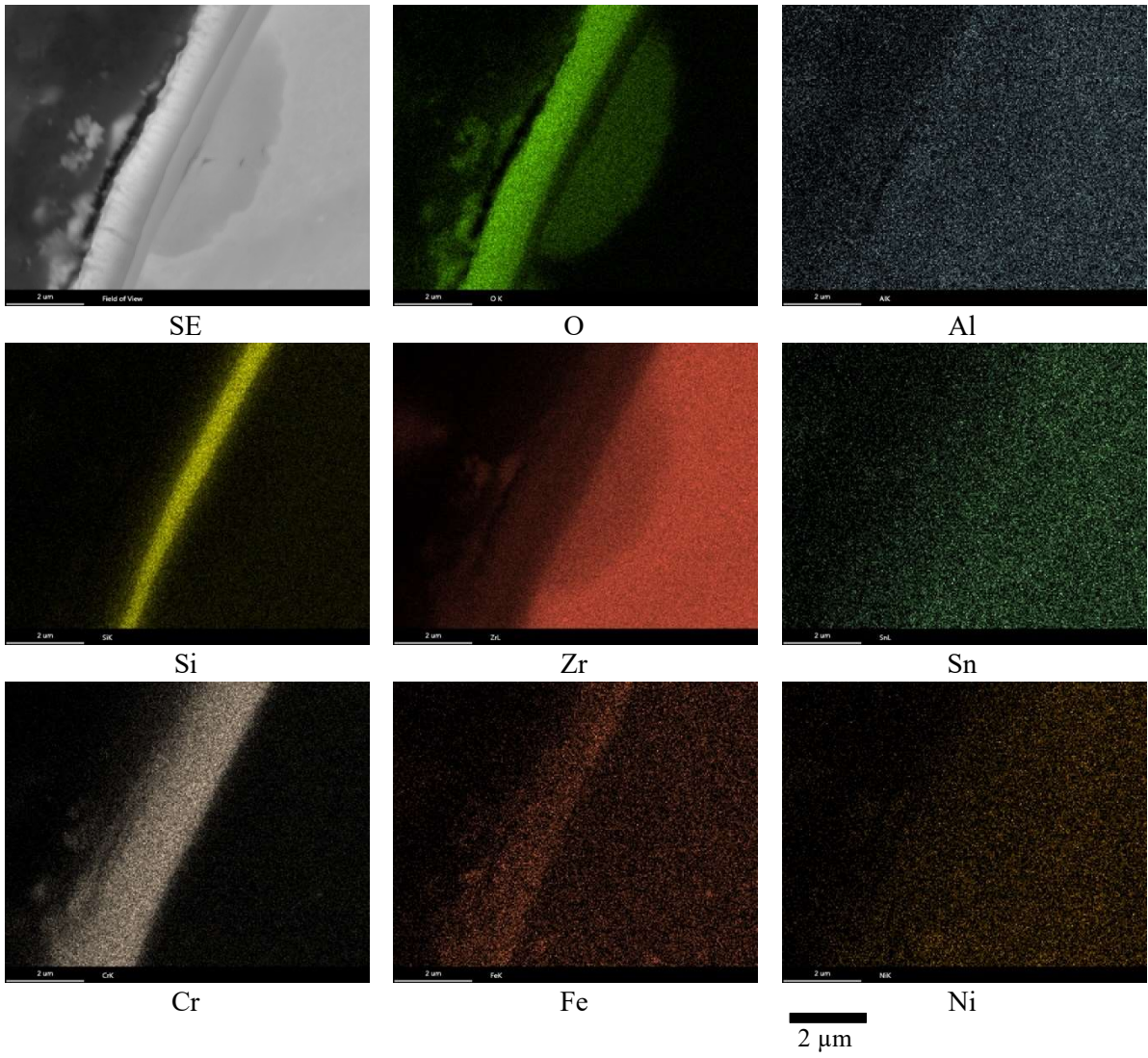
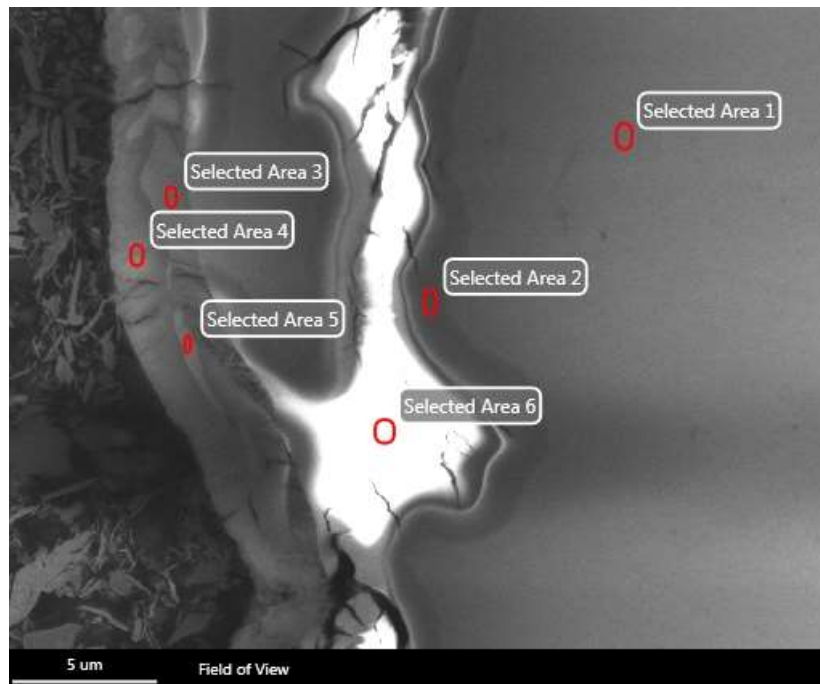


FIG. 42. SEM-EDS maps showing the distribution of O, Al, Si, Zr, Sn, Cr, Fe and Ni of the ZrSi-Cr coated Zry-2 INCT specimen (16.5-day exposure).



|                 | O K  | Ni L | Al K | Si K | Zr L | Sn L | Cr K | Fe K |
|-----------------|------|------|------|------|------|------|------|------|
| Selected Area 1 | 1.8  | 1.1  | —    | —    | 94.0 | 0.8  | 0.9  | 1.4  |
| Selected Area 2 | 25.8 | 0.7  | —    | —    | 71.4 | 0.7  | 0.5  | 0.9  |
| Selected Area 3 | 4.7  | 0.6  | —    | 28.6 | 31.5 | 0.2  | 33.7 | 0.7  |
| Selected Area 4 | 27.8 | —    | 0.1  | 1.1  | 27.4 | —    | 31.4 | 9.0  |
| Selected Area 5 | 13.7 | —    | —    | 17.0 | 25.1 | —    | 44.3 | —    |
| Selected Area 6 | 27.8 | —    | —    | —    | 69.8 | 1.1  | 0.4  | 0.7  |

FIG. 43. The SEM-EDS chemical composition (wt%) for the ZrSi-Cr coated Zry-2 INCT specimen after 16.5 days of exposure. K and L X-ray emission lines were used for quantification.

### 3.6.5. AISI 348 SS

The morphology of the AISI 348 specimen, which was exposed for 63 days, is shown in Fig. 44. The specimens exposed for 21 and 42 days are not reported here in terms of cross section / elemental analyses due to the insignificant oxidation of the specimens. The oxide layer on the specimen exposed for 63 days was not continuous and most parts of it flaked off during the sample preparation. Locally, layers of metal were observed on top of a thin oxide layer possibly as a result of the initial surface machining. In general, the thickness of these local areas of the oxide layer was about 1 µm as shown in Fig. 44.

The SEM-EDS mapping of O, Nb, Cr, Mn, Fe and Ni, where the oxide layer is on the left side of the photos, are shown in Fig. 45. The SEM-EDS Selected Area analyses are shown in Fig. 46. In Fig. 46, the Nb-mapping shows the presence of some Nb particles (carbide stabilizer).

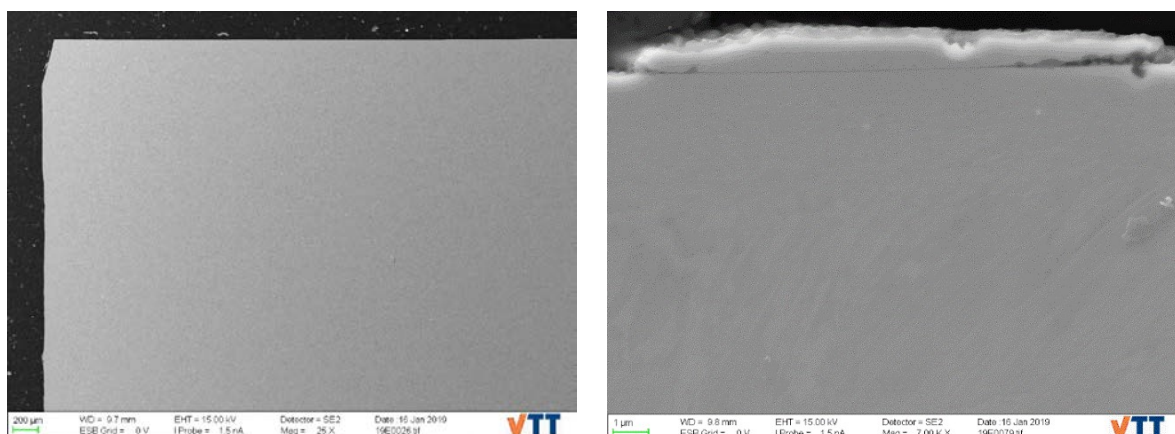


FIG. 44. SE images of AISI 348 specimen (63 days).

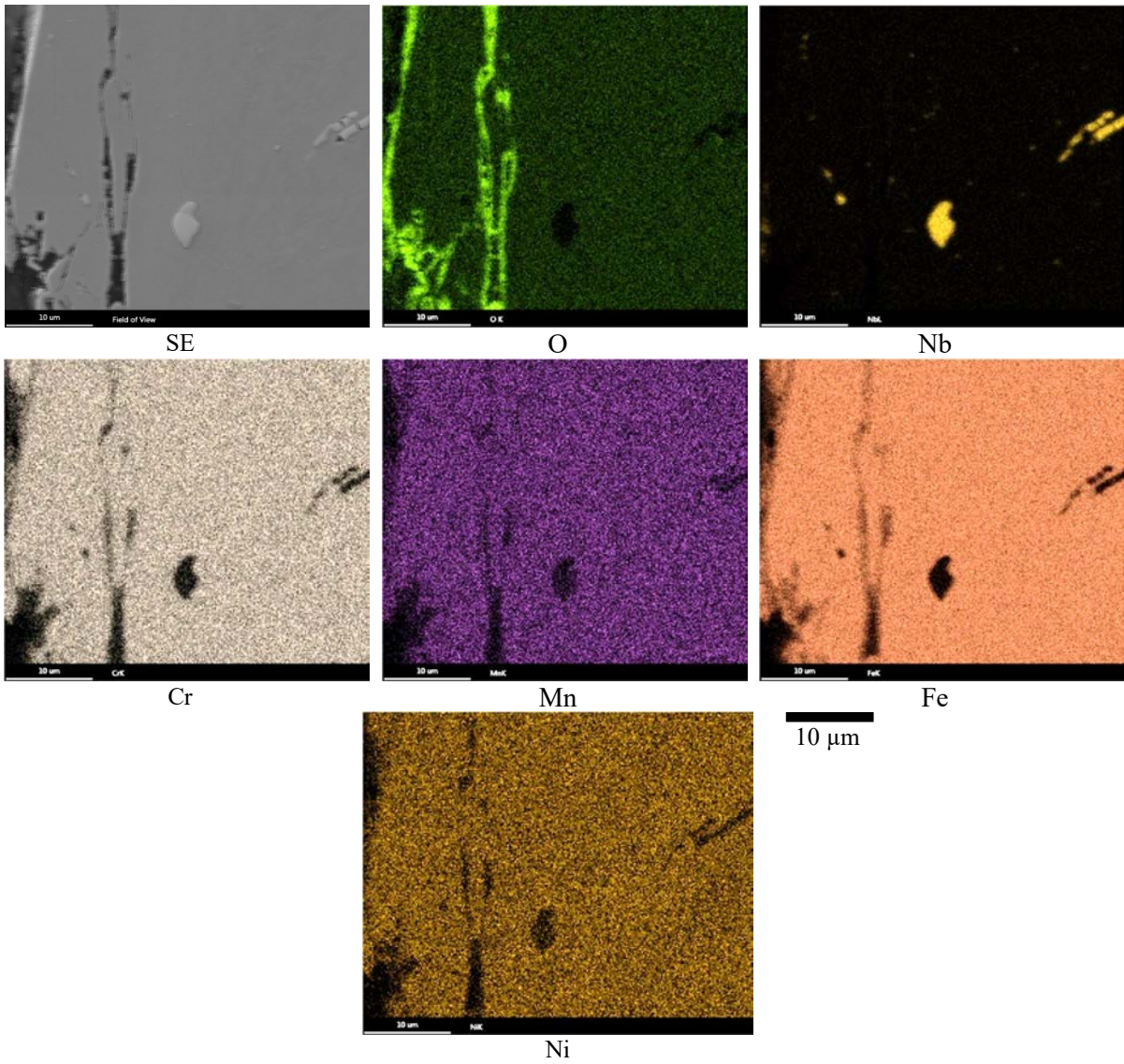
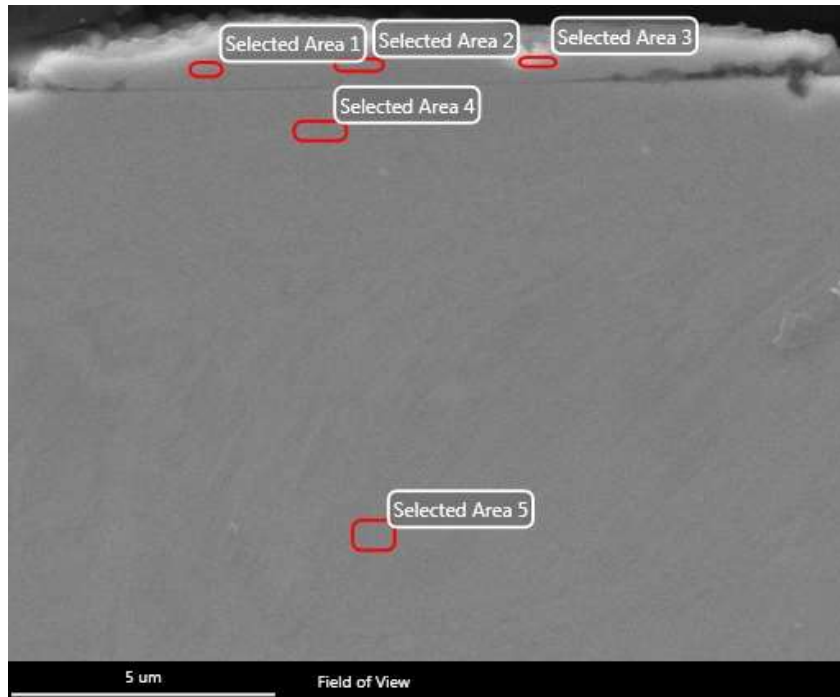


FIG. 45. SEM-EDS maps showing the distribution of O, Nb, Cr, Mn, Fe and Ni of the AISI 348 specimen (63 days).



|                 | O K | Al K | Si K | Nb L | Cr K | Mn K | Fe K | Ni K |
|-----------------|-----|------|------|------|------|------|------|------|
| Selected Area 1 | —   | 0.1  | 0.6  | 0.4  | 17.0 | 1.7  | 71.1 | 9.1  |
| Selected Area 2 | —   | —    | 0.6  | 0.4  | 17.0 | 2.0  | 71.0 | 9.1  |
| Selected Area 3 | 6.2 | —    | 0.4  | 43.3 | 9.7  | —    | 36.0 | 4.5  |
| Selected Area 4 | —   | —    | 0.6  | 1.7  | 17.1 | 2.1  | 69.8 | 8.7  |
| Selected Area 5 | —   | —    | 0.6  | 0.4  | 17.0 | 2.0  | 70.1 | 9.1  |

FIG. 46. The SEM-EDS chemical composition (wt%) for the specimen AISI 348 after exposure for 63 days. K and L X-ray emission lines were used for quantification.

### 3.7. RESULTS: INCT

#### 3.7.1. Uncoated Zr-based alloys: reference samples

The visual inspection of the Zry-2 samples before and after the test is shown in Fig. 47. The sample surfaces did not change color – they were still grey but getting darker as the test progressed.

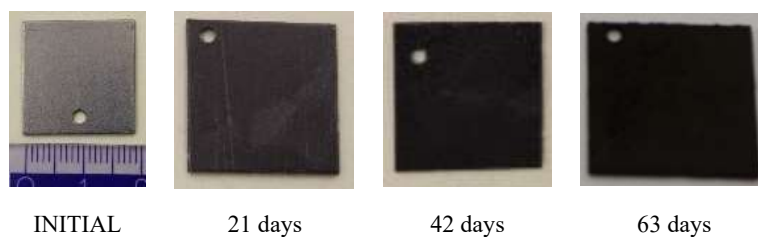


FIG. 47. Overview of the Zry-2 sample during the corrosion test.

The SEM micrographs of the samples are shown in Fig. 48. The surface roughness increased as the sample was oxidized. Fiber-like, needle-like and plate-like oxides were visible. Higher magnification image shows needle-structure and plates shaped oxides agglomerate after 63 days.

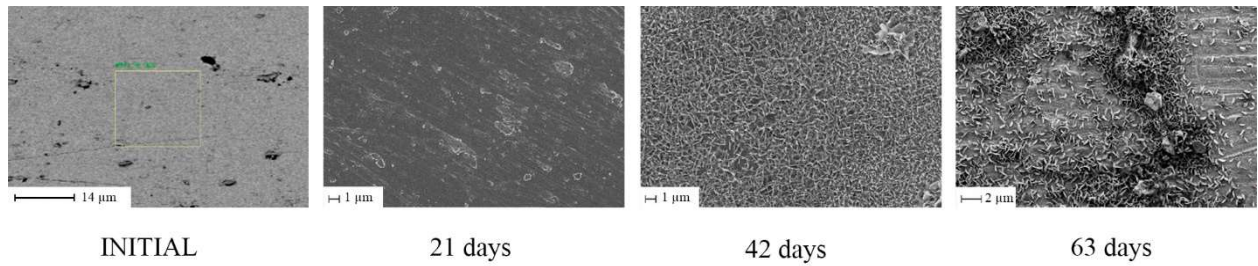


FIG. 48. SEM micrographs of the Zry-2 sample during the test; mag. 1000X.

It was observed that the oxide layer was formed after 21, 42 and 63 days in the autoclave. The elemental analysis showed that the oxide layer contained only zirconium and oxygen as can be seen in the cross section SEM in Fig. 49.

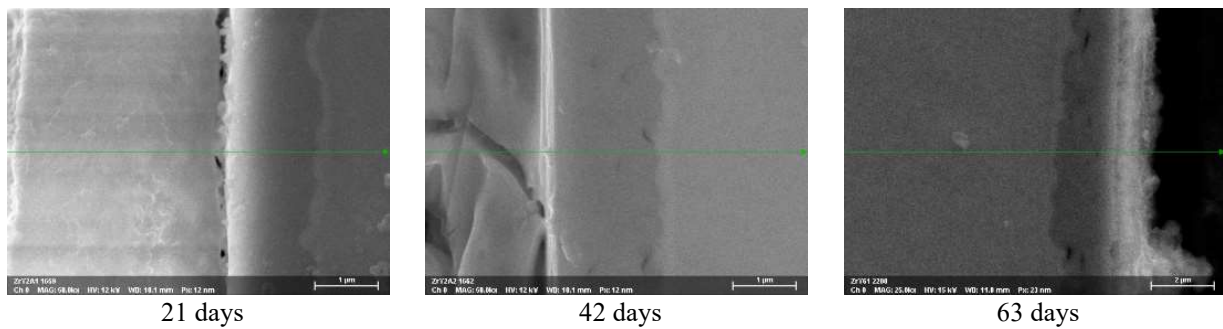


FIG. 49. Zry-2 cross section after 21, 42 and 63 days (SEM).

The mass gain data is shown in Table 18.

TABLE 18. MASS GAINS OF THE ZRY-2 SAMPLE

|                         | 21 days | 42 days | 63 days |
|-------------------------|---------|---------|---------|
| Surface mass change [%] | 2.79    | 4.209   | 5.313   |

Presence of Zr in the hexagonal structure was confirmed by XRD phase analysis. Presence of zirconium oxide  $ZrO_2$  phase in the monoclinic structure was confirmed after exposure.

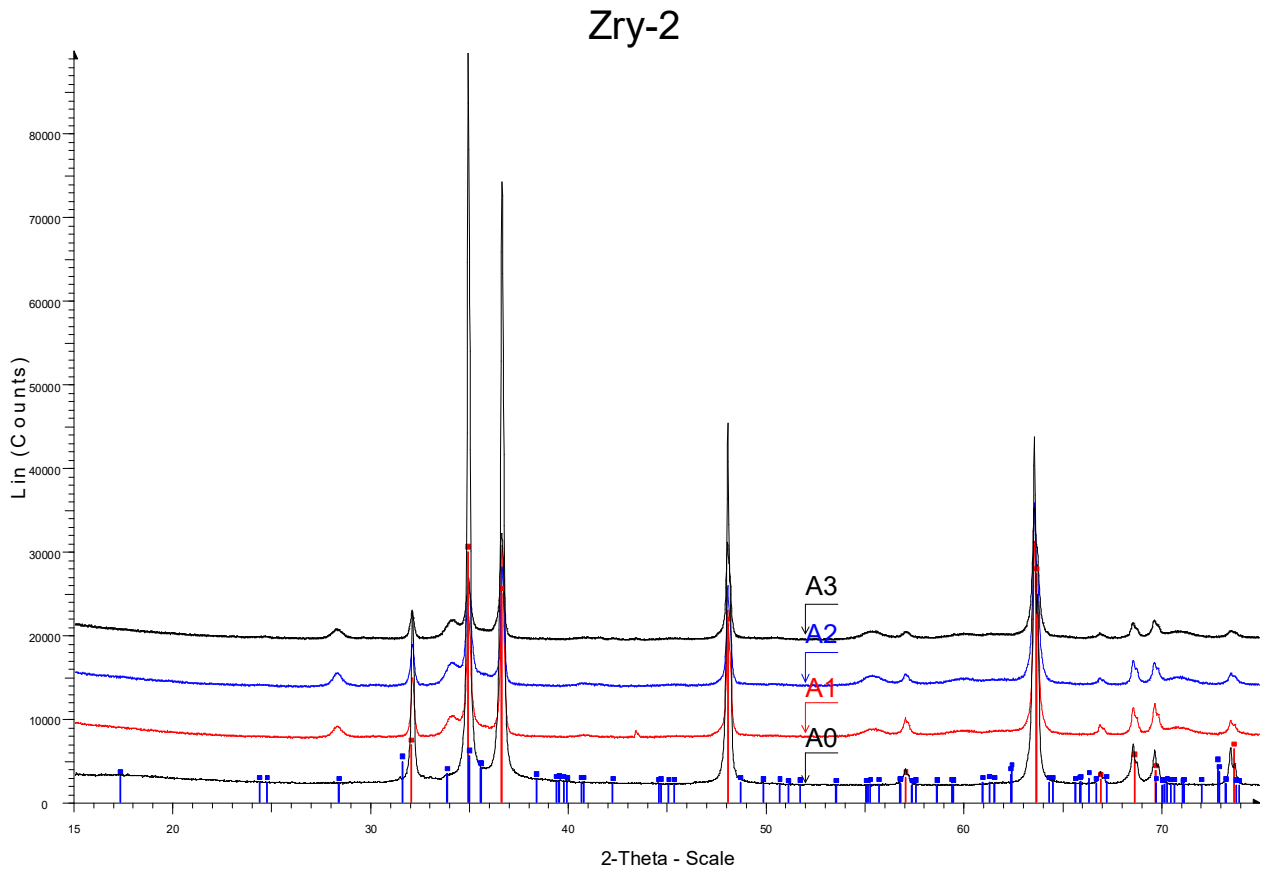


FIG. 50. XRD analysis of Zry-2 sample during the long term corrosion test (red markers – hexagonal Zr; blue markers – ZrO<sub>2</sub>; A0 – 0 days, A1 – 21 days, A2 – 42 days, A3 – 63 days).

The sample morphology before and after the tests is shown in Fig. 51.

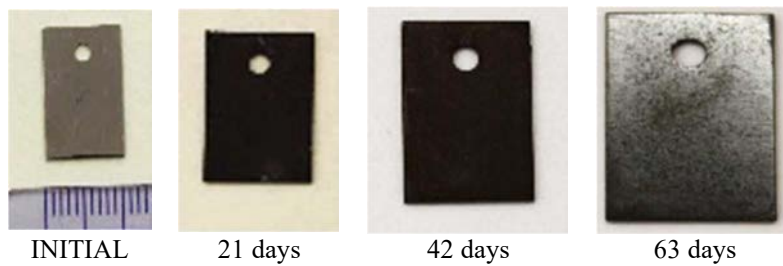


FIG. 51. Overview of the Zry-4 sample during the test.

It was observed that the surface roughness and irregularities increased as a result of surface oxidation, and visible morphological objects like grains and agglomerates can be found as shown in Fig. 52.

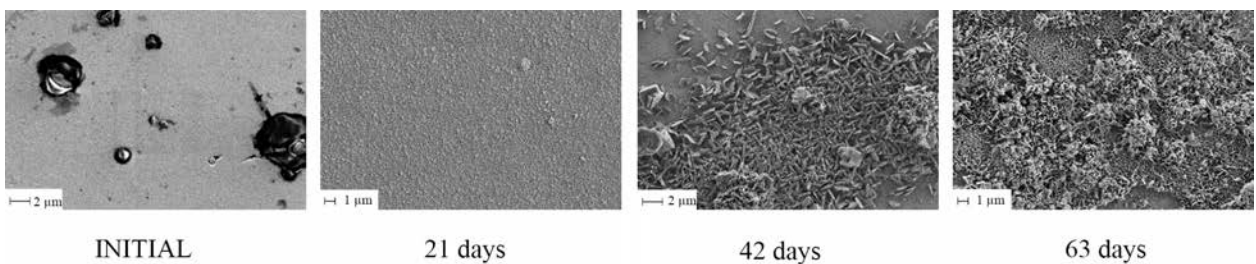


FIG. 52. SEM micrographs of the Zry-4 sample during the test.

The oxide layers were formed after 21, 42 and 63 days. The elemental analysis showed that the oxide layers contained only zirconium and oxygen as shown in Fig. 53.

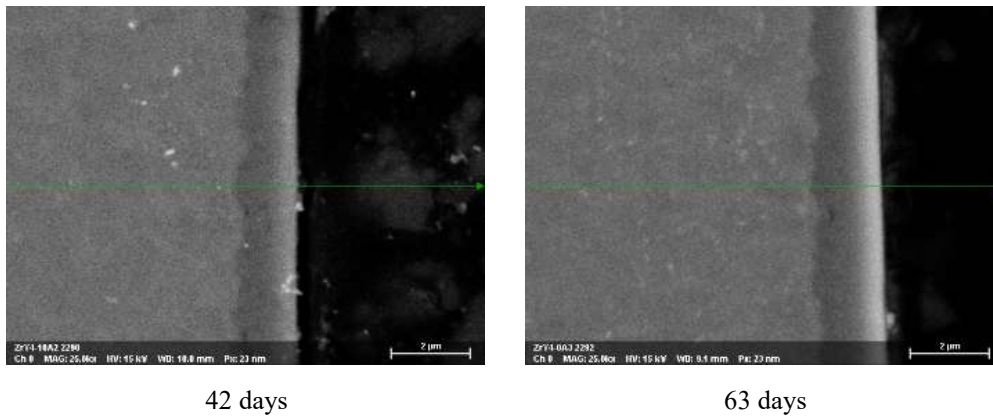


FIG. 53. Zry-4 cross section after 42 and 63 days (SEM).

The mass gain data are summarized in Table 19, showing similar results after 21, 42 and 63 days. The formation of the oxidized layer appeared to be continuous.

TABLE 19. MASS GAINS OF THE ZRY-4 SAMPLE

|                         | 21 days | 42 days | 63 days |
|-------------------------|---------|---------|---------|
| Surface mass change [%] | 3.1     | 3.525   | 3.45    |

### 3.7.2. PVD Cr coated Zry-2

The morphology of the Cr-coated sample before and after the test is shown in Fig. 54. The sample surface changed its color from grey to golden after 21 days. The surface colour became darker after 42 and 63 days.

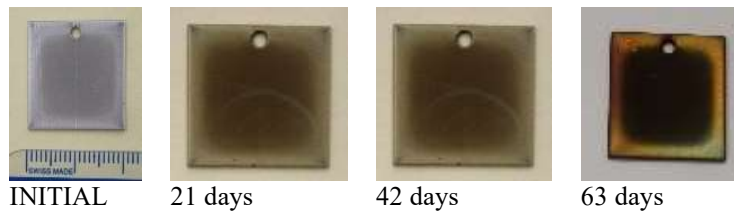


FIG. 54. Overview of the Cr coated Zry-2 sample during the test.

The granular surface morphology was preserved after the test. The grains density remains the same.

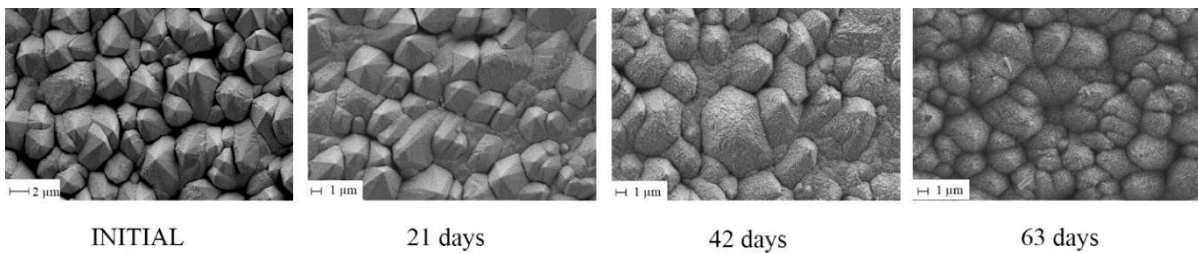


FIG. 55. SEM micrographs of the Cr coated Zry-2 sample during the test X 10000.

The thickness of the coatings was measured to be 26 μm. A thin oxide layer after 21, 42 and 63 days can be seen in Fig. 56.

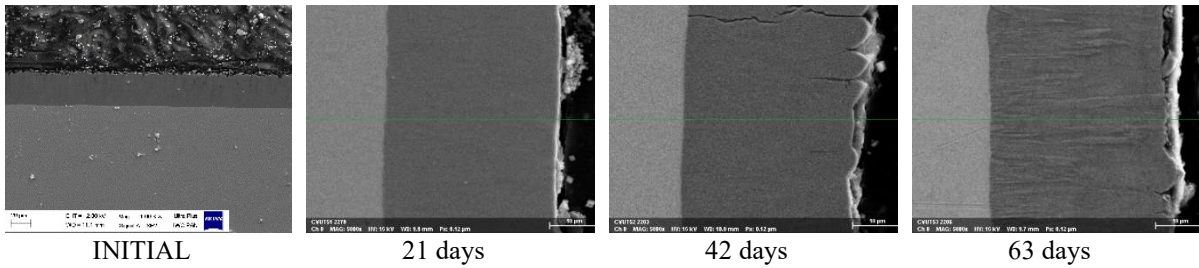


FIG. 56. Cr coated Zry-2 as-received cross section and after the exposition of 21, 42 and 63 days (SEM).

The mass gains after different exposure times are shown in Table 20.

TABLE 20. SURFACE MASS GAINS OF THE CR PVD COATED ZRY-2 SAMPLE

|                         | 21 days | 42 days | 63 days |
|-------------------------|---------|---------|---------|
| Surface mass change [%] | 0.375   | 0.51    | 0.94    |

The presence of pure Cr was confirmed by XRD. The red markers show pure Cr metal peaks. Weak reflections/peaks are visible at  $2\theta = 33.75^\circ$  and  $2\theta = 55.096^\circ$ . They probably belong to chromium oxide. Due to the thickness of the Cr coating (about 26  $\mu\text{m}$ ), no Zry-2 substrate phase was seen.

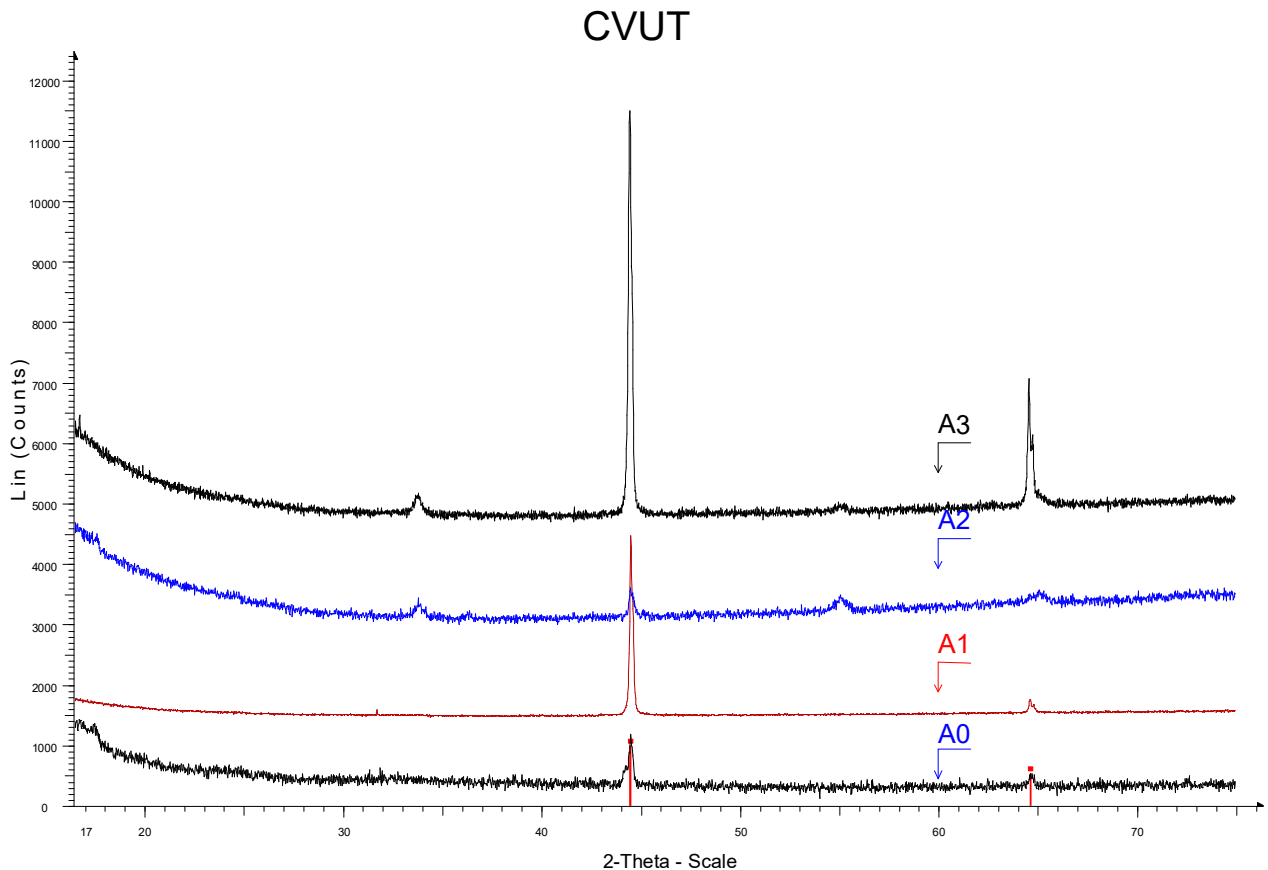


FIG. 57. XRD analysis of Cr coated Zry-2 sample during the long term corrosion test (A0 – as-received, A1 – 21 days, A2 – 42 days, A3 – 63 days). The main peak corresponds to (110), second to (200). Growth of  $\text{Cr}_2\text{O}_3$  in A2 and A3 can be seen in peak at  $33^\circ$  (2-Theta).

### 3.7.3. PVD Cr/Cr<sub>2</sub>AlC/Cr (MAX phase) coated Zry-4

The Morphology of PVD MAX coating samples is shown in Fig. 58. Cracking and spallation of the coating was observed. Some coating materials spalled during sample handling for post test characterization. Dark oxides were formed after oxidation.

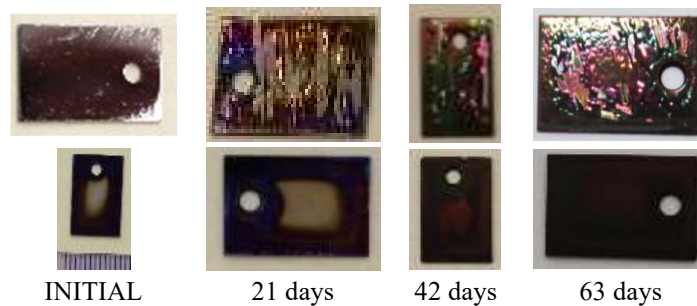


FIG. 58. Overview of the MAX phase coated Zry-4 sample during the test.

The coating appears to be smooth, although some cracks were visible. After the exposure, new morphological objects were visible as for example: grains, agglomerates. The samples exposed to 21 days were partially covered while the samples exposed to 42 and 63 days were fully covered.

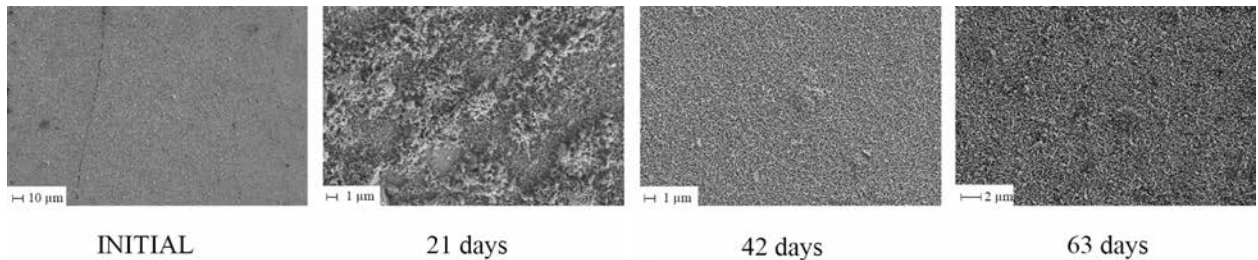


FIG. 59. SEM micrographs of the MAX phase coated Zry-4 sample during the test X 1000 and X 10000.

The SEM/EDS analysis of cross section after 63 days shows an additional layer formed between the material and coating, consisting mostly of Cr (not present before). On both edges of this layer, there is a higher concentration of oxygen. The coating layer includes a small amount of Al.

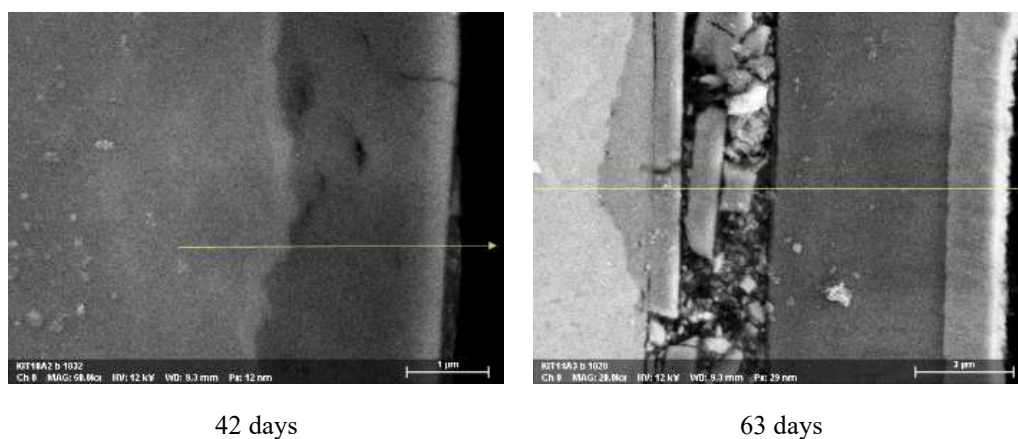


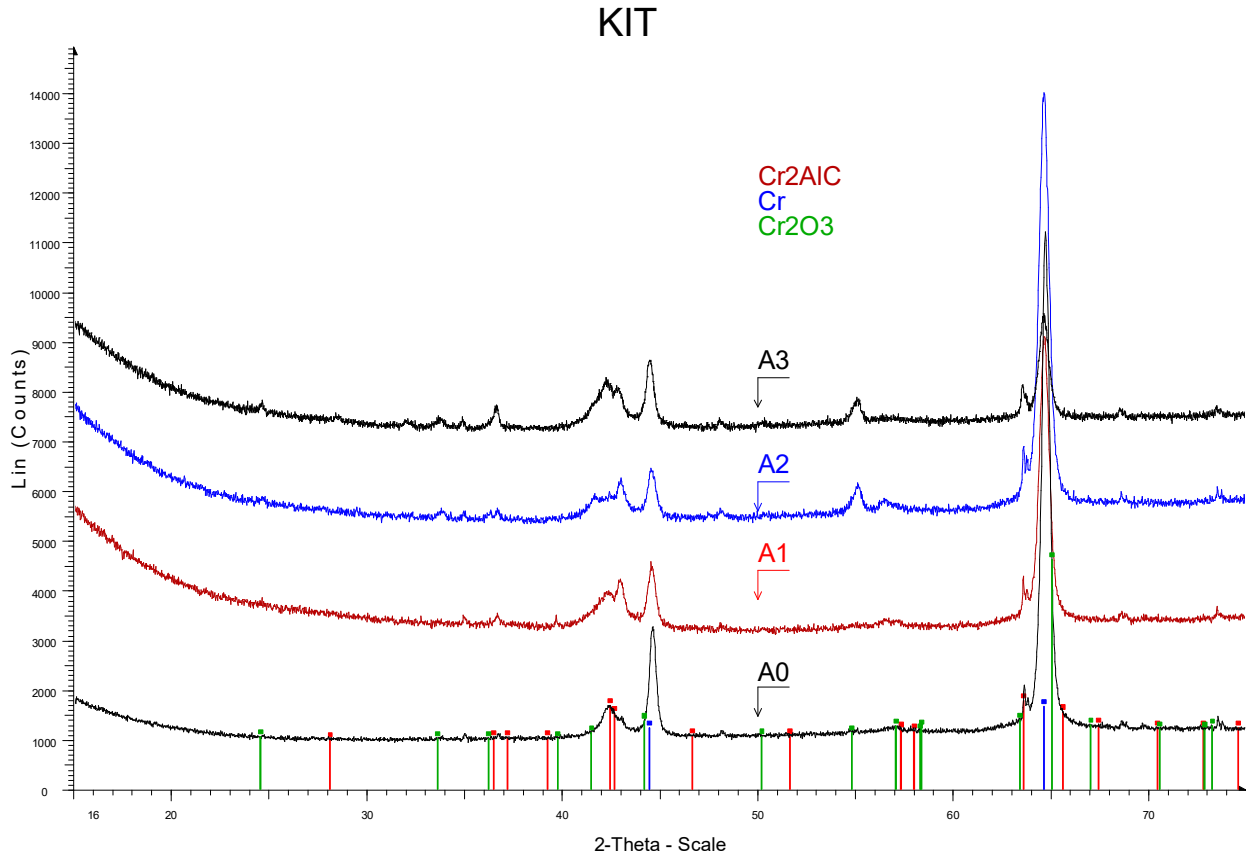
FIG. 60. MAX phase coated Zry-4 cross section after 42 and 63 days (SEM).

The mass gain data are shown in Table 21. The mass change is a result of three combined processes: oxidation of the coating and substrate, spallation of the coating and dissolution of elements in PWR environment.

TABLE 21. SURFACE MASS GAINS OF THE MAX PHASE PVD COATED ZRY-4 SAMPLE

|                 | 21 days | 42 days | 63 days |
|-----------------|---------|---------|---------|
| Mass change [%] | -3.555  | -0.783  | 1.05    |

XRD analysis confirmed the presence of Cr as well as chromium oxide  $\text{Cr}_2\text{O}_3$  – blue and green markers. Red



markers are positioned at lines place from phase  $\text{Cr}_2\text{AlC}$  (database).

FIG. 61. XRD analysis of MAX phase coated Zry-4 sample during the long term corrosion test (A0 – 0 days, A1 – 21 days, A2 – 42 days, A3 – 63 days).

### 3.7.4. ZrSi-Cr PVD coated Zry-2

The appearance of the ZrSi-Cr coated samples during the corrosion test is shown in Fig. 62.

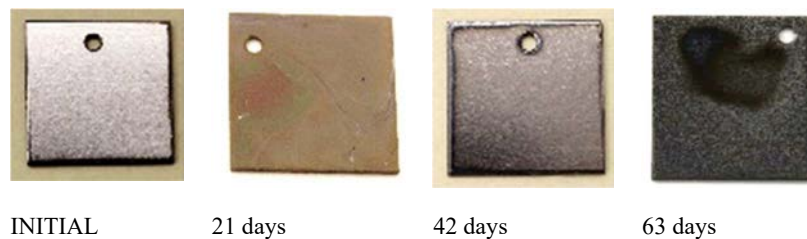


FIG. 62. Morphology of the ZrSi-Cr coated Zry-2 sample during the test.

The surface of samples became rougher with irregular structures and visible morphological objects like grains and agglomerates formed after exposure.

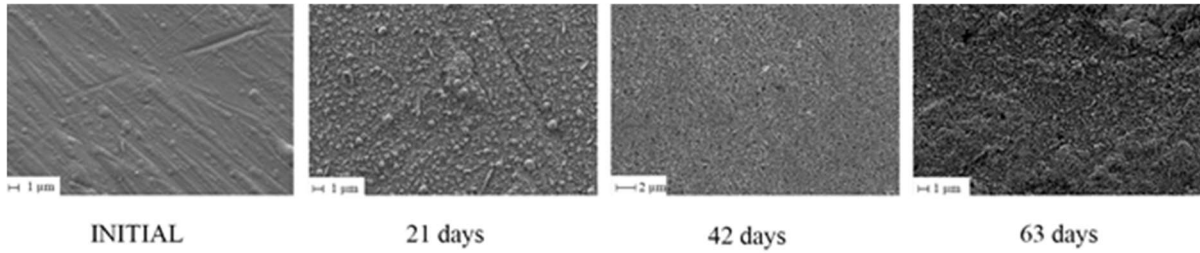


FIG. 63. SEM micrographs of the ZrSi-Cr coated Zry-2 sample during the test.

The samples were completely covered by oxidized products of various shapes such as fibers, needles, and plates after exposure.

The oxide layer is formed on top of the coating after the 21 days test. Cross section of the sample after 42 days exposure suggests the presence of oxides, including Cr oxide and oxide complex. Cross section of the sample after 63 days test shows a different profile of composition cross the oxides. The coating thickness is lower, but the concentration of elements is on the same level as previously. The Cross section of samples after 21 days and 42 days exposure shows the presence of oxide layers as well as coating layers.

It is shown that the coating was oxidized and protected the substrate from oxidation.

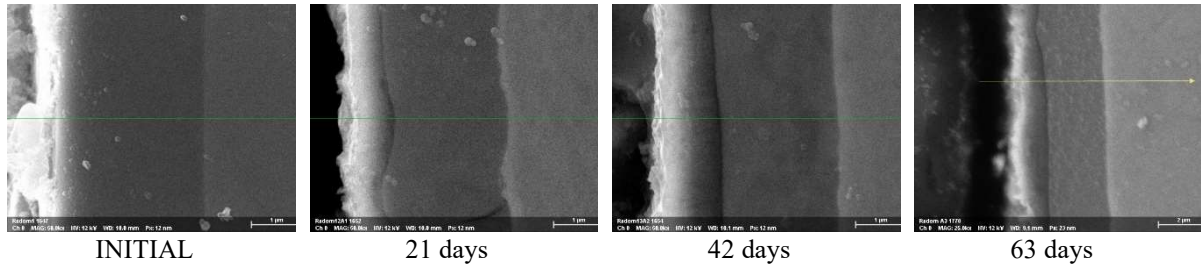


FIG. 64. As-prepared ZrSi-Cr coated Zry-2 cross section and after 21, 42 and 63 days (SEM).

The mass gains are summarized in Table 22. It was observed that there was no mass change after 21 days at all, and a small mass gain after 42 days but a large mass gain after 63 days. The results suggested that the coating may lose protection for the substrate after a short exposure.

TABLE 22. SURFACE MASS GAINS OF THE ZrSi-Cr PVD COATED ZRY-2 SAMPLE

|                         | 21 days | 42 days | 63 days |
|-------------------------|---------|---------|---------|
| Surface mass change [%] | 0.0     | 4.733   | 72.625  |

Figure 65 shows the XRD results for the as received sample and the oxidized samples. The red markers are the hexagonal zirconium crystal structure. These peaks belong to the base material (Zry-2) spectrum. The zirconium structure was detected because the coating thickness is small and only around 2.5 µm. The Monoclinic zirconium oxide ZrO<sub>2</sub> phase is also visible and shown as blue markers. No peak was identified for the coating material. The bulge at the position about 2θ = 40 deg at A0 spectrum suggests that the coating is amorphous. For the oxidized samples, the intensity for the coating decreases and the intensity of the zirconium oxide increases, suggesting the coating may be consumed during the exposure.

The set of XRD spectra of initial and after autoclave tests of Zry-2 coated with Zr<sub>40</sub>Si<sub>24</sub>Cr<sub>36</sub> confirmed that the oxidation process took place during the autoclave tests. Peaks characteristic for ZrO<sub>2</sub> monoclinic phase were observed after A1 test at the point of 2θ = 51° and after A2 test at the points, 2θ = 34, 42, 51 (stronger than after A1), 56 and 66°. The peaks widening was attributed to the dispersive oxide grains.

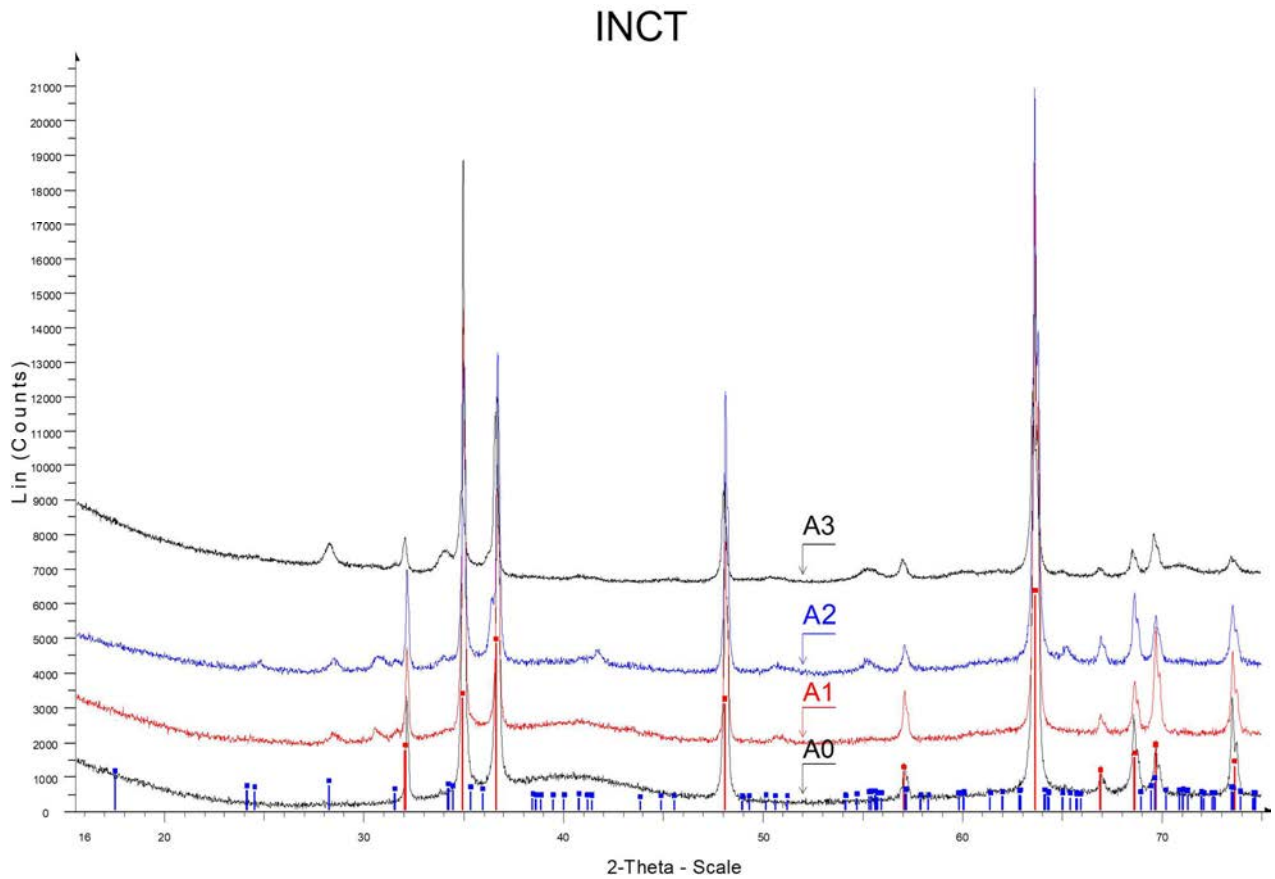


FIG. 65. XRD analysis of ZrSi-Cr coated Zry-2 sample during the long term corrosion test (A1 – 21 days in red, A2 – 42 days in blue, A3 – 63 days).

### 3.7.5. AISI 348 SS

The images of AISI 348 sample showed a surface color change from grey to gold/brown after oxidation tests. The same golden color was also observed for the oxidized Cr-coated samples.

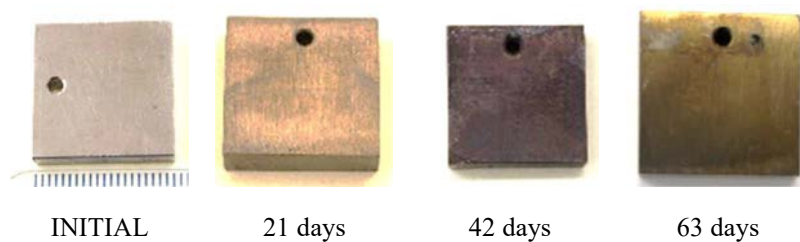


FIG. 66. Overview of the AISI 348 SS sample during the test.

The surface morphology of the samples before and after autoclave tests is shown in Fig. 67. As the figures show the surface became rougher due to oxidation. Surface cracks were also observed. Various oxide forms were observed, including needle like grains, plate like grains and sphere like grains.

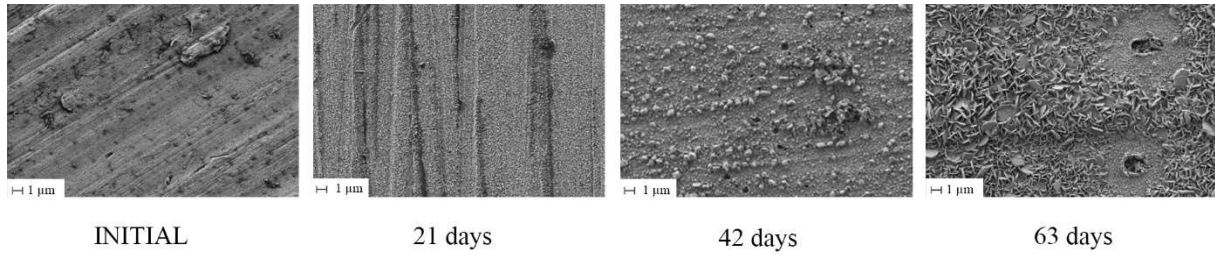


FIG. 67. SEM micrographs of the AISI 348 sample during the test X10000.

No difference was observed in the elemental composition of the samples before and after the autoclave tests. The oxide layer formed at the surfaces contains all elements present in the substrate. The thickness of the formed oxide layer was about 1.0  $\mu\text{m}$ .

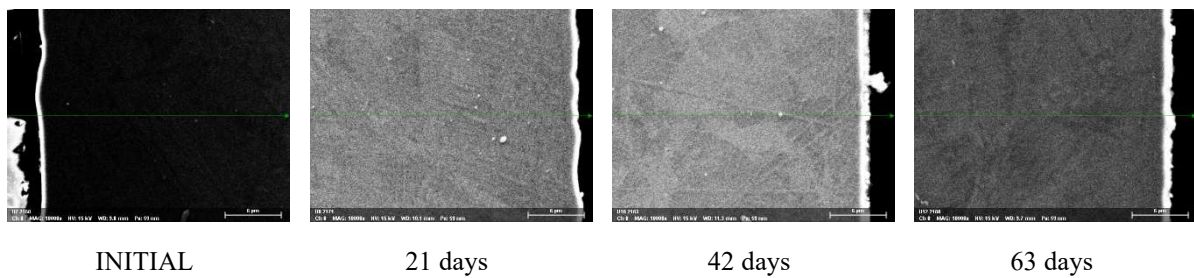


FIG. 68. AISI 348 as-received cross section and after 21, 42 and 63 days (SEM).

The mass gain data are summarized in Table 23.

TABLE 23. SURFACE MASS GAINS OF THE AISI 348 SS SAMPLE

|                       | 21 days | 42 days | 63 days |
|-----------------------|---------|---------|---------|
| Surface mass gain [%] | 0.204   | 1.127   | 0.736   |

The presence of regular phase in Fm-3M symmetry with the lattice parameter of  $a = 3.5843 \text{ \AA}$  was confirmed with the red markers. The presence of iron oxide  $\text{Fe}_2\text{O}_3$  was confirmed, starting from A2 spectrum with the blue markers. The peak at  $2\theta = 44.514^\circ$  may belong to the bcc phase (Im-3m) with the lattice parameter  $a = 2.87787 \text{ \AA}$ .

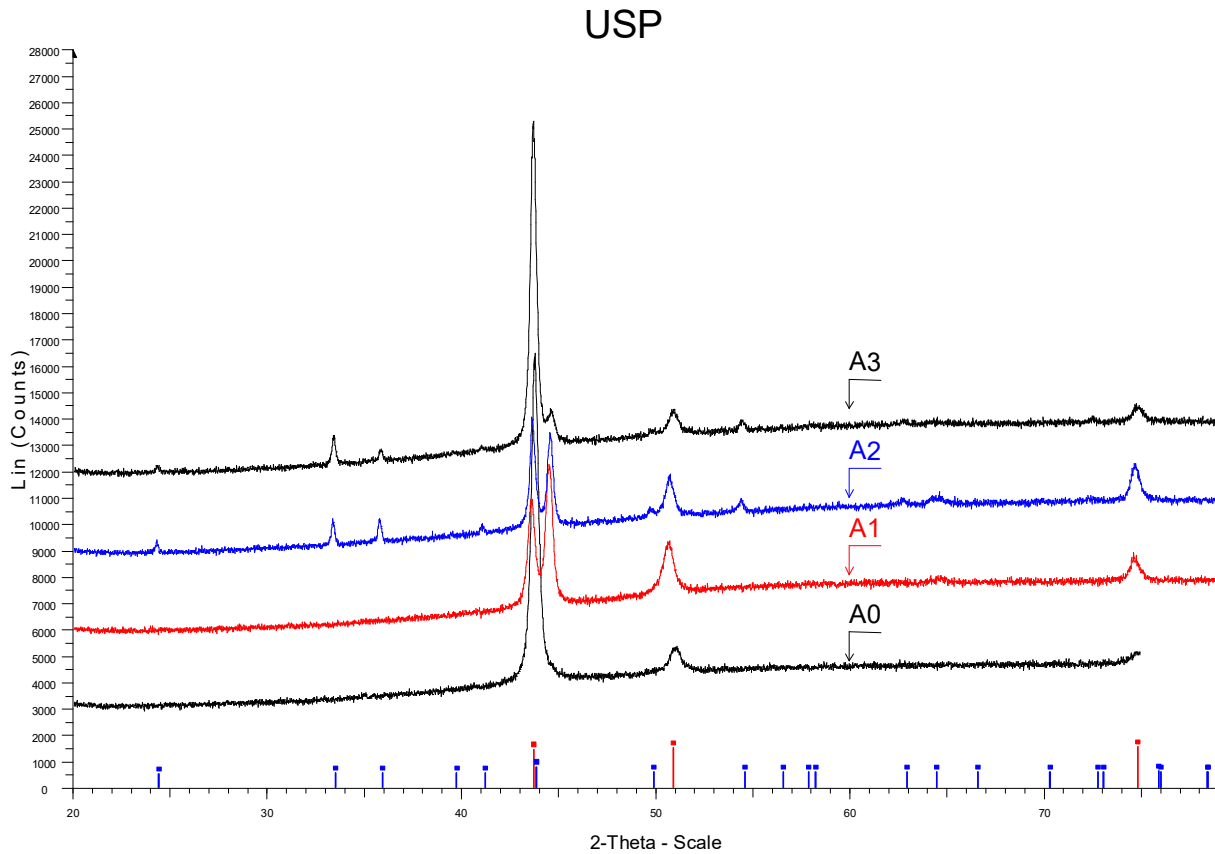


FIG. 69. XRD analysis of AISI 348 sample during the long term corrosion test (A1 – 21 days, A2 – 42 days, A3 – 63 days).

### 3.8. DISCUSSION

Even though the ATF materials are generally perceived to improve the accident tolerance, they should perform at least as good as the reference fuel system, namely the zirconium cladding and  $UO_2$  pellets. As a result, the out-of-pile long term corrosion tests were conducted to determine the oxidation behaviour of the candidate ATF cladding materials at normal operation conditions in comparison to the reference Zr-based materials.

As discussed previously six potential cladding materials were investigated:

- Two reference alloys – Zry-2 and Zry-4;
- PVD Cr coated Zry-2;
- PVD Cr/Cr<sub>2</sub>AlC/Cr coated Zry-2;
- PVD ZrSi-Cr PVD coated Zry-2;
- AISI 348 stainless steel.

The autoclave test conditions were described previously in the report. A summary of the weight changes measured by all participants is shown in Fig. 70.

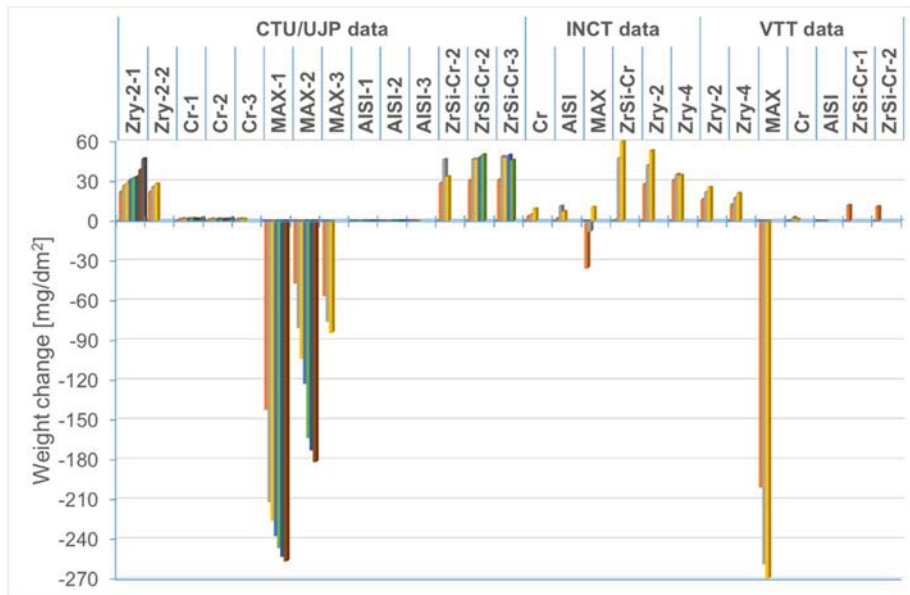


FIG. 70. Weight change data of the ATF cladding candidate materials tested at the three labs, CTU, INCT and VTT.

The characterization results for the AISI 348 samples indicate that there is a continuous oxide layer formed on the surface but its adherence is weak. The oxide thickness was about 1  $\mu\text{m}$  after 63 days. The MAX phase PVD coated Zry-4 specimens didn't show adequate protection for the substrate. Through Cracks was found at the coating layers and between the coating and substrate interface. The cracking may be due to the different thermal expansion coefficients for the oxidation products. The observed coating/oxide layer thickness was from 0.5  $\mu\text{m}$  to 5  $\mu\text{m}$  after the 21 day exposure, from 3  $\mu\text{m}$  to 10  $\mu\text{m}$  after the 42 day exposure and from 2  $\mu\text{m}$  to 40  $\mu\text{m}$  after the 63 day exposure. The original coating thickness was around 6.5  $\mu\text{m}$  thick. The observed coating/oxide layer thicknesses are rather inaccurate estimates as most of the coatings were lost most likely during the Post test sample preparation. Most significant coating loss was observed after the 63 day exposure. For the reference sample (without coating), the oxide layer thickness ranged from 1  $\mu\text{m}$  to 10  $\mu\text{m}$  after 63 days of exposure. The layer was continuous but slightly porous and several cracks through the oxide layer were observed.

The PVD Cr coated Zry-4 specimens provided by CTU had rather uniform coating layer with the coating thickness ranging from 20 to 30  $\mu\text{m}$ . The coating was uniform but some cracks through the coating and between the coating and the substrate were observed. The Cr and O contents and the integrity of the coating were not notably affected by the exposure time. The Zry-4 reference specimen exposed up to 63 days showed 1  $\mu\text{m}$  to 10  $\mu\text{m}$  thick continuous oxide layer with some porosity and several cracks through the oxide layer after the longest exposure.

The PVD ZrSiCr coated Zry-2 samples provided by INCT show a continuous but brittle oxide layer formed on the surface after autoclave exposure. Also, cracks through the oxide and cracks between the oxide layer and the substrate were observed. It was found the substrate picked up oxygen after 16.5 days of exposure, suggesting that the coating was no longer protective after short period of exposure.

In summary, the PVD Cr coating showed good corrosion resistance in both WWER and PWR chemistry with low weight gains, although the hydrogen pickup still needs to be determined. The AISI 348 SS also showed good corrosion resistance with negligible weight gains. Extremely thin Fe-rich oxide layer formed on the outer surface. The PVD Cr/Cr<sub>2</sub>AlC/Cr coating and the PVD ZrSi-Cr coating did not show adequate corrosion resistance and the coatings may need further optimization. Meanwhile, the hydrogen pickup is high for the PVD ZrSi-Cr coated samples.

The Cr coated Zr alloys show extremely low weight gain but hydrogen pickup in comparison with uncoated materials is similar or higher. The AISI 348 SS samples show both low weight gain and hydrogen pickup. The weight changes of the two promising ATF candidates in comparison with uncoated reference Zirconium samples are shown in Fig. 71.

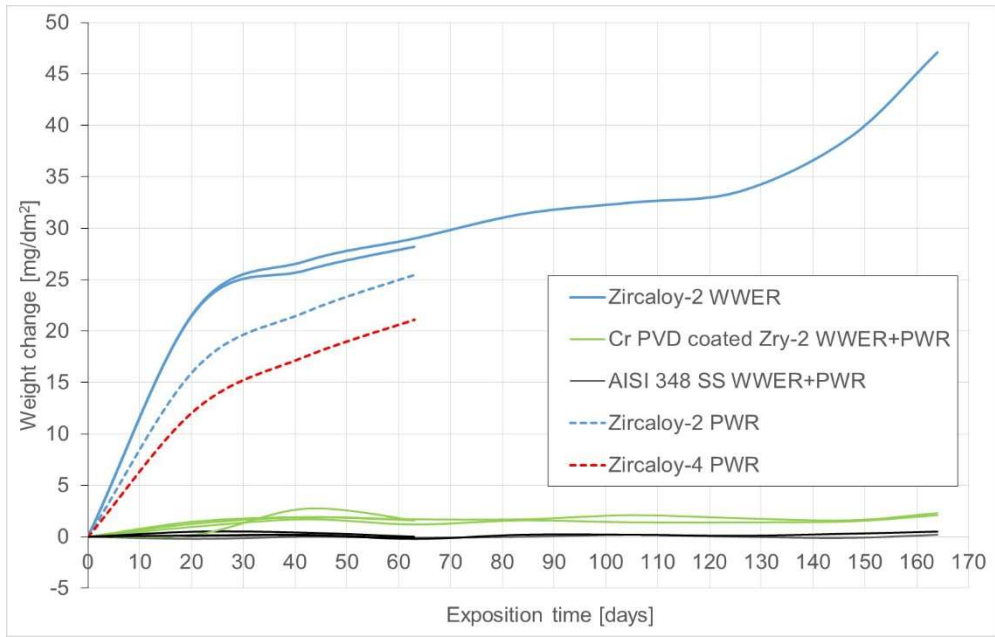


FIG. 71. Weight changes of the PVD Cr coated samples and the AISI SS cladding samples in comparison to the reference uncoated zirconium samples in PWR and WWER chemistry.

#### 4. HIGH TEMPERATURE OXIDATION

Four participants (CTU, VTT, KIT, MTA EK) performed high temperature (HT) oxidation testing. The HT test conditions were summarized below:

- Flowing steam 1100°C, 60 minutes;
- Flowing steam 1200°C, 30 minutes;
- Flowing steam 1300°C, 5 minutes.

These conditions were defined based on considerations for the standard DBA fuel safety criteria such as 17% ECR limit and cladding embrittlement calculated using the Cathcart-Pawel correlation [79]. Additionally, previous experience with testing of ATF cladding materials was used to define the test duration [80].

Some of the participants decided to perform more tests if larger quantities of samples were available. The summary of tested samples including the test matrix is shown in Table 24.

TABLE 24. STEAM OXIDATION TESTS PERFORMED BY INDIVIDUAL PARTICIPANTS

| CTU — Czech Republic   |  |
|------------------------|--|
| Cladding material      | HT steam oxidation — 1100,60'; 1200,30'; 1300°C,5'                         |
| AISI 348               | X  |
| Cr coated Zry-2        | X  |
| MAX phase coated Zry-4 | X  |
| ZrSi-Cr coated Zry-2   | —  |
| E110 ref.              | X  |
| Cr coated E110         | X  |
| VTT — Finland          |  |
| Cladding material      | HT steam oxidation — 1100,60'; 1200,30'; 1300°C,5'                         |
| AISI 348               | X  |
| Zry-4 ref.             | X  |
| Cr coated Zry-2        | X  |
| MAX phase coated Zry-4 | X  |
| ZrSi-Cr coated Zry-2   | —  |
| KIT — Germany          |  |
| Cladding material      | HT steam oxidation — 1100,60'; 1200,30'; 1300°C,5'                         |
| AISI 348               | X  |
| Zry-4 ref.             | X  |
| Cr coated Zry-2        | X  |
| MAX phase coated Zry-4 | X  |
| ZrSi-Cr coated Zry-2   | X  |
| MTA EK — Hungary       |  |
| Cladding material      | HT steam oxidation — 1100,60'; 1100,180';<br>1200,30';1200,45'; 1200°C,60' |
| Cr coated E110         | X  |
| E110 ref.              | X  |

The exact testing parameters may vary among labs, such as the heating rates, steam flow rates, quench parameters, temperature measurements, sample holders, etc. In addition, different laboratories and setups can measure different parameters such as hydrogen production or online weight changes. The samples were characterized before and after testing. The characterization techniques include visual inspections, XRD, SEM,

microhardness, metallography, ring compression tests, hydrogen production, weight changes or hydrogen absorption measurements. The testing methods and setups used are described in detail in this report or in the individual reports (see Annex).

#### 4.1. EXPERIMENTAL PROCEDURES AND SETUPS

##### 4.1.1. CTU/UJP

Resistance furnace (“CLASSIC”) that can perform tests up to 1450°C was used. One sample was inserted into a pre heated furnace at a required temperature in the argon steam atmosphere. After the exposition, the sample was quenched into ice water. Pt-thermocouple was placed near the specimen surface. The schematics of the system used is shown in Fig. 72.

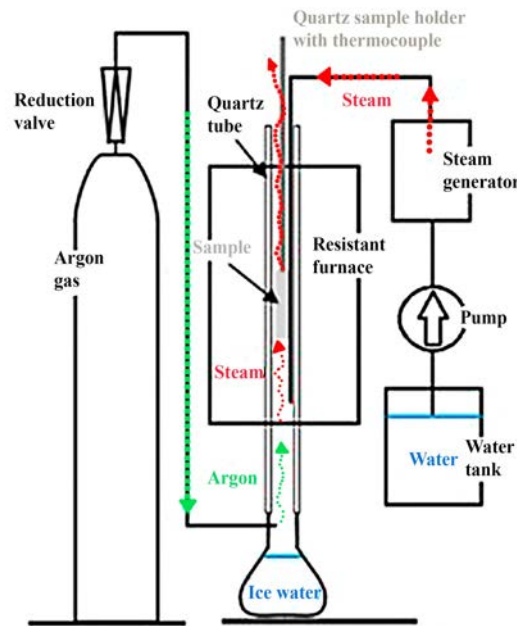


FIG. 72. Scheme of the experimental setup for high temperature oxidation at CTU/UJP (Reproduced courtesy of Elsevier [182]).

The measured temperature profiles for the tested specimens during the heating phase up to 1200°C are shown in Fig. 73(left). It can be seen that the heating rates are the highest for the reference uncoated samples and KIT specimens. This is caused by the exothermic reaction of the material with steam which suggest also higher hydrogen production of these materials at the beginning of oxidation. The AISI 348 specimens show the slowest heating rates and the target temperature was reached with a slight delay, this is due to the higher weight of the AISI samples and its higher heat capacity. The evaluated heating rates are shown in Fig. 73 (right).

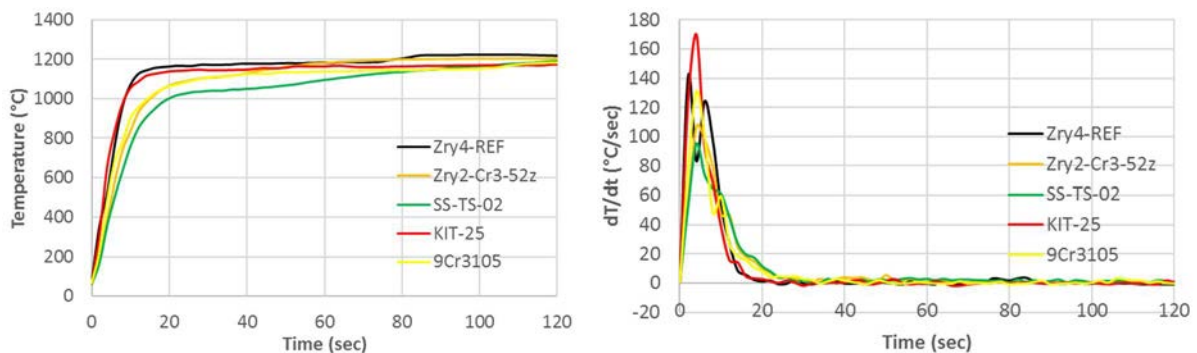


FIG. 73. Measured temperatures (left) and heating rates (right) for 1200 °C steam oxidation tests.

All the test samples were degreased in acetone, ethanol and distilled water before the test. The dimensions and the weights of each sample were measured. Specimens after exposition were measured, weighed and cut into several segments. Hydrogen analysis, metallography and microhardness analysis were performed with coupon samples. Ring compression tests, hydrogen and oxygen measurements, cross sections metallographic and microhardness analysis were performed with segments cut from tubular specimens. The metallographic cross sections were prepared using the standard polishing procedure and metallographic evaluation followed. The thickness of the oxide layer, coatings, the  $\alpha$ -Zr(O) layer was measured in several directions at both inner and outer cladding edges. The optical microscope NIKON Eclipse MA200 and LUCIA G image analyser were used for the metallographic analysis. The metallographic cross sections were used for microhardness measurements in several positions of the tube wall. Two rows with 10 measurements in the middle of the wall were performed. Two 7 mm long rings were cut from the specimens after single sided oxidation tests and the ring compression tests (RCT) at 135°C were performed using the INSTRON 1185 machine. Other parts of the samples intended for bulk hydrogen content measurements using the Analyser G8 GALILEO (Bruker), which is based on the inert gas fusion principle. Several rings without outer oxidized layers and coating were prepared on a lathe machine. Using this methodology, it was possible to analyse bulk oxygen content in the inner and outer part of the wall. Bulk oxygen content was measured using the Analyser G8 GALILEO.

The high temperature steam oxidation tests and samples can be divided into three subgroups:

- Tubular samples — one sided oxidation with uncoated end plugs (test matrix shown in Table 25);
- Coupons (test matrix is shown in Table 26);
- Tubular samples — one sided oxidation with Zr1%Nb substrate – with coated end plugs (test matrix is shown in Table 27).

Additionally, oxidation in the air was performed on one of the samples to study effect of air oxidation.

TABLE 25. TEST MATRIX FOR HIGH TEMPERATURE STEAM OXIDATION OF THE TUBE SAMPLES

| Specimen ID | Material           | Temperature [°C] | Oxidation time [min] |
|-------------|--------------------|------------------|----------------------|
| Zry2-REF-51 | Reference Zry-2    | 1200             | 30                   |
| Zry2-Cr3-51 | Zry-2 + Cr-coating | 1300             | 5                    |
| Zry2-Cr3-52 | Zry-2 + Cr-coating | 1200             | 30                   |
| Zry2-Cr3-53 | Zry-2 + Cr-coating | 1100             | 60                   |
| SS-TS-01    | AISI 348           | 1300             | 5                    |
| SS-TS-02    | AISI 348           | 1200             | 30                   |
| SS-TS-03    | AISI 348           | 1100             | 60                   |
| SS-TS-05    | AISI 348           | 1400             | 2                    |

TABLE 26. TEST MATRIX FOR HIGH TEMPERATURE STEAM OXIDATION OF THE COUPONS

| Specimen ID | Material          | Temperature [°C] | Oxidation time [min] |
|-------------|-------------------|------------------|----------------------|
| Zry2-REF    | Reference Zry-2   | 1200             | 30                   |
| KIT-24      | Zry-4 + Max phase | 1300             | 5                    |
| KIT-25      | Zry-4 + Max phase | 1200             | 30                   |
| KIT-26      | Zry-4 + Max phase | 1100             | 60                   |
| SS-PS-17    | AISI 348          | 1200             | 30                   |

TABLE 27. TEST MATRIX FOR HIGH TEMPERATURE OXIDATION OF THE Cr-COATED Zr1%Nb - TUBE SAMPLES

| Specimen ID         | Material  | Temperature [°C]    | Oxidation time [min] |      |    |
|---------------------|---|---------------------|----------------------|------|----|
| 9Cr3101             | Zr1%Nb + Cr-coating   | 1200                | 30                   |      |    |
| 9Cr3102             | Zr1%Nb + Cr-coating   | 1200                | 45                   |      |    |
| 9Cr3103             | Zr1%Nb + Cr-coating   | 1200                | 60                   |      |    |
| 9Cr3104             | Zr1%Nb + Cr-coating   | 1200                | 45                   |      |    |
| 9Cr3105             | Zr1%Nb + Cr-coating   | 1200                | 30                   |      |    |
| 9Cr3106             | Zr1%Nb + Cr-coating   | 1300                | 5                    |      |    |
| 9Cr3107             | Zr1%Nb + Cr-coating   | 1100                | 60                   |      |    |
| 9Cr3108             | Zr1%Nb + Cr-coating   | 1100                | 180                  |      |    |
| 9Cr3109             | Zr1%Nb + Cr-coating   | 1200                | 75                   |      |    |
| 9Cr3110             | Zr1%Nb + Cr-coating   | 1200                | 90                   |      |    |
| 9Cr3111             | Zr1%Nb + Cr-coating   | 1300                | 9                    |      |    |
| 9Cr3112             | Zr1%Nb + Cr-coating   | 1300                | 9                    |      |    |
| 9Cr3113             | Zr1%Nb + Cr-coating </tr <tr> <td>9Cr3V01 air-exposed</td> <td>Zr1%Nb + Cr-coating</td> <td>1200</td> <td>60</td> </tr> | 9Cr3V01 air-exposed | Zr1%Nb + Cr-coating  | 1200 | 60 |
| 9Cr3V01 air-exposed | Zr1%Nb + Cr-coating   | 1200                | 60                   |      |    |

#### 4.1.2. VTT

Steam tests were performed using a steam furnace in flowing steam at 1100–1300°C described Fig. 74. The furnace consists of an alumina tube (working tube), a specimen tube and a sample holder, all manufactured from recrystallized alumina (RCA). The furnace has one zone, i.e. uniform heat is produced in the middle of the test section. The desired temperature can be maintained in a 100 mm long zone with silicon carbide heating elements. The maximum temperature of the steam furnace is 1600°C. More details about the results of the high temperature tests performed at VTT in the framework of the CRP ACTOF is given in the individual VTT TECDOC report “Performance of candidate ATF cladding materials in simulated high temperature steam and normal LWR conditions” (see Annex).

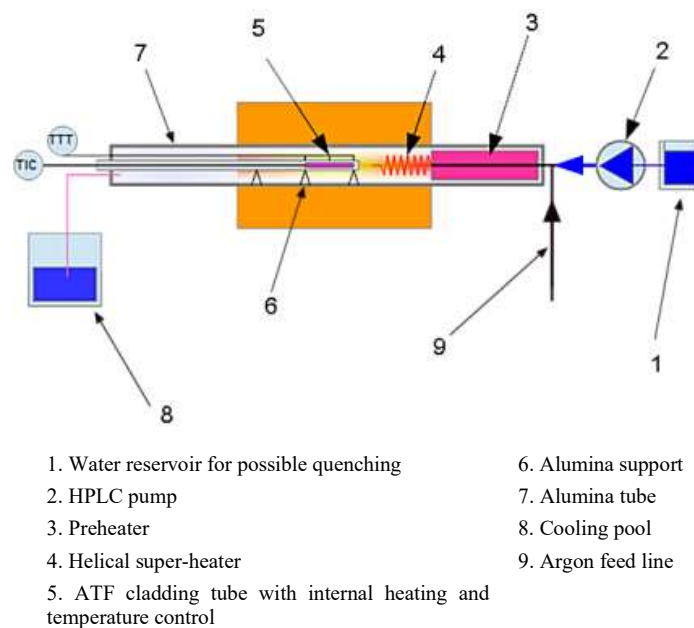


FIG. 74. Schematic arrangement of the VTT's steam-oxidation test furnace for ATF cladding samples.

### 4.1.3. KIT

The high temperature steam oxidation experiments were performed using the horizontal Box tube furnace. Figure 75 gives a scheme of the furnace. The tests were done at three temperatures and times: 60 min at 1100°C, 30 min at 1200°C, and 5 min 1300°C. The specimens were placed on a corundum crucible sample holder located in the center of the furnace, not at a sample holder rod as shown in Fig. 75. Heat-up and cool-down were in high purity Ar atmosphere with a flow rate of 20 l/h from and to ambient temperature to designated value with 10 K/min heating rate. Steam was injected into the furnace by changing the gas flow to 20 l/h Ar and 20 g/h H<sub>2</sub>O. The concentration of the steam during the oxidation phase was about 55 vol.%. The specimens were oxidized in steam for the predefined time. Fig. 76. shows a scheme of the temperature profile during the oxidation test.

The gas compositions and flow rates during the test were defined by flow controllers and a Controlled Evaporation and Mixing (CEM) system. The composition of the off-gas was in-situ analysed by a quadrupole mass spectrometer (Balzers GAM300). The analysis of the gas composition was focused on the evolution of the hydrogen release rate in the off-gas during the tests, which was used as a measurement for the oxidation rate. The pure steam atmosphere cannot be achieved due to argon is needed as the carrier gas and reference gas for mass spectrometer analysis.

The mass of the specimens before and after the HT tests was measured using an analytical balance. The specimens were also characterized using XRD (Seifert PAD II) and SEM (Philips XL30S).

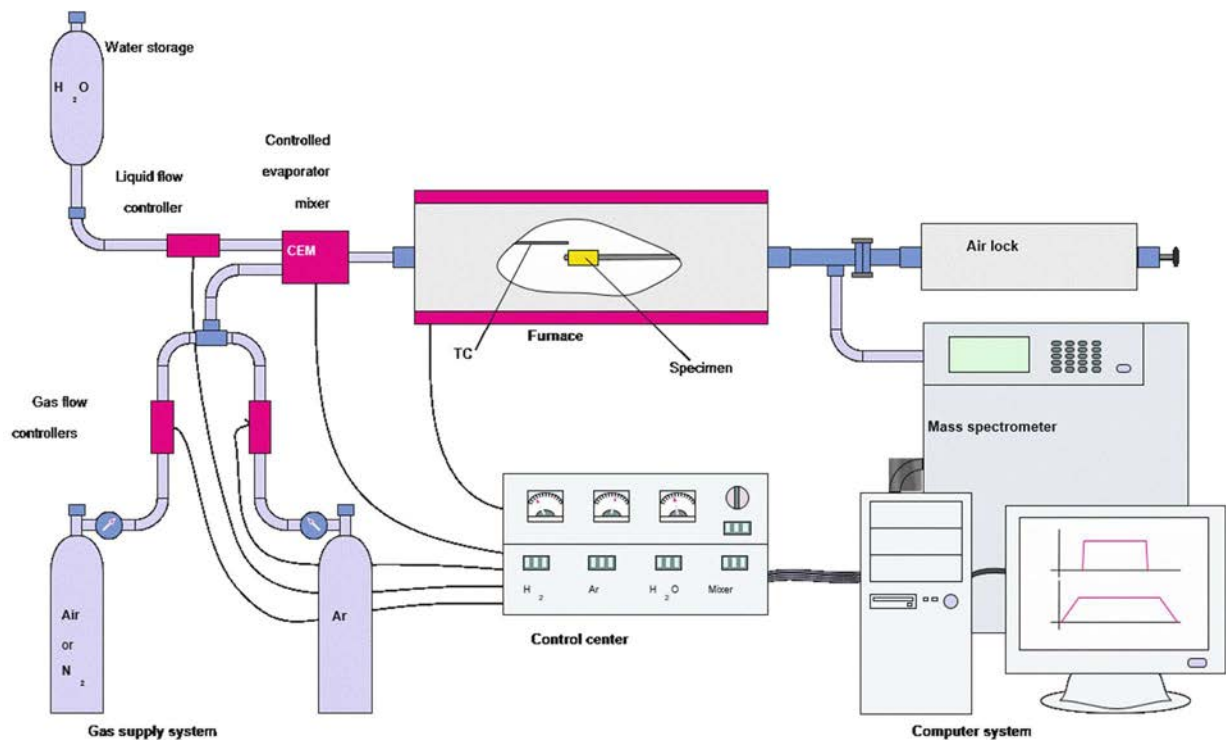


FIG. 75. Schematics of the Box furnace system.

More details about the results of the high temperature tests performed at KIT in the framework of the CRP ACTOF is given in the individual KIT TECDOC report “Round Robin High temperature Oxidation Tests at KIT” (see Annex).

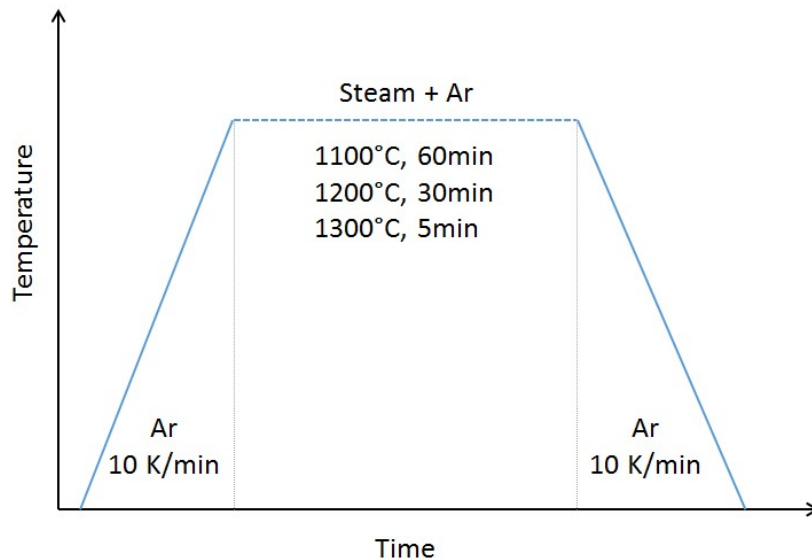


FIG. 76. Schematic illustration of the temperature during the oxidation test at three different temperatures.

#### 4.1.4. MTA EK

MTA EK carried out the HT tests for 8 pieces of 60 mm long sponge based Zr1%Nb cladding tube samples summarized in Table 24 within the RRT activity. Two types of specimens were tested – PVD Cr coated Zr1Nb samples and the reference uncoated Zr1Nb samples. All of the tubular specimens were enclosed by two end plugs, so that only one-side oxidation took place.

In the presented test series 8 samples were tested – 5 Cr coated in steam, 2 reference samples (uncoated) in steam and 1 Cr coated in air. The test matrix is shown in Table 28.

TABLE 28. TEST MATRIX FOR OXIDATION OF THE SAMPLES

| Sample  | Sample              | Atmosphere | Temperature [°C] | Oxidation time [s] |
|---------|---------------------|------------|------------------|--------------------|
| IAEA-01 | Cr PVD coated Zr1Nb | air        | 1200             | 3600               |
| IAEA-02 | Reference Zr1Nb     | steam      | 1100             | 3600               |
| IAEA-03 | Cr PVD coated Zr1Nb | steam      | 1100             | 3600               |
| IAEA-04 | Cr PVD coated Zr1Nb | steam      | 1100             | 10800              |
| IAEA-05 | Reference Zr1Nb     | steam      | 1200             | 1800               |
| IAEA-06 | Cr PVD coated Zr1Nb | steam      | 1200             | 1800               |
| IAEA-07 | Cr PVD coated Zr1Nb | steam      | 1200             | 2700               |
| IAEA-08 | Cr PVD coated Zr1Nb | steam      | 1200             | 3600               |

The samples were degreased in acetone before testing. The dimensions and weights of each sample were measured.

The Zirconium specimens were oxidized in steam mixed with 12 vol.% argon or in a pure air atmosphere under isothermal conditions, at 1200°C and 1100°C. A high temperature tube furnace with a quartz tube was used for the oxidation of the samples. The experimental setup (Fig. 77) consisted of a steam generator, a three-zone horizontal furnace with a temperature control system and a condensing system. A large vessel (approx. 6 dm<sup>3</sup>) filled with cold water was placed under the outlet part of the furnace to quench the oxidized samples. The steam flow rate was about 2 mg/cm<sup>2</sup>/s. The air flow rate was about 8 mg/cm<sup>2</sup>/s. After stabilization of the temperature and the steam flow, the quartz boat with the sample was pushed into the heated zone of the furnace. At the end of oxidation, the sample was quenched. In case of air oxidation, the steam generator was not used, but air from the balloon was supplied to the furnace.

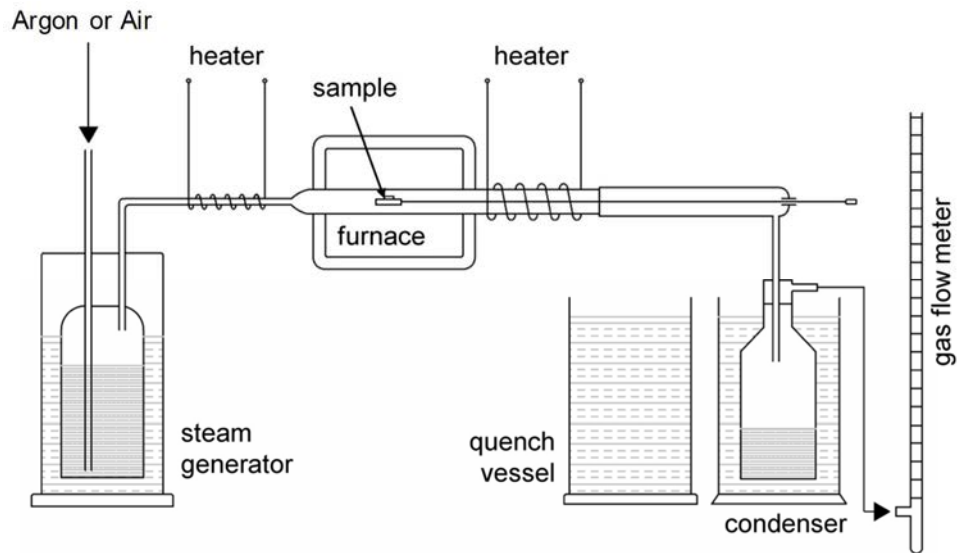


FIG. 77. Schematics of the experimental setup for oxidation of zirconium samples.

Radial ring compression tests were carried out with a standard INSTRON 1195 type tensile test machine at 135°C (Fig. 78). The tensile test machine was equipped with a special furnace in order to keep the high temperature during the test. Each measurement started with a heat-up period (10 min) to establish uniform temperature distribution in the test section. The applied crosshead velocity was 2 mm/min. During the tests, the load-displacement curves were recorded.

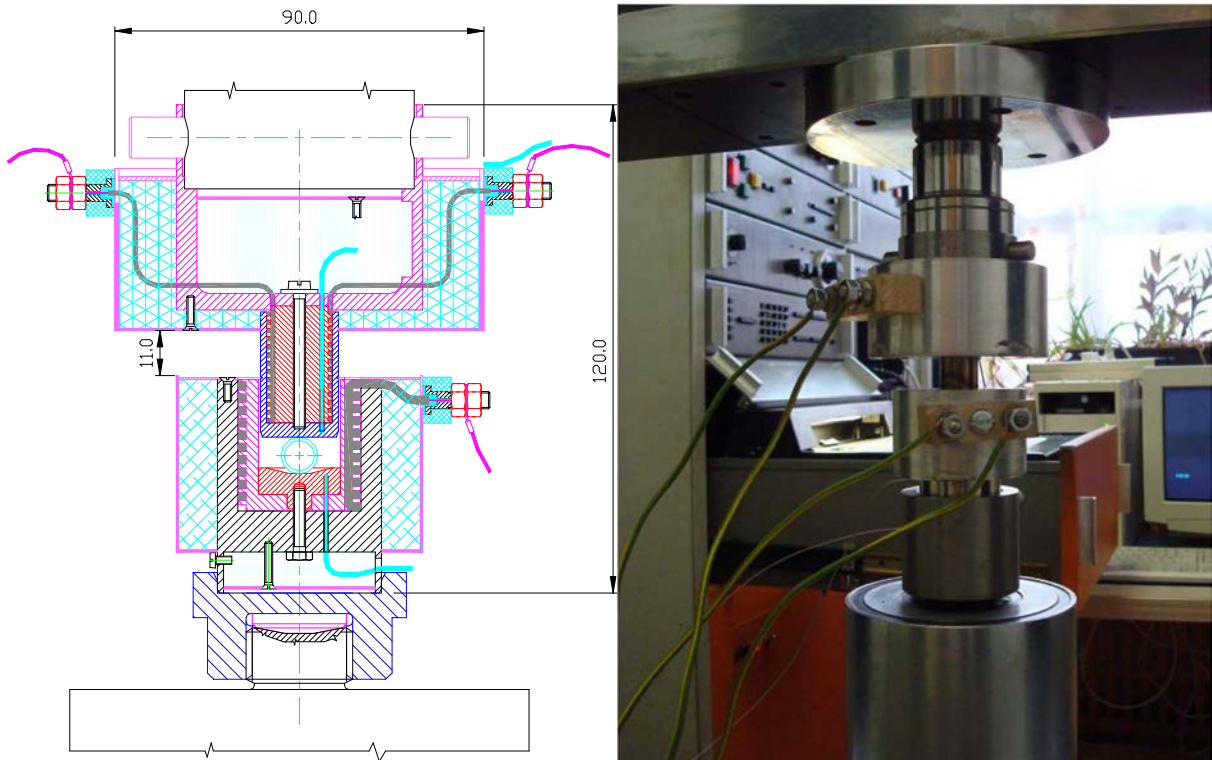


FIG. 78. Schematics and image of the tensile/compression test machine with a furnace.

## 4.2. RESULTS: CTU/UJP

As described in previous section, the samples were divided into three groups according to the geometry and materials used. The pictures of the samples after exposure and the microstructures are shown in Table 29 for the coupons, in Table 30 for tubular samples, and in Table 31 for Cr coated Zr1%Nb tubular samples.

The visual evaluation of the reference uncoated specimens showed dark grey oxide layer which spall off for tubular Zry-2 samples during quenching. The microstructure analysis showed a uniform oxide layer and  $\alpha$ -Zr(O) layer underneath. For the double sided oxidized plate specimen, the sample was fully oxidized: 113  $\mu\text{m}$  thick  $\text{ZrO}_2$  layer was followed by  $\alpha$ -Zr(O) layer. No remaining prior  $\beta$ -Zr phase was found. For the single-sided oxidized tubular specimen with the endplugs, 150  $\mu\text{m}$  thick uniform  $\text{ZrO}_2$  layer and 162  $\mu\text{m}$  thick  $\alpha$ -Zr(O) layer with some additional incursions towards prior  $\beta$ -Zr phase were found.

The visual evaluation showed local spallation of the MAX phase coating for temperatures 1100 and 1200°C. From the microstructure evaluation, the coating remains protective if it survived after the test. For the HT test done at 1300°C, the coating was oxidized and lost its protective behavior. Both the  $\text{ZrO}_2$  and  $\alpha$ -Zr(O) layers were formed under the coating.

The Zry-2 Cr-coated specimens showed a dark-green coloured oxide layer on the surface in comparison with a black oxide formed on the uncoated Zr1%Nb end plugs. The specimen Zry-2-Cr3-51 exposed at 1300°C had a wavy surface, which indicated Cr-Zr eutectic formation, which was confirmed in the cross section analysis. This is likely due to temperature overshoot and may be above 1330°C due to over heating from exothermal reaction during oxidation of uncoated end plugs. The Zr1%Nb Cr coated specimens (including end plugs) had a dark green colored oxide layer on the surface. The analysis of Cr coated specimens showed a compact Cr layer without any cracks with a waved layer of  $\text{Cr}_2\text{O}_3$  on the surface. For the specimen 9Cr3V01 exposed in air, more detailed investigation of the surface was done. It showed waved formation on the surface. It can be attributed to the volume expansion when Cr oxidized into  $\text{Cr}_2\text{O}_3$ . This growing and bending of the  $\text{Cr}_2\text{O}_3$  oxide layer is observed. The coating substrate interaction was also observed. For specimens exposed in a steam environment, it was found that the Cr coating was diffusing into the substrate and absorbed oxygen was dissolved in  $\beta$ -Zr, no typical  $\alpha$ -Zr(O) was found. For the air exposed specimen, the 2  $\mu\text{m}$  thin ZrN layer under the Cr coating was found followed by  $\alpha$ -Zr(N, O) layer.

All of the AISI 348 SS specimens showed substantial oxide spallation. Different colors and structures of oxidized end plugs were observed in the visual inspection. The end plugs were made in-house of AISI 304L alloy. The cross section analysis showed that the wall thickness of specimens decreased. It is clear especially for the SS-TS-05 specimen exposed at 1400°C. While the outer oxide layer ( $\text{Fe}_3\text{O}_4$ ) was not adherent and delaminated, the inner oxide layer (denoted as  $\text{FeCr}_2\text{O}_4$  by KIT) stayed dense and uniform and partially protected the underlying steel.

TABLE 29. VISUAL EVALUATION AND METALLOGRAPHY OF COUPONS AFTER HIGH TEMPERATURE STEAM OXIDATION

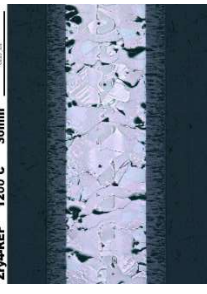
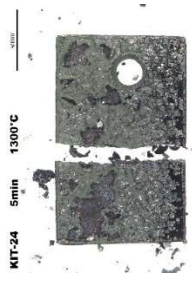
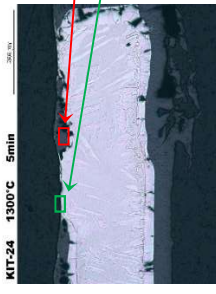
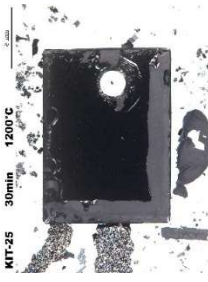
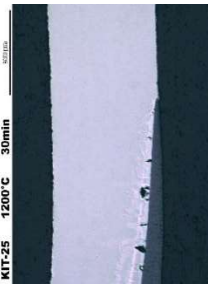
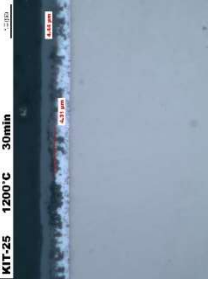
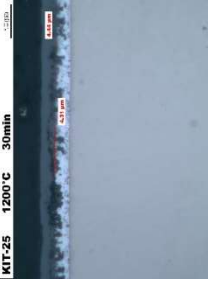
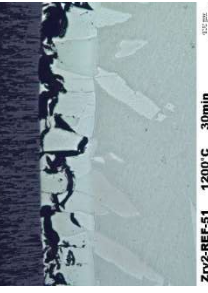
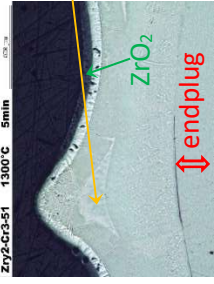
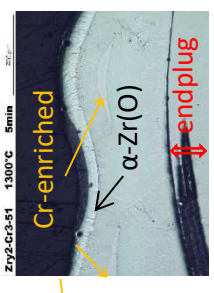
| ID                            | Temp. [°C] | Time [min] | Photography   | Cross section microstructure   |   | Cross section microstructure - details  |   |
|-------------------------------|------------|------------|---|--|---|---|---|
|                               |            |            |   |  |   |   |   |
| Uncoated Zry4-REF             | 1200       | 30         |    |    |    |    |   |
|                               |            |            |   |  |   |   |   |
| MAX phase coated Zry-4 KIT-24 | 1300       | 5          |    |    |    |    |  |
|                               |            |            |   |  |   |   |   |
| MAX phase coated Zry-4 KIT-25 | 1200       | 30         |   |   |   |   |   |
|                               |            |            |   |  |   |   |   |
| MAX phase coated Zry-4 KIT-26 | 1100       | 60         |  |  |  |  |   |
|                               |            |            |   |  |   |   |   |



TABLE 29. VISUAL EVALUATION AND METALLOGRAPHY OF COUPONS AFTER HIGH TEMPERATURE STEAM OXIDATION (cont.)

| ID   | Temp. [°C] | Time [min] | Photography   | Cross section microstructure  | Cross section microstructure - details  | ID |
|--|------------|------------|---|---|---|----|
| AISI 348 SS-PS-17z (not quenched into ice-water) | 1200       | 30         |  |  |  | —  |

TABLE 30. TUBULAR SAMPLES (UNCOATED, CR-COATED, AISI 348) AFTER HIGH TEMPERATURE STEAM OXIDATION

| ID                       | Temp. [°C] | Time [min] | Photography   | Cross section microstructure   | Cross section microstructure – details  |
|--------------------------|------------|------------|---|--|---|
| Uncoated Zr2-REF-51      | 1200       | 30         |    |    |    |
| Cr PVD coated Zr2-Cr3-51 | 1300*      | 5          |  |  |  |

\* T-higher (overshoot from oxidation of uncoated endplugs)

TABLE 30. TUBULAR SAMPLES (UNCOATED, Cr-COATED, AISI 348) AFTER HIGH TEMPERATURE STEAM OXIDATION (cont.)

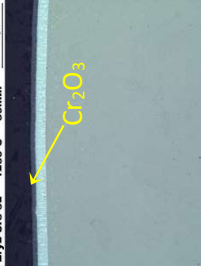
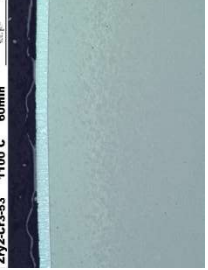
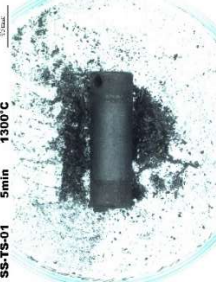
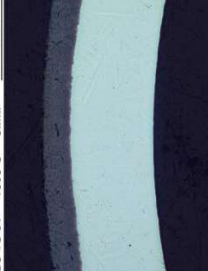
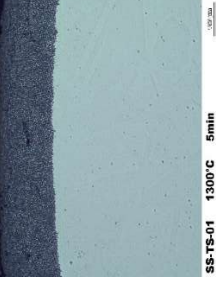
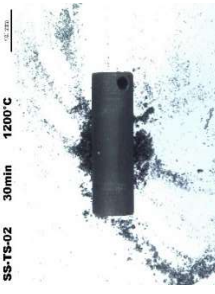
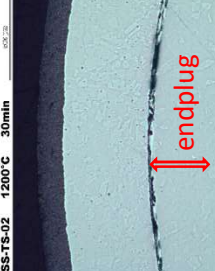
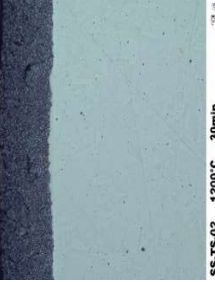
| ID  | Temp. [°C] | Time [min] | Photography   | Cross section microstructure   | Cross section microstructure – details  |
|---|------------|------------|---|--|---|
| Cr PVD coated<br>Zry2-Cr3-52z (not quenched into ice-water) | 1200       | 30         |    |    |    |
|   |            | 60         |    |    |    |
| AISI 348 SS-TS-01   | 1300       | 5          |   |   |   |
|   |            | 30         |  |  |  |

TABLE 30. TUBULAR SAMPLES (UNCOATED, Cr-COATED, AISI 348) AFTER HIGH TEMPERATURE STEAM OXIDATION (cont.)

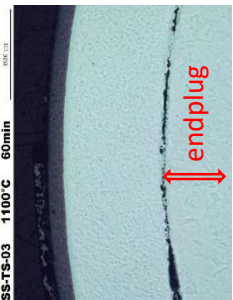
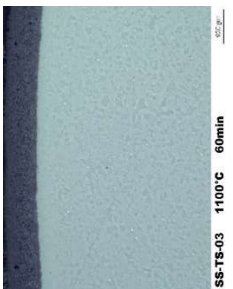
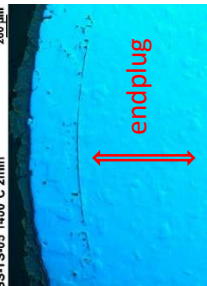
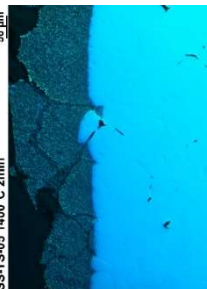
| ID                | Temp. [°C] | Time [min] | Photography   | Cross section microstructure   | Cross section microstructure – details  | ID |
|-------------------|------------|------------|---|--|---|----|
| AISI 348 SS-TS-03 | 1100       | 60         |  |  |  | —  |
| AISI 348 SS-TS-05 | 1400       | 2          |  |  |  | —  |

TABLE 31. Zr1%Nb TUBULAR CR PVD COATED SAMPLES AFTER STEAM AND AIR OXIDATION

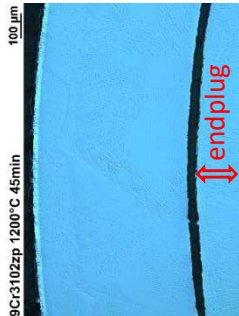
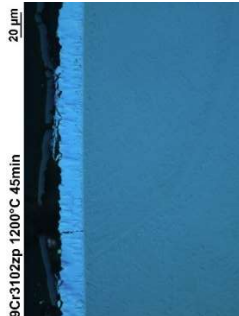
| ID                                     | Temp. [°C] | Time [min] | 10x   | 20x  | 50x   |
|--|------------|------------|---|--|---|
| 9Cr3101                                | 1200       | 30         | —   | —  | —   |
| 9Cr3102z (not quenched into ice-water) | 1200       | 45         |  |  |  |

TABLE 31. Zr1%Nb TUBULAR CR PVD COATED SAMPLES AFTER STEAM AND AIR OXIDATION (cont.)

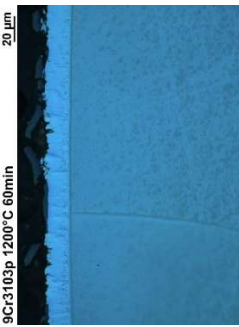
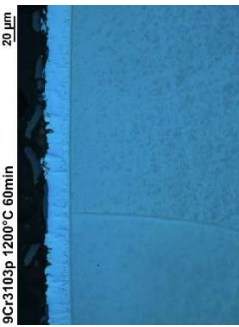
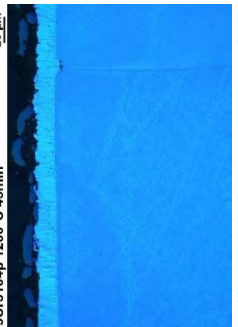
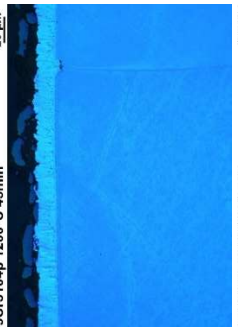
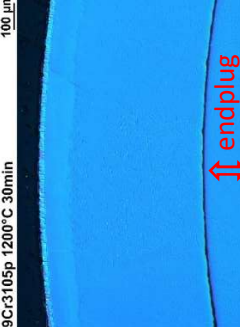
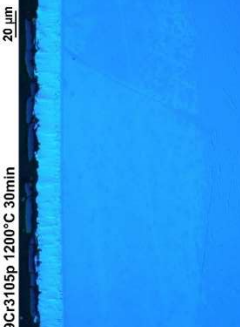
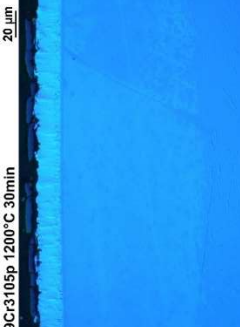
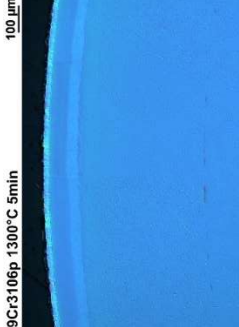
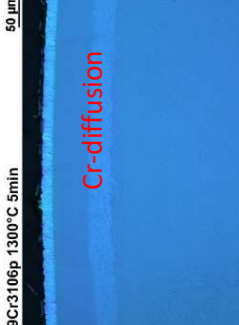
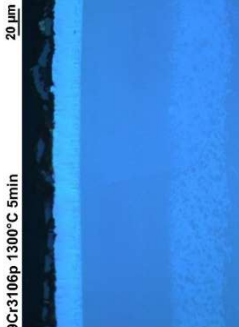
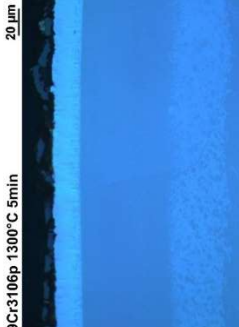
| ID      | Temp.<br>[°C] | Time<br>[min] | Magnification   |  |   |   |
|---------|---------------|---------------|---|--|---|---|
|         |               |               | 10x   | 20x  | 50x   | 50x   |
| 9Cr3103 | 1200          | 60            |    |    |    |    |
|         |               |               |    |    |    |    |
| 9Cr3105 | 1200          | 30            |   |   |   |   |
|         |               |               |  |  |  |  |

TABLE 31. Zr1%Nb TUBULAR Cr PVD COATED SAMPLES AFTER STEAM AND AIR OXIDATION (cont.)

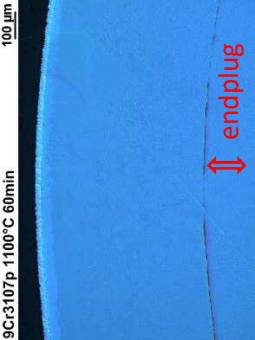
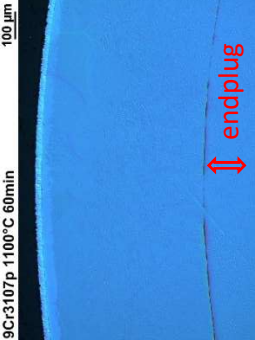
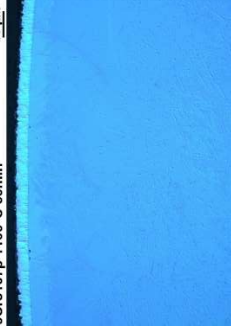
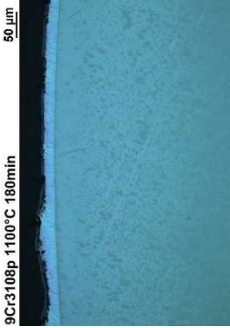
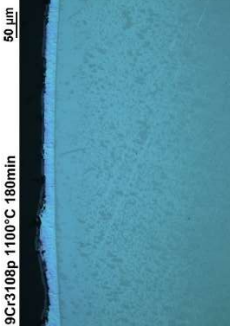
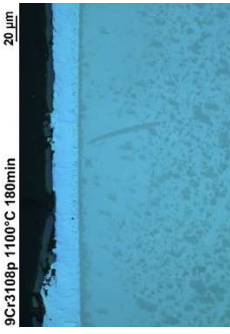
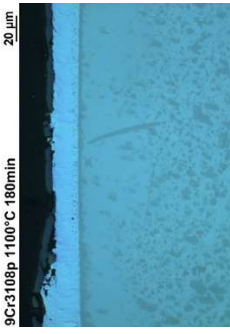
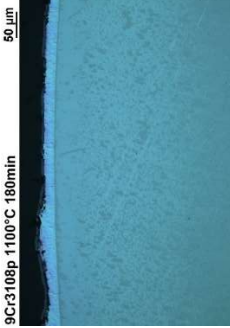
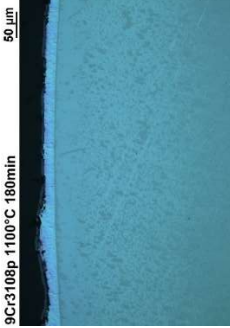
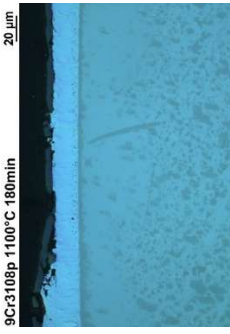
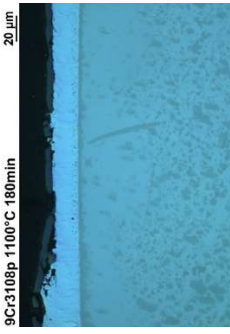
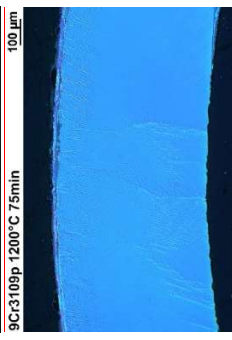
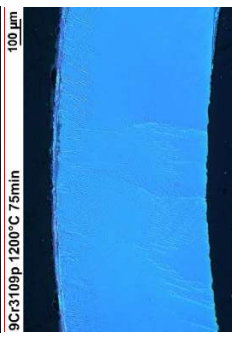
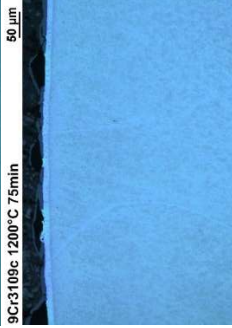
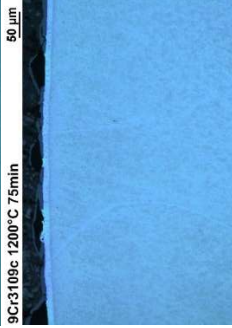
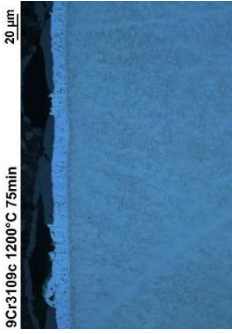
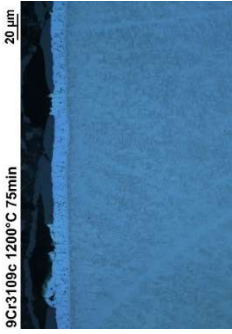
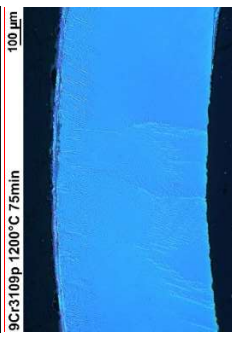
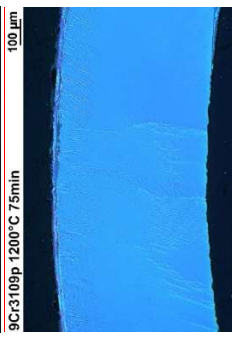
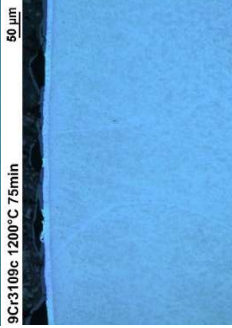
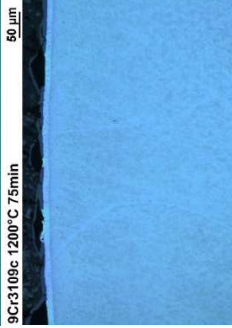
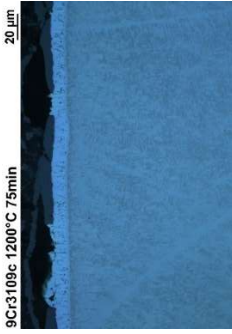
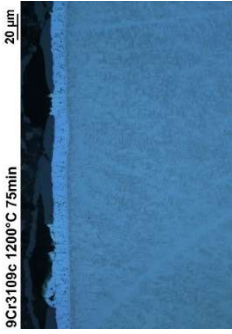
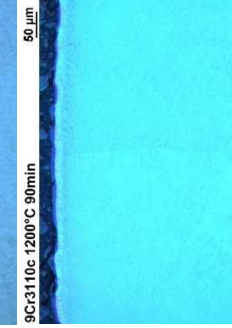
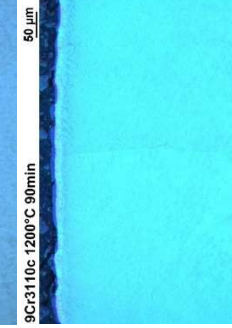
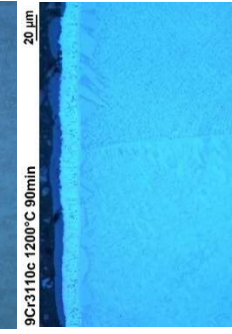
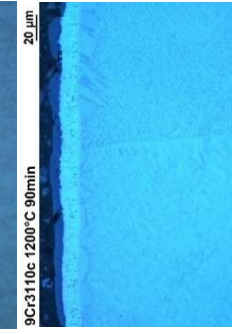
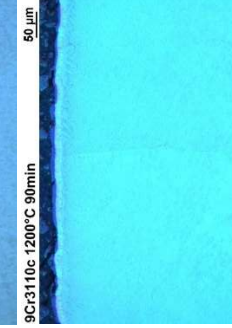
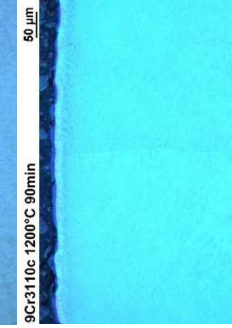
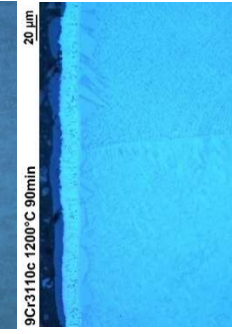
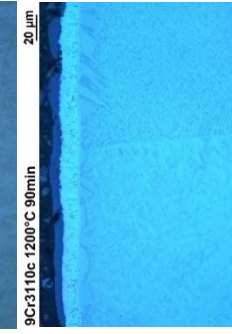
| ID      | Temp.<br>[°C] | Time<br>[min] | 10x   |   | 20x  |  | 50x   |   |
|---------|---------------|---------------|---|---|--|--|---|---|
|         |               |               | Image   | Image   | Image  | Image  | Image   | Image   |
| 9Cr3107 | 1100          | 60            |    |    |    |    |    |    |
|         |               |               |    |    |    |    |    |    |
| 9Cr3108 | 1100          | 180           |    |    |    |    |    |    |
|         |               |               |   |   |   |   |   |   |
| 9Cr3109 | 1200          | 75            |   |   |   |   |   |   |
|         |               |               |  |  |  |  |  |  |
| 9Cr3110 | 1200          | 90            |  |  |  |  |  |  |

TABLE 31. Zr1%Nb TUBULAR Cr PVD COATED SAMPLES AFTER STEAM AND AIR OXIDATION (cont.)

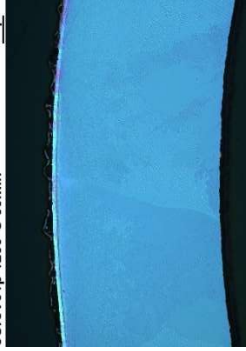
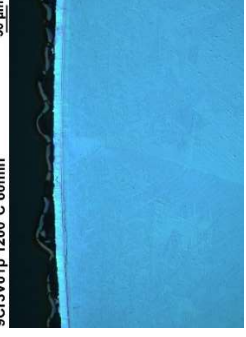
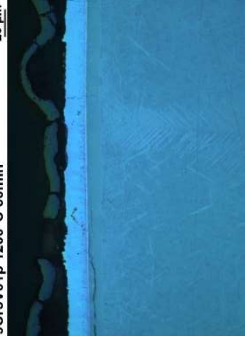
| ID  | Temp.<br>[°C] | Time<br>[min] | Time   |   |  |
|---|---------------|---------------|--|---|--|
|   |               |               | 10x  | 20x   | 50x  |
| AIR – 9Cr3V01 (not quenched into ice-water) | 1200          | 60            | <br>9Cr3V01 60min 1200°C  | <br>9Cr3V01 d1 60min 1200°C | <br>9Cr3V01 d3 60min 1200°C |
|   |               |               | <br>9Cr3V01p 1200°C 60min | <br>9Cr3V01p 1200°C 60min   | <br>9Cr3V01p 1200°C 60min   |
|   |               |               |  |   |  |

TABLE 32. SUMMARY OF THE RESULTS FROM THE HT TESTS OF PLATE SAMPLES

| ID                            | T<br>[°C] | Time<br>[min] | ECR-CP<br>[%] | WG-CP<br>[mg/dm <sup>2</sup> ] | WG-exp<br>[mg/dm <sup>2</sup> ] | dL<br>[%] | Ox<br>[mic] | α-Zr(O)<br>[mic] | HVM<br>0.1 | H<br>[ppm] |
|-------------------------------|-----------|---------------|---------------|--------------------------------|---------------------------------|-----------|-------------|------------------|------------|------------|
| Uncoated Zry2-REF             | 1200      | 30            | 43.4          | 2820                           | 2281                            | 2.33      | 113.6       | balance          | 545        | 29         |
| AISI 348 SS-PS-17z            | 1200      | 30            | 43.0          | 2791                           | 214                             | -0.50     | —           | —                | 153        | —          |
| MAX phase coated Zry-4 KIT-24 | 1300      | 5             | 30.6          | 1984                           | 2041                            | Q-fail    | 3.9         | 4.8              | 583        | 685        |
| MAX phase coated Zry-4 KIT-25 | 1200      | 30            | 44.3          | 2874                           | 2509                            | 2.36      | 4.4         | 4.3              | 281        | 120        |
| MAX phase coated Zry-4 KIT-26 | 1100      | 60            | 37.1          | 2411                           | 464                             | -0.34     | 3.4         | 5.8              | 265        | 52         |

**Note:** z – not quenched into ice-water

TABLE 33. SUMMARY OF THE RESULTS FROM THE HT TESTS OF TUBULAR SAMPLES

| ID                         | T<br>[°C] | Time<br>[min] | ECR-CP<br>[%] | WG-CP<br>[mg/dm <sup>2</sup> ] | WG-exp<br>[mg/dm <sup>2</sup> ] | dL<br>[%] | Ox<br>[mic] | Cr-coat<br>[mic] | HVM<br>0.1 | H<br>[ppm] | O<br>[%] | RCT1<br>[%] | RCT2<br>[%] | Load 1<br>[N] | Load 2<br>[N] |
|----------------------------|-----------|---------------|---------------|--------------------------------|---------------------------------|-----------|-------------|------------------|------------|------------|----------|-------------|-------------|---------------|---------------|
| Uncoated Zry2-REF-51       | 1200      | 30            | 21.7          | 2805                           | 2491                            | 1.10      | —           | —                | 500        | —          | —        | 0.05        | 0.1         | 125           | 132           |
| PVD Cr coated Zry2-Cr3-51  | 1300      | 5             | 16.2          | 2088                           | 1260                            | 0.69      | 46.1        | 59.4             | 340        | 87         | —        | 0.44        | 5.95        | 196           | 336           |
| PVD Cr coated Zry2-Cr3-52z | 1200      | 30            | 21.7          | 2801                           | 1336                            | 0.60      | 8.4         | 17.5             | 197        | 38         | 0.1273   | 16.68       | 16.19       | 312           | 307           |
| PVD Cr coated Zry2-Cr3-53  | 1100      | 60            | 18.6          | 2394                           | 1056                            | 0.46      | 4.1         | 18.3             | 256        | 356        | 0.1113   | 7.16        | 7.96        | 452           | 411           |
| AISI 348 SS-TS-01          | 1300      | 5             | 15.7          | 2026                           | 1687                            | 0.71      | 168         | 485*             | 150        | 5.9        | —        | 17.04       | 18.12       | 183           | 174           |
| AISI 348 SS-TS-02          | 1200      | 30            | 21.9          | 2823                           | 938                             | 0.47      | 133         | 516*             | 145        | 8.3        | —        | 17.06       | 18.24       | 166           | 190           |
| AISI 348 SS-TS-03          | 1100      | 60            | 18.7          | 2419                           | 1114                            | 0.42      | 96          | 538*             | 162        | 9.2        | —        | 11.49       | 10.6        | 213           | 183           |
| AISI 348 SS-TS-05          | 1400      | 2             | 12.7          | 1644                           | 3278                            | 0.46      | —           | —                | 160        | 12.1       | —        | 18.55       | 19.59       | 112           | 134           |

**Note:** \* – remaining wall thickness;  
z – not quenched into ice-water.

TABLE 34. MEASURED PARAMETERS OF Zr1%Nb Cr-COATED TUBULAR SAMPLES AFTER THE HT TESTS

| ID       | T<br>[°C] | Time<br>[min] | ECR-CP<br>[%] | WG-CP<br>[mg/dm <sup>2</sup> ] | WG-exp<br>[mg/dm <sup>2</sup> ] | dL<br>[%] | Ox<br>[mic] | Cr-coat<br>[mic] | HVM<br>0.1 | H<br>[ppm] | O<br>[%] | RCT1<br>[%] | RCT2<br>[%] | Load 1<br>[N] | Load 2<br>[N] |
|----------|-----------|---------------|---------------|--------------------------------|---------------------------------|-----------|-------------|------------------|------------|------------|----------|-------------|-------------|---------------|---------------|
| 9Cr3101  | 1200      | 30            | 21.9          | 2831                           | 183                             | 0.02      | —           | —                | —          | —          | 0.12     | —           | —           | —             | —             |
| 9Cr3102z | 1200      | 45            | 26.7          | 3451                           | 160                             | 0.28      | 5.4         | 19.2             | —          | 29         | 0.10     | 18.45       | 18.28       | 328           | 308           |
| 9Cr3103  | 1200      | 60            | 30.8          | 3974                           | 231                             | 0.32      | 8.4         | 14.1             | 203        | 40         | 0.15     | 8.91        | 10.58       | 414           | 406           |
| 9Cr3104  | 1200      | 45            | 27.0          | 3486                           | 220                             | 0.27      | 7.0         | 14.3             | 205        | 32         | 0.15     | 8.20        | 7.17        | 364           | 372           |
| 9Cr3105  | 1200      | 30            | 22.1          | 2857                           | 125                             | 0.12      | 5.4         | 20.0             | 196        | 18         | 0.095    | 15.40       | 12.70       | 373           | 377           |
| 9Cr3106  | 1300      | 5             | 15.0          | 1934                           | 115                             | 0.11      | 5.6         | 20.9             | 184        | 12         | 0.096    | 4.92        | 4.53        | 348           | 350           |
| 9Cr3107  | 1100      | 60            | 18.7          | 2407                           | 70                              | 0.07      | 4.3         | 22.2             | 191        | 19         | 0.085    | 17.08       | 16.65       | 428           | 426           |
| 9Cr3108  | 1100      | 180           | 32.2          | 4157                           | 144                             | 0.18      | 5.3         | 20.4             | 208        | 25         | 0.095    | 16.86       | 17.08       | 461           | 466           |
| 9Cr3109  | 1200      | 75            | 34.2          | 4417                           | 419                             | 0.70      | —           | —                | 395        | 66         | 0.49     | 7.21        | 1.41        | 584           | 466           |
| 9Cr3110  | 1200      | 90            | 37.2          | 4804                           | 434                             | 0.82      | —           | —                | 478        | 55         | 0.86     | 0.20        | 0.17        | 373           | 380           |
| 9Cr3111  | 1300      | 9             | 19.2          | 2478                           | 412                             | 0.46      | —           | —                | —          | 47         | 0.097    | 7.48        | 5.28        | 371           | 369           |
| 9Cr3112  | 1300      | 9             | 18.6          | 2396                           | 155                             | 0.30      | —           | —                | 204        | 12         | 0.10     | 7.66        | 7.77        | 378           | 373           |
| 9Cr3113  | 1100      | 480           | 52.0          | 6710                           | 375                             | 1.00      | —           | —                | 391        | 57         | 0.54     | 0.58        | 1.07        | 478           | 461           |
| 9Cr3V01  | 1200      | 60            | air           | air                            | 330                             | 0.40      | —           | —                | —          | 6.4        | —        | 16.87       | 18.1        | 355           | 311           |

After the HT test, the specimen was dried at 90°C, and then weighed. From the temperature measurement, the WG-CP (Weigh gain - Cathcart-Pawel) and ECR-CP (Equivalent cladding reacted – Cathcart-Pawel) were calculated. The destructive analysis then followed. The cross section analysis was performed and the oxide layer,  $\alpha$ -Zr(O) layer, coating, and the remaining wall thickness were measured. The Vickers microhardness was measured twenty times in the middle of the wall (2×10 points). One or two 0.5 mm long rings were analysed for H-content. For the oxygen content in prior  $\beta$ -Zr measurement, a ring without oxide or coating (upper layer of the specimen was removed using machining) were prepared. Two 7 mm rings were used for the ring compression test at 135°C. All of the results are shown in Table 29 (plate samples), Table 30 (tubular samples), and Table 31 (Zr1%Nb - tubular samples).

The following figures summarize the results presented in the tables. Experimental weight gain, hydrogen content, microhardness, and oxygen content are plotted as a function of temperature or ECR. To evaluate the results, the calculated weight gain values according to measured temperatures and the Cathcart-Pawel correlation (originally developed for Zry-4 alloy) were also used.

For the uncoated reference tubular specimen, the experimental weight gain was about 12 % lower than the predicted one. It is considered as an acceptable deviation. For the plate specimen, the difference was higher due to oxidation through the whole wall thickness (19%). The hydrogen absorption was very low up to 30 ppm. Results of microhardness (HV0.1 = 500–550) confirmed that in the middle of the wall, where the analysis very done,  $\alpha$ -Zr(O) phase was present.

The MAX phase coating proved protective behaviour only for temperature 1100°C, for higher temperatures 1200 and 1300°C the results were very similar to the uncoated reference specimens. Hydrogen absorption into the substrate was a result of coating failures, and thus the measured values are high: 120 ppm (for 1200°C) and 685 ppm (for 1300°C). Microhardness results for temperatures 1100 and 1200°C showed values HV0.1 from 260 to 280, which are typical values confirming presence of ductile  $\beta$ -Zr. On the other hand, for test at temperature 1300°C the HV0.1 value was 583. This very high microhardness value together with high hydrogen content indicate precipitation of hydrides and extreme brittleness of the sample.

The Cr coated Zr1%Nb specimens showed the lowest weight gain and very low hydrogen content (up to 60 ppm) in all tests. The microhardness was very low - about HV0.1 = 200. For special cases that were significantly beyond planned durations: 1100°C/480min, 1200°C/75min, 1200°C/90min the microhardness is higher. The value of weight gain is not a fully representative parameter for the Cr coated Zry-2 specimens, because the uncoated end plugs were used. There is an increase in hydrogen content of the Cr coated Zry-2 specimens with uncoated end plugs measured. The uncoated end plugs produce more free hydrogen during the transient compared to coated areas of the sample. The results suggest that these free hydrogen atoms are preferentially absorbed by a coated cladding which suggests potential issues related to increased hydrogen pickup with the Cr-coated sample in steam or hydrogen atmosphere in regions with a higher concentration of free hydrogen (e.g. upper part of the core or close to the space grids). This phenomenon needs to be further investigated and mechanisms of hydrogen pickup with coated cladding materials explained.

The AISI 348 alloy showed lower weight gains than the reference specimens, which is partially due to the spallation of the oxides. The hydrogen content inside the sample and microhardness were the lowest.

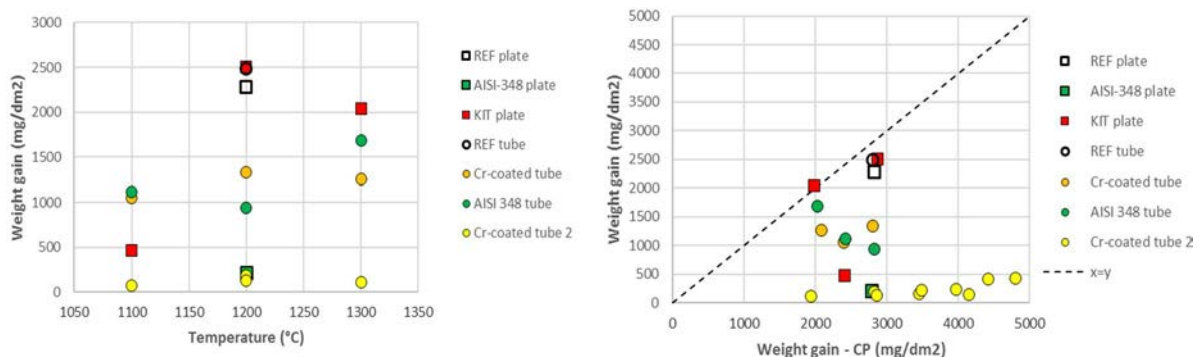


FIG. 79. Experimentally measured weight gains in relation with temperature (left) and calculated weight gain using Cathcart-Pawel correlation (right).

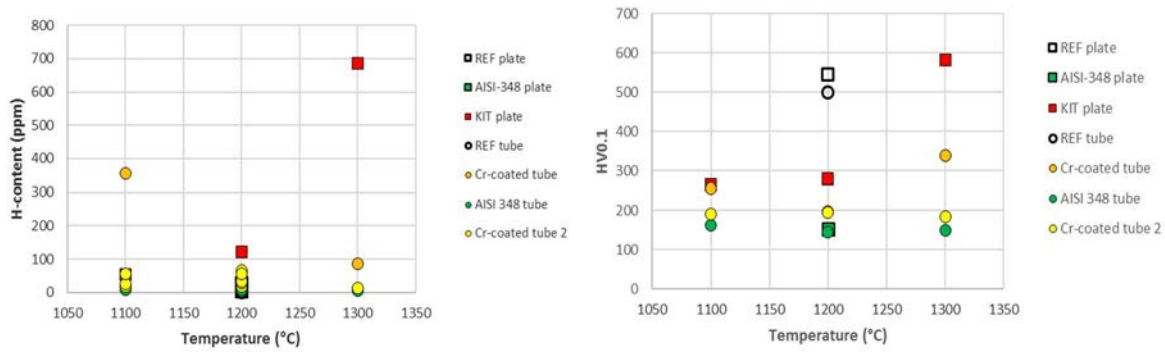


FIG. 80. Hydrogen content (left) and microhardness in the middle of the wall (right) of specimens in relation with temperature for different exposure times.

Two 7 mm-long segments were cut from the tubular specimens (uncoated, Cr coated and AISI 348) and ring compression test at temperature 135°C was performed.

The Cr coated Zr1%Nb specimens were ductile with the lowest residual ductility of about 4% for the specimen exposed at 1300°C/5min. When comparing Cr coated Zry-2 and Cr coated Zr1Nb sample, there is a higher hydrogen content (356 ppm) for 1100°C/60 min and the temperature above Cr-Zr melting point for the case 1300°C/5min when using Zry-2 as a substrate. This causes also reduction of the ductility. The specimen exposed at 1300°C was brittle. All AISI 348 specimens showed very high residual ductility corresponding to the low weight gain (remaining wall thickness respectively). On the other hand, the maximal load for all specimens was similar and very low: 150–200 N.

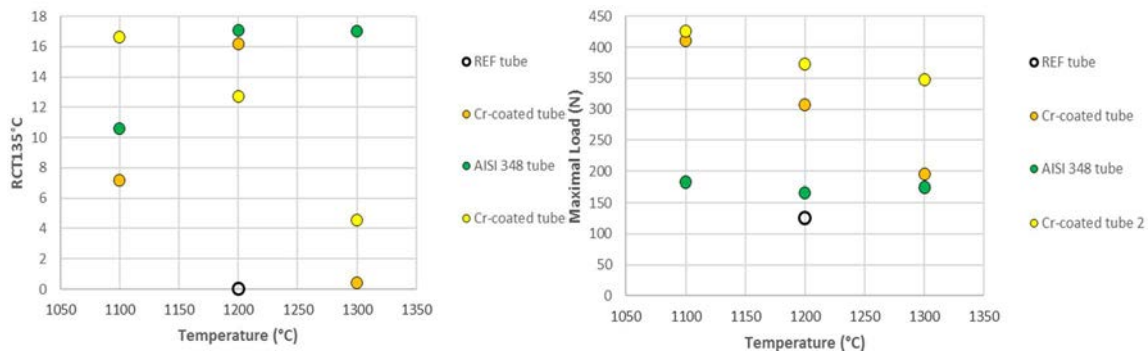


FIG. 81. Results of the ring compression tests at 135°C after quenching of the tubular samples: residual ductility (left) and maximal load (right).

The more detailed investigation was done for Cr coated Zr1%Nb specimens, and the residual ductility in relation with exposure time was determined. Additionally, experimental equivalent cladding reacted (theoretical value for Zr-alloys) and calculated (using Cathcart-Pawel correlation), microhardness, and oxygen content were measured. The results are summarized in the following figures.

Figure 82 shows the results of residual ductility in relation with exposition time. For temperature 1100°C the “ductile-brittle-transition” (DBT) was in between 180 and 480 minutes of exposure (ECR-CP 17% for uncoated is about 50 min). For temperature 1200°C the brittle sample was in between 60 and 75 min of exposure (ECR-CP 17 % for uncoated is about 18 min). From Fig. 82(right), it can be seen that the standard methodology used for Zr-based alloys cannot be used for coated materials. It shows that measured weight gains cannot be directly compared with weight gains of uncoated specimens. The DBT for coated specimens is present for lower ECR values than ECR 17%, which is considered to be limiting value for uncoated specimens without any absorbed hydrogen. On the other hand, from Fig. 83, a very good agreement of DBT with limiting values microhardness (left) and oxygen content (right) for uncoated Zr1%Nb alloy can be seen. Fig. 84(left) shows the direct connection of weight gain and oxygen content (except the point with Cr-Zr eutectic formation). Therefore, it can be concluded, that there is

a limiting value of weight gain that will correspond to the limiting oxygen concentration reached in prior  $\beta$ -Zr. Reaching this value will cause a DBT transition to occur.

The weight gain of the coated samples can be predicted if there will be a good understanding of the oxidation kinetics, shown in Fig. 84 (right). Due to limited experiments conducted in this RRT, it is not possible to develop any reliable model describing the oxidation kinetics in the relevant temperature range from 1000 to 1300°C, and future work is needed.

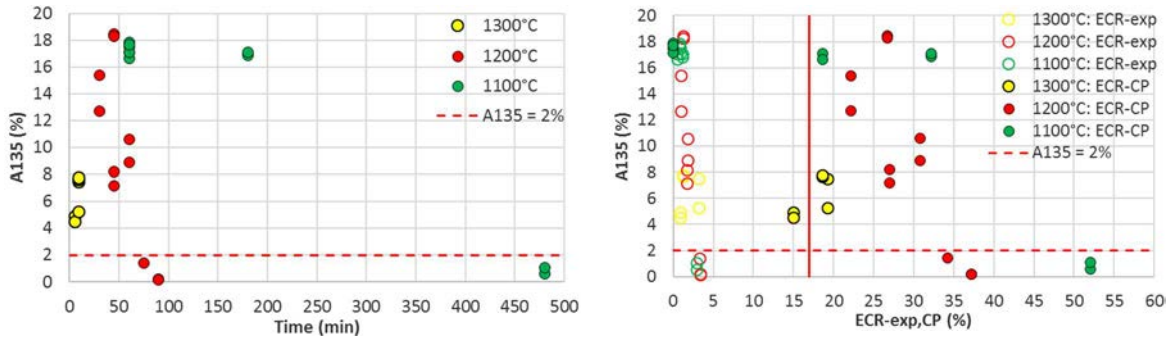


FIG. 82. Residual ductility of the Cr-coated Zr1%Nb samples in relation with time (left) and ECR (right).

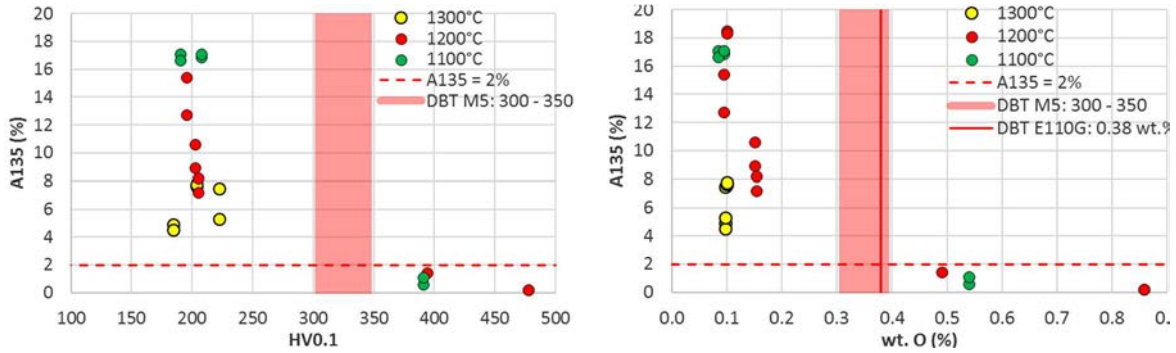


FIG. 83. Residual ductility of the Cr-coated Zr1%Nb samples in relation with microhardness (left) and oxygen content in prior  $\beta$ -Zr (right).

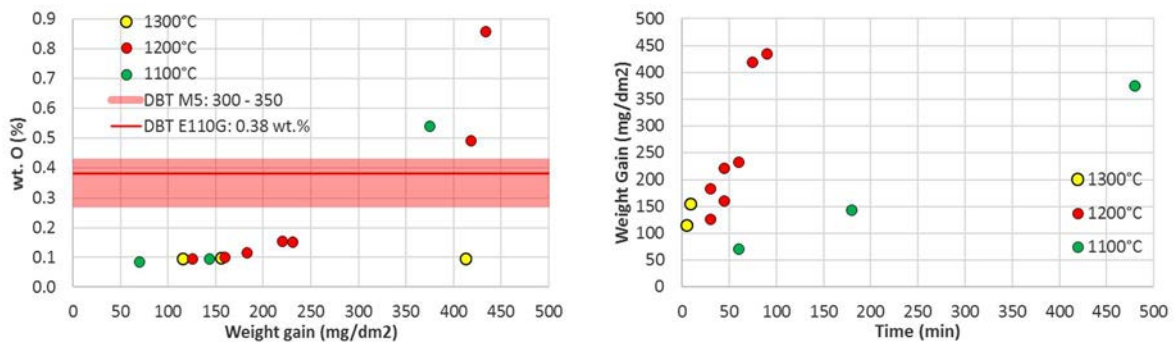


FIG. 84. Oxygen content of the Cr-coated Zr1%Nb specimens in relation to weight gain (left) and weight gain in relation with time (right).

The above results suggest that the standard methodology used for Zr cladding materials based on the experimental ECR evaluation is not applicable for coated specimens. On the other hand, it was shown that DBT occurs for the same limiting values of microhardness and oxygen content as for uncoated alloys. New safety criteria may be established for coated cladding materials.

### 4.3. RESULTS: VTT

#### 4.3.1. Cr coated Zry-2

Three Cr coated Zry-4 samples provided by CTU were exposed to the flowing steam: sample 1 at 1100°C for 60 minutes, sample 2 at 1200°C for 30 minutes and sample 3 at 1300°C for 5 minutes. The weigh changes are shown in Table 35. A moderate increase in weight was observed from 1100 to 1200°C although the exposure time decreased down to 30 min. The observed weight gain after exposure at 1300°C was about 6-20 times higher compared to lower temperatures.

TABLE 35. CALCULATED WEIGHT CHANGES ( $\Delta W$ ) ON Cr COATED Zry-2 CTU SPECIMEN AFTER STEAM EXPOSURES

| Spec. 1 Zry-2 1100°C / 60 min | Spec. 2 Zry-2 1200°C / 30 min | Spec. 3 Zry-2 1300°C / 5 min |
|-------------------------------|-------------------------------|------------------------------|
| $\Delta w = 0.46 \%$          | $\Delta w = 1.37 \%$          | $\Delta w = 8.59 \%$         |

The morphology of the Cr coated Zry-4 specimen exposed to 1100°C steam for 60 minutes, is shown in Fig. 85. The thickness of the coating and the oxide layers together was about 10  $\mu\text{m}$ . The observed coating was otherwise continuous but cracks between the coating and the oxide layer were found.

The SEM-EDS maps of O, Zr, Sn, Cr and Fe are shown in Fig. 86 The SEM-EDS Selected Area analyses are shown in Fig. 87. A thin layer of Cr and Zr between the coating and the substrate in SEM-EDS maps in Fig. 86 and in SA2 in Fig. 87 shows that Cr is diffusing towards the Zr substrate.

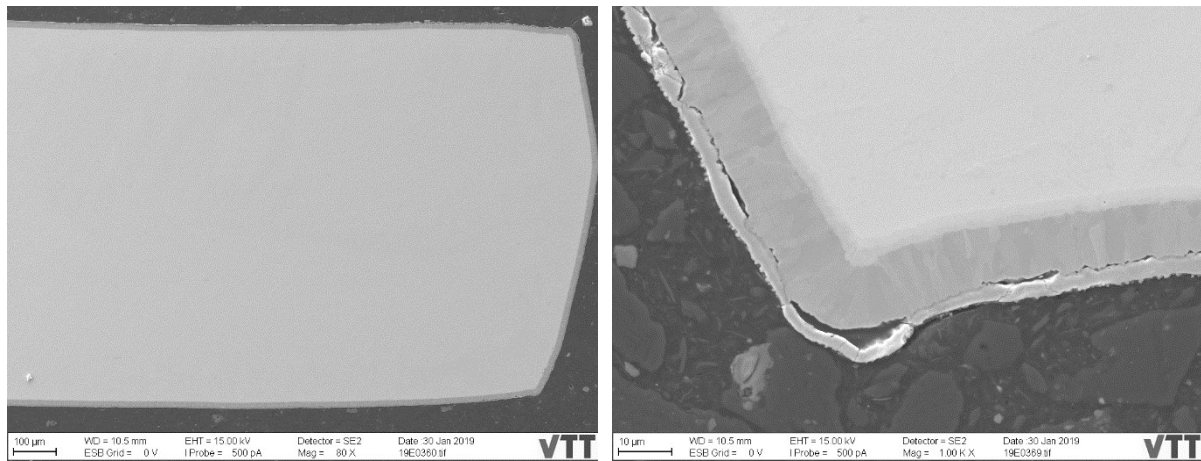


FIG. 85. SE images of Cr coated Zry-2 CTU specimen (1100°C, 60 min).

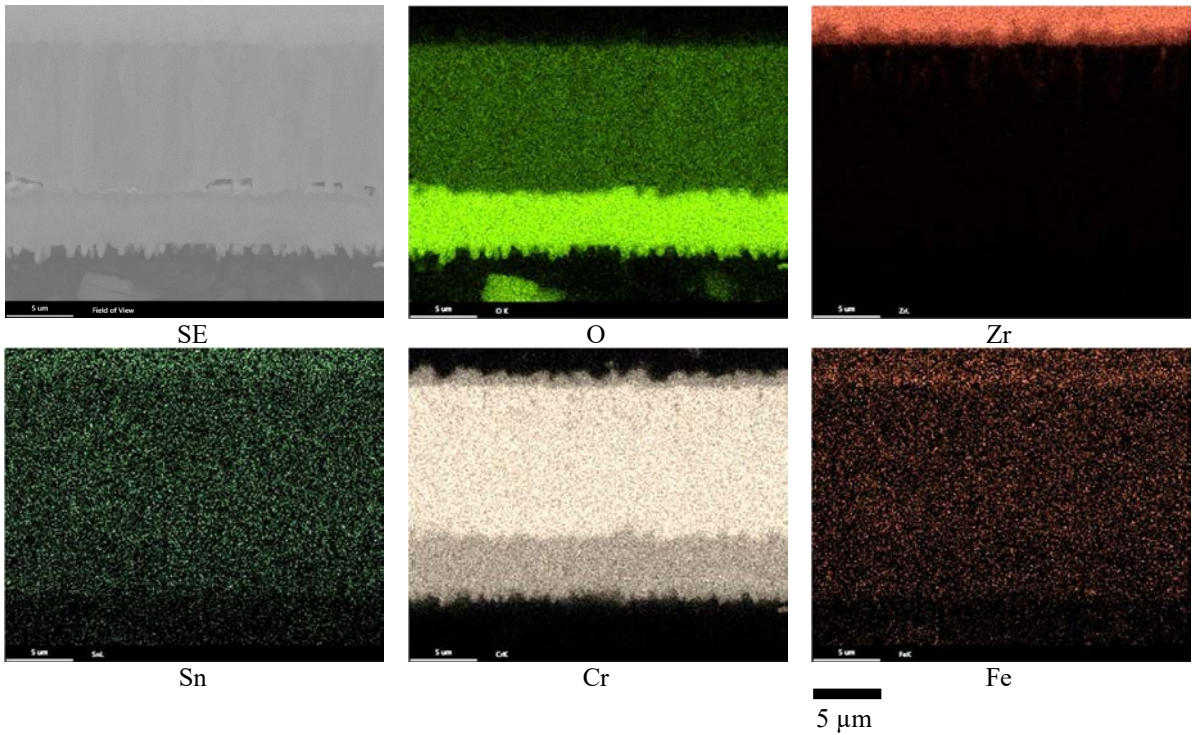
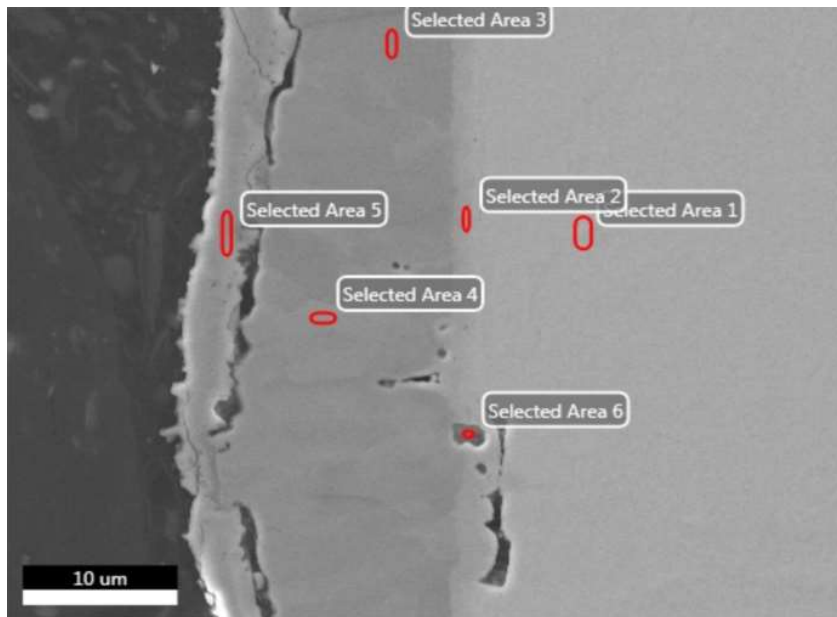


FIG. 86. SEM-EDS maps showing the distribution of O, Zr, Sn, Cr and Fe of the Cr coated Zry-2 CTU specimen (1100°C, 60 min).



|                 | C K  | O K  | Si K | Zr L | Sn L | Cr K | Fe K | Ni K |
|-----------------|------|------|------|------|------|------|------|------|
| Selected Area 1 | —    | 1.7  | —    | 94.1 | 1.3  | 2.0  | 0.3  | 0.5  |
| Selected Area 2 | —    | 2.3  | —    | 38.6 | 0.3  | 56.7 | 1.8  | 0.4  |
| Selected Area 3 | —    | 3.0  | 0.2  | —    | 0.2  | 96.2 | 0.5  | —    |
| Selected Area 4 | —    | 3.1  | 0.1  | —    | 0.1  | 96.2 | 0.4  | —    |
| Selected Area 5 | —    | 27.3 | 0.2  | —    | 0.1  | 72.2 | 0.2  | —    |
| Selected Area 6 | 26.0 | 3.5  | 1.0  | 15.8 | 0.2  | 52.8 | 0.8  | —    |

FIG. 87. SEM-EDS chemical composition (wt%) SA analyses of Cr coated Zry-2 CTU specimen (1100°C, 60 min). K and L X-ray emission lines were used for quantification.

Overview and detailed SE images of Cr coated Zry-2 CTU specimen, which was exposed at 1200°C for 30 minutes, are shown in Fig. 88. The thickness of the coating and the oxide layers together was about 15 µm. The

observed coating layer was continuous. As with the 1100°C specimen, cracks through the oxide layer and between the coating and the oxide layer were found.

The SEM-EDS maps of O, Zr, Sn, Cr and Fe are shown in Fig. 89. The SEM-EDS Selected Area analyses are shown in Fig. 90. A thin layer of Cr and Zr between the coating and the substrate in SEM-EDS maps in Fig. 89 and the observed elemental compositions of Cr and Zr in SA2 in Fig. 90 shows that Cr diffused towards the Zr substrate as was observed also at the lower temperature of 1100°C.

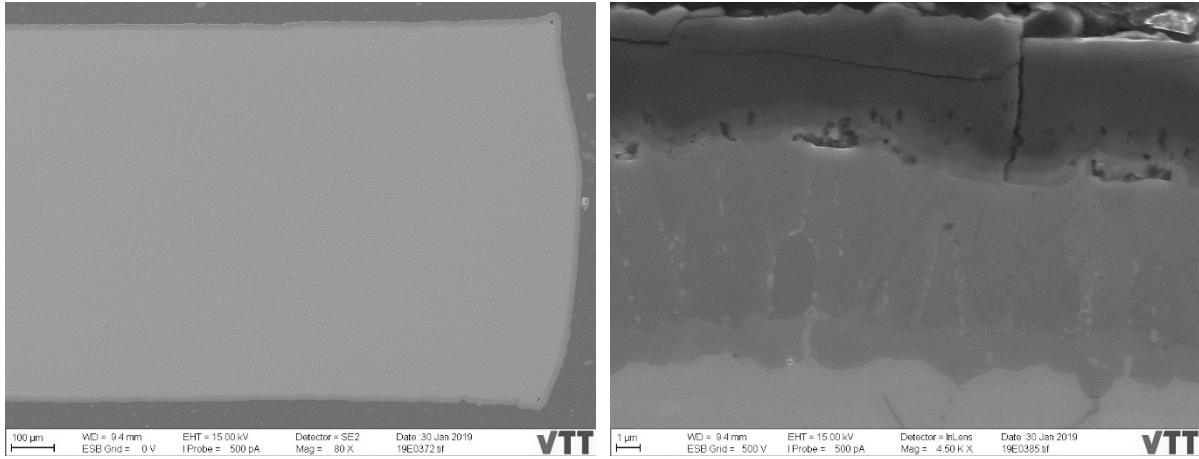


FIG. 88. SE images of Cr coated Zry-2 CTU specimen (1200°C, 30 min).

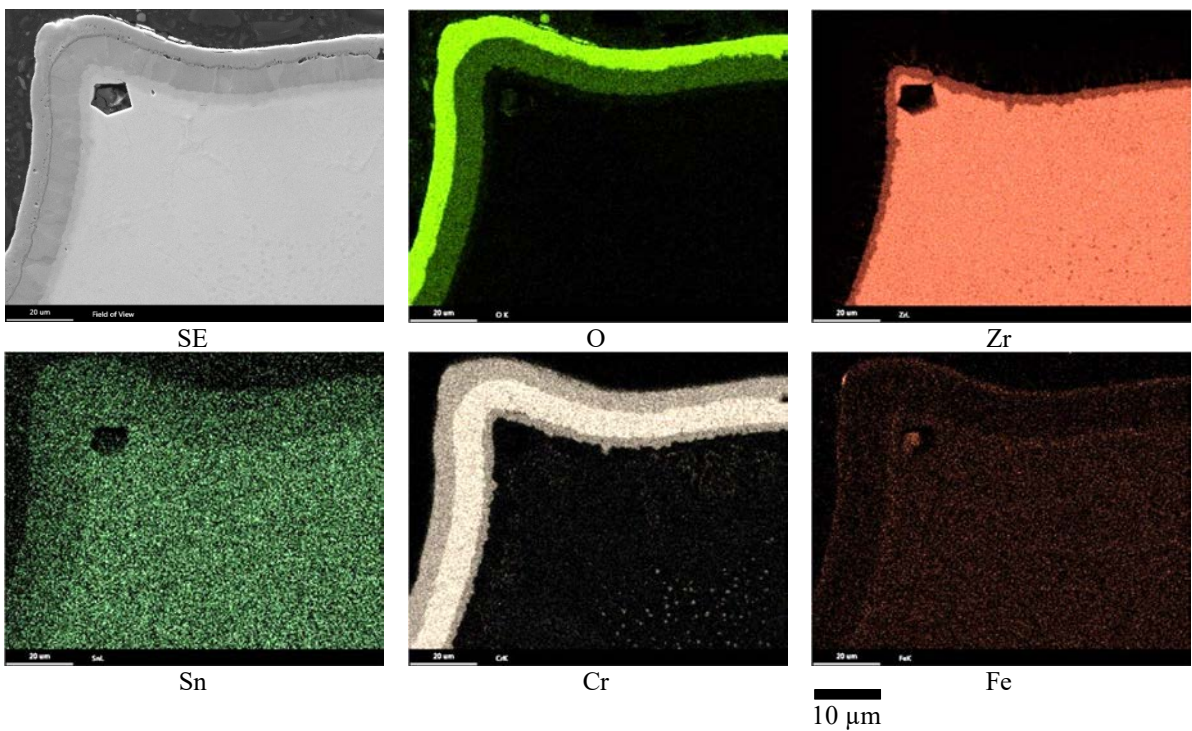
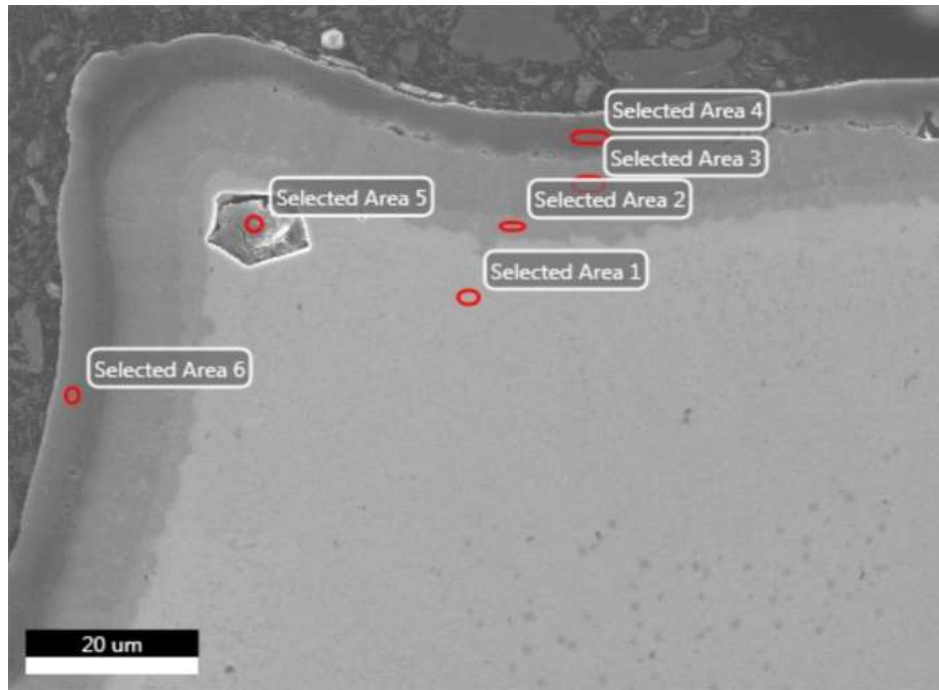


FIG. 89. SEM-EDS maps showing the distribution of O, Zr, Sn, Cr and Fe of the Cr coated Zry-2 CTU specimen (1200°C, 30 min).



|                 | C K  | O K  | Al K | Si K | Zr L | Sn L | Ca K | Cr K | Fe K |
|-----------------|------|------|------|------|------|------|------|------|------|
| Selected Area 1 | —    | 2.1  | —    | —    | 93.7 | 1.4  | —    | 2.1  | 0.8  |
| Selected Area 2 | —    | 2.2  | —    | —    | 38.3 | 0.4  | —    | 58.6 | 0.5  |
| Selected Area 3 | —    | 3.3  | —    | —    | 0.3  | 0.2  | —    | 96.2 | —    |
| Selected Area 4 | —    | 28.2 | 0.2  | 0.1  | —    | 0.2  | —    | 70.8 | 0.5  |
| Selected Area 5 | 60.7 | 16.3 | 0.5  | 1.6  | 2.2  | —    | 2.9  | 2.4  | 13.4 |
| Selected Area 6 | —    | 26.7 | 0.5  | 0.2  | —    | —    | 0.2  | 71.3 | 1.1  |

FIG. 90. SEM-EDS chemical composition (wt%) SA analyses of Cr coated Zry-2 CTU specimen (1200°C, 30 min). K and L X-ray emission lines were used for quantification.

Overview and detailed SE images of Cr coated Zry-2 CTU specimen, which was exposed at 1300°C for 5 minutes, are shown in Fig. 91. The thickness of the coating and the oxide layer ranged from 40 to 400 μm. The coating was continuous, but the coating and the substrate may have partly come loose during the sample preparation as concluded via observation of several substrate cracks.

The SEM-EDS maps of O, Zr, Sn, Cr and Fe, where the oxide layer is on the top, are shown in Fig. 92. In the Cr map, Cr-rich line-shaped features in the substrate are resulted from grinding and polishing during sample preparation. The SEM-EDS Selected Area analyses are shown below in Fig. 93.

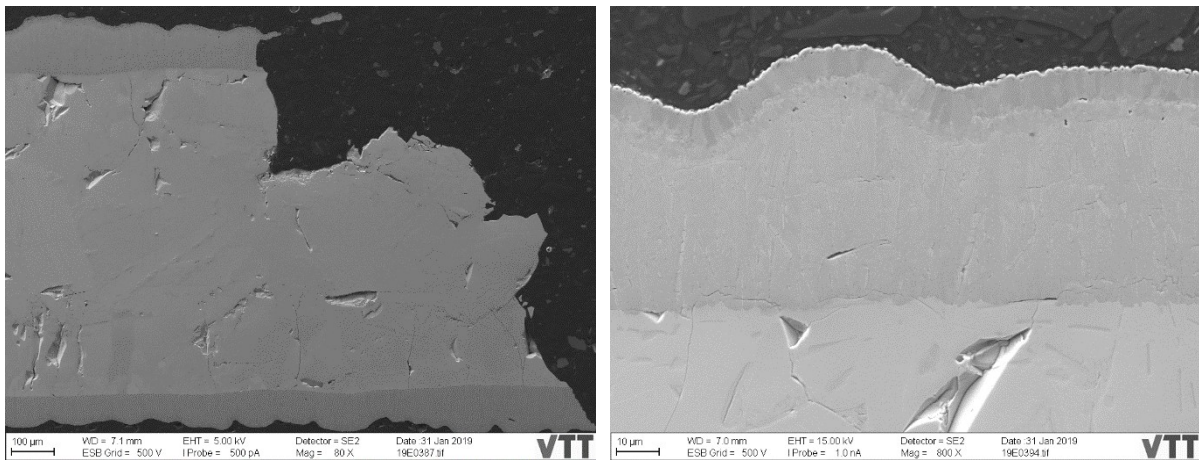


FIG. 91. SE images of Cr coated Zry-2 CTU specimen (1300°C, 5 min).

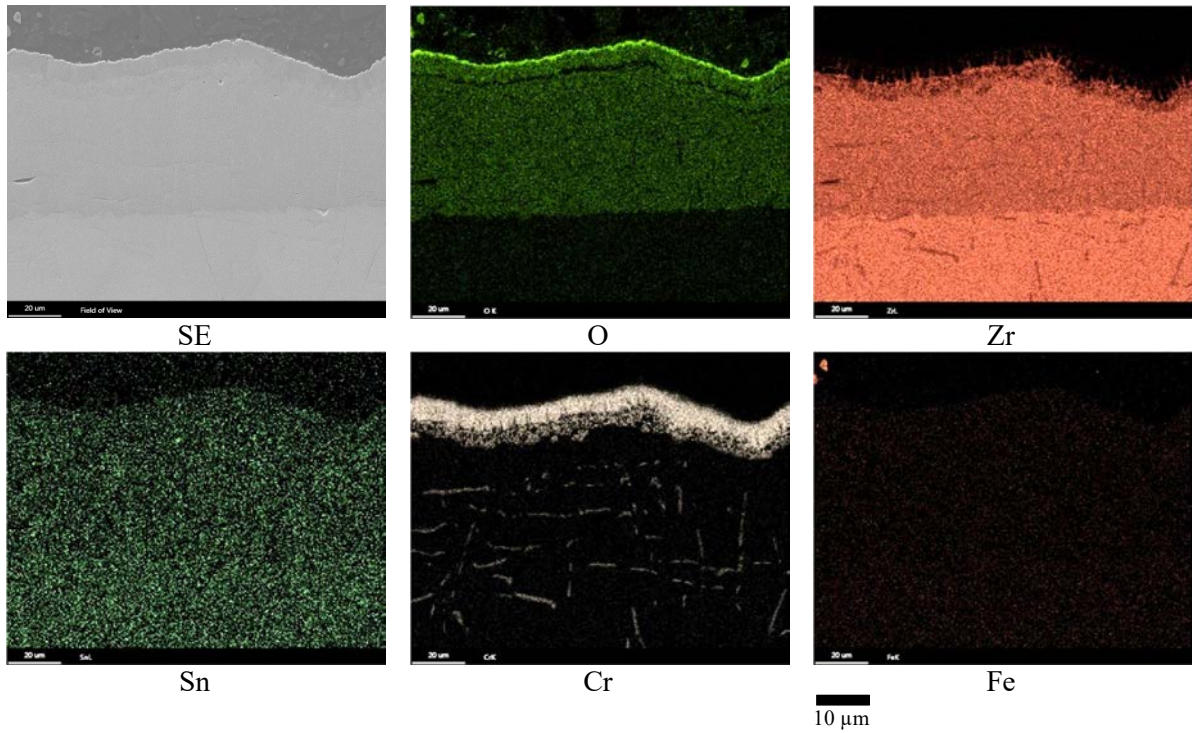
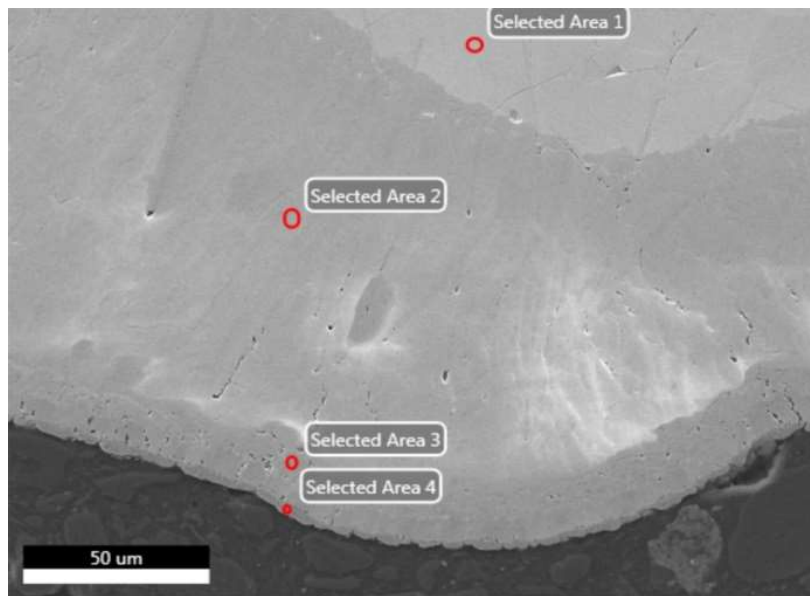


FIG. 92. SEM-EDS maps showing the distribution of O, Zr, Sn, Cr and Fe of the Cr coated Zry-2 CTU specimen (1300°C, 5 min).



|                 | O K  | Zr L | Sn L | Cr K | Fe K |
|-----------------|------|------|------|------|------|
| Selected Area 1 | 7.2  | 91.3 | 1.5  | —    | —    |
| Selected Area 2 | 24.5 | 72.7 | 1.2  | 0.8  | 0.8  |
| Selected Area 3 | 11.0 | 35.9 | 0.4  | 51.2 | 1.5  |
| Selected Area 4 | 25.9 | —    | 0.1  | 73.5 | 0.5  |

FIG. 93. SEM-EDS chemical composition (wt%) SA analyses of Cr coated Zry-2 CTU (1300°C, 5 min). K and L X-ray emission lines were used for quantification.

#### 4.3.2. Cr/Cr<sub>2</sub>AlC/Cr (MAX phase) PVD coated Zry-4

The calculated weight changes of the MAX phase (Cr<sub>2</sub>AlC) coated Zry-4 / KIT samples after steam exposures at different temperatures are shown in Table 36. The weight of the samples increased as a function of

test temperature although the exposure time decreased from 60 min to 5 min, respectively. At 1300°C, the weight gain was as high as 30 % when all peeled off oxide was included.

TABLE 36. THE MEASURED MASS CHANGES ( $\Delta w$ ) OF THE MAX PHASE COATED Zry-4 SAMPLES AFTER THE STEAM EXPOSURES

| SPP4 1100°C / 60 min | SPP5 1200°C / 30 min | SPP6 1300°C / 5 min |
|----------------------|----------------------|---------------------|
| $\Delta w$ 6.57 %    | $\Delta w$ 15.19 %   | $\Delta w$ 30.36 %  |

As shown in Fig. 94, the MAX phase coating is still visible in both sides of the specimen SPP 4 after the exposure (see Fig. 94(a), red arrows). Based on the observations, one can see that the oxide has grown fast towards the centre from the edge of the specimen. However, almost no oxide formation under the intact coating is observed in Fig. 94(b). In an area outlined with a red ellipse in the figure multiple coating cracks were observed and oxides were formed. On the arrow pointed area, where only the top layer of coating was breached, no oxide formation was found (Fig. 94(b)). In addition, no fragile  $\alpha$ -Zr was found most probably due to the fact that there was no oxygen penetration.

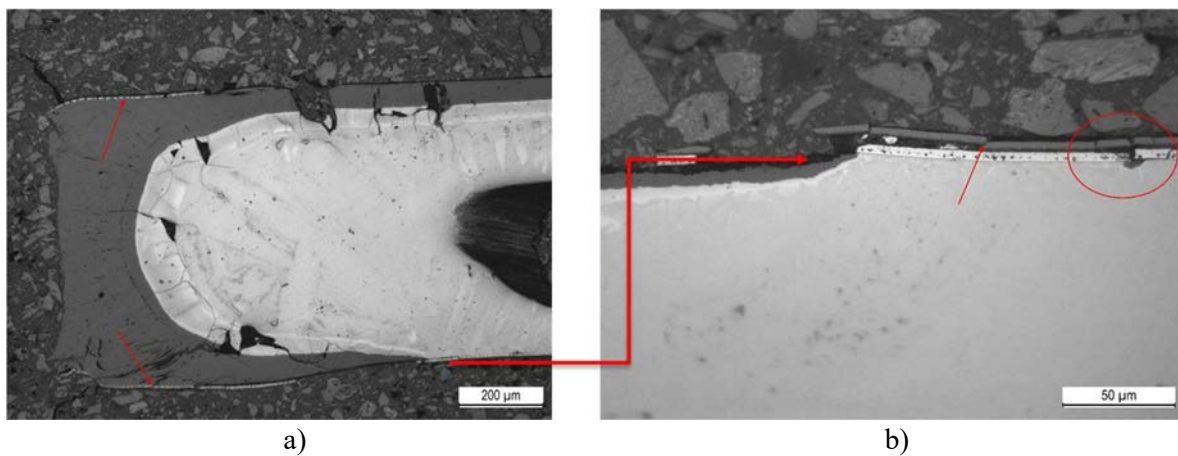


FIG. 94. SPP 4 sample after steam exposure at 1100°C for 60 minutes.

The observed coating condition underneath of sample SPP 4 seems to be intact. There is no brittle  $\alpha$ -Zr present, i.e. no oxidation. However, it seems that the coating has dispersed quite strongly from the original coating layer. This is most probably due to the fact that Al has dispersed from the coating layer as shown by SEM-EDS analyses in Fig. 95. It is evident that the specimen alignment during the exposure is not optimal and this results in uneven behaviour. This issue is under consideration in order to achieve the same testing environment on both sides of the specimen.

Figure 95 shows the SEM-EDS maps of specimen SPP 4, indicating the elements of interest and showing the greyscale image from the area where the MAX phase was intact and no  $ZrO_2$  was formed yet. As mentioned, it is noteworthy that Al has dispersed heavily from the assumed uniform initial middle layer, i.e. from the original layer of  $Cr_2AlC$ . Due to this, there would be a clear need to characterize also an unexposed specimen in order to understand the behaviour of Al at this temperature.

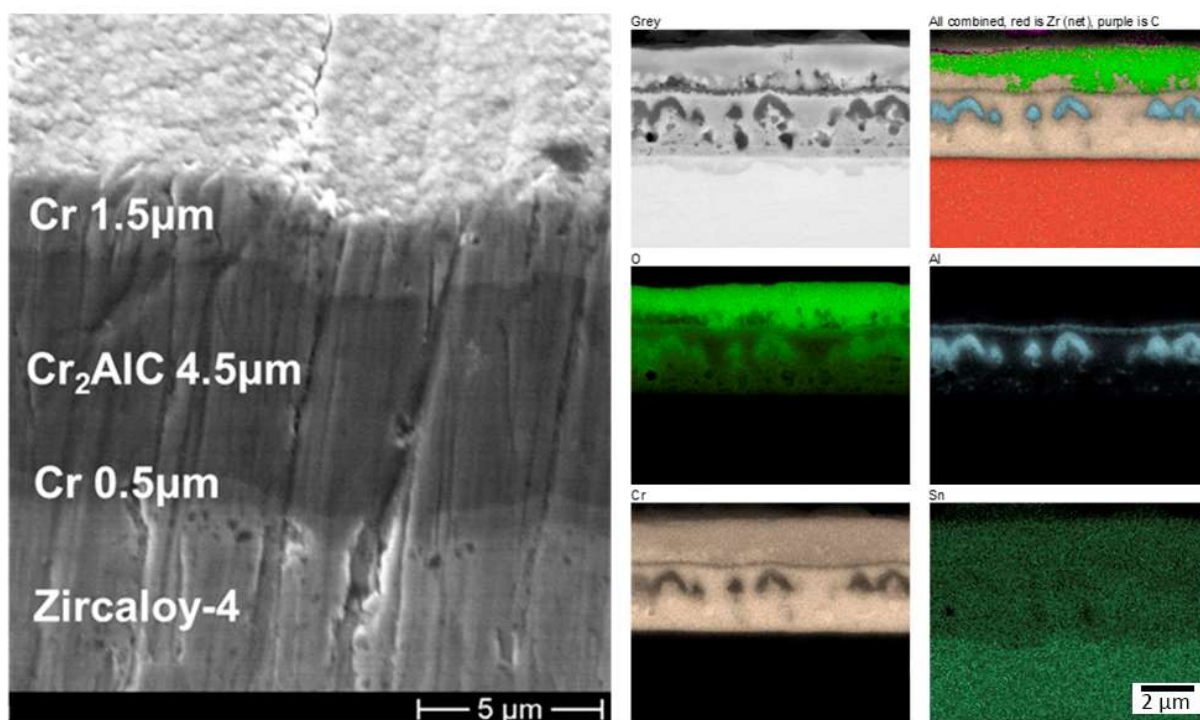


FIG. 95. Original (unexposed) coating configuration of MAX phase coated Zry-4 (left) and SEM-EDS maps of individual elements after exposure at 1100°C (right).

The surface morphology of sample SPP 4 is shown in Fig. 96. Some precipitates were found on the sample surface after the exposure at 1100°C for 60 min. The SEM-WDS analysis was performed in order to characterize the observed precipitate shown in Fig. 96 within the red circle. The SEM-WDS analysis suggested that the sample surface precipitates could be  $Zr_5Sn_4$  (55.5 at.% of Sn), a phase of which existence in a model material has been confirmed in open literature [83].

The SEM-EDS analysis was performed on the same precipitate showing that only Sn, Zr, and small amounts of O are present. If the precipitate is assumed an intermetallic, then a relatively firm assumption could be made that the intermetallic is  $Zr_5Sn_4$ .

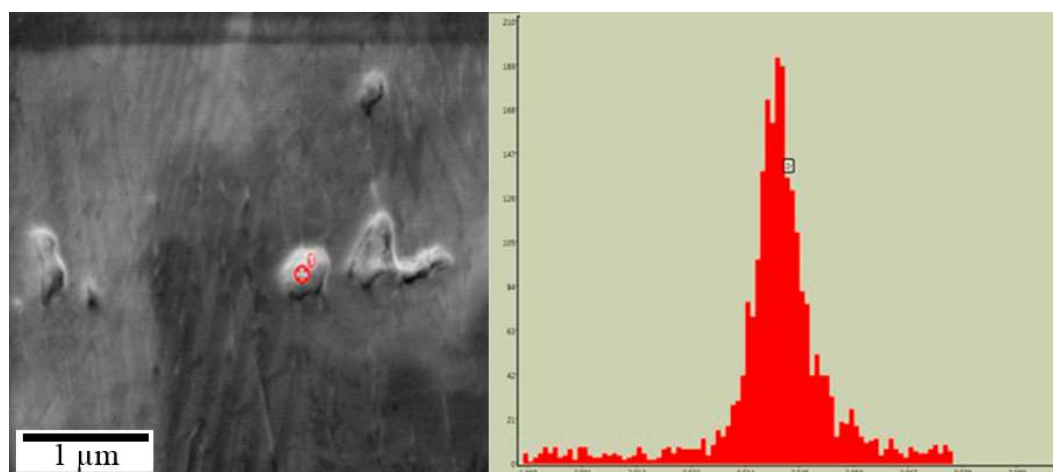


FIG. 96. The precipitate location observed on the sample surface of SPP 4(left) and corresponding SEM-WDS analysis from the precipitate (right).

Sample SPP 5 was exposed at 1200°C for 30 minutes. After exposure, the outer oxide layer is  $ZrO_2$  and it has some clear cracks most probably due to differences of thermal expansion coefficients of different phases. For the uniform part of the oxide film, the thickness is estimated to be around 150 µm. A cross section image is shown

in Fig. 97. The area outlined with the red-lined rectangle is probably  $\alpha$ -Zr, below that, is  $\beta$ -Zr and above the  $\alpha$ -Zr is  $ZrO_2$ . The SEM-EDS line scan over the oxide layer and the assumed  $\alpha$ -Zr in specimen SPP 5 is shown in Fig. 98. Note that the assumed  $\alpha$ -Zr contains more oxygen than the initial  $\beta$ -Zr (observed change in slope in the green curve).  $\alpha/\beta$ -Zr identification is based on literature as described in refs [83, 84].

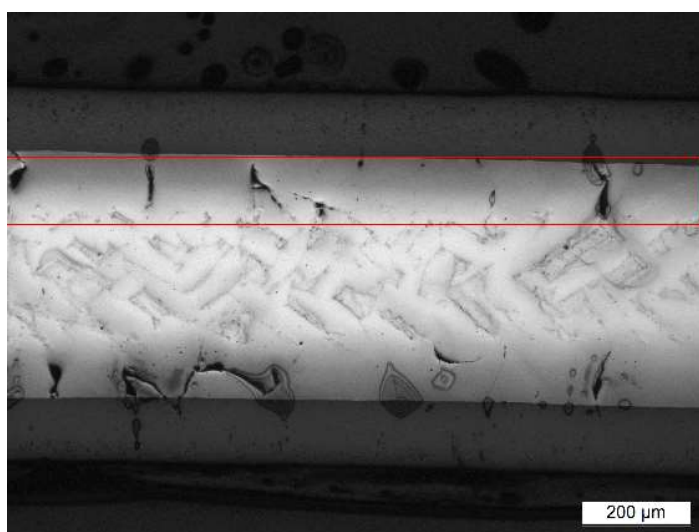


FIG. 97. Post test appearance of the specimen SPP 5 after exposure at 1200°C / 30 min., including  $ZrO_2$  layer (upper),  $\alpha$ -Zr layer (in the red-lined rectangle) and prior  $\beta$ -Zr layer (lower).



FIG. 98. The SEM-EDS line-scan over the oxide and  $\alpha$ -Zr layers in the specimen SPP 5 after exposure at 1200 °C / 30 min.

The exposure time of sample SPP 6 was 5 minutes at 1300°C. The Remnants of MAX phase coated Zry-4 coupon sample after the exposure is shown in Fig. 99. Inside the red-lined rectangle shown in Fig. 99, different layers can be seen. No analysis of this part was possible by SEM because the sample was so fragile. Fig. 99(a) shows the top side of the sample and Fig. 99(b) the bottom side of the sample. The cross section was prepared approximately along the red horizontal line shown in Fig. 99. The SEM images from the almost thoroughly oxidized areas are shown in Fig. 99(a) and Fig. 99(b).

The SEM images from the middle of the cross section with evidently less oxidation are shown in Fig. 100(a) (full cross section from the middle of specimen SPP 6) and Fig. 100(b) at a higher magnification. In these images, the cracked areas are possibly  $\alpha$ -Zr according to literature. Only limited oxidation was observed at the spots where the MAX phase coating has cracked (outlined with red-lined ellipses in Fig. 101(a). Fig. 102 shows compositional analysis (SEM-EDS maps) from one part of the area shown in Fig. 101(b). The map shows roughly similar composition profile on the surface region as to the specimen SPP 4 after the exposure at 1100°C.

Figure 103 zoomed into one crack seen in the middle of Fig. 102(a). Elevated Sn was found into the crack and into the oxide shown as the white horizontal layers. The existence of Sn is verified with the SEM-EDS maps of different elements shown in Fig. 104. Based on the Zr-Sn phase diagram shown in Fig. 105, the test temperature was above a critical temperature seen in the Zr-Sn diagram. Similar microstructure is also reported in the literature [85, 86].

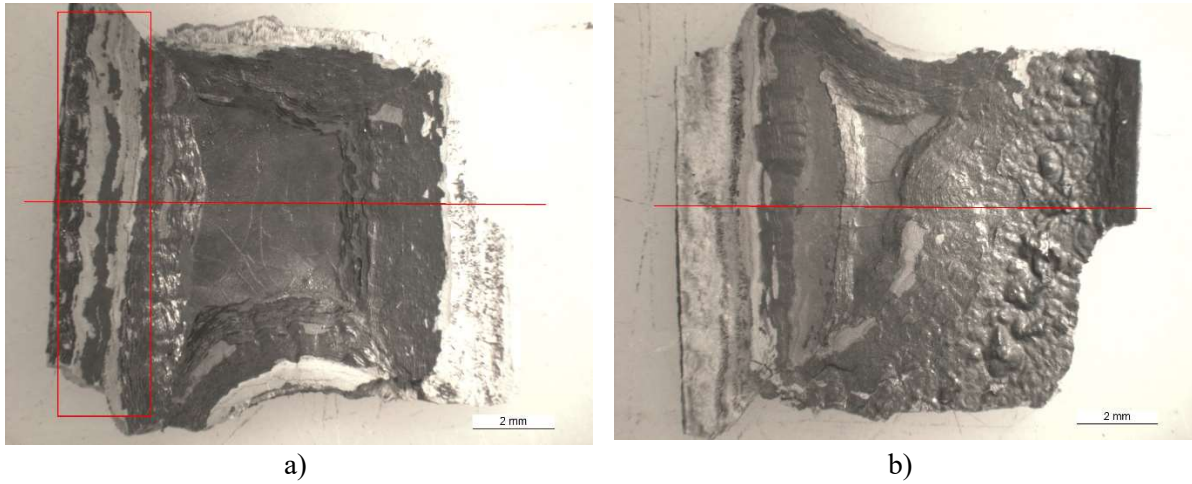


FIG. 99. The Remnants of sample SPP 6 after exposure at 1300°C for 5 minutes. The bottom side of the sample a) and the top side of sample b) are shown. The red horizontal line indicates the line of cross-sectioning.

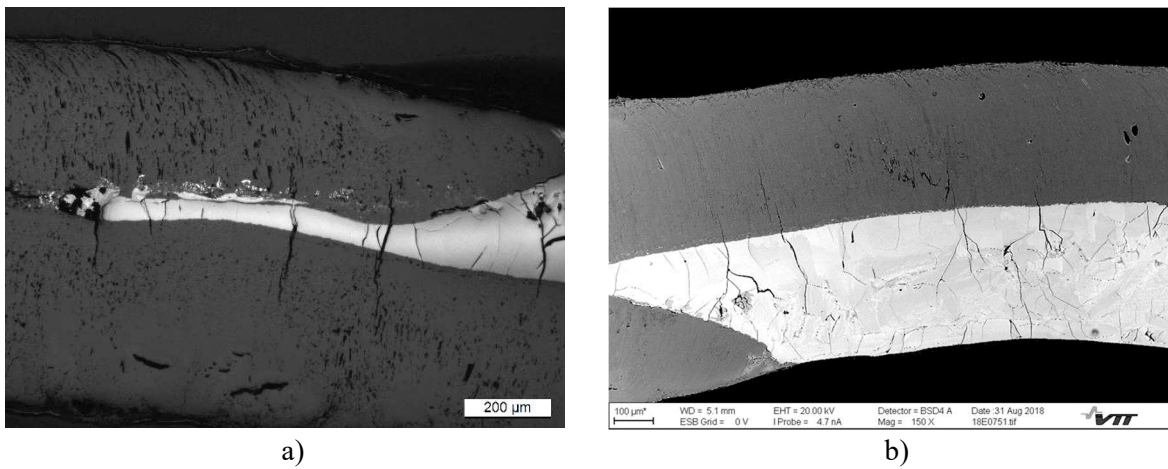


FIG. 100. Specimen SPP 6 cross-section: a) close to the left side in Fig. 99. and b) close to the right side after exposure at 1300°C for 5 minutes. The SEM-EDS analysis revealed Sn inside the cracks. The remaining metallic part is probably brittle  $\alpha$ -Zr.



FIG. 101. Specimen SPP 6 after exposure at 1300°C / 5 min. a) Full cross section from the middle of specimen SPP 6, b) detail from the upper part shown in the left-hand side image.

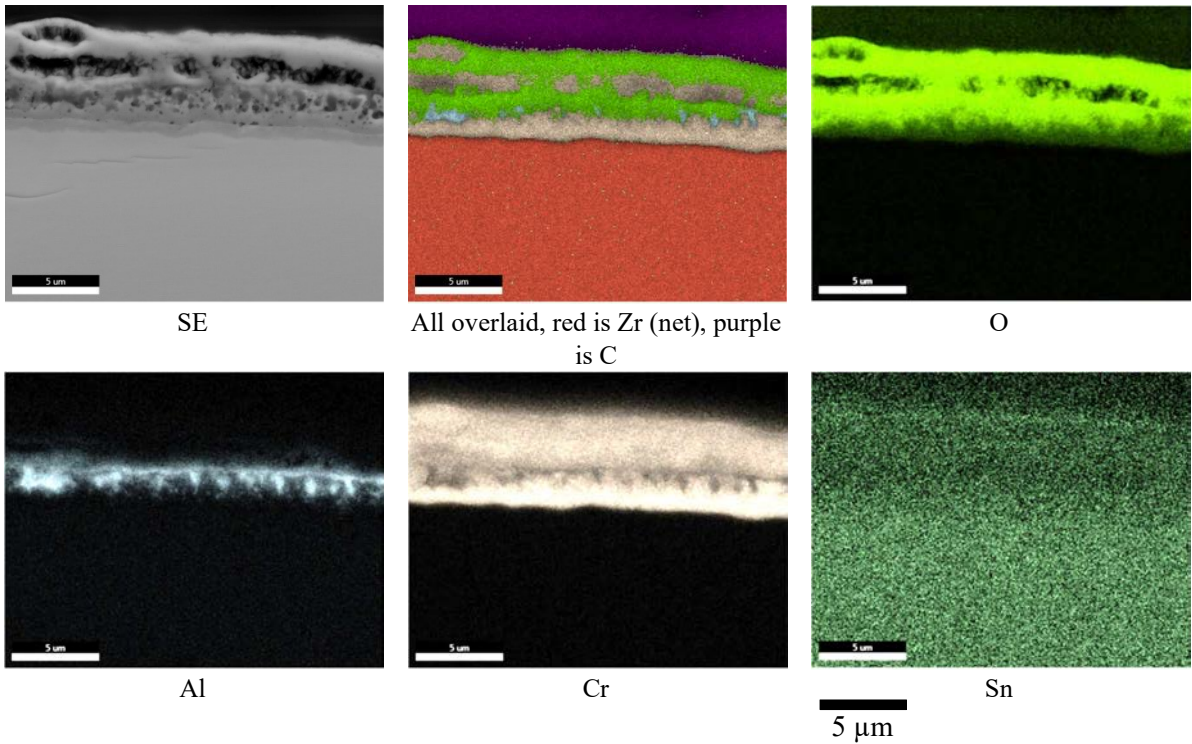


FIG. 102. The SEM-EDS maps of different elements in the MAX phase coated Zry-4, specimen SPP 6, after exposure at 1300°C for 5 minutes. This analysis is from the surface zone of the central area of the specimen where no significant oxidation has occurred.

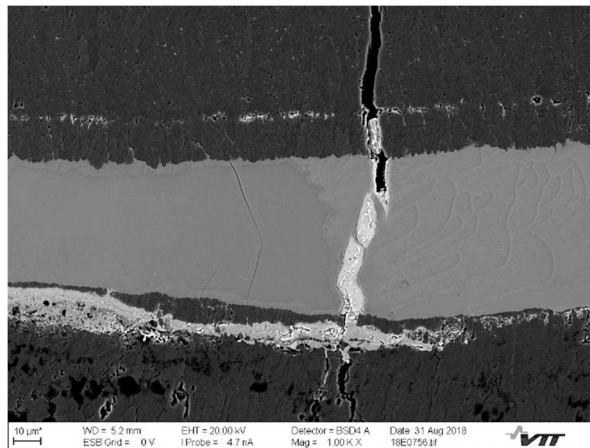


FIG. 103. The SEM cross section of specimen SPP 6 after exposure at 1300°C / 5 min. In the middle is a crack filled with Sn-rich material. Left with a thin crack is most likely  $\alpha$ -Zr, top and below is  $ZrO_2$ .

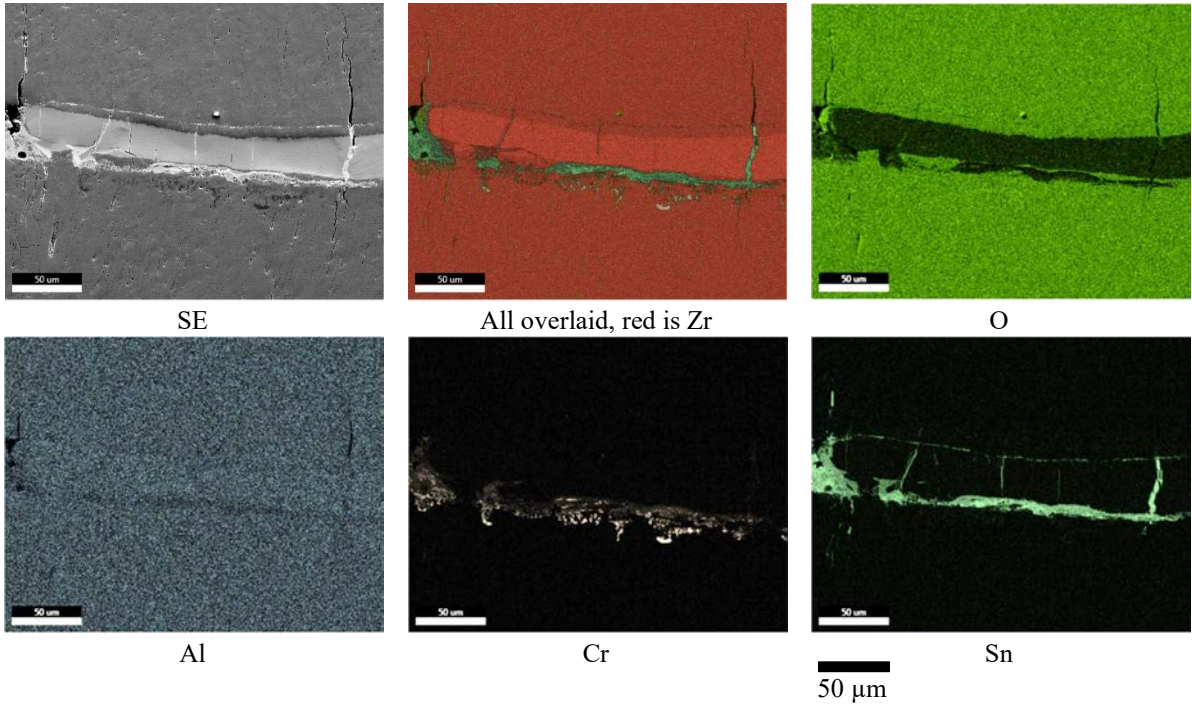


FIG. 104. The MAX phase coated Zry-4, specimen SPP 6, after exposure at 1300°C / 5 min. This analysis is from the area shown in Fig. 103. representing the cracks filled with Sn.

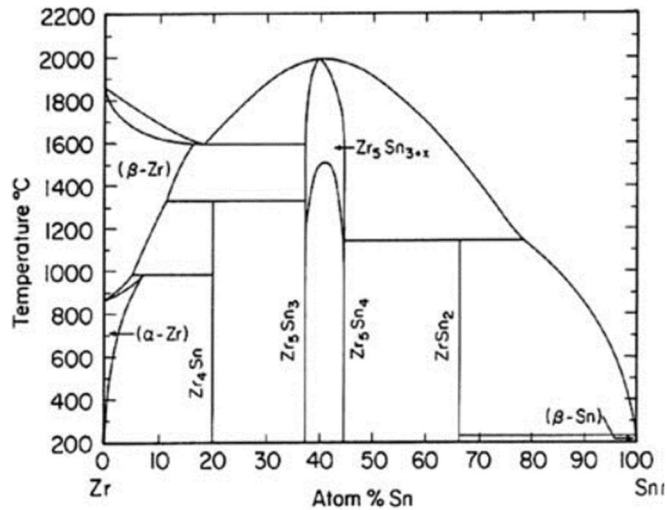


FIG. 105. Phase diagram of the Zr-Sn binary system.

#### 4.3.3. AISI 348 SS

Three AISI 348 samples were exposed to the flowing steam: sample SPP 1 at 1100°C for 60 minutes, SPP 2 at 1200°C for 30 minutes and SPP 3 at 1300°C for 5 minutes. Prior to testing, sample dimensions were measured. The samples were weighed before and after testing in order to calculate the weight change per unit surface area. The weigh changes are shown in Table 37. A moderate increase in weight was observed with increasing temperature regardless of considerably reduced exposure time.

TABLE 37. CALCULATED WEIGHT CHANGES ( $\Delta w$ ) OF AISI 348 AFTER STEAM EXPOSURES.

| SPP 1 1100°C / 1h   | SPP 2 1200°C / 30 min | SPP 3 1300°C / 5 min |
|---------------------|-----------------------|----------------------|
| $\Delta w = 1.62\%$ | $\Delta w = 4.74\%$   | $\Delta w = 5.86\%$  |

The SE and BSE images are shown in Fig. 106. In the SE image, the outer oxide layer is on the left side and the inner oxide layer is in the middle. It can be seen in the BSE image that the outer oxide layer is partly loosened during the sample preparation. This layer has porosity and multiple cracks. The thickness of the whole oxide layer varied from 200  $\mu\text{m}$  to 450  $\mu\text{m}$ .

The SEM-EDS maps of main elements like O, Si, Cr, Mn, Fe and Ni are shown in Fig. 107, where the outer oxide layer is on the left side. The SEM-EDS Selected Area (SA) analyses are shown in Fig. 108. Based on the SEM-EDS map analyses, a typical double oxide layer structure is observed including the outer oxide rich in Fe and the inner oxide layer rich in Cr, most probably Fe-Cr spinel, with a certain amount of Si, Mn, and Ni. In addition to this, some Mn was found close to the original sample surface, see Fig. 108 (Selected Area 2).

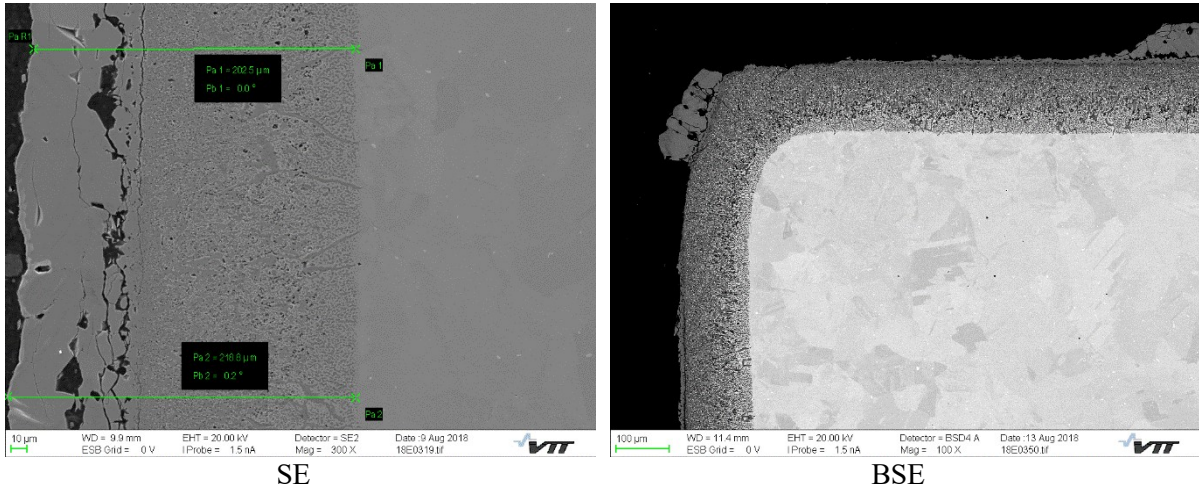


FIG. 106. Specimen SPP 1 SE and BSE images after exposure at 1100°C / 60 min.

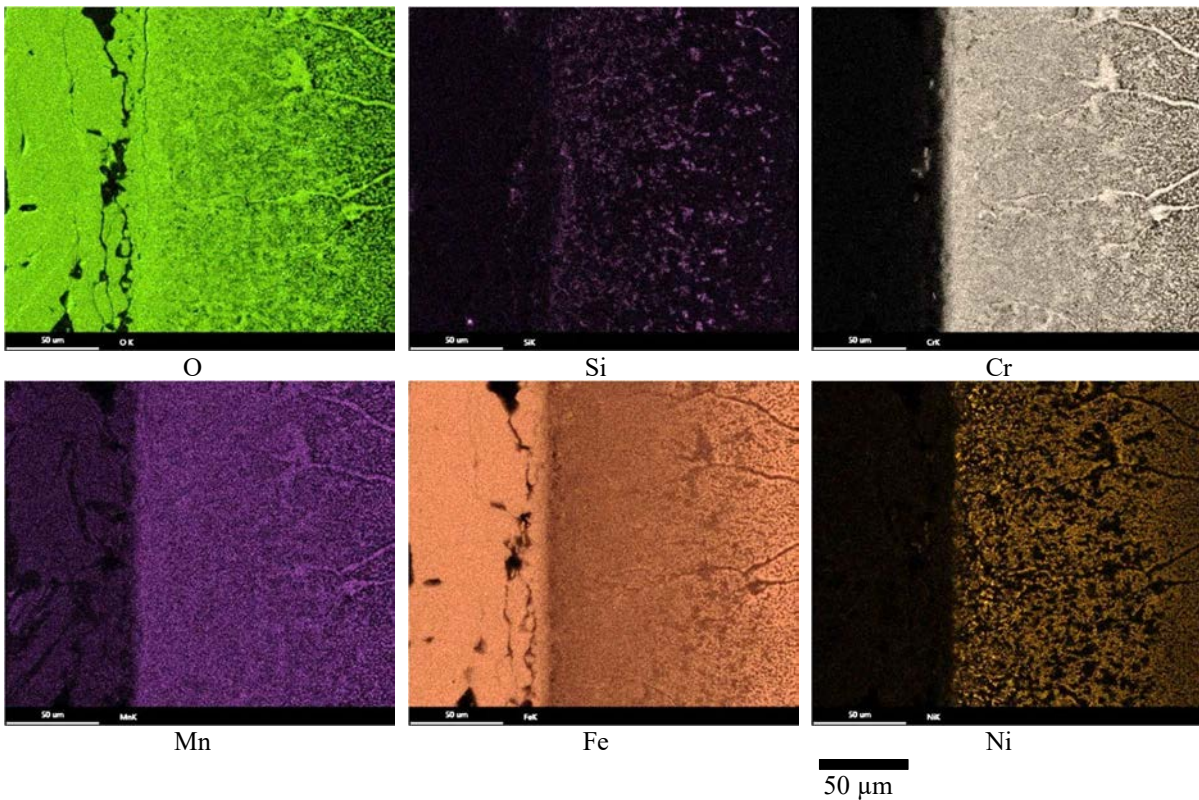
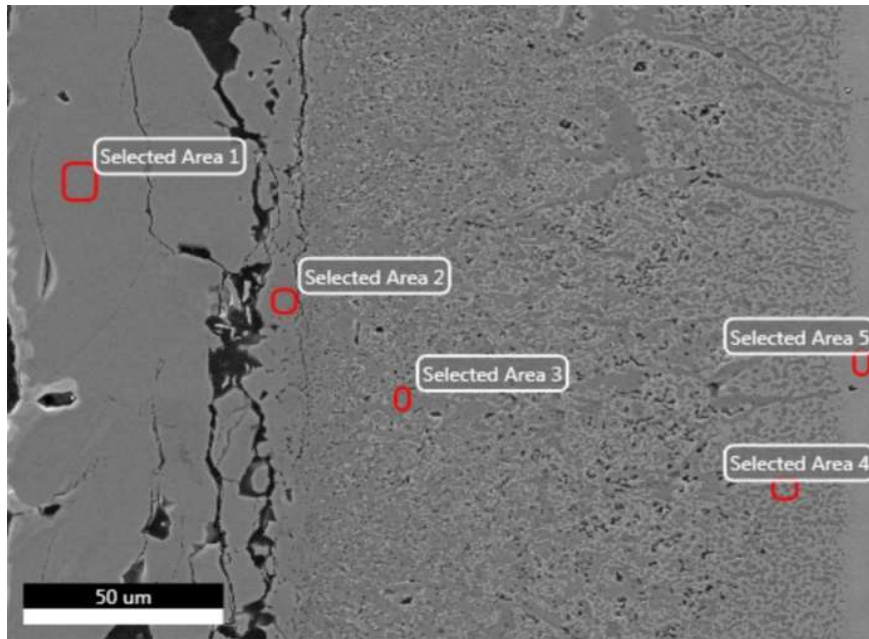


FIG. 107. Specimen SPP 1 SEM-EDS maps showing the distribution of O, Si, Cr, Mn, Fe and Ni after exposure at 1100°C / 60 min. The outer oxide layer is on the left side.

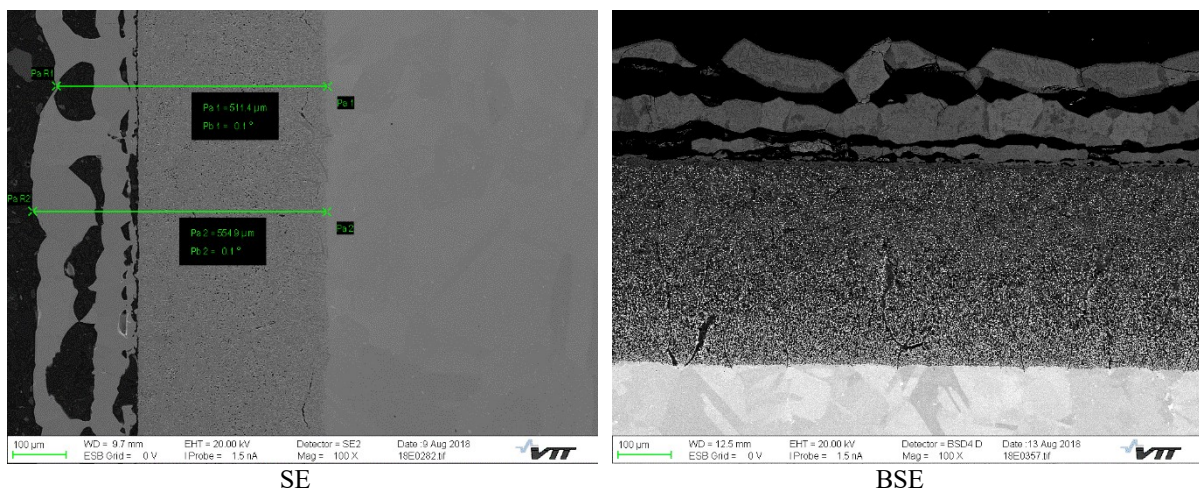


|                 | O K  | Si K | Nb K | Mo L | Cr K | Mn K | Fe K | Ni K |
|-----------------|------|------|------|------|------|------|------|------|
| Selected Area 1 | 26.4 | 0.1  | 0.1  | 0.1  | 0.2  | 1.6  | 71.0 | 0.5  |
| Selected Area 2 | 24.8 | 0.2  | 0.4  | 0.1  | 14.0 | 2.1  | 56.8 | 1.5  |
| Selected Area 3 | 23.3 | 1.6  | 0.9  | 0.1  | 28.0 | 1.2  | 40.7 | 4.1  |
| Selected Area 4 | 11.7 | 0.6  | 0.4  | 0.1  | 18.2 | 1.2  | 60.4 | 7.3  |
| Selected Area 5 | 0.8  | 0.5  | 0.3  | 0.1  | 19.0 | 1.6  | 69.1 | 8.7  |

FIG. 108. Specimen SPP 1 SEM-EDS chemical composition (wt%) SA analyses. K and L X-ray emission lines were used for quantification.

The SE and BSE images are shown in Fig. 109 on specimen SPP 2 after exposure at 1200°C / 30 min. In the SE image, the outer oxide layer is on the left side, the inner oxide layer next to the outer oxide layer in the middle and the bulk is on the right side. In the BSE image, the outer oxide layer is on the top. The outer oxide layer is porous and partly loosened due to sample preparation and some cracks can be seen in the inner oxide layer. The thickness of the whole oxide layer varied from 500 µm to 650 µm.

The SEM-EDS maps of O, Si, Cr, Mn, Fe and Ni, where the outer oxide layer is on the bottom part, are shown in Fig. 110. The corresponding SEM-EDS SA analyses are shown in Fig. 111.



SE

BSE

FIG. 109. Specimen SPP 2 after exposure at 1200°C / 30 min.

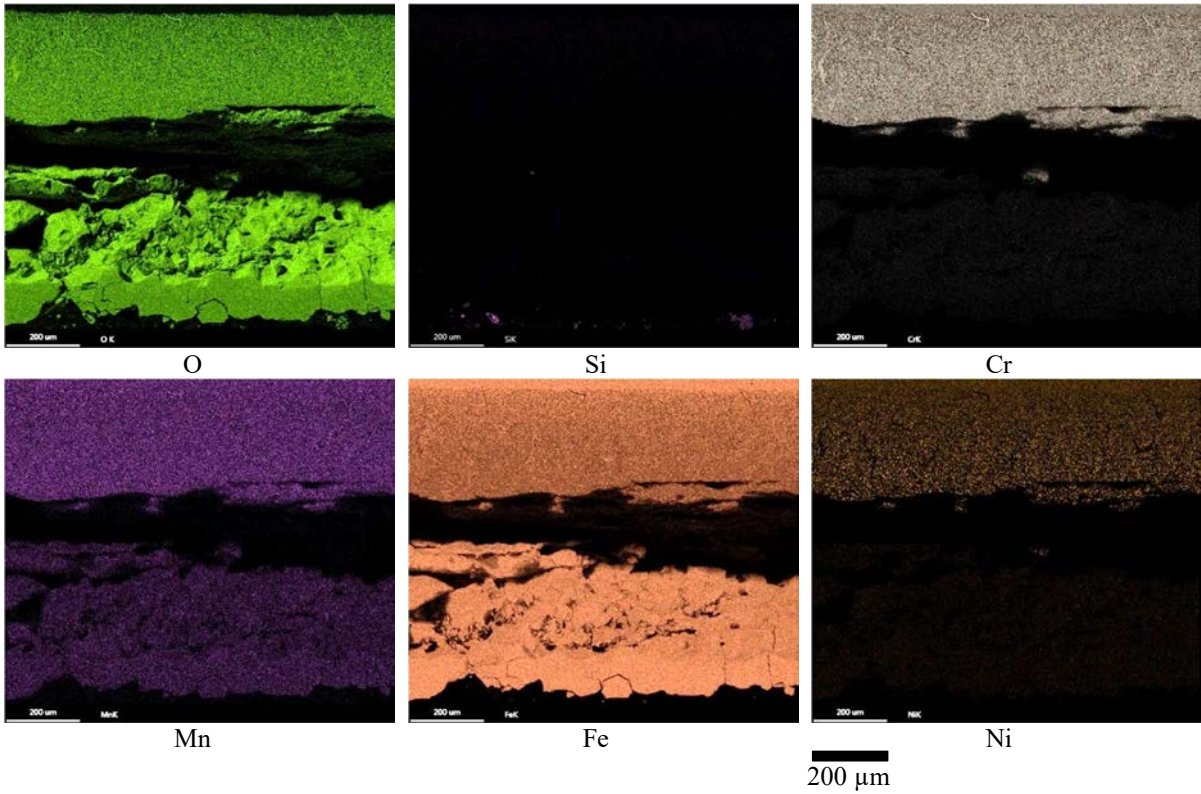
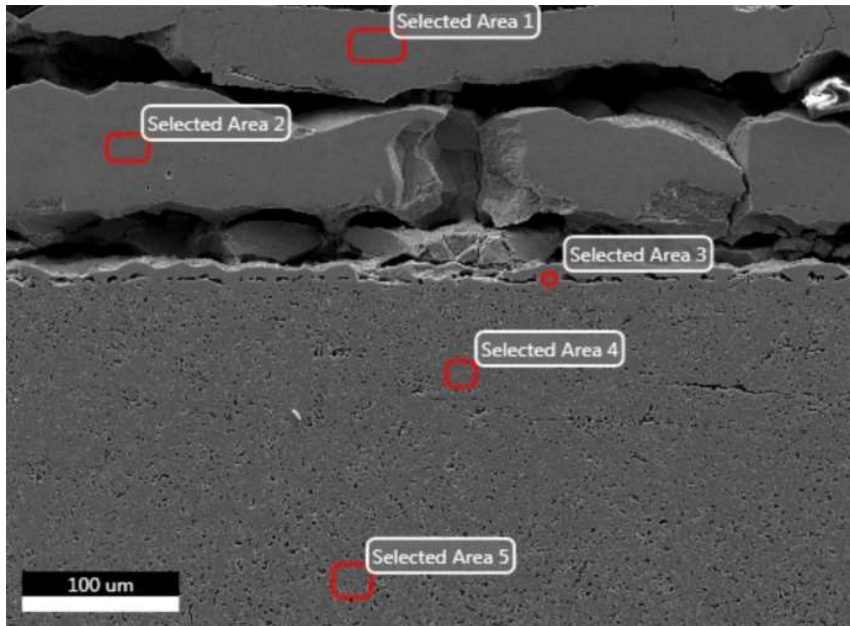


FIG. 110. Specimen SPP 2 SEM-EDS maps showing the distribution of O, Si, Cr, Mn, Fe and Ni. The outer oxide layer is on the bottom, the inner oxide layer on the upper part of the maps and a narrow zone of the bulk alloy is seen on the top.

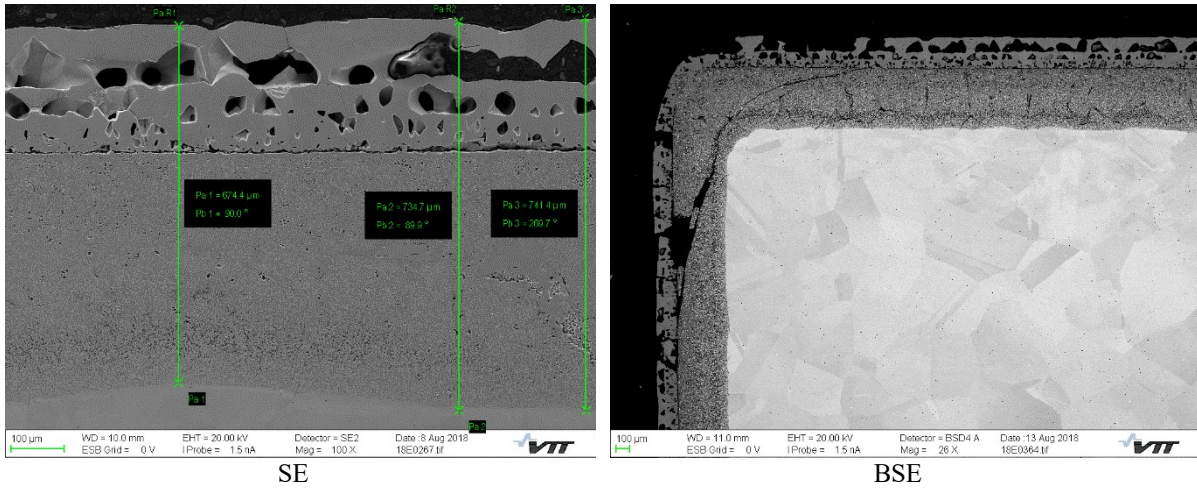


|                 | O K  | Si K | Nb K | Mo L | Cr K | Mn K | Fe K | Ni K |
|-----------------|------|------|------|------|------|------|------|------|
| Selected Area 1 | 23.2 | —    | —    | —    | 0.2  | 2.2  | 73.9 | 0.6  |
| Selected Area 2 | 23.2 | 0.1  | 0.2  | 0.1  | 0.3  | 1.9  | 74.0 | 0.2  |
| Selected Area 3 | 23.9 | 0.7  | 0.9  | 0.1  | 7.0  | 2.0  | 64.5 | 0.7  |
| Selected Area 4 | 21.3 | 0.2  | 0.5  | 0.1  | 24.9 | 1.0  | 44.5 | 7.4  |
| Selected Area 5 | 18.9 | 0.5  | 0.6  | 0.1  | 26.9 | 0.9  | 44.7 | 7.3  |

FIG. 111. Specimen SPP 2 SEM-EDS chemical composition (wt%) SA analyses. The K and L X-ray emission lines were used for quantification.

The SE and BSE images are shown in Fig. 112. for specimen SPP 3 after exposure at 1300°C / 5 min. In the SE image, the outer oxide layer is on the top, the inner oxide layer is below the outer oxide layer and the bulk can be seen on the bottom. The BSE image shows that the outer oxide layer is porous and partly loosened as a result of sample preparation. The inner oxide layer has large cracks. The thickness of the whole oxide layer varied from 520 μm to 1050 μm.

The SEM-EDS maps of O, Si, Cr, Mn, Fe and Ni are shown in Fig. 113. where the outer oxide layer is on the left side. The SEM-EDS SA analyses are shown in Fig. 114.



SE

BSE

FIG. 112. Specimen SPP 3 after exposure at 1300°C / 5 min.

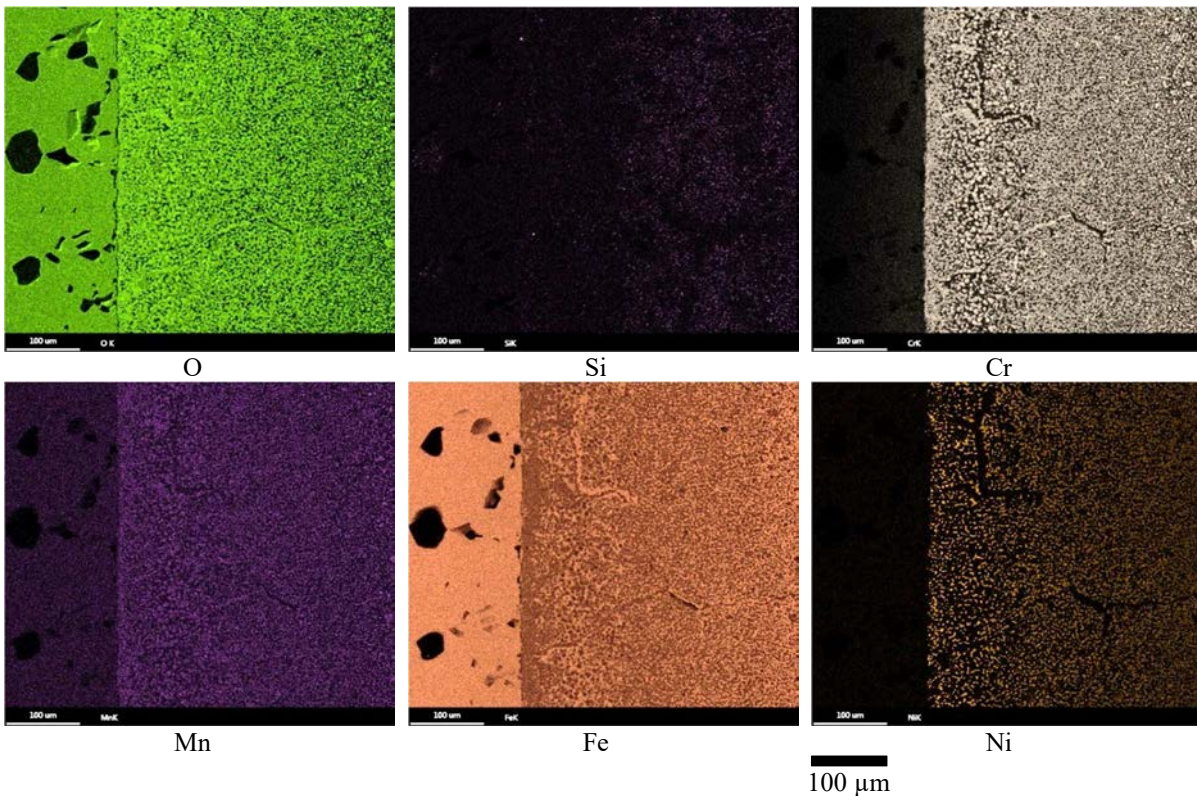
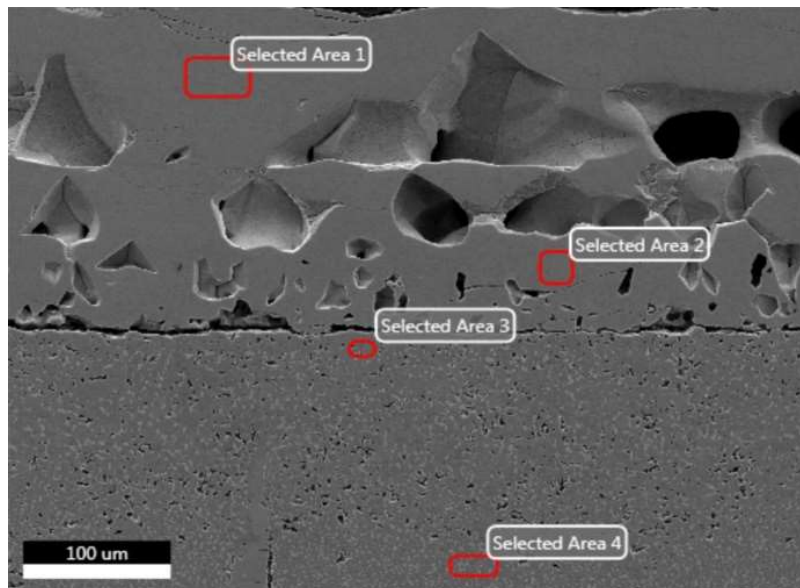


FIG. 113. Specimen SPP 3 SEM-EDS maps after exposure at 1300°C / 5 min showing the distribution of O, Si, Cr, Mn, Fe and Ni. The outer oxide layer is on the left side, the inner oxide layer in the middle and the bulk is on the right side outside the images.



|                 | O K  | Si K | Nb K | Mo L | Cr K | Mn K | Fe K | Ni K |
|-----------------|------|------|------|------|------|------|------|------|
| Selected Area 1 | 23.5 | 0.1  | 0.2  | 0.1  | 0.2  | 1.8  | 74.0 | 0.2  |
| Selected Area 2 | 23.7 | 0.2  | 0.3  | 0.1  | 2.2  | 1.6  | 71.7 | 0.2  |
| Selected Area 3 | 22.8 | 0.4  | 0.7  | 0.1  | 19.9 | 1.5  | 49.3 | 5.4  |
| Selected Area 4 | 16.3 | 0.3  | 0.5  | 0.1  | 21.1 | 0.9  | 45.0 | 15.8 |

FIG. 114. Specimen SPP 3 SEM-EDS chemical composition (wt%) SA analyses. The K and L X-ray emission lines were used for quantification.

A common feature in the specimens was the double layer structure of the oxide. The outer layer contained mainly Fe with some Mn and the inner layer Fe, Mn, Cr and Ni. The Fe content in the outer oxide layer slightly increased as the test temperature increased. At 1100°C the Fe content is 71.0 wt% and at 1200 and 1300°C around 74 wt%. The thickness of the whole oxide layer also increased when the test temperature increased. At 1100°C, the average thickness measured from the SEM cross sections varied between 200 and 450 µm, and at 1300°C from 520 to 1050 µm.

At the highest temperature, Cr diffused from the inner layer to the outer layer, as shown in the SEM-EDS maps in Fig. 113. The chemical content of Cr and Fe in the SA1 (Cr 0.2 wt% and Fe 74.0 wt%) and SA2 (Cr 2.2 wt% and Fe 71.7 wt%) are shown in Fig. 114.

#### 4.4. RESULTS: KIT

KIT performed the high temperature steam oxidation tests with four available candidate ATF cladding materials at the three predefined conditions. More details about the results for the high temperature tests performed at KIT in the framework of the ACTOF CRP is given in the individual KIT report “Round Robin High Temperature Oxidation Tests at KIT” (see Annex).

##### 4.4.1. PVD Cr Coated Zry-2

The macroscopic post test appearance of the chromium coated Zry-2 specimens after the oxidation tests is given in Fig. 115. A change of colour, induced by oxidation, was observed for all temperatures. Localized spallation of the Cr coating was presented at 1100°C, only at the side which contacts with the sample holder. The adherence of the Cr coatings was improved at 1200 and 1300°C compared to oxidation at 1100°C, likely arising from substantial interaction between coating and substrate at a higher temperature.

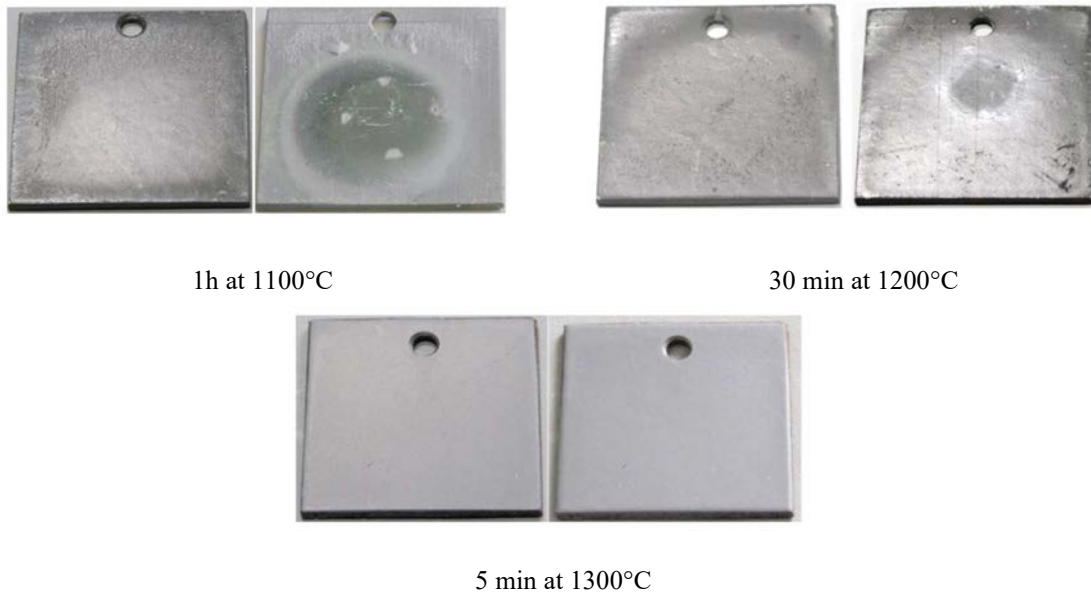


FIG. 115. Post test appearance of the Cr coated Zry-2 sample after the oxidation tests.

The sample mass gain and the hydrogen release during the oxidation tests are low for the chromium coated Zry-2 samples as shown in Fig. 116. The ratio between sample mass gain and the mass of released molecular hydrogen is 8.04 (Molar mass of atomic oxygen divided by the molar mass of molecular hydrogen) if only processes resulting in mass gain and no process reducing the mass occur. Therefore, the hydrogen mass is multiplied by a factor of 8. At 1100°C less mass gain was measured after the test than expected from the hydrogen release. The sample mass loss was caused by the local spallation of the coating mentioned before. The differences between hydrogen mass and sample mass gain are small for the other two test temperatures and can be attributed to the uncertainty in the hydrogen measurement.

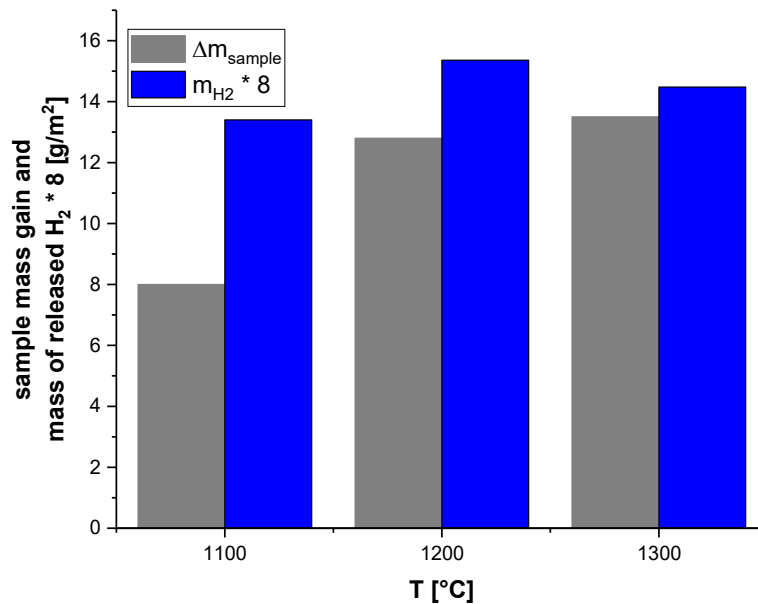


FIG. 116. Comparison of sample mass gain and mass of hydrogen released (multiplied by 8) for the chromium coated Zry-2 samples.

The oxide formed at the coated surface at 1100°C is dense and uniform except some spallation and cracking. In addition, some needle shaped grains existed on the surface layer as shown in Fig. 117. The oxidation of the Cr coating led to the formation of a 5.5  $\mu\text{m}$  Cr<sub>2</sub>O<sub>3</sub> scale on top of the remaining 22  $\mu\text{m}$  Cr layer. The actual Cr coating

thickness was close to 25  $\mu\text{m}$  before oxidation. The underneath Zry-2 substrate was not oxidized, except for the detached areas.

A large number of needle shaped grains (whiskers) existed on the surface after oxidation at 1200°C, accompanied by a smooth layer beneath. The EDX analysis found that both are  $\text{Cr}_2\text{O}_3$  grains. The growth of such needle shaped grains generally originates from the fast outward diffusion of chromium ions via grain boundaries or lattice defects [9]. It is necessary to point out that the smooth layer contains considerably fine pores. The  $\text{Cr}_2\text{O}_3$  oxide scale after 30 min oxidation at this temperature is around 7.3  $\mu\text{m}$  thick. No oxidation of the Zry-2 substrate was found, but an inter-diffusion layer was observed after.

The oxidation rate of the Cr coating was much higher at 1300°C for 5 minutes, and the  $\text{Cr}_2\text{O}_3$  layer reached 8  $\mu\text{m}$ . The higher oxidation temperature facilitates the inward diffusion of Cr from the coatings into the substrate.

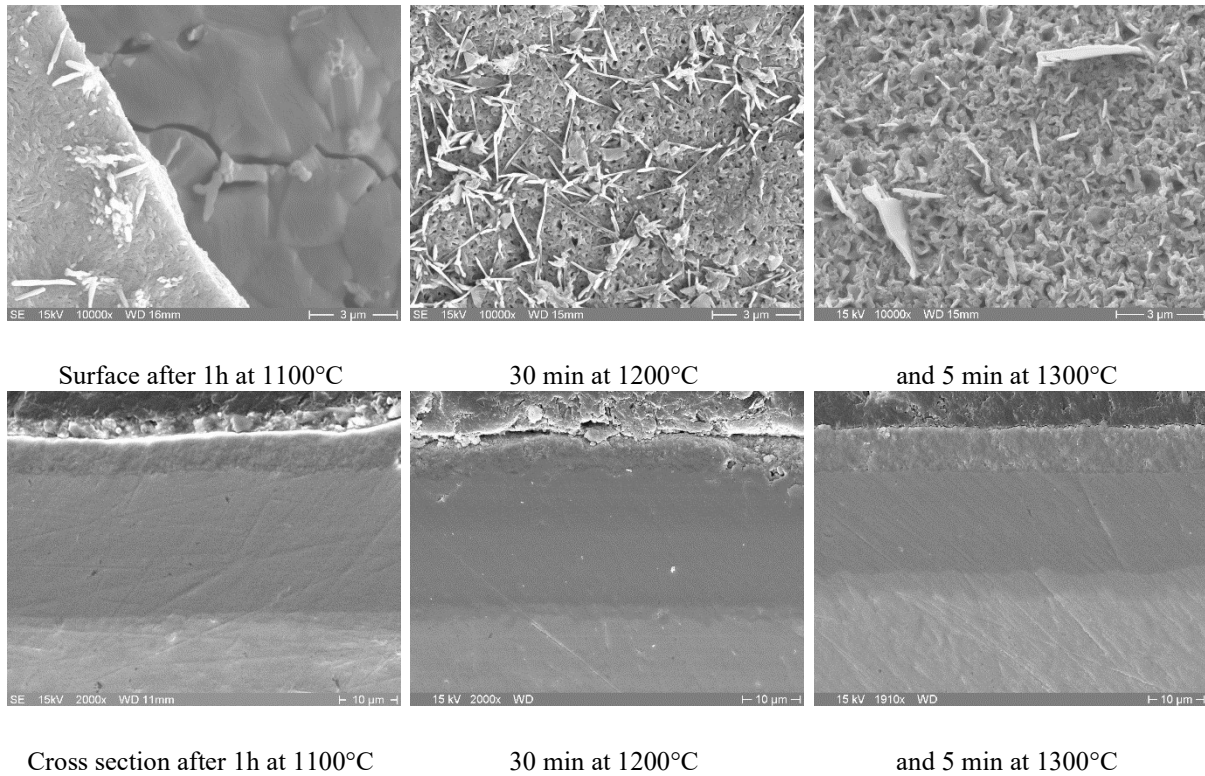


FIG. 117. The SEM images of the surfaces and the cross sections of the chromium coated Zry-2 samples.

#### 4.4.2. PVD MAX Phase Coated Zry-4

The macroscopic Post test appearance of the tested MAX phase coated Zry-4 samples is shown in Fig. 118. Significant delamination of the coating was observed and was found to originate from the sample edges. The best adherence was found for the 1300°C test. The sample mass gain and masses of released hydrogen are plotted in Fig. 119. It is shown that the high tendency of delamination the higher the sample mass gain and the hydrogen release. The mass of release hydrogen multiplied by 8 is always slightly higher than the sample mass gain, which can be attributed to the formation of the volatile carbon oxides which slightly reduces the sample mass during oxidation. The mass gain and hydrogen release are higher at all conditions than for the chromium coated Zry-2 by a factor of 7–20.

The SEM images of typical surface and cross section morphologies after the oxidation tests are shown in Fig. 120. The remaining oxide layer has a compact structure. The oxidation of uncovered edges led to cracking parallel to the substrate/coating interface as well as delamination and spallation of the coatings. In other areas, the coating is adherent and protective, and the oxide scale has a compact structure.



1h at 1100°C

30 min at 1200°C

5 min at 1300°C

FIG. 118. Post test appearance of the  $\text{Cr}_2\text{AlC}$  MAX phase coated Zry-4 sample after the oxidation tests.

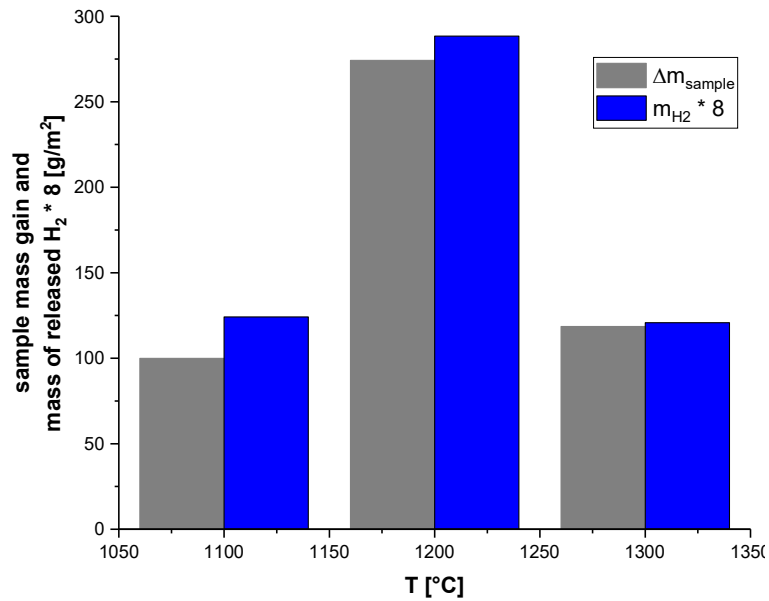


FIG. 119. Comparison of sample mass gain and mass of hydrogen released (multiplied by 8) for the chromium coated Zry-2 samples.

Significant oxidation of the substrate was observed at positions where the coatings were delaminated. In contrast, there was no oxidation of the substrate if the coating is intact. The oxidation of the  $\text{Cr}_2\text{AlC}$  generated an alumina layer beneath the surface  $\text{Cr}_2\text{O}_3$  layer, which hinders the quick consumption of the coatings.

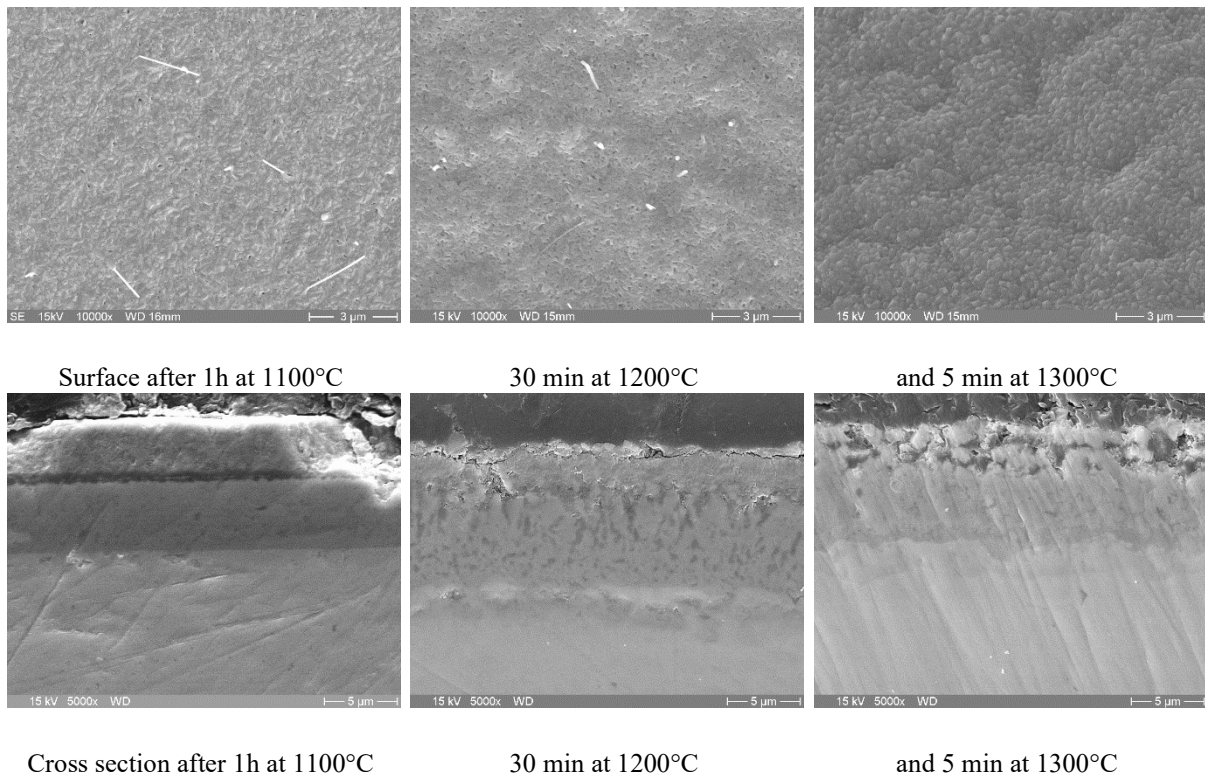


FIG. 120. The SEM images of the surfaces and the cross sections of the chromium coated Zry-2 samples.

#### 4.4.3. PVD ZrSi-Cr Coated Zry-2

The ZrSi-Cr coatings had a shiny colour without any spallation. The discoloration seen for the 1100 and 1200°C exposed samples because the surface was in contact with the sample holder.

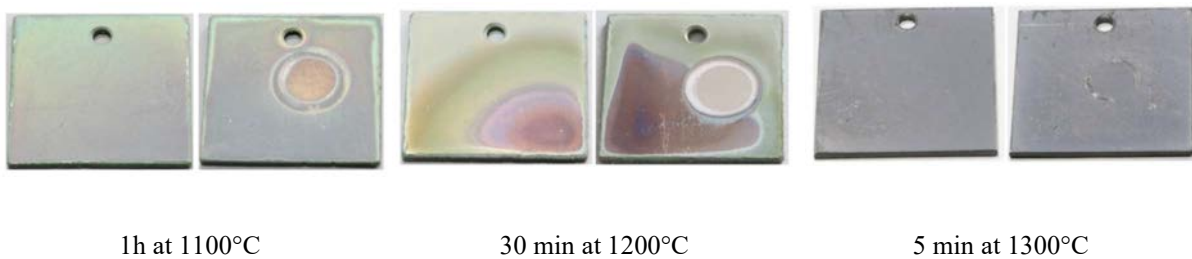


FIG. 121. Post test appearance of the ZrSi-Cr coated Zry-2 samples after the oxidation tests.

The mass change is shown in Fig. 122 and significant mass loss was observed. The ZrSi-Cr coatings were fully oxidized at all temperature investigated, but no spallation occurs. However, the oxidized coatings cannot serve as a diffusion barrier for steam. An even  $ZrO_2$  layer of 73 μm thick, grew under the coating. The oxide scale formed on the ZrSi-Cr coated Zry-2 is mainly made of monoclinic  $ZrO_2$ , probably with some inclusion of  $Cr_2O_3$  and low crystallinity (or amorphous)  $SiO_2$ . However, the surface is covered by isolated round-shaped grains after oxidation at 1100°C and 1200°C. At 1300°C the oxide grains are not round shape anymore, but more angular. Voids and pores were observed.

A nearly pure  $ZrO_2$  layer grew on the surface as shown in Fig. 123. A Si-rich layer was observed beneath the  $ZrO_2$  and Zr(O) layer. The absence of Si and Cr elements in the oxide scale is likely due to the volatilization and inward diffusion of these two elements.

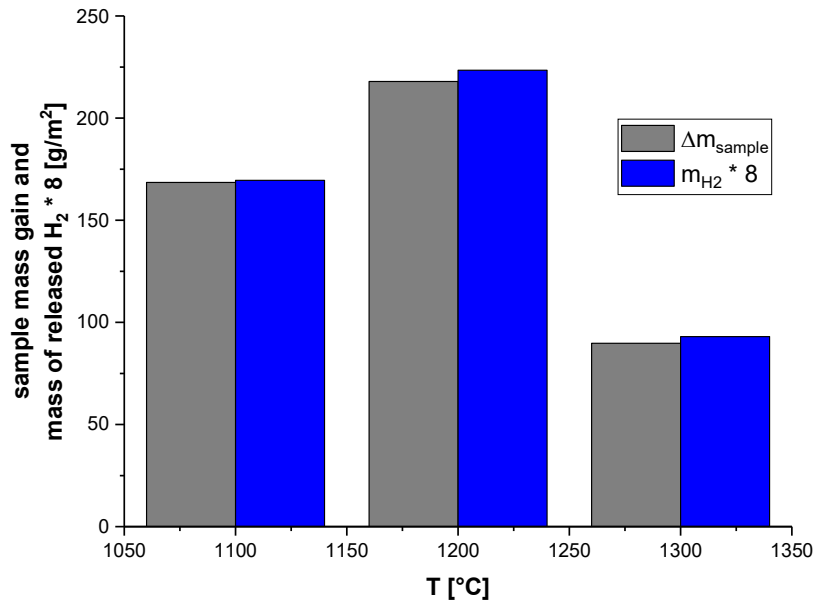


FIG. 122. Comparison of sample mass gain and mass of hydrogen released (multiplied by 8) for the ZrSi-Cr coated Zry-2 samples.

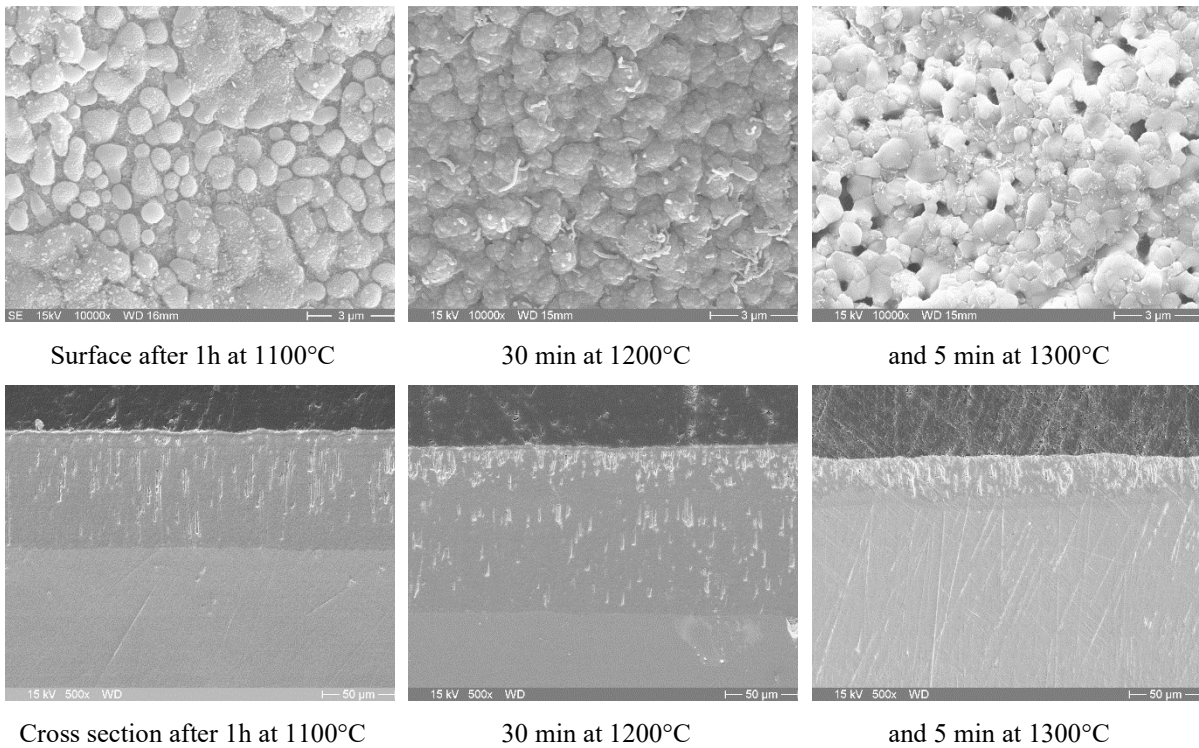


FIG. 123. The SEM images of the surfaces and the cross sections of the ZrSi-Cr coated Zry-2 samples.

#### 4.4.4. AISI 348 SS

The oxide scale formed on the surface of the AISI 348 samples at 1100°C exhibited a low adherence, with substantial spallation as shown in Fig. 124. The delaminated oxide layer parts indicated that the oxide scale was appreciably thick. At both higher temperatures, no strong oxide spallation was detected.

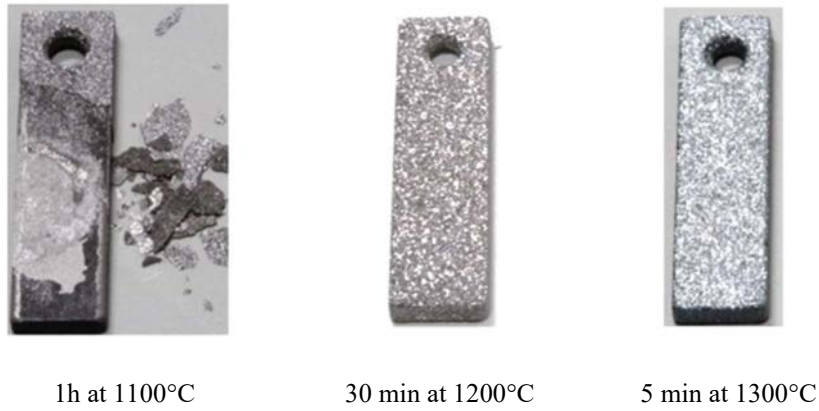


FIG. 124. Post test appearance of the AISI 348 samples after the oxidation tests.

The oxidation of steel AISI 348 resulted in the growth of an oxide scale with two sublayers as seen in Fig. 125. The outer layer was loosely adherent  $\text{Fe}_3\text{O}_4$  layer and the inner layer was relatively dense  $\text{FeCr}_2\text{O}_4$  layer.

The sample mass gain was high, compared with the other material systems investigated. The comparison between sample mass gain and mass of released hydrogen gives suggests that spallation of oxide occurred.

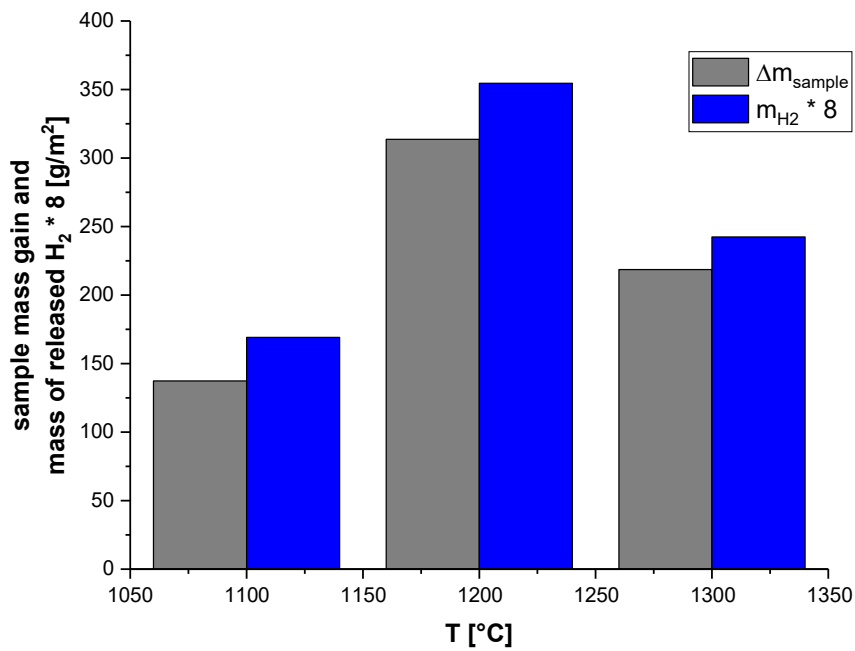


FIG. 125. Comparison of the sample mass gain and the mass of hydrogen released (multiplied by 8) for the AISI 348 samples.

The surface oxide developed a convoluted morphology, featured by angular grains on the austenitic steel AISI 348 at 1100°C and 1300°C. At 1300°C, the oxidation of steel AISI 348 formed a double layered, thick oxide scale, as shown in Fig. 126. However, the outer layer changed to  $\text{Fe}_2\text{O}_3$ , instead of  $\text{Fe}_3\text{O}_4$  as seen at lower temperatures.

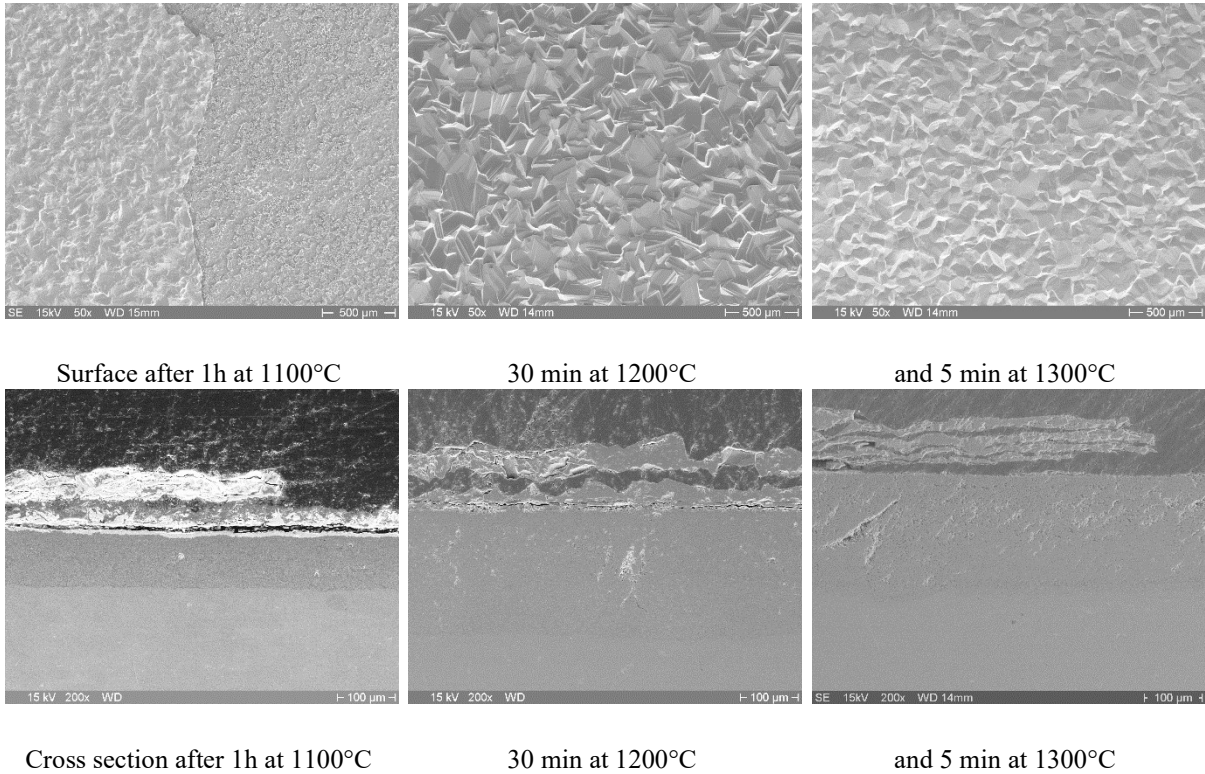


FIG. 126. The SEM images of the surfaces and the cross sections of the AISI 348 samples.

#### 4.5. RESULTS: MTA EK

MTA EK joined the RRT activity in 2018 as a cooperating organization and received PVD Cr coated Zr1%Nb samples shown in Fig. 127 from CTU/UJP for oxidation testing at 1100 and 1200°C. Beyond high temperature oxidation, ring compression tests were carried out.



FIG. 127. Cr coated (top) and reference Zr (bottom) specimens.

##### 4.5.1. Steam oxidation: PVD Cr coated Zr1%Nb

The steam oxidation experiments were successfully completed, with the test conditions and results shown in Table 38. The thickness of the chromium oxide was calculated based on the mass gain measured during the test and the surface area.

$$L = \frac{\Delta m \cdot 2M_{Cr} \cdot 10000}{\rho_{Cr} \cdot A \cdot 1.5M_{O_2}} \quad (49)$$

where:

- $L$  thickness of the chromium oxide layer ( $\mu\text{m}$ );
- $\Delta m$  mass gain of the sample (g);
- $M_{Cr}$  molar mass of chromium = 52.0 (g/mol);

$\rho_{Cr}$  density of chromium = 7.15 (g/cm<sup>3</sup>);  
 $A$  surface area of the sample (cm<sup>2</sup>);  
 $M_{O_2}$  molar mass of oxygen = 32.0 (g/mol).

TABLE 38. HIGH TEMPERATURE OXIDATION TEST RESULTS AND CONDITIONS

| Sample  | Type      | Atm.  | Ox. temp. (°C) | Ox. time (s) | Initial mass (g) | Mass gain (g) | A (cm <sup>2</sup> ) | $\Delta m/A$ (g/m <sup>2</sup> ) | L (mm) | D (mm) | L ( $\mu$ m) |
|---------|-----------|-------|----------------|--------------|------------------|---------------|----------------------|----------------------------------|--------|--------|--------------|
| IAEA-01 | Cr coated | air   | 1200           | 3600         | 10.31819         | 0.07356       | 18.29                | 40.2                             | 57.0   | 9.17   | 12.2         |
| IAEA-02 | Zr ref.   | steam | 1100           | 3600         | 11.02454         | 0.35719       | 18.64                | 191.6                            | 58.9   | 9.12   | —            |
| IAEA-03 | Cr coated | steam | 1100           | 3600         | 9.96257          | 0.01582       | 17.96                | 8.8                              | 56.0   | 9.17   | 2.7          |
| IAEA-04 | Cr coated | steam | 1100           | 10800        | 10.26797         | 0.02497       | 18.25                | 13.7                             | 57.0   | 9.15   | 4.1          |
| IAEA-05 | Zr ref.   | steam | 1200           | 1800         | 10.98722         | 0.43748       | 18.75                | 233.3                            | 58.9   | 9.14   | —            |
| IAEA-06 | Cr coated | steam | 1200           | 1800         | 10.34523         | 0.02312       | 18.29                | 12.6                             | 57.0   | 9.17   | 3.8          |
| IAEA-07 | Cr coated | steam | 1200           | 2700         | 9.83425          | 0.02837       | 17.88                | 15.9                             | 55.8   | 9.15   | 4.8          |
| IAEA-08 | Cr coated | steam | 1200           | 3600         | 10.37083         | 0.03443       | 18.33                | 18.8                             | 57.1   | 9.18   | 5.7          |

Cr coating remains after the oxidation tests. Taking the sample, IAEA-01 as an example, the remaining Cr layer was about 19  $\mu$ m thick with  $\sim$ 5  $\mu$ m thickness reduction.

The mass gain of Cr coated samples was very low compared to the reference Zr samples oxidised under similar conditions. The mass gain for Zr samples was 0.3–0.4 g, while the Cr coated samples showed only 0.01–0.04 g increase in the steam atmosphere.

Photographs were taken from the specimens before and after the oxidation tests. The photos of the as-received (reference and Cr-coated) samples before oxidation are shown in Fig. 128.

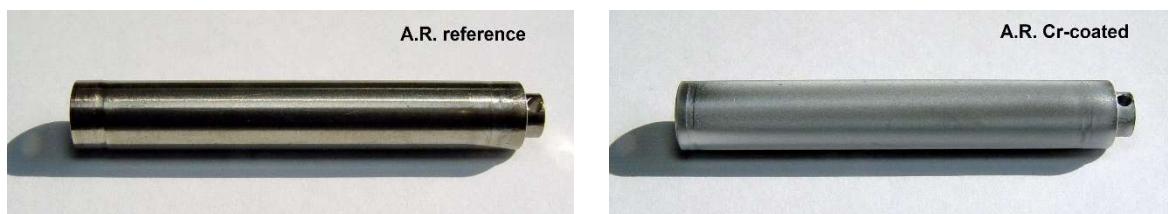


FIG. 128. As-received Zr reference (left) and coated (right) samples before oxidation.

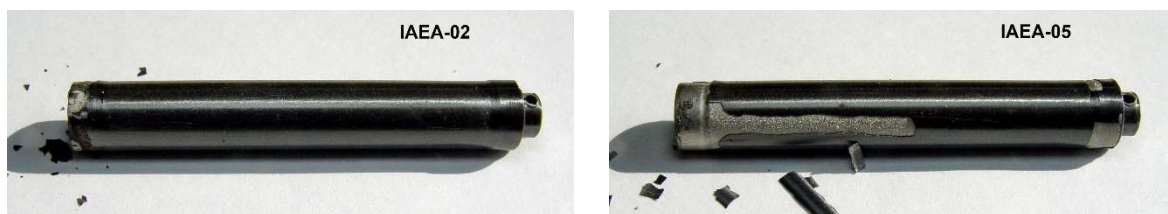


FIG. 129. Zr reference samples after steam oxidation at 1100°C (left) and 1200°C (right).

Figure 129 shows the reference samples after steam oxidation at 1100 and 1200 °C. Oxides spallation was observed in the vicinity of welds probably during the water quench. The Cr-coated specimens after the high temperature steam oxidation are shown in Fig. 130. with a compact dark oxide layer grown on the surface.

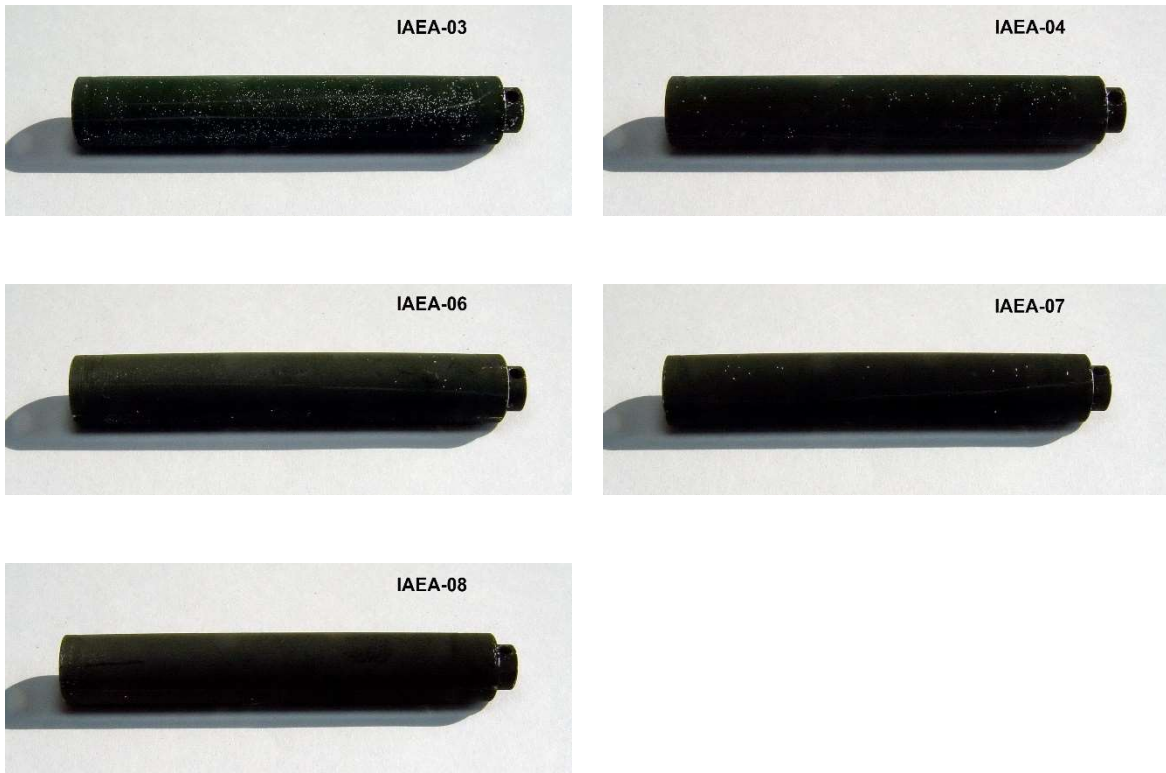


FIG. 130. Cr-coated specimens after the steam oxidation.

#### 4.5.2. Air oxidation test for PVD Cr coated Zr1%Nb

In the air atmosphere the mass gain of the Cr coated sample was higher (IAEA-01: 0.07 g) than that of steam oxidised samples at the same temperature and for the same time (IAEA-08: 0.03 g), shown in Table 38.

The mass gain per unit of the surface was  $\Delta m/A=40 \text{ g/m}^2$ . The surface of the samples became dark as shown in Fig. 131, but not as dark as after oxidation in steam as shown in Fig. 130. Zirconium sample under similar conditions given in Fig. 132. shows about ten times higher increase ( $491 \text{ g/m}^2$ ).

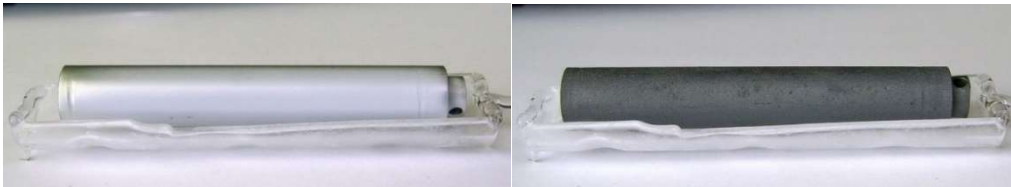


FIG. 131. The Cr-coated IAEA-01 specimen in the quartz boat before (left) and after oxidation (right) in the air at  $1200^\circ\text{C}$  for 3600 s.



FIG. 132. Zr sample before (left) and after (right) oxidation in air at  $1200^\circ\text{C}$  for 2700 s with the normalized mass gain  $\Delta m/A=491 \text{ g/m}^2$ .

The close view of the Cr coated tube surface showed (Fig. 133 and Fig. 134) that after oxidation in the air a non-uniform structure was developed.

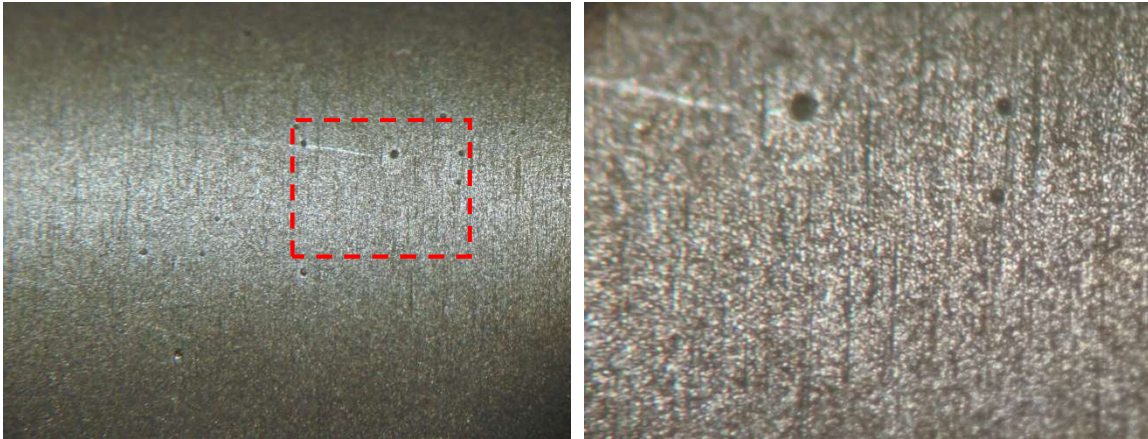


FIG. 133. Surface of the Cr-coated sample in as-received conditions.

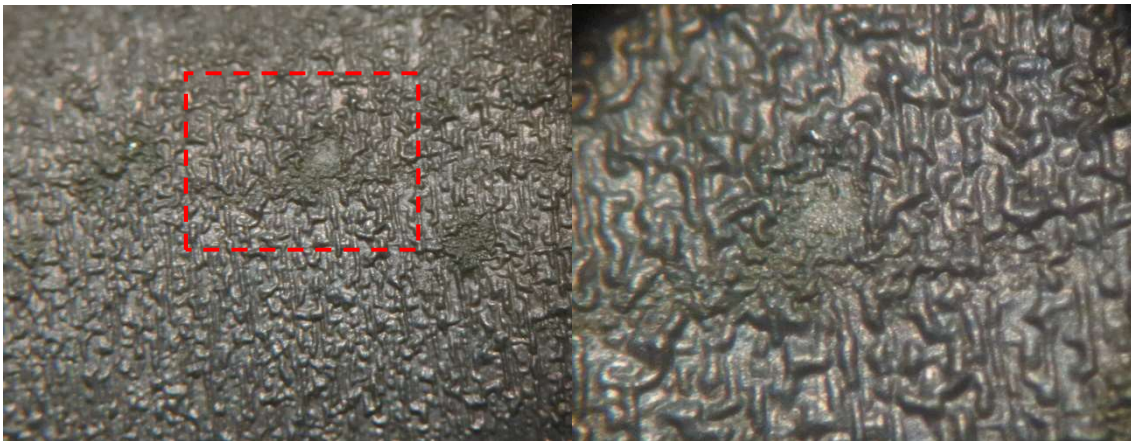


FIG. 134. Surface of the Cr-coated sample IAEA-01 after oxidation in the air (1200°C, 3600 s).

#### 4.5.3. Ring compression test

The results of the ring compression tests showed significant differences between the reference Zr1Nb cladding and the Cr coated tubes.

The Cr coated IAEA-03 sample oxidised at 1100°C for 3600 s showed a ductile behaviour. The ductile plateau continued after the plastic deformation for a long displacement. The Zr reference sample IAEA-02 reached 450 N maximum load. After that less and less load was enough to cause further deformation, but no clear breakdown was observed for this sample as shown in Fig. 135.

The oxidation at 1200°C for 1800 s resulted in brittle Zr IAEA-05 sample with a maximum force  $\approx 300$  N. The large breakdown at 1.5 mm displacement indicated brittle fracture of the specimen. The Cr coated IAEA-06 rings could withstand loads above 500 N and remained ductile (Fig. 136).

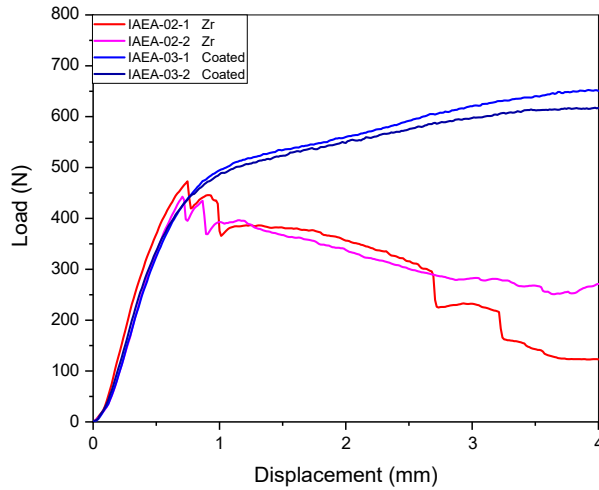


FIG. 135. Load-displacement curves of ring compression tests with Zr and coated samples after oxidation at 1100°C for 3600 s.

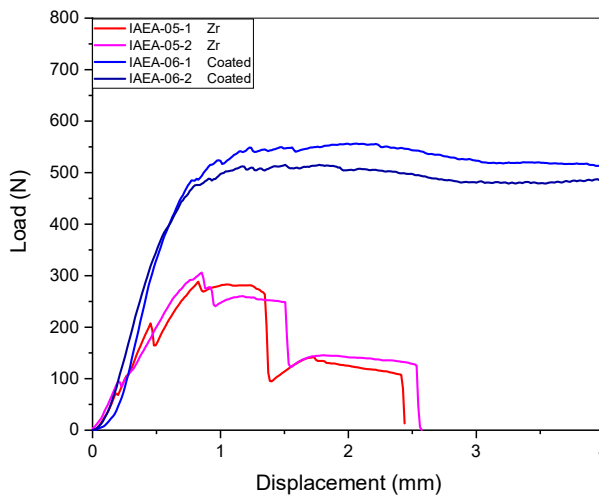


FIG. 136. Load-displacement curves of ring compression tests with Zr and coated samples after oxidation at 1200°C for 1800 s.

Long oxidation exposure did not lead to significant changes in the mechanical behaviour of the Cr coated samples. The load-displacement curves for the rings from samples IAEA-03 and IAEA-04 oxidized at 1100°C were close to each other in spite of the big difference in oxidation times (3600 s and 10800 s). The load-displacement curves of Cr coated samples IAEA-06, IAEA-07 and IAEA-08 oxidised at 1200°C for 1800 s, 2700 s and 3600 s, respectively, showed similar trends in Fig. 137. and Fig. 138.

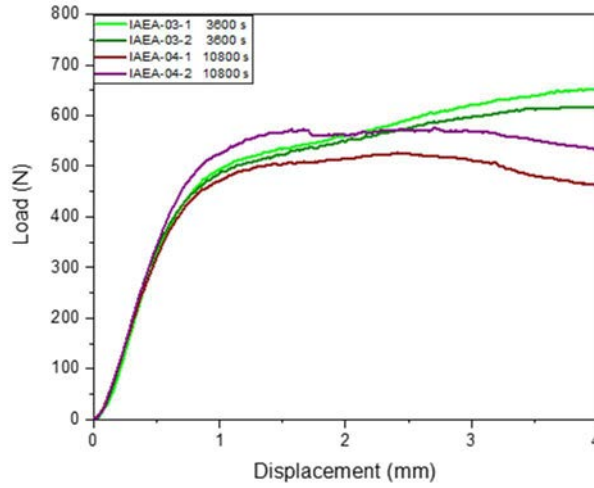


FIG. 137. Load-displacement curves of ring compression tests with coated samples after oxidation at 1100°C for 3600 s and 10800 s.

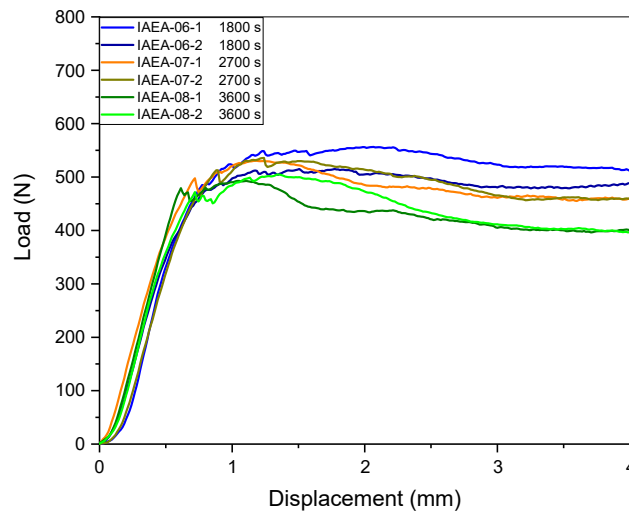


FIG. 138. Load-displacement curves of ring compression tests with coated samples after oxidation at 1200°C for 1800 s, 2700 s and 3600 s.

The mass changes for the samples oxidized in steam and air were significantly different. However, the mass gain did seem to influence significantly the load-bearing capabilities of the samples. The recorded curves were close to each other for these samples as shown in Fig. 139.

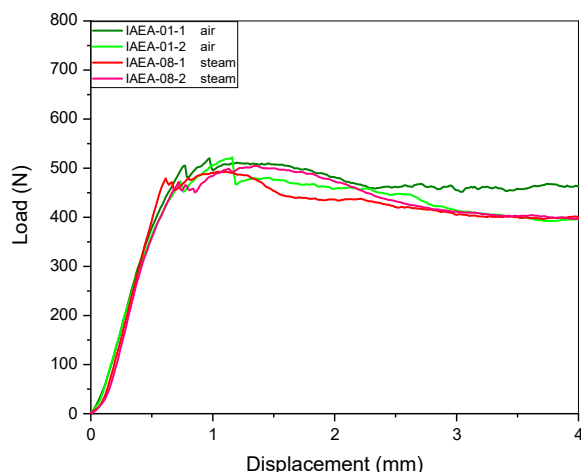


FIG. 139. Load-displacement curves of the ring compression tests with coated samples after oxidation at 1200°C for 3600 s in steam and air.

The geometrical parameters of the ring samples were measured before the mechanical tests (Table 39).

TABLE 39. GEOMETRICAL DATA OF RING SAMPLES

| Ring sample | Diameter (mm)  |                |                |      | Length (mm)    |                |                |      | Thickness (mm) |                |                |      |
|-------------|----------------|----------------|----------------|------|----------------|----------------|----------------|------|----------------|----------------|----------------|------|
|             | d <sub>1</sub> | d <sub>2</sub> | d <sub>3</sub> | d    | l <sub>1</sub> | l <sub>2</sub> | l <sub>3</sub> | l    | v <sub>1</sub> | v <sub>2</sub> | v <sub>3</sub> | v    |
| IAEA-01-1   | 9.16           | 9.18           | 9.20           | 9.18 | 7.98           | 8.01           | 8.00           | 8.00 | 0.72           | 0.73           | 0.72           | 0.72 |
| IAEA-01-2   | 9.23           | 9.18           | 9.30           | 9.24 | 7.82           | 7.75           | 7.83           | 7.80 | 0.74           | 0.70           | 0.73           | 0.72 |
| IAEA-02-1   | 9.10           | 9.15           | 9.09           | 9.11 | 8.25           | 8.26           | 8.19           | 8.23 | 0.64           | 0.63           | 0.62           | 0.63 |
| IAEA-02-2   | 9.15           | 9.21           | 9.14           | 9.17 | 8.20           | 8.14           | 8.18           | 8.17 | 0.62           | 0.64           | 0.62           | 0.63 |
| IAEA-03-1   | 9.12           | 9.13           | 9.16           | 9.14 | 7.68           | 7.72           | 7.67           | 7.69 | 0.64           | 0.62           | 0.64           | 0.63 |
| IAEA-03-2   | 9.15           | 9.16           | 9.19           | 9.17 | 8.00           | 8.10           | 7.92           | 8.01 | 0.72           | 0.73           | 0.65           | 0.70 |
| IAEA-04-1   | 9.10           | 9.18           | 9.12           | 9.13 | 7.40           | 7.39           | 7.38           | 7.39 | 0.60           | 0.63           | 0.70           | 0.64 |
| IAEA-04-2   | 9.17           | 9.14           | 9.19           | 9.17 | 8.13           | 8.15           | 8.17           | 8.15 | 0.66           | 0.70           | 0.64           | 0.67 |
| IAEA-05-1   | 9.08           | 9.14           | 9.21           | 9.14 | 7.13           | 7.14           | 7.06           | 7.11 | 0.64           | 0.54           | 0.66           | 0.61 |
| IAEA-05-2   | 9.07           | 9.12           | 9.26           | 9.15 | 7.30           | 7.32           | 7.28           | 7.30 | 0.63           | 0.64           | 0.64           | 0.64 |
| IAEA-06-1   | 9.20           | 9.16           | 9.13           | 9.16 | 8.15           | 8.13           | 8.15           | 8.14 | 0.64           | 0.65           | 0.66           | 0.65 |
| IAEA-06-2   | 9.18           | 9.15           | 9.17           | 9.17 | 7.90           | 7.90           | 7.90           | 7.90 | 0.64           | 0.67           | 0.64           | 0.65 |
| IAEA-07-1   | 9.17           | 9.18           | 9.13           | 9.16 | 8.19           | 8.19           | 8.16           | 8.18 | 0.62           | 0.64           | 0.66           | 0.64 |
| IAEA-07-2   | 9.15           | 9.21           | 9.18           | 9.18 | 8.21           | 8.23           | 8.20           | 8.21 | 0.64           | 0.62           | 0.68           | 0.65 |
| IAEA-08-1   | 9.16           | 9.18           | 9.24           | 9.19 | 8.13           | 8.09           | 8.12           | 8.11 | 0.63           | 0.60           | 0.62           | 0.62 |
| IAEA-08-2   | 9.12           | 9.15           | 9.19           | 9.15 | 7.79           | 7.79           | 7.78           | 7.79 | 0.60           | 0.63           | 0.64           | 0.62 |

The maximum force, the specific energy at failure and the maximum displacement values were listed in Table 40. The maximum loads for the Cr coated rings – with the exception of one sample – reached 500 N and higher values. The maximum forces for uncoated Zr samples were lower. The specific energy at failure with values below 50 mJ/mm [96] indicated brittle behaviour only for the Zr sample IAEA-05.

TABLE 40. CHARACTERISTIC DATA OF RING COMPRESSION TESTS

| Ring sample | Max. force [N] | Specific energy at failure [mJ/mm] | Temperature [°C] | Max. displacement [mm] |
|-------------|----------------|------------------------------------|------------------|------------------------|
| IAEA-01-1   | 575.0          | 298.8                              | 135              | 5.21                   |
| IAEA-01-2   | 522.6          | 225.7                              | 135              | 4.31                   |
| IAEA-02-1   | 473.0          | 139.6                              | 135              | 4.11                   |
| IAEA-02-2   | 442.9          | 171.7                              | 135              | 4.67                   |
| IAEA-03-1   | 652.5          | 440.5                              | 135              | 6.08                   |
| IAEA-03-2   | 959.8          | 476.1                              | 135              | 6.60                   |
| IAEA-04-1   | 526.8          | 341.5                              | 135              | 5.67                   |
| IAEA-04-2   | 575.4          | 317.4                              | 135              | 5.00                   |
| IAEA-05-1   | 288.5          | 38.3                               | 135              | 5.19                   |
| IAEA-05-2   | 306.1          | 42.8                               | 135              | 1.51                   |
| IAEA-06-1   | 575.1          | 364.3                              | 135              | 6.05                   |
| IAEA-06-2   | 636.2          | 357.8                              | 135              | 6.01                   |
| IAEA-07-1   | 678.1          | 339.6                              | 135              | 5.81                   |
| IAEA-07-2   | 535.8          | 325.7                              | 135              | 5.93                   |
| IAEA-08-1   | 492.8          | 230.2                              | 135              | 4.67                   |
| IAEA-08-2   | 504.9          | 240.6                              | 135              | 4.56                   |

#### 4.5.4. SEM investigations

The studied sample was labelled as IAEA-08, oxidized at 1200°C in a steam atmosphere. The oxidation period was 3600 s. It was examined both in as received state and after grinding and polishing. The elemental composition and the distribution of the most interesting elements were investigated with an Oxford energy dispersive X-ray microanalyser (EDX) with a silicon drift detector. This type of EDX can be used with high beam current appropriate for microanalysis of various solid samples. 5 and 30 kV accelerating voltages were applied. Mostly backscattered electron images (BEI) were taken on the outer oxide layer and on the neighbouring metal of the sample. 5 kV was used for line scans of chromium, oxygen and zirconium along the various regions of the sample. Line profiles were recorded from about 30 µm distance from the edge of the coated cladding sample.

Figure 140 shows a typical SEI image from the outer oxide layer and the neighbouring metal of the as-received sample. The BEI image for the polished surface is shown on the right.

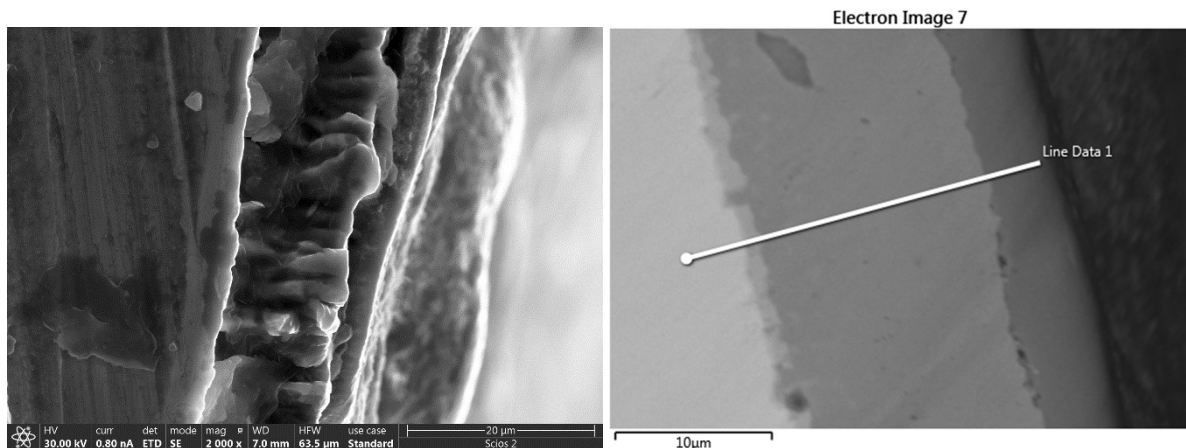


FIG. 140. SEI and BEI images of IAEA-08 cladding sample taken at 2000x (left) and 3500x (right).

On the left-hand side part of the SEI image the surface of the Zr1%Nb ring sample can be seen, which has remnants of the cutting process during sample preparation. At the edge of the sample two layers can be distinguished:

- a chromium layer, consisting of columnar crystallites, with a thickness between 12 and 16  $\mu\text{m}$ ;
- a rather smooth layer of chromium oxide with thickness varying between 2.1 and about 5  $\mu\text{m}$ , which is in good agreement with the data estimated on the basis of mass gain measurements (Table 38).

For the BEI image shown at the right hand side of Fig. 140, besides the above mentioned two layers, a third layer between the zirconium and the chromium layer was found. The thickness of this layer is about 1  $\mu\text{m}$ .

Figure 141 shows a BEI image of the coated cladding sample, where areas of EDX analysis are presented. The results of the EDX are summarized in Table 41. Area No. 11 is probably a grain with impurities as C, Na, S and Cl.

TABLE 41. EDX RESULTS FOR SAMPLE IAEA-08

| Spectrum No./quantity (mass %) | C     | O     | Na   | S    | Cl   | Cr    | Zr    |
|--------------------------------|-------|-------|------|------|------|-------|-------|
| 9                              | 2.62  | 34.14 | —    | —    | —    | 63.17 | 0.07  |
| 10                             | 1.73  | 0.69  | —    | —    | —    | 97.58 | —     |
| 11                             | 22.86 | 3.24  | 0.65 | 0.97 | 0.26 | 67.95 | 4.06  |
| 12                             | 3.03  | 0.31  | —    | —    | —    | 50.51 | 46.15 |
| 13                             | 4.23  | —     | —    | —    | —    | 2.81  | 92.96 |

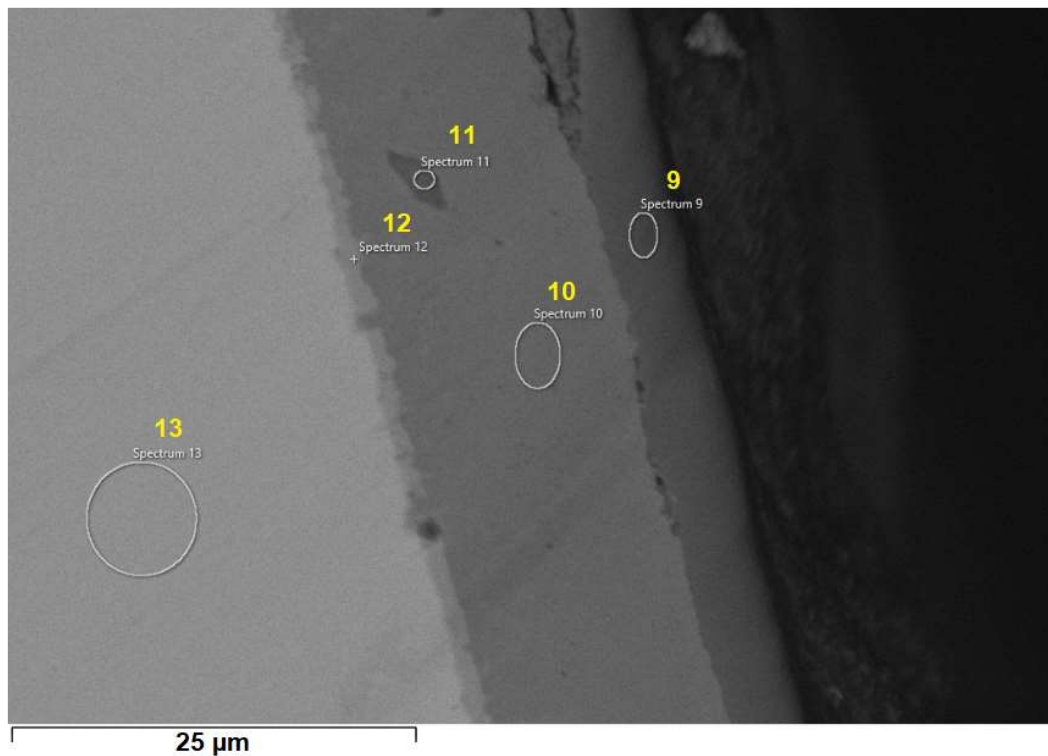


FIG. 141. The BEI image together with the EDX spectra taken from the selected areas for sample No. IAEA-08.

In the intermediary layer between the chromium and the zirconium there is almost the same amount of chromium and zirconium. In the zirconium metal at the analyzed area a small amount of chromium was recorded. As impurity carbon was present in a small amount. A larger amount of carbon and small amounts of sodium, sulphur and chlorine were found in area No. 11.

Figure 142 contains another BEI image and the line profiles of the most interesting elements, taken along a selected line on the sample.

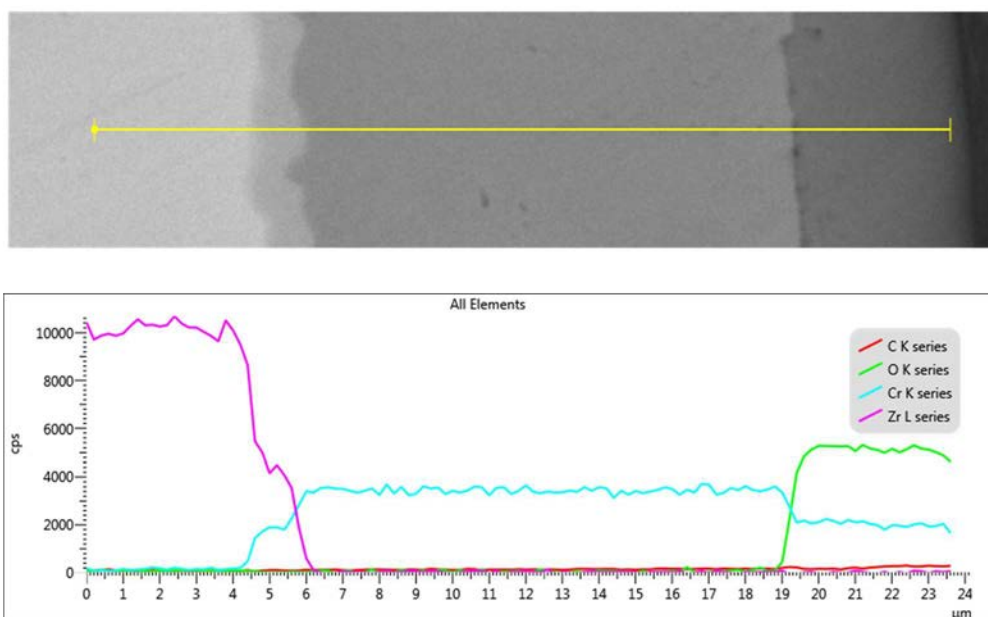


FIG. 142. BEI image with a line of the line scan for some important elements present in sample IAEA-08.

It can be seen that in the very thin ( $\approx 2 \mu\text{m}$ ) intermediary layer between the zirconium and the chromium, the amounts of these two important elements are about the half of that in the pure zirconium metal and the chromium layer. The same was shown in Table 41 for the analyzed area No. 12. The oxygen line profile is increased at the boundary between the chromium and the chromium oxide layers. Small amounts of carbon are detected in the chromium oxide layer.

#### 4.5.5. Metallography and Microhardness

The structure and the hardness measurements of a Cr coated and a Zr reference sample was carried out using optical microscopy. The oxidation conditions were the same. Two samples were selected for metallography analyses and microhardness measurements:

- IAEA-05 (Zr reference,  $1200^\circ\text{C}$  oxidation in steam for 1800 s) — Fig. 143;
- IAEA-06 (Cr coated,  $1200^\circ\text{C}$  oxidation in steam for 1800 s) — Fig. 144.

The metallographic examinations were carried out with an OLYMPUS GX53F type inverted optical microscope. The microhardness measurements were performed using the Vickers hardness test method. A pyramid type diamond indenter with an angle of  $136^\circ$  between opposite faces was used with 20 g load. The indentation left on the surface of the samples was evaluated according to the ASTM E384-17 standard and using a Reichert Me-F2 type optical microscope.

The end plug parts of the original samples were used in these examinations. The samples were embedded in epoxy and the cross sections were ground and polished.

The Zr sample IAEA-05 showed the classical structure [97] of oxidized sponge based Zr1%Nb cladding. A  $110 \mu\text{m}$  thick oxide scale was developed at the surface and appeared to be dense as shown in Fig. 143. The oxygen-rich  $\alpha$ -layer under the oxide was not uniform and can be characterized by large incursions into the  $\beta$ -phase. The average thickness of the  $\alpha$ -phase was about  $200 \mu\text{m}$ . The inner part of the cladding showed the prior  $\beta$ -phase structure, but the  $\alpha$ -incursions were long and, in some positions, reached the inner surface of the tube. The long  $\alpha$ -incursions (which are typical at an oxidation temperature of  $1200^\circ\text{C}$ ) may facilitate fracture development through the cladding wall.

On the external surface of Cr coated Zr sample IAEA-06 only a few  $\mu\text{m}$  thick chromium-oxide was formed during the oxidation. A significant part ( $15\text{-}20 \mu\text{m}$ ) of the original Cr coating remained. The Zr cladding under the Cr coating suffered only minor changes. A light layer about  $100 \mu\text{m}$  from the surface was observed, and the remaining part of the Zr metal had a darker colour.

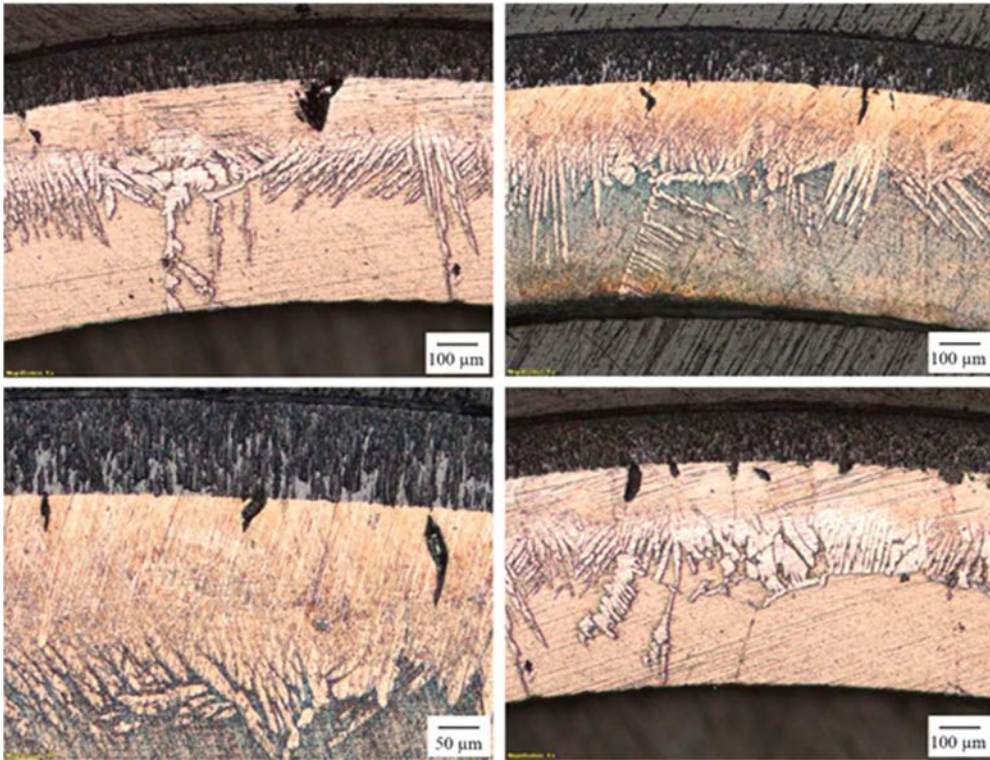


FIG. 143. Metallography images of sample IAEA-05 (Zr1Nb).



FIG. 144. Metallography images of sample IAEA-06 (PVD Cr coated Zr1Nb).

Microhardness measurements were taken in several radial positions of the metallic part of the sample. The zero points at the horizontal axes shown in Fig. 145. and Fig. 146. correspond to the oxide-metal interface in case of the Zr sample IAEA-05 and to the Cr-Zr interface for the Cr coated IAEA-06.

The measured points indicated that the local hardness changed significantly from the periphery to the inner surface of sample IAEA-05 as shown in Fig. 145. The  $\alpha$ -layer in the cladding had very high hardness values (between 400 and 900) with a decreasing trend in the radial direction. In the  $\beta$ -layer, the hardness was below 300.

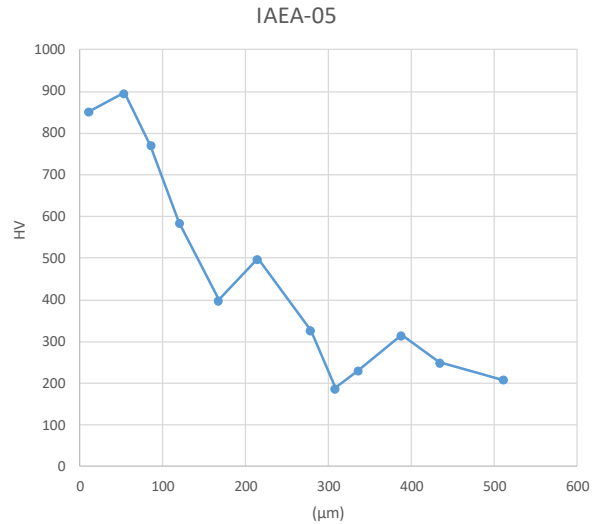


FIG. 145. Microhardness of the metallic part of sample IAEA-05.

In the case of IAEA-06 sample, the hardness for the outer 100 μm layer was around 350–400. The hardness in the rest part of the cladding tube was between 170 and 240 as shown in Fig. 146. This explains the high residual ductility of the sample with a slight increase in the hardness near the coating probably due to inter diffusion.

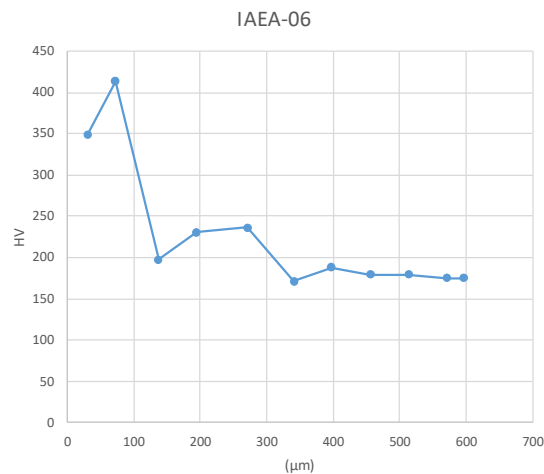


FIG. 146. Microhardness of the metallic part of sample IAEA-06.

#### 4.6. DISCUSSION

Four different laboratories performed high temperature oxidation tests at the predefined conditions with four ATF cladding candidate samples.

In summary, the oxidation the AISI 348 bulk material is highly dependent on steam. At 1100°C, the thickness varied from 200 μm to 450 μm and at 1300°C from 520 μm to 1050 μm. Fe increase and Cr decreases in the inner layer and Fe increases (slightly) also in the outer oxide layer with increasing temperature. There is very little Cr in the outer layer regardless of the temperature (overall a typical double layer oxide structure). An elevated Mn content was observed in the outer layer compared to the inner layer. Overall, a typical fuel cladding with ~0.5 mm

wall thickness made of AISI 348 would be breached quickly at this temperature range. As a result, the base material AISI 348 may not provide sufficient accident tolerance as expected.

The thickness of coating and the oxide layers in the Cr coated Zry-4 CTU specimens is also dependent on steam temperature. At 1100°C the thickness was about 10 µm, at 1200°C about 15 µm and at 1300°C the thickness ranged from 40 to 400 µm. The coating of the specimens after exposures at 1100°C and 1200°C was continuous. However, cracks between the coating and the oxide layer were found. The specimen exposed at 1200°C also had cracks through the oxide layer. The coating of specimen exposed at 1300°C was also continuous, but the coating and the substrate partly came loose during the Post test sample preparation. The thickness of the coating and the oxide layer together ranged from 40 to 400 µm, i.e. at 1300°C the oxidation progresses quickly. In 1100°C and 1200°C specimens, Fe enrichment was observed on the outer oxide layer as well as in the thin Cr/Zr-rich zone between Zr substrate and oxide layer.

In general, very high oxidation rates were observed for PVD MAX phase coated Zry-4 steam specimens. It appears the coating was protective, but oxidation progressed quickly from the peripheral areas.

MTA EK and CTU have done series of experiments with chromium PVD coated Zr1Nb cladding tubes. The procedure included oxidation in steam and air with oxidation times between half an hour and three hours. The change in mechanical properties of the oxidized materials was investigated by ring compression tests. Optical and scanning electron microscopy and microhardness measurements were applied to characterize the structural changes in the tube specimens.

The comparison of Cr coated Zr tubes with the non-coated Zr specimens proved that the coated samples could withstand the high temperature steam conditions without severe degradation. Only small oxide scale was formed on the Cr coating and the tube samples remained ductile.

SEM and DES studies suggest that the chromium layer on the Zr cladding was only slightly oxidized at 1200°C in steam during one hour. A very thin ( $\leq 10$  µm) intermediary layer with zirconium and chromium content was found at the interface. The thickness of the chromium layer was found to be 12–15 µm, and the chromium oxide layer was about 5–6 µm. Therefore, only the outer part of the chromium coating was oxidized after the steam oxidation tests.

The AISI 348 SS show higher hydrogen production than the reference uncoated Zr-based alloys shown in Fig. 147.

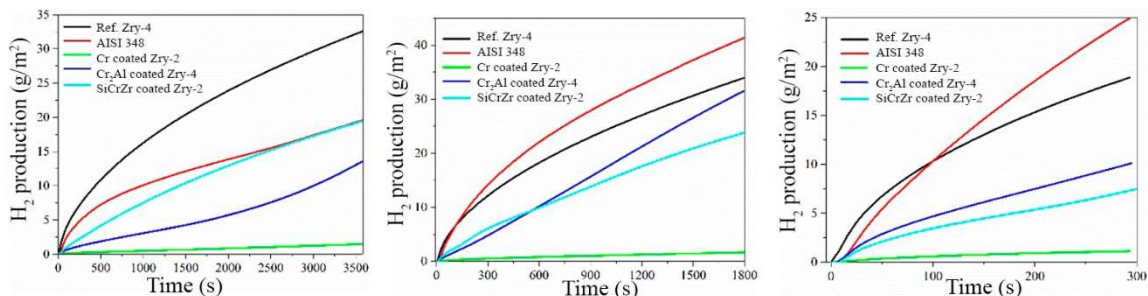


FIG. 147. Integral hydrogen production for 1100 °C, 60min; 1200°C, 30min and 1300°C, 5min steam oxidation tests.

The Cr coating showed superior oxidation resistance and it fully protected zirconium substrate from oxidation up to 1300°C. Accelerates oxidation and fast degradation of the cladding occurred when the temperature reached the eutectic point 1320–1330°C. It was also shown that some of the current criteria (e.g. DBT) are not directly applicable to coated materials and the hydrogen pickup fraction remains questionable. Overall it shows the best oxidation resistance for both uniform corrosion and high temperature steam oxidation. ZrSi-Cr and MAX phase coated Zr alloys showed limited benefits in accidental conditions. The benefits of the coating are clear especially at lower oxidation temperature (1100°C) but at higher temperatures the behaviour is comparable to uncoated reference material. Further optimization may be needed.

## 5. MODELLING BENCHMARK FOR FeCrAl CLADDING

### 5.1. INTRODUCTION

During the Second Research Coordination Meeting of the CRP ACTOF in June 2017 [98], a modelling benchmark was proposed as a collaborative activity for the participants. In particular, it was agreed that the interested organizations would perform fuel performance calculations with their respective fuel performance codes on a set of fuel rod problems with iron chromium aluminium (FeCrAl) steel as cladding material. The aim of the work was to perform an initial, meaningful investigation of FeCrAl cladding performance and to compare results from different fuel performance codes. This effort would ultimately bring about important indications about the performance of FeCrAl claddings, the current capabilities of nuclear fuel performance codes in modelling FeCrAl, and the important areas of future research.

For the purpose of a modelling benchmark among different fuel performance codes, it is desirable to agree upon one specific alloy in the first place, and to apply a consistent set of material models and properties in the codes in order to obtain meaningful comparisons. FeCrAl alloys for application as nuclear fuel cladding material are currently under development and characterization. Material property data are still limited and mostly from out-of-pile tests. Hence, it is important to select a fairly well characterized alloy with a sufficiently complete set of models and properties available. Specifically, for this work, the laboratory optimized alloy C35M developed recently at Oak Ridge National Laboratory (ORNL) [99–103] has been considered. This alloy (or similar) is a leading contender to be included in a lead test rod or assembly in a commercial reactor in 2022 as irradiation testing has been performed in the Halden Reactor [103] and is underway in the Advanced Test Reactor (ATR) at INL [104]. Based on the experimental data from tests performed at ORNL and at the Halden Reactor, researchers at ORNL and INL have developed empirical models for C35M thermo mechanical properties and behaviour [99],[100],[102],[103],[105]. These include models for thermophysical properties as a function of temperature, thermal and irradiation creep, volumetric swelling and oxidation. Moreover, a FeCrAl burst failure criterion for loss-of-coolant accident conditions has been developed [105].

As a result of this work, a sufficiently complete set of material models and properties for fuel performance calculations with FeCrAl-C35M has been constructed, and the detailed information has been made available to the participants for implementation in the codes, along with detailed standard specifications for the benchmark cases, by INL in October 2017 [106]. The FeCrAl material models and properties used in the benchmark are described in Section 2.1 of this report. The benchmark cases consisted of idealized problems with FeCrAl cladding covering both normal operating reactor conditions and loss-of-coolant accidental conditions.

The concept of the modelling benchmark is along the lines of previous international benchmark exercises (such as the CRPs FUMEX and FUMAC of the IAEA), but with an ATF candidate material being targeted for the simulations. The selected cases are realistic, in order to allow for a meaningful assessment of FeCrAl performance, but simple, as is necessary for initial simulations with a new material and in order to facilitate consistency between the analyses from different participants. This has been a first time fuel modelling benchmark exercise for ATF and will potentially pave the way for future coordinated research activities in this area.

A total of 5 organizations participated in the ACTOF modelling benchmark for FeCrAl, i.e. INL (BISON code), NINE (TRANSURANUS), JAEA (FEMAXI-7), University of São Paulo (FRAPCON) and CNEA (BACO). Note that in the cases of TRANSURANUS and FRAPCON, calculations for the present benchmark exercise were performed by external users and not by the official developers of the code. Also, versions of these codes used in the present benchmark were modified by the user organizations and differ from the official ones. Hence, results from these codes are to be considered as representative of the users' work only and are not necessarily recognized by the official developer organizations of TRANSURANUS and FRAPCON.

In this Chapter, we give an account of the FeCrAl modelling benchmark in ACTOF. The structure of the chapter is as follows. In Section 5.2, the specifications for the benchmark cases are summarized. In Section 5.3, we provide descriptions of the fuel performance codes applied in the benchmark. In Sections 5.4 and 5.5, we present and discuss the results of the benchmark calculations for normal operating and loss-of-coolant conditions, respectively. Conclusions from the work are drawn in Section 5.6.

## 5.2. SPECIFICATIONS FOR THE BENCHMARK CALCULATIONS

INL provided detailed standard specifications for the benchmark cases to the other ACTOF participating organizations [106]. Proposed cases are relatively simple and include a short PWR fuel rod irradiated under idealized normal operating conditions and cladding only cases for loss-of-coolant accident (LOCA) conditions. Specifications are reported below.

### 5.2.1. Normal operating conditions cases

The proposed benchmark case for LWR normal operating conditions is a simple, idealized test case of a short (10-pellet) rod with typical PWR specifications irradiated under steady state conditions. This case was designed for the purpose of analyzing FeCrAl cladding behaviour during irradiation under normal operating conditions, and to perform a comparison with the analogous problem with Zry-4 cladding instead. UO<sub>2</sub> fuel is considered in either case.

The assumed geometry includes a UO<sub>2</sub> fuel stack of 118.6 mm height, FeCrAl (or Zry-4) cladding, an initial 80 µm pellet cladding radial gap, and plena. To enable comparisons between the two systems (UO<sub>2</sub>/Zry-4 and UO<sub>2</sub>/FeCrAl) the initial rodlet diameter (cladding outer diameter) and fuel-to-cladding gap are the same. The cladding thickness varies depending upon the cladding material used. For the FeCrAl case the cladding is thinner to accommodate the neutronic penalty introduced by the increased neutron absorption cross section. This allows for slightly larger pellets to give the same cold gap width in the rod. The cladding thicknesses for both Zry-4 and FeCrAl were obtained from [101]. FeCrAl cladding thickness is based on the neutronic analysis from [107]. The specifications of both rodlets are summarized in Table 42.

The linear heat rate history consists of a linear ramp from 0 to 25 kW/m over 3 hours, a hold at constant power for about 4 years (precisely, 35037 hours, which makes it 4 years from startup), and a final power shutdown over 3 hours (Fig. 148). Hence, the power variations (startup and shutdown) are considered to occur at a power ramp rate of about 0.14 kW/m-min. A flat axial profile is assumed. The same power history is used for either the FeCrAl and Zry-4 cases. In reality, rod power will be different for FeCrAl clad rods relative to Zr-based claddings, due to the increased fuel loading and enrichment necessary to overcome the neutronic penalty. Nevertheless, the comparisons obtained using a simplified power history can provide valuable insight into the response of FeCrAl clad rods. Note that a 25 kW/m power level is relatively high compared to typical average operating power for PWR rods, and a 4-year irradiation is relatively long. These choices were made to analyze cladding behaviour including the effect of prolonged Pellet-Cladding-Material-Interaction (PCMI) driven by fuel thermal expansion and gaseous swelling. The power and time chosen for this case correspond to a rod average burnup reached at the end of irradiation of ~67 GWd/tU for the Zry-4 case (lower pellet radius) and ~61 GWd/tU for the FeCrAl case.

TABLE 42. SPECIFICATIONS OF THE BENCHMARK CASE FOR NORMAL OPERATING CONDITIONS.

|                              | UO <sub>2</sub> /Zry-4 Rodlet | UO <sub>2</sub> /FeCrAl Rodlet |
|------------------------------|-------------------------------|--------------------------------|
| Fuel stack length (mm)       | 118.6                         | 118.6                          |
| Pellet outer diameter (mm)   | 8.19                          | 8.57                           |
| Pellet inner diameter (mm)   | 0                             | 0                              |
| Chamfer, dishes              | no                            | No                             |
| Radial gap width (µm)        | 80                            | 80                             |
| Cladding inner diameter (mm) | 8.35                          | 8.73                           |
| Cladding thickness (mm)      | 0.575                         | 0.385                          |
| Cladding outer diameter (mm) | 9.5                           | 9.5                            |
| Upper plenum height (mm)     | 26                            | 26                             |

TABLE 42. SPECIFICATIONS OF THE BENCHMARK CASE FOR NORMAL OPERATING CONDITIONS (cont.).

|   | UO <sub>2</sub> /Zry-4 Rodlet | UO <sub>2</sub> /FeCrAl Rodlet |
|---|-------------------------------|--------------------------------|
| Lower plenum height (mm)                      | 1                             | 1                              |
| Total free volume (cm <sup>3</sup> )          | 1.725                         | 1.874                          |
| Initial fill gas pressure (MPa)               | 2                             | 2                              |
| Initial fill gas                              | He                            | He                             |
| Initial fuel density (%TD)                    | 95                            | 95                             |
| Initial fuel enrichment (%)                   | 5                             | 5                              |
| Initial fuel grain radius (μm)                | 5                             | 5                              |
| Coolant inlet mass flux (kg/m <sup>2</sup> s) | 3800                          | 3800                           |
| Coolant inlet temperature (K)                 | 580                           | 580                            |
| Coolant pressure (MPa)                        | 15.5                          | 15.5                           |

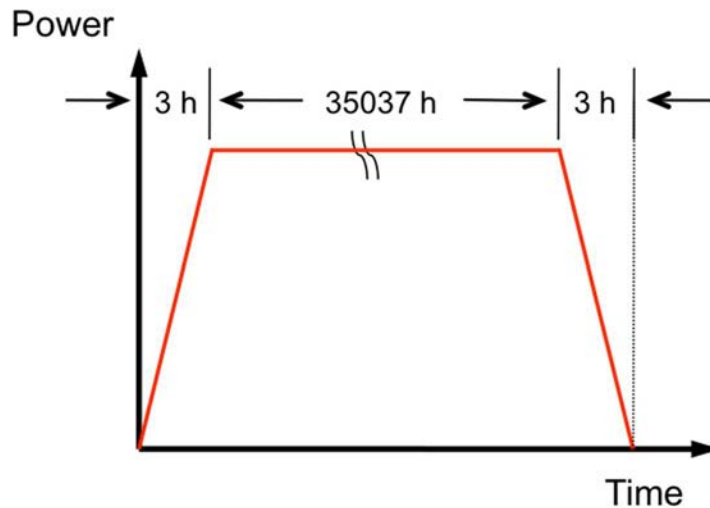


FIG. 148. Schematic of power history for the normal operation benchmark case. Steady-state linear power level is 25 kW/m.

### 5.2.2. Loss of coolant conditions cases

For FeCrAl cladding behaviour calculations under LOCA conditions, the specifications of the separate-effects experimental tests PUZRY from AEKI [108] were considered. These are cladding-only ballooning and burst tests performed on Zry-4 tubes under well-defined conditions. In these experiments, tube samples were investigated in a resistance furnace providing isothermal conditions in the temperature range of 700–1200 C. The inner pressure of the test tube was increased linearly until the burst of the sample. The specimens were 50 mm long. The specimen was placed in a quartz test tube filled with inert argon gas and heated up in an electrical furnace. The gas pressure in the quartz tube was kept constant at 0.1 MPa. After an approximately 1000 s heat-up period, the sample was pressurized with argon gas at a constant pressurization rate. Pressurization rates between  $7 \times 10^{-4}$  and  $2.6 \times 10^{-2}$  MPa/s were tested.

The actual PUZRY experiments were performed on Zry-4 tubes with inner/outer diameters of 9.3/10.75 mm, respectively (i.e. 725 μm thickness). For the ACTOF calculations we considered FeCrAl material instead, however, we used the experimental conditions and geometry of the PUZRY tests. The exception is the considered cladding thickness that is lower in order to perform realistic simulations. In particular, the adopted cladding thickness for FeCrAl is 385 μm (same as with the normal operation case, see Section 5.2.1). Cladding tube specifications for the LOCA calculations are summarized in Table 43. Six tests from the PUZRY series were

considered for the benchmark simulations. The choice is based upon the selected cases for the CRP FUMAC [109]. Temperature and pressure conditions for the selected tests are summarized in Table 44.

The reason for the choice of the PUZRY cases is that considering separate-effects, cladding-only tests with well-defined experimental conditions (temperature, pressure histories) avoids complexities associated with integral fuel rod behaviour (thermal and mechanical analyses of fuel and cladding, fuel-cladding interactions). Isolating cladding behaviour is thought to be ideal for testing codes' capabilities and performing a first modelling benchmark for a new material. Integral fuel rod cases can be considered in a future benchmark.

Because the PUZRY experiments were performed in inert gas (Ar) atmosphere, they do not allow for investigating the effect of oxidation. This can be appropriate for this first modelling benchmark because, to the best of our knowledge, models for the high temperature oxidation of FeCrAl-C35M are not yet available. In a future perspective, simulations of loss of coolant conditions considering an oxidizing environment can be carried out.

TABLE 43. ROD SPECIFICATIONS FOR THE BENCHMARK CALCULATIONS FOR LOCA CONDITIONS

|                             |        |
|-----------------------------|--------|
| Tube specimen alloy         | FeCrAl |
| Inner radius (mm)           | 4.65   |
| Thickness ( $\mu\text{m}$ ) | 385    |
| Specimen length (mm)        | 50     |
| End plug length (mm)        | 5      |
| Atmosphere                  | Ar     |
| Outer pressure (MPa)        | 0.1    |

TABLE 44. CONDITIONS OF THE 6 LOCA TESTS SELECTED FOR THE BENCHMARK CALCULATIONS.

| Rod number | Temperature (C) | Pressure ramp rate (MPa/s) |
|------------|-----------------|----------------------------|
| 8          | 1000            | 0.00763                    |
| 10         | 1100            | 0.00710                    |
| 12         | 1200            | 0.00723                    |
| 18         | 900             | 0.01151                    |
| 26         | 700             | 0.01193                    |
| 30         | 800             | 0.02630                    |

### 5.3. DESCRIPTION OF FUEL PERFORMANCE CODES

#### 5.3.1. BISON

The US Department of Energy (DOE) has been developing capabilities to simulate nuclear fuel behaviour within the Nuclear Energy Advanced Modelling and Simulation (NEAMS) and Consortium for Advanced Simulation of Light Water Reactors (CASL) programmes. One of the result is the BISON code [110], a multidimensional, finite element based fuel performance code developed at Idaho National Laboratory (INL).

BISON is built using the INL Multiphysics Object Oriented Simulation Environment, or MOOSE [111]. MOOSE is a massively parallel, finite element based framework developed to solve systems of coupled non linear partial differential equations using the Jacobian-Free Newton Krylov (JFNK) method. BISON allows for 1D, 2D or 3D geometric representations to analyze the global fuel element behaviour including local multidimensional effects. BISON's ability to use massively parallel computing allows for analyzing integral fuel rods in 2D for a detailed irradiation history as well as large 3D problems. BISON has been applied to a variety of fuel forms including LWR fuel rods, TRISO particle fuel, fast oxide fuel, and metallic fuel in both rod and plate geometries. The code is applicable to both steady state and transient conditions and is used for the analysis of fuel behaviour during both operational and design basis accident conditions.

The BISON governing equations consist of fully coupled partial differential equations for energy, species, and momentum conservation. Nonlinear kinematics in BISON follows the approach described in [112]. Material models are included in BISON for  $\text{UO}_2$  fuel to describe temperature and burnup dependent thermal properties, solid and gaseous fission product swelling, densification, cracking, pellet fragment relocation, thermal and irradiation creep [110, 113]. Fission gas swelling and release are calculated using the model described in [114]. For zircaloy cladding, models are available for thermophysical properties, instantaneous plasticity, thermal and irradiation creep, irradiation growth, oxidation, as well as cladding phase transition, ballooning and burst failure during LOCAs. Gap heat transfer is modelled in the traditional manner with the total conductance across the gap computed as a sum of the gas conductance, the increased conductance due to solid solid contact, and the conductance due to radiant heat transfer. Mechanical contact between materials is implemented through the use of node/face constraints [110, 113].

A variety of other material models are available in BISON. These include fuel models for MOX,  $\text{U}_3\text{Si}_2$ , U-Pu-Zr and U-10Mo, and cladding models for HT9, 316 and FeCrAl. The BISON models are described in more detail in the reference [110].

For BISON an extensive set of code verification problems exists, from fundamental finite element solid mechanics and heat transfer tests, to problems specific to nuclear fuel models. In addition to code verification, solution verification (i.e. of the numerical accuracy of the solution) was performed [113].

Validation work for BISON has focused initially on LWR fuel during normal operating conditions and power ramps [115, 116]. In recent years, significant work has also been performed on the analysis of design basis accident scenarios (DBAs), including both LOCA [117, 118] and RIA [119, 120]. For TRISO particle fuel, several benchmark cases have been considered which compare BISON results to those from other fuel performance codes [116, 121].

The extension of the BISON code to the analysis of FeCrAl cladding is described in [105].

### 5.3.2. TRANSURANUS

TRANSURANUS is a computer programme written in FORTRAN95 for the thermal and mechanical analysis of fuel rods in nuclear reactors that is owned by the Joint Research Centre of the European Commission. TRANSURANUS has been used by research centres, nuclear safety authorities, universities and industrial partners (see references [122–134]).

TRANSURANUS is generally referred to as a fuel performance code meaning that it solves the equations for the radial heat transfer, the radial displacement along with the stress distribution in both the fuel and its surrounding cladding, and the release of fission product and its behaviour as a function of time. The equations, in general for fuel performance prediction, embody the following phenomena:

- Thermal performance: heat conduction, radiation and convection;
- Mechanical performance: creeps (radiation and high temperature), densification, thermal expansion, pellet cracking and relocation, solid and gaseous swelling;
- Actinide behaviour: depletion and build-up of main Th, U, Np, Pu, Am and Cm nuclides, impact on the radial power profile;
- Fuel restructuring: Pu and Am redistribution, grain growth (normal and columnar), central void formation;
- Fission products behaviour: creation in the fuel matrix, diffusion to grain boundaries, release to free rod volume after saturation of grain boundaries, athermal release, recoil, formation of High Burnup Structure (HBS, which is depleted and contain porosity).

The heat transfer in the fuel-to-cladding gap is simulated by means of a combination of heat conduction, radiation and convection (URGAP model [135]). Main assumptions and equations for mechanical performance are provided in reference [123].

Main assumptions and equations for actinide concentrations can be found in references [133, 134]. In the TUBRNP model the calculation of the radial power profiles is split into (a) the approximation of the neutron flux through thermal diffusion theory, and (b) the computation of the local concentrations of the relevant actinide isotopes with simplified depletion equations. The most recent extension covers the nuclides  $^{232}\text{Th}$ ,  $^{233-236,238}\text{U}$ ,  $^{237}\text{Np}$ ,  $^{238-242}\text{Pu}$ ,  $^{241}\text{Am}$ ,  $^{243}\text{Am}$ ,  $^{242-245}\text{Cm}$ . More details are given in Reference [136].

The TRANSURANUS code consists of a well defined mechanical and mathematical framework, in which additional physical models can easily be incorporated. The code has a comprehensive material data files for oxide,

mixed oxide, carbide and nitride fuel types, zircaloy and steel claddings and several different coolants (water, sodium, potassium, lead, bismuth). TRANSURANUS can be used as a single code system for simulating both long term irradiations under normal operating conditions as well as transient tests. The 'restart' mode allows simulating re-fabricated (recycled) fuel rods, where the fill gas has been completely changed as an example.

The code can be employed in two different approaches: as a deterministic or a statistical code. Restart may be used to perform a statistical analysis employing the Monte Carlo technique. This option may be helpful for the analysis of a long base irradiation then followed by a transient. Figure 149 gives an overview of these possibilities.

Besides its flexibility for fuel rod design, the TRANSURANUS code can deal with a wide range of different situations, as demonstrated in experiments, under normal, off-normal and accident conditions, although some models specific for RIA (e.g. plenum temperature) are still under development. Furthermore, the code is being used for BWRs, PWRs and WWERs. The time scale of the problems to be treated may range from milliseconds to years. Hence complex irradiation experiments can be simulated including re-fabricated instrumented fuel rods and changing operating conditions.

In the present modelling benchmark TRANSURANUS calculations were performed by NINE. In particular, the TRANSURANUS code version v1m1j15, modified with incorporation of FeCrAl models, was used. The extension of TRANSURANUS to the analysis of FeCrAl cladding is described in the NINE individual contribution to ACTOF (see Annex).

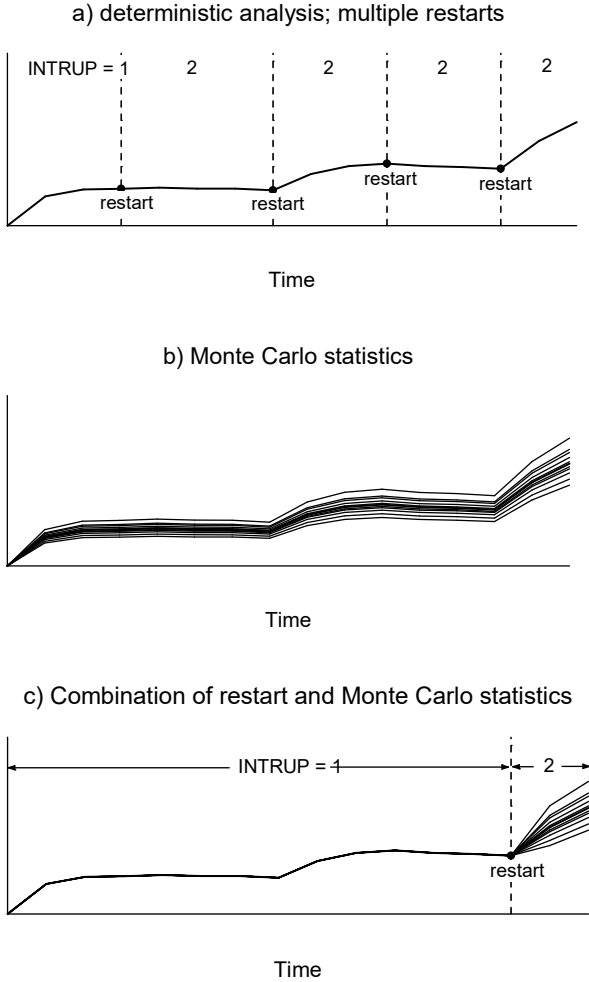


FIG. 149. An illustration of deterministic and probabilistic approaches with restarts.

### 5.3.3. FEMAXI

The original version of FEMAXI was developed in 1970s based on the finite element analysis of local deformations of fuel rods [137]. Since then, numerous improvements have been made such as implementation of creep models and model developments for high burnup fuel behaviour. Features of FEMAXI-7 are briefly described as follows. Details are available in the references [138, 139].

The code analyzes behaviour of a single fuel rod and the adjacent coolant channel based on the single channel model. FEMAXI is based on Finite Element Method in AXI-symmetric system. As described in Fig. 150, a fuel rod is divided into a number of axial segments. Each segment is divided into ring elements for one dimensional heat conduction/transfer and mechanics calculations. The power history is provided as input as a function of time or burnup.

The calculation flow is as follows. Firstly, based on the results of the previous time step, heat generation, conduction, transfer (to the coolant) calculations are carried out to evaluate temperature profile. Secondly, based on the evaluated temperature profile, diffusion and release of fission product (FP) gases are calculated and the rod internal pressure is evaluated. Then, based on the evaluated temperature and pressure, 1D mechanical analyses are carried out and these calculations are iterated to obtain convergence before proceeding to the next time step (The code also has an option to perform local PCMI analysis for a specific fuel segment in R-Z two-dimensional geometry). The models and correlations relevant to modelling the UO<sub>2</sub> pellet behaviour and used in this exercise are summarized in Table 45.

In this exercise, the cladding properties are modelled by following the benchmark specifications for: thermal conductivity, specific heat, Young's modulus, coefficient of thermal expansion, Poisson's ratio, thermal creep, irradiation creep, stress-strain curve (plasticity) with some minor modifications for code implementation. For example, the volumetric swelling of FeCrAl alloy C35M has been implemented by converting volumetric expansion to linear expansion.

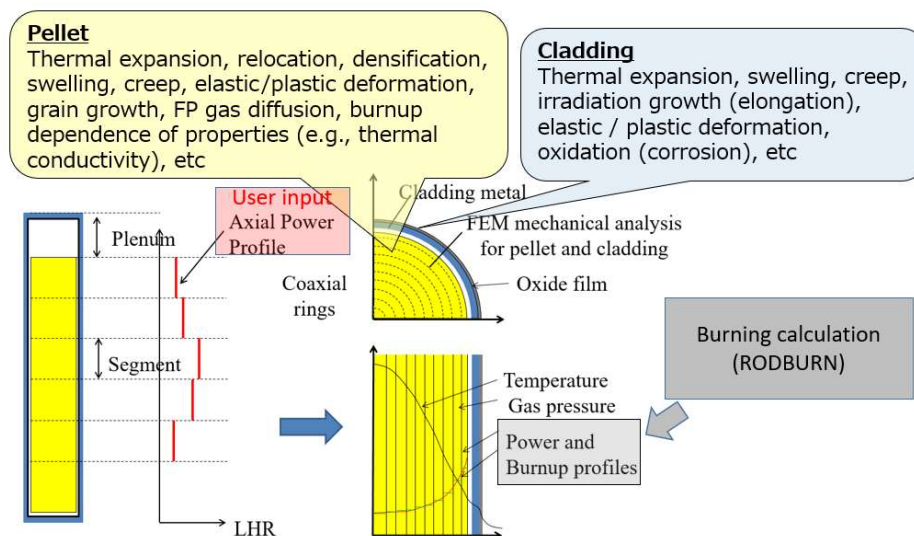


FIG. 150. Overview of FEMAXI-7 analysis meshing and modelled phenomena.

TABLE 45. MODELS AND CORRELATIONS FOR UO<sub>2</sub> PELLETS USED IN BENCHMARK EXERCISE

|                                  | Model  | Reference |
|----------------------------------|--|-----------|
| Thermal conductivity             | Halden   | [140]     |
| Coefficient of thermal expansion | Halden   | [140]     |
| Density                          | MATPRO-09  | [141]     |
| Young's modulus                  | MATPRO-11  | [142]     |
| Poisson's ratio                  | MATPRO-09  | [141]     |
| Emissivity                       | MATPRO-11  | [142]     |
| Creep                            | MATPRO-11  | [142]     |
| Cut off temperature of creep     | 1273 K   | Tentative |
| Swelling                         | FEMAXI   | [138]     |
| Densification                    | FEMAXI-III   | [138]     |
| Max. densification               | 1 %  | Tentative |
| 90% completion of densification  | 5 GWd/tUO <sub>2</sub>   | Tentative |
| Pellet relocation at startup     | 55% of the gap is assumed to be occupied by the relocated pellet fragments | Tentative |
| Plasticity                       | Tachibana  | [143]     |
| Specific heat                    | MATPRO-11  | [142]     |
| Grain growth                     | Itoh   | [144]     |

#### 5.3.4. FRAPCON-USP

FRAPCON developed at Pacific Northwest National Laboratory (PNNL) [145] is an analytical tool that calculates LWR fuel rod behaviour when power and boundary condition changes are sufficiently slow for the term "steady state" to apply. This includes situations such as long periods at constant power and slow power ramps that are typical of normal power reactor operations. The code calculates the variation with time of all significant fuel rod variables, including fuel and cladding temperatures, cladding hoop strain, cladding oxidation, hydriding, fuel irradiation swelling, fuel densification, fission gas release, and rod internal gas pressure. In addition, the code is designed to generate initial conditions for transient fuel rod analysis by FRAPTRAN, the companion transient fuel rod analysis code.

FRAPCON uses fuel, cladding, and gas material properties from MAPTRO that have been recently updated to include burnup dependent properties and properties for advanced zirconium based cladding alloys. Other material properties not included in the updated MATPRO document are fission gas release, cladding corrosion, and cladding hydrogen pickup. Models are described in [145]. The material properties in FRAPCON-3 are contained in modular subroutines that define material properties for temperatures ranging from room temperatures to temperatures above melting and for rod average burnup levels between 0 and 62 gigawatt days per metric ton of uranium (GWd/MTU). Each subroutine defines only a single material property. For example, FRAPCON-3 contains subroutines defining fuel thermal conductivity as a function of fuel temperature, fuel density, and burnup; fuel thermal expansion as a function of fuel temperature; and the cladding stress strain relation as a function of cladding temperature, strain rate, cold work, hydride content, and fast neutron fluence.

#### 5.3.5. BACO

BaCo is a code for the simulation of the thermo mechanical and fission gas behaviour of a cylindrical fuel rod under operation and storage conditions. Modelling the UO<sub>2</sub> pellet includes elastic deformation, thermal

expansion, creep, swelling, densification, restructuring, cracks and fission gas release [146, 147]. For zircaloy cladding, the code models elastic deformation, thermal expansion, anisotropic plastic deformation, creep and growth under irradiation.

Experimental validation was based on a variety of cases from the IAEA CRPs such as D-COM, FUMEX I, II, III and FUMAC, from the NEA-IAEA International Fuel Performance Experiments (IFPE) database, from the OECD Halden Reactor Project database, from the blind tests: BARC PHWR fuel codes comparison [148] and the OECD/NEA benchmark on PCMI [149].

Originally focused on PHWR fuels as the CANDU [150] and Atucha [151] fuels, BaCo's capabilities also extend to PWR, BWR, WWER, MOX, experimental advanced prototypes and unusual fuels. The evolution of the code was historically oriented to the Nuclear Programme led by the Argentine National Atomic Energy Commission (CNEA), namely the fuel of the Integral PWR CAREM [152], PHWR MOX fuels [153] and advanced PHWR fuels (such as the CARA fuel) [154].

The BaCo modelling of UO<sub>2</sub> pellets includes elastic deformation, thermal expansion, creep, swelling, densification, restructuring, relocation, cracks and fission gas release. For zircaloy cladding, the code models elastic deformation, thermal expansion, anisotropic plastic deformation, creep and growth under irradiation. The modular structure of the code easily allows different material properties to be implemented. It can be used for any geometrical dimension of cylindrical fuel rods with UO<sub>2</sub> pellets (either compact or hollow, with or without dishing) and Zry cladding. A special feature of the BaCo code is complete treatment of the fuel with or without mechanical contact between the pellet and the clad, at any irradiation stage.

Fuel rod power history and either cladding or coolant external temperatures must be given to the programme. Rod performance is numerically simulated using finite time steps (finite differences scheme). The code automatically selects time steps according to physical criteria. Temperature profiles within pellet and cladding, main stresses at pellet and cladding, radial and axial crack pattern in the pellet, main strains and hot geometry of pellet and cladding, change in porosity, grain size and restructuring of the pellet, fission gas release to the free volume in the rod, trapped gas distribution in the fuel and in the UO<sub>2</sub> grain boundary, internal gas pressure and current composition of the internal gas and dishing shape evolution, are calculated. The output contains the distribution along the rod axis of these variables. The details of the mechanical and thermal treatment and the pellet, cladding and constitutive equations are available in reference [146] and an extended description of the code is included in reference [147].

BaCo assumes azimuthal bi-dimensional symmetry in cylindrical coordinates for the fuel rod [146]. Although angular coordinates are not considered explicitly, angular dependent phenomena, as well as radial cracking, are simulated through the angular averaging method [155]. Also, axial pellet cracking and relocation are included in BaCo. The hypotheses of axial symmetry and modified plane strains (constant axial strain) are used in the numerical modelling. The fuel rod is separated in axial sections to simulate its axial power profile dependence.

The BaCo code package contains the BaCo3D tools [156], statistical analysis [157], full core calculations [151], graphical data post processing [147] and simulation of storage conditions [158].

#### 5.4. BENCHMARK RESULTS FOR NORMAL OPERATING CONDITIONS

The cases considered for the normal operating conditions simulations are described in Section 5.2.1. A total of five organizations provided results for these benchmark cases:

- INL (USA), BISON code;
- JAEA with Waseda University (Japan), FEMAXI-7 code;
- NINE (Italy), TRANSURANUS code;
- University of São Paulo (Brazil), FRAPCON-USP code;
- CNEA (Argentina), BACO code.

Participants were asked to provide results for the following figures of merit:

- Hoop strain at cladding inner and outer surfaces;
- Hoop stress at cladding inner and outer surfaces;
- Fuel cladding radial gap width;
- Oxide layer thickness;
- Fuel centreline temperature;

- Rod inner pressure;
- Fission gas release.

Note that cladding hoop strain and stress, gap width, oxide thickness and fuel centreline temperature are local values at an axial location corresponding to the mid plane of the fuel stack.

Comparisons of calculation results are presented below: selected results for the calculations considering Zry-4 cladding – in Section 5.4.1, an extensive comparison of results for FeCrAl cladding –in Section 5.4.2.

#### 5.4.1. Reference calculations for Zircaloy-4 cladding

Fuel rod simulations for normal operating conditions case were performed for both cases with FeCrAl and Zry-4 as cladding material. Other than for the cladding material and thicknesses, the two cases are analogous (see Section 5.2.1.). Presentation of the benchmark results is started with the code-to-code comparisons for the Zry-4 case. This is motivated by consideration that modelling of the traditional UO<sub>2</sub>/zircaloy system (i) is generally more consolidated in the fuel performance codes and serves as a reference for comparison to the parallel FeCrAl performance simulation results presented afterwards, and (ii) provides a verification of the consistency of the specified boundary conditions.

Figure 151 illustrates the comparison of calculations from the five fuel performance codes in terms of hoop strain evolution at the outer surface of the cladding. (Note that the FRAPCON results are in terms of average strain across the cladding thickness instead.) Codes predict the outward strain due to thermal expansion during the initial start-up, cladding creep down strain under the outer coolant pressure prior to the onset of PCMI, and outward creep driven by fuel expansion after gap closure (i.e. under PCMI). During the final shut down period, the gap reopens resulting in removal of the fuel cladding contact pressure and a consequent cladding inward strain under the outer coolant pressure. Differences in the results from different codes are expected to be primarily due to the different models applied for Zry-4 cladding creep and the contributions to UO<sub>2</sub> fuel deformation, such as swelling. However, the results appear qualitatively consistent. Results for the hoop strain at the cladding inner surface are similar and are not shown here for brevity.

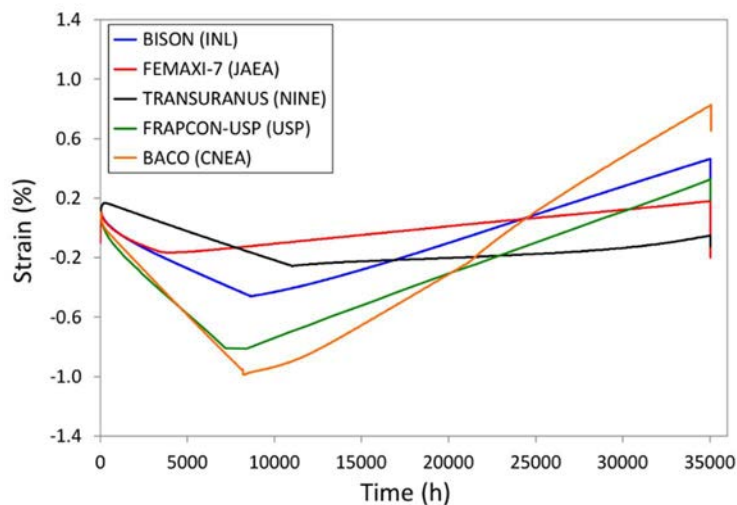


FIG. 151. Comparison of code calculations of hoop strain at the cladding outer surface (axial location corresponding to the mid plane of the fuel stack) for fuel rod with Zircaloy-4 cladding during normal operation.

Figure 152 illustrates the evolution of the calculated radial width of the fuel cladding gap at the fuel stack axial mid plane. Differences between codes are associated with different creep down kinetics (Fig. 151) and models for the other contributions to fuel and cladding deformation. In particular, the initial drop in gap width is associated with fuel thermal expansion and relocation, while the increase in gap width early in life is due to fuel densification. Predicted times of gap closure correspond to the slope changes in the cladding strain curves in Fig. 151, as the cladding begins to deform outwards in consequence of fuel expansion under PCMI conditions.

Figure 153 shows the comparison of results in terms of hoop stress evolution at the outer surface of the cladding. (The FRAPCON results are in terms of average stress across the cladding thickness instead.) The codes all predict the compressive (negative) stress before PCMI is established as the cladding is under compression as a result of the outer coolant pressure. The fuel cladding contact pressure under PCMI results in a reduction of the compressive stresses within the cladding, as is predicted by the codes. Ultimately the stress may turn tensile (positive) because of the pressure exerted by the expanding fuel during PCMI.

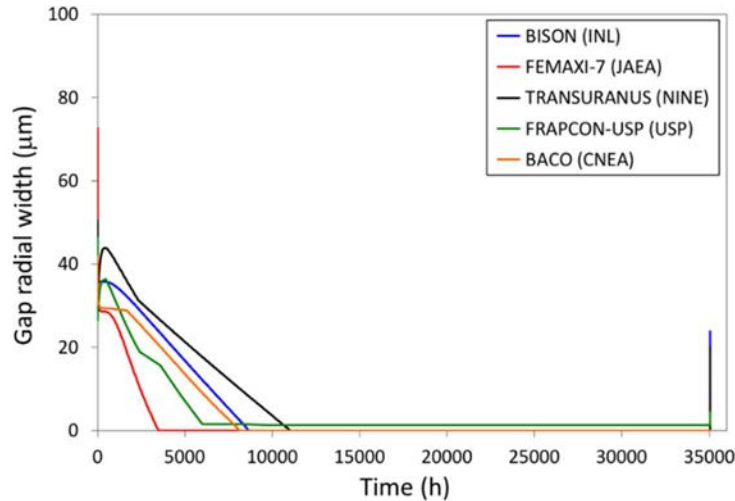


FIG. 152. Comparison of code calculations of gap radial width (axial location corresponding to the mid plane of the fuel stack) for fuel rod with Zircaloy-4 cladding during normal operation.

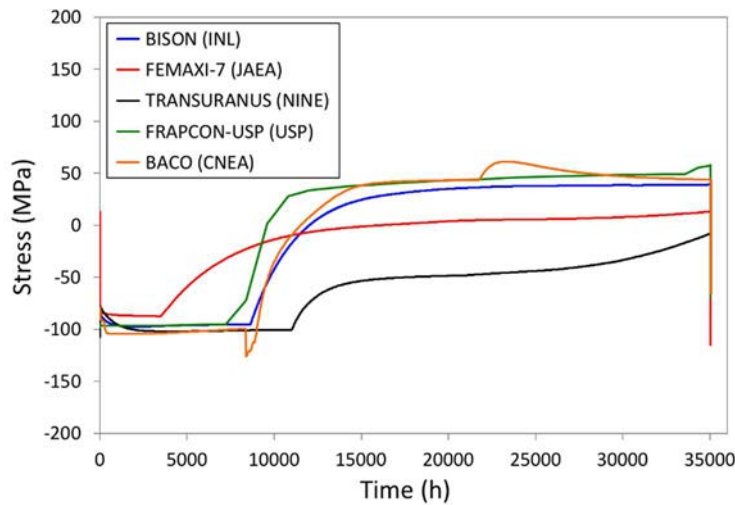


FIG. 153. Comparison of code calculations of hoop stress at the cladding outer surface (axial location corresponding to the mid plane of the fuel stack) for fuel rod with Zircaloy-4 cladding during normal operation.

However, the predicted stresses under PCMI differ significantly among the different codes. Note that calculated stresses in the cladding during PCMI depend on the models used for the various contributions to fuel deformation. Hence, they are largely dependent on the approximations used to represent the effect of fuel cracking and creep, and the large uncertainties that are associated with these modelling aspects [159].

Figure 154 illustrates the codes' predictions of oxide layer thickness at the outer surface of the cladding at the axial position corresponding to the mid plane of the fuel stack. Predictions from the different codes are reasonably consistent. Qualitatively, all codes predict the initial cubic time dependence of oxide layer growth (pre transition oxidation) and the subsequent, approximately linear growth (post transition oxidation). This two stage behaviour is typical of zircaloy oxidation, e.g. [160]. The maximum spread of the calculated oxide thickness at the end of life (EOL) is  $\sim 15\text{--}20\ \mu\text{m}$ .

Figure 155 shows the comparison of calculated fuel centreline centreline temperatures for the Zry-4 cladding case. Initially, the dispersion of the calculated temperatures is up to  $\sim 100$  K, which is expected to be mostly due to different models used for the fuel thermal conductivity and fuel relocation. The latter affects the gap width at beginning of life (BOL) and hence the gap conductance and fuel temperature. With the exception of BACO, the calculated temperatures appear fairly consistent, with differences being within the uncertainties. Higher differences late in life may be due to differences in modelling the complexities associated with high burnup behaviour, such as thermal conductivity degradation and the effects associated with the formation of the high burnup structure (HBS).

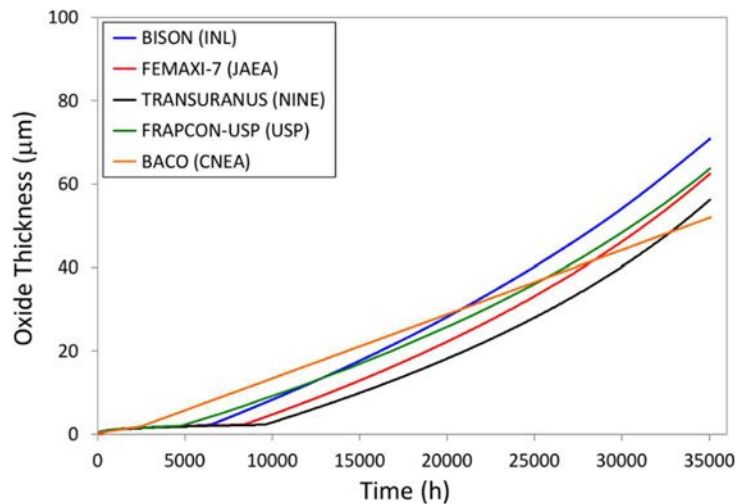


FIG. 154. Comparison of code calculations of oxide layer thickness (axial location corresponding to the mid plane of the fuel stack) for fuel rod with Zircaloy-4 cladding during normal operation.

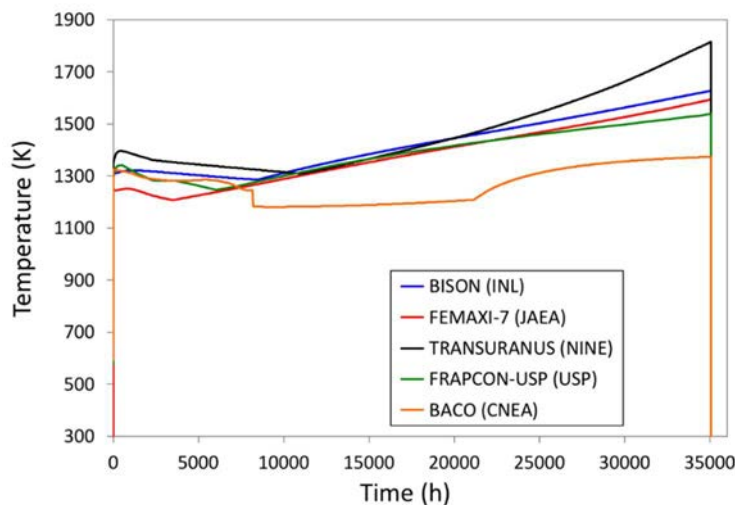


FIG. 155. Comparison of code calculations of fuel centreline centreline temperature (axial location corresponding to the mid plane of the fuel stack) for fuel rod with Zircaloy-4 cladding during normal operation.

The codes' results for the integral fuel rod fission gas release are shown in Fig. 156. All codes reproduce the incubation behaviour of FGR [160], although the predicted times for the onset of significant (thermal) release are significantly different. In this respect, it is noted that the FEMAXI-7 calculation was shown to be consistent with the Vitanza FGR threshold. Differences among the calculations from the different codes tend to increase with increasing irradiation time. This is in part associated with the differences in the predicted onset of thermal FGR but also with the different calculated FGR rates after the incubation period. These are ascribed to different models and parameters used in the codes. Also, as FGR is a temperature-dependent phenomenon, differences in the FGR calculations are partly due to the spread in calculated fuel temperatures by the different codes. Finally, consideration of FGR from the HBS is expected to play a role at the burnup reached for the fuel rod problem

considered here. The TRANSURANUS code includes a specific capability for FGR from the HBS, which was applied in this work. Finally, the BISON and FEMAXI codes predict a rapid increase of FGR ("burst release") during the final shut-down. This is consistent with experimental observations, e.g. [162]. In BISON, the burst release model described in [163, 164] has been applied in the present calculations. A similar capability is available in TRANSURANUS [164], although it was not applied in this work.

Calculations of fuel rod inner pressure are shown in Fig. 157. All codes predict the increase in fuel rod inner pressure with irradiation time. Differences between codes are partly associated with the different amounts of FGR predicted. In addition to this, the different approaches used in the codes for the calculation of the plenum temperature are expected to play a significant role in the observed differences. This latter aspect is a known issue for the prediction of fuel rod inner pressure, including during postulated LOCA accidents [109].

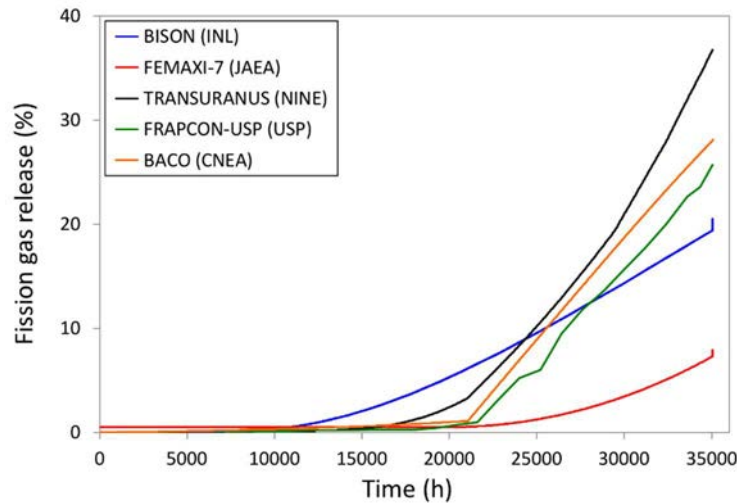


FIG. 156. Comparison of code calculations of integral fission gas release for fuel rod with Zircaloy-4 cladding during normal operation.

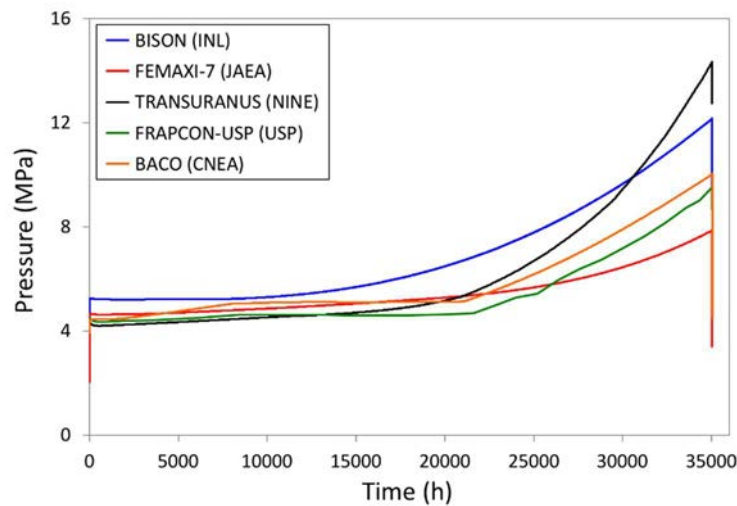


FIG. 157. Comparison of code calculations of rod inner pressure for fuel rod with Zircaloy-4 cladding during normal operation.

#### 5.4.2. Comparisons of calculation results for FeCrAl cladding

In this subsection, the benchmark comparisons of fuel performance codes for the analysis of the normal operation case with FeCrAl cladding are presented. The material models and properties of the FeCrAl alloy C35M provided by INL and described in Section 2.1 and in [106] were applied in the codes. The one exception is the BACO code, in which models for a commercial FeCrAl alloy (Kanthal) were applied.

Figure 158 illustrates the comparison of calculations from the five fuel performance codes in terms of hoop strain evolution at the cladding outer surface of the cladding at the axial location corresponding to the mid plane of the fuel stack. (Note that the FRAPCON results are in terms of average strain across the cladding thickness instead.) All calculations show the expected qualitative behaviour of (i) a positive strain after the initial start-up due to thermal expansion, (ii) a negative slope of the curves prior to the onset of PCMI as the cladding creeps down under the external coolant pressure, (iii) a positive slope after pellet cladding contact is established (at this axial location), and (iv) an inward strain during the final shut-down period as the gap reopens resulting in removal of the pellet cladding contact pressure. FeCrAl has a slightly higher thermal expansion coefficient compared to Zry-4 resulting in a higher hoop strain after the first rise to power. Prior to the onset of PCMI, the creep-down strain rate of the FeCrAl cladding is lower than Zry-4 due to the lower creep rate of this material (see Section 2.1).

After PCMI is established, the time evolution of cladding strain is determined by cladding creep along with fuel deformation models such as swelling and creep models. Observed differences in the cladding strain rates during PCMI are ascribed to differences between the models used in the different codes for these phenomena. Also note that calculated fuel stresses in the codes are largely depended on the approximations used to represent the effect of fuel cracking, and that large uncertainties are associated with this modelling aspect. In turn, this results in uncertainties in the calculated stress dependent contributions to fuel strain, such as creep and gaseous swelling.

Results for the hoop strain at the cladding inner surface are similar and are not shown here for brevity.

Figure 159 shows the evolution of the calculated radial width of the fuel cladding gap at the fuel stack axial mid plane. The initial drop in gap width is associated with fuel thermal expansion and relocation, while the increase in gap width early in life is due to fuel densification. Differences in the gap size evolution from the different codes are due to differences in the cladding strain kinetics (Fig. 158.) as well as the UO<sub>2</sub> models that determine calculated fuel deformation. All codes predicted a delayed gap closure with FeCrAl cladding compared to Zry-4. This is primarily due to the reduced creep rate of FeCrAl, which is reproduced by the codes.

The evolution of the hoop stress at the outer surface of the cladding at the same axial location as the hoop strain is shown in Fig. 160. (The FRAPCON results are in terms of average stress across the cladding thickness instead.) Initially, the cladding is under compression until after PCMI is established. The fuel cladding contact pressure under PCMI results in a reduction of the compressive stresses within the cladding. As before, the point in time at which contact occurs is when the slope of the curves changes significantly. The FeCrAl cladding experiences higher compressive stresses than zircaloy (Fig. 153.) due to its lower thickness and creep rate. Reopening of the fuel cladding gap during the final shut down period results in a reversal of the cladding stress back to compressive under the outer coolant pressure.

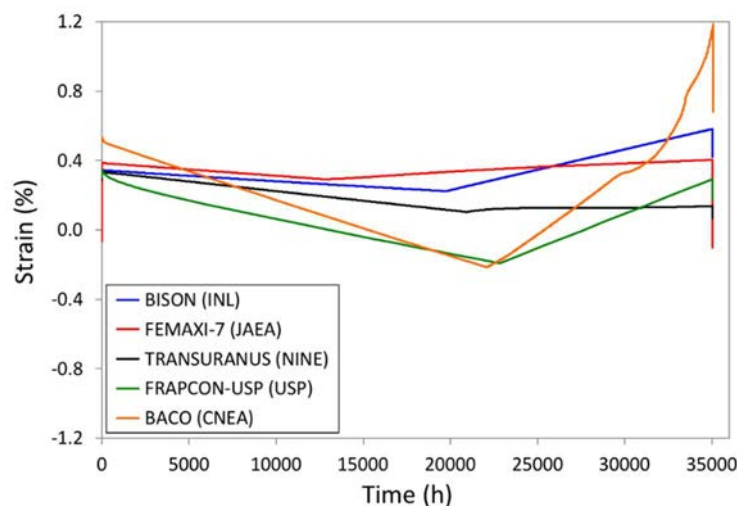


FIG. 158. Comparison of code calculations of hoop strain at the cladding outer surface (axial location corresponding to the mid plane of the fuel stack) for fuel rod with FeCrAl cladding during normal operation.

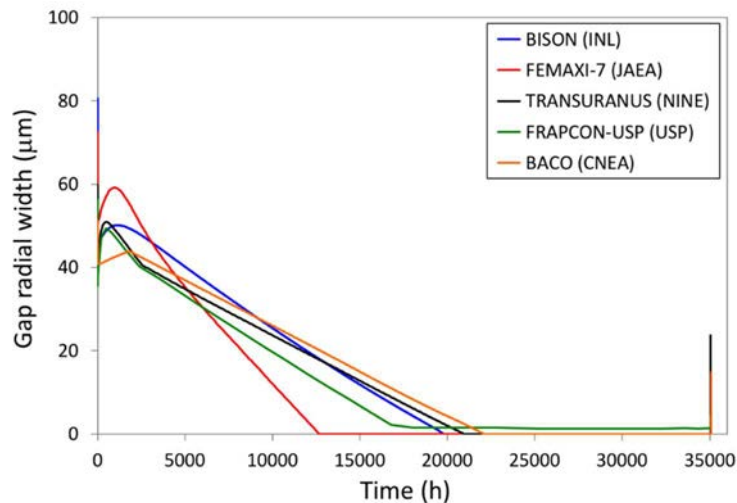


FIG. 159. Comparison of code calculations of gap radial width (axial location corresponding to the mid plane of the fuel stack) for fuel rod with FeCrAl cladding during normal operation.

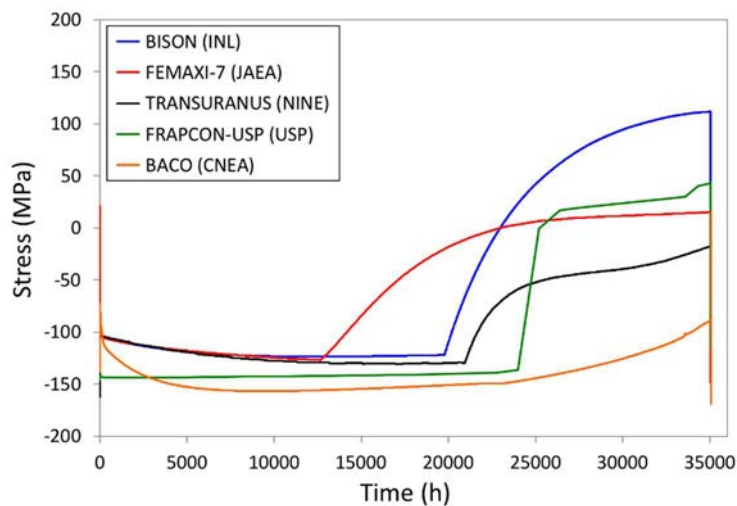


FIG. 160. Comparison of code calculations of hoop stress at the cladding outer surface (axial location corresponding to the mid plane of the fuel stack) for fuel rod with FeCrAl cladding during normal operation.

Predictions of cladding hoop stress from BISON, FEMAXI-7 and TRANSURANUS in open gap conditions before PCMI is established are very consistent among each other. Such an agreement is deemed encouraging, also in view of the significant modelling uncertainties involved in fuel rod analysis and the larger scatter of results that was observed in previous benchmark exercises that involved more complex fuel rod problems (e.g. CRP FUMEX-III).

The predicted stresses under PCMI differ more significantly among the different codes. Note that calculated strains in the fuel, and consequently the cladding stresses and strains during PCMI, are largely dependent on the approximations used to represent the effects of fuel cracking and creep, and that large uncertainties are associated with these modelling aspects [159].

The growth kinetics of the oxide thickness on the outer surface of the cladding is illustrated in Fig. 161. Oxidation results are available for four codes. The oxide growth predictions from BISON, TRANSURANUS and BACO are mutually consistent. This is a consequence of using the same oxidation model (Section 2.1.4) and also indicates consistent calculations for the thermal boundary conditions at the cladding outer surface based on the provided coolant conditions (Section 5.2.1). In FEMAXI, oxidation kinetics was not modelled in detail for these calculations, and a constant oxide thickness of 0.1 mm was considered. For all code calculations, the predicted oxide scale thickness in the FeCrAl cladding is much lower than in Zry-4. The significantly reduced oxidation would result in a lower hydrogen production. While advanced zirconium based alloys such as M5 and ZIRLO

experience reduced oxidation kinetics compared to Zry-4, the observed trends seen here are expected to be the same.

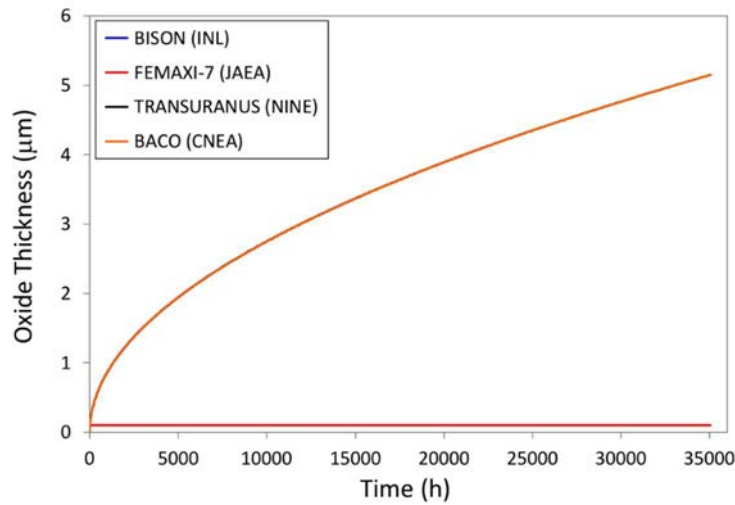


FIG. 161. Comparison of code calculations of oxide layer thickness (axial location corresponding to the mid plane of the fuel stack) for fuel rod with FeCrAl cladding during normal operation.

Figure 162 shows the evolution of fuel centreline centreline temperature as a function of time. As with the Zry-4 case (Fig. 155.), initially the dispersion of the calculated temperatures is up to ~100 K, which is expected to be due to different models used for the fuel thermal conductivity and fuel relocation. With the exception of BACO, the calculated temperatures appear fairly consistent, with differences being within the uncertainties. As also mentioned for the Zry-4 case, higher differences late in life may be due to differences in modelling the complexities associated with high burnup behaviour, such as thermal conductivity degradation and the effects associated with the formation of the high burnup structure (HBS).

When comparing the present fuel temperature calculations with FeCrAl cladding to those for the Zry-4 case (Fig. 155.), it is noted that codes tend to predict a higher temperature in the FeCrAl cladded rod at early irradiation times. This is consistent with the reduced creep down and larger thermal expansion coefficient of the cladding material, resulting in a larger gap and correspondingly in a lower gap conductance. The sharp change in slope of the temperature curves indicates the onset of PCMI. After contact, differences in temperatures between the FeCrAl and Zry-4 cases are caused by differences in the magnitude of fission gas release (which still affects heat transfer during contact in presence of fuel and cladding roughness's) and cladding thermal conductivity.

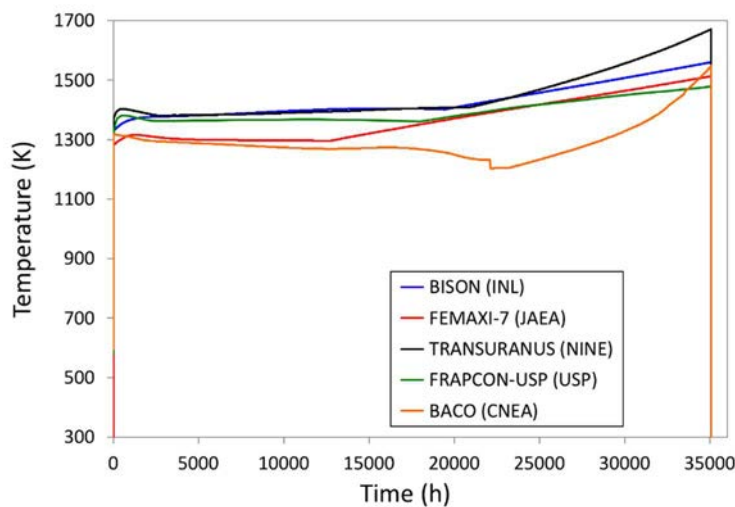


FIG. 162. Comparison of code calculations of fuel centreline centreline temperature (axial location corresponding to the mid plane of the fuel stack) for the normal operation fuel rod case with FeCrAl cladding.

Comparisons of code calculations for integral fission gas release are shown in Fig. 163. Differences with respect to the Zry-4 case are expected to be primarily due to the different calculated fuel temperatures. Qualitatively, the same considerations made for the Zry-4 case hold, i.e. all codes predict an incubation behaviour for FGR, although with different incubation times.

Increasing differences are observed at high burnup, which are interpreted as associated with the spread in calculated fuel temperatures and with the differences in the FGR models and parameters. Also, consideration of FGR from the HBS is expected to play a role at the burnup reached for the fuel rod problem considered here. The TRANSURANUS code includes a specific capability for FGR from the HBS, which was applied in this work.

BISON and FEMAXI predict a rapid increase (burst) in the FGR during the final shut-down, which is consistent with the experimental observations, e.g. [162]. The fission gas model in BISON includes a specific burst release capability [163, 164]. A similar capability is also available in TRANSURANUS [164], although it was not applied in the present work.

The evolution of rod internal pressure as predicted by the five codes is shown in Fig. 164. As expected, the pressure inside each rodlet increases as irradiation progresses and fission gas is released into the gap and plenum. The sharp rise in internal pressure from 2 MPa during the initial rise to power is due to temperature increase from ambient. As with the case with Zry-4 cladding, all codes predict the increase in fuel rod inner pressure with irradiation time. Differences are expected to be associated with the differences in the predicted FGR and the different approaches used for the calculation of plenum temperature. Plenum temperature calculation, in particular, has been identified as an open issue for the accurate prediction of fuel rod inner pressure, including during postulated LOCA accidents [109].

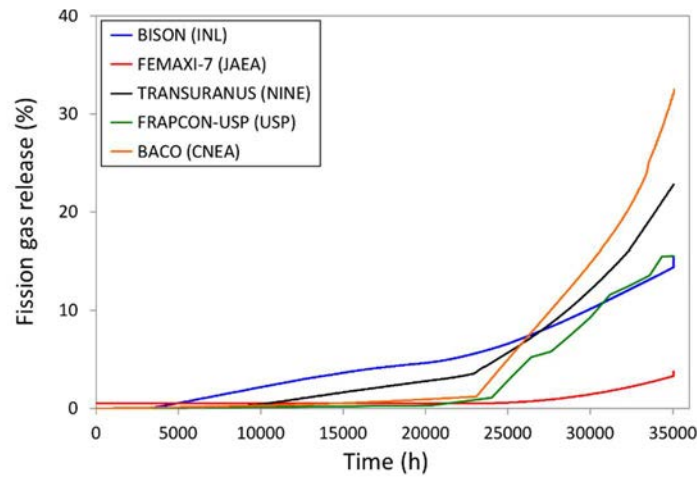


FIG. 163. Comparison of code calculations of integral fission gas release for the normal operation fuel rod case with FeCrAl cladding.

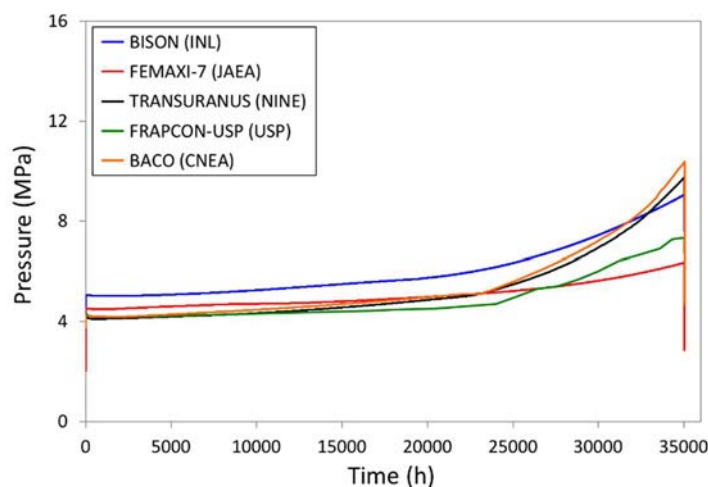


FIG. 164. Comparison of code calculations of rod inner pressure for the normal operation fuel rod case with FeCrAl cladding.

## 5.5. BENCHMARK RESULTS FOR LOSS OF COOLANT CONDITIONS

The LOCA cases considered for the simulations are described in Section 5.2.2. A total of three organizations provided results for the benchmark cases for loss of coolant conditions:

- INL (USA), BISON code;
- JAEA with Waseda University (Japan), FEMAXI-7 code;
- NINE (Italy), TRANSURANUS code.

For these LOCA cases, figures of merit considered for the code-to-code comparisons are:

- Time to cladding burst failure;
- Cladding inner pressure at burst;
- Hoop strain (at cladding outer surface and peak axial location) at the time of burst;
- Hoop strain (at cladding outer surface and peak axial location) as a function of time.

### 5.5.1. Time-dependent hoop strain predictions for FeCrAl

Figures 165 and 166 show the comparison of calculated time evolution of maximum hoop strain at the outer surface of the cladding for the LOCA cases n. 8 (1000°C) and n. 12 (1200°C) (see Section 5.2.2).

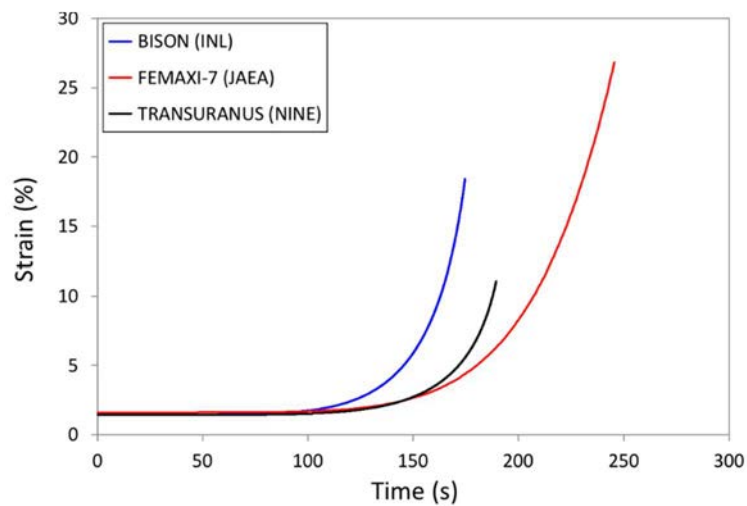


FIG. 165. Comparison of code calculations of hoop strain at cladding outer surface and peak axial location as a function of time for the LOCA benchmark case n. 8.

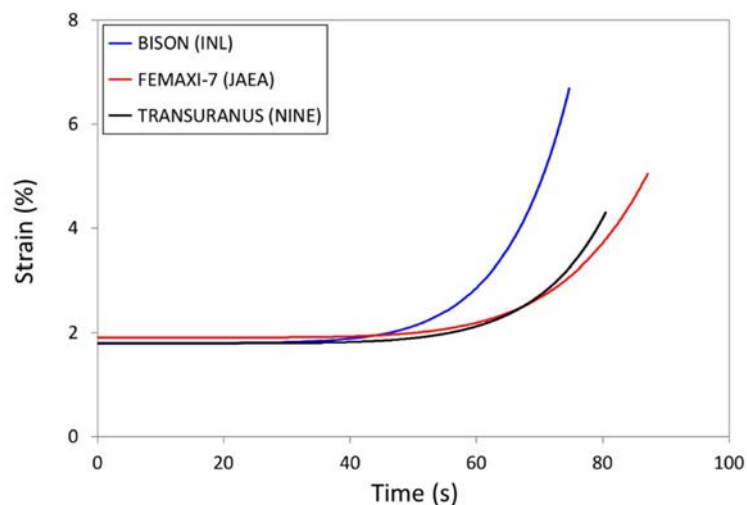


FIG. 166. Comparison of code calculations of hoop strain at cladding outer surface and peak axial location as a function of time for the LOCA benchmark case n. 12.

The initial non-zero strains are due to thermal expansion. All codes predict an increasing strain rate during the (pressure) transient until the time of burst is attained. Observed differences in the strain rates may be due to the different treatments of mechanical behaviour in the codes (e.g. the way the geometrical nonlinearity is dealt with, or whether a large strain formulation is adopted). The predictions from TRANSURANUS and FEMAXI appear fairly consistent, at least for strains below 3-5%. These cases are representative of the behaviour observed for the whole set of simulations.

### 5.5.2. Burst failure predictions for FeCrAl and comparisons to Zircaloy-4

Result from participants in terms of time to burst failure for all the six LOCA benchmark cases are reported in histogram form in Fig. 167. Experimental data for Zry-4 under the same conditions (PUZRY experiments, see Section 5.2.2. and [108]) are also included. Order of cases is one of decreasing test temperature. The TRANSURANUS calculations for case 26 are not available. The corresponding predictions for the cladding inner pressure at burst are illustrated in Fig. 168.

Some differences are observed between predictions with different codes. These can be ascribed to differences in the strain calculation (Section 5.5.1.) and consequently, the calculated stress, which determines the burst prediction according to the criterion described in Section 2.1.5. However, the current simulations compared to the experimental data for Zry-4 indicate that FeCrAl has a similar burst resistance to Zry-4. Note that the experiments were performed with a Zry-4 cladding thickness of 725  $\mu\text{m}$ , which is almost twice of the thickness used for the FeCrAl cladding calculations (385  $\mu\text{m}$ , based on neutronics considerations, see Section 5.2.1.).

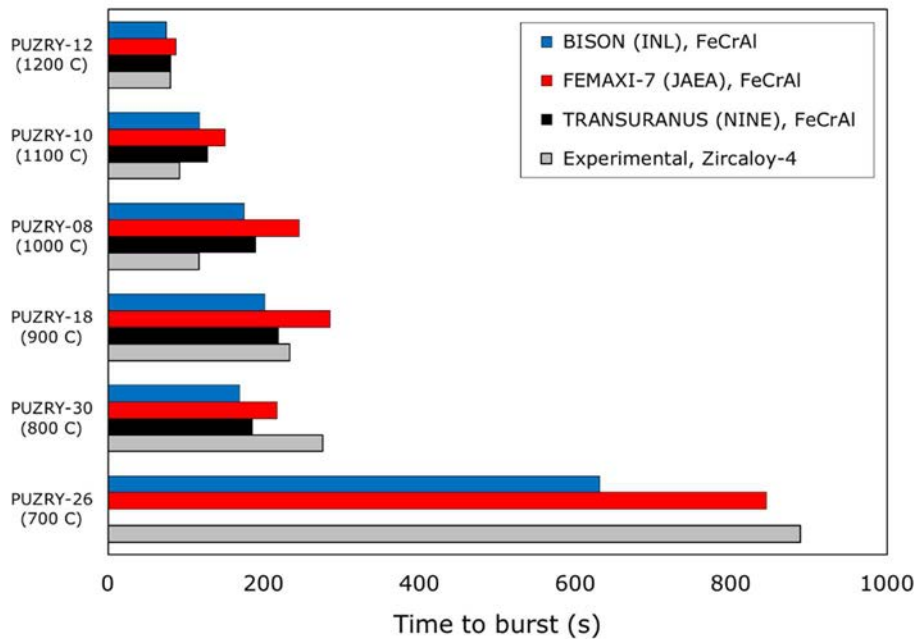


FIG. 167. Time to cladding burst failure for the LOCA benchmark cases. Code-to-code comparisons for FeCrAl and experimental data for Zircaloy-4 under the same conditions.

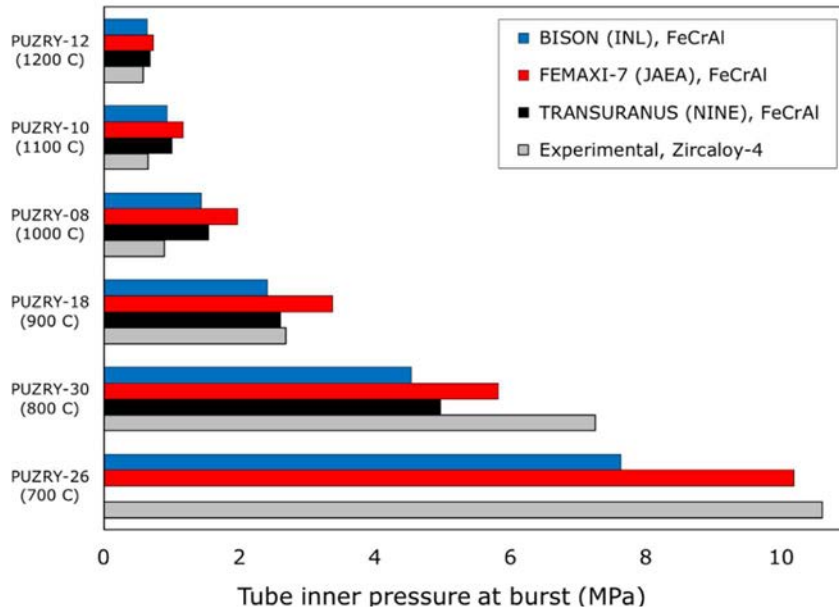


FIG. 168. Cladding inner pressure at burst for the LOCA benchmark cases. Code-to-code comparisons for FeCrAl and experimental data for Zircaloy-4 under the same conditions.

Furthermore, the burst failure criterion adopted here was in fact developed based on experimental data for 1st generation FeCrAl alloys [101], and even higher resistance is expected for 2<sup>nd</sup> generation alloys such as C35M [99].

In addition to this, FeCrAl is anticipated to be characterized by substantially lower oxidation kinetics, hence a lower reduction of load bearing capacity due to cladding thinning and a lower hydrogen and heat generation during LOCA scenarios. However, the effect of oxidation was not investigated in the present calculations.

Figure 169 shows results from participants in terms of engineering hoop strain at axial peak position (burst location) on the cladding outer surface at the time of burst failure. While differences are observed between the FeCrAl predictions, all codes predict a markedly lower maximum strain in the FeCrAl cladding compared to the experimentally observed strains for Zry-4. This result is consistent with the conclusion in [101] that ballooning under LOCA conditions is very limited for FeCrAl, unlike Zr-based alloys.

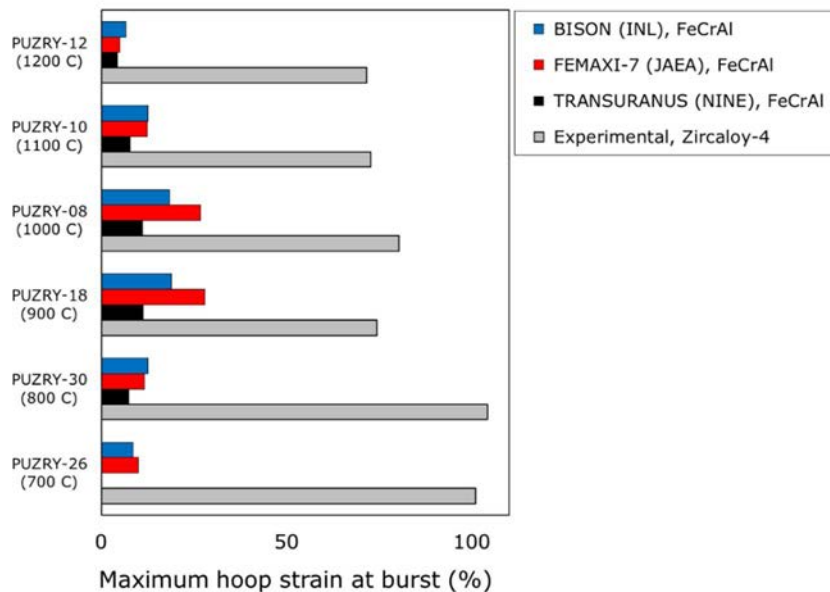


FIG. 169. Cladding maximum hoop strain at burst for the LOCA benchmark cases. Code-to-code comparisons for FeCrAl and experimental data for Zircaloy-4 under the same conditions

## 5.6. CONCLUSIONS AND RECOMMENDATIONS

The modelling benchmark organized within the CRP ACTOF was focused on the analysis of iron-chromium aluminium (FeCrAl) steel cladding behaviour and performance. FeCrAl cladding is an ATF concept that is currently the subject of interest and active research in various IAEA Member States. A total of five organizations participated in the ACTOF modelling benchmark for FeCrAl: INL (United States of America, BISON fuel performance code), NINE (Italy, TRANSURANUS code), JAEA with Waseda University (Japan, FEMAXI-7 code), University of São Paulo (Brazil, FRAPCON-USP code) and CNEA (Argentina, BACO code). Focusing on the laboratory-optimized FeCrAl alloy C35M developed at ORNL, material properties and models were made available by INL to the participants for implementation in selected codes. INL also provided specifications for the benchmark cases to be analyzed. The ACTOF modelling benchmark resulted in extensive comparisons of fuel rod calculations with FeCrAl cladding under both LWR normal operating and loss-of-coolant accident (LOCA) conditions.

For the normal operating conditions calculations, a fuel rodlet with UO<sub>2</sub> fuel and FeCrAl cladding irradiated under steady-state power was considered. Reference calculations for an analogous case with a standard cladding alloy (Zry-4) were also performed. For the LOCA calculations, FeCrAl claddings subject to internal pressure transients were considered. Specifically, pressure histories and temperatures used in the calculations were based on experimental conditions of the separate effects tests PUZRY on ballooning and burst of fuel rod segments. For these experimental tests, the inner pressure of the cladding tube was increased linearly and isothermally until burst failure occurred. Six LOCA cases, corresponding to six different test temperatures, were selected for the benchmark calculations.

The normal operating conditions calculations for FeCrAl resulted in fairly consistent predictions among the different codes, especially in regard to the simulated cladding behavior in open gap conditions (i.e., before PCMI was established). In particular, calculations of hoop stress from BISON, FEMAXI-7 and TRANSURANUS before PCMI were very consistent.

The comparisons between the results from BISON, FEMAXI-7 and TRANSURANUS in terms of cladding strains and stresses, seem encouraging. This conclusion is to be evaluated in consideration of the significant modelling uncertainties involved in fuel rod analysis and of the larger scatter of results observed in previous benchmark exercises that involved more complex fuel rod problems (e.g. CRP FUMEX-III), for which it is known that predictions from different fuel performance codes may differ significantly. Indeed, with a view to future work, the consistency between the results from different codes for this relatively simple steady-state case appears to be a suitable starting point to build on for further benchmark calculations, possibly involving more complex cases.

The predicted times for the onset of PCMI were significantly different among the codes. This circumstance can be ascribed to the different models applied in the codes for the contributions to fuel deformation, leading to different predictions in terms of gap closure kinetics. Despite the observed differences in the predictions from different codes, in general the calculations reproduced (i) a lower creep rate for FeCrAl compared to Zry-4, resulting in a delayed gap closure, and (ii) a higher compressive stress in open gap conditions for the FeCrAl cladding, due to the lower thickness of the cladding wall and reduced creep rate compared to Zry-4. For all calculations, however, the predicted stresses in the FeCrAl cladding were comparable to those calculated for Zry-4 and well below the yield stress and ultimate tensile strength of the material during the whole irradiation. Calculated strains in the FeCrAl cladding were comparable to or lower than in Zry-4.

Differences in the calculated fuel centreline temperatures from the different codes were up to ~100 K and higher for high burnup. At early irradiation times the fuel centreline temperature tends to be higher in the FeCrAl clad rod compared to the experimentally observed behaviour of Zry-4 case due to the reduced creep down and larger thermal expansion coefficient of the cladding material, corresponding to a larger gap width and associated lower gap conductance.

Results for oxidation behaviour indicated that a much lower oxide layer thickness (up to 5 µm) developed in FeCrAl cladding compared to Zry-4 (several tens of microns according to all code calculations). This is expected and constitutes the main advantage of FeCrAl for nuclear fuel cladding applications.

Fission gas release and rod inner pressure calculations showed significant differences among the different codes. For FGR, this is expected to be associated with the different models and parameters applied, and the differences in the calculated fuel temperatures. For the plenum pressure calculations, in addition to the effect of FGR, a significant impact of the approaches used in the codes for the calculation of plenum temperature is expected, also based on the conclusions of the CRP FUMAC.

Calculations for the LOCA cases were performed only with the codes BISON, TRANSURANUS and FEMAXI-7. Results of cladding strain behaviour during the transients were qualitatively consistent among each other, although significant differences in the predicted creep rates and times to cladding burst failure were observed. In general, however, calculations indicated that the FeCrAl cladding is characterized by a resistance to burst failure similar to Zry-4, despite the lower cladding thickness considered for FeCrAl in view of neutronics considerations. This conclusion is based on the burst times and pressures calculated with the three applied fuel performance codes (BISON, TRANSURANUS, FEMAXI-7) compared to the experimentally observed behaviour of Zry-4 under the same conditions. Moreover, while a burst failure criterion based on data for earlier FeCrAl alloys was used for the present calculations, a higher resistance is expected for more advanced alloys such as C35M. Finally, the cladding maximum hoop strains at burst for the FeCrAl cladding calculated with all codes were considerably lower than the strains observed experimentally for Zry-4 claddings. This is consistent with the lower creep rate of FeCrAl compared to Zircaloy and with the available experimental observations, which have demonstrated that no significant ballooning occurs in FeCrAl claddings under LOCA transients up to the point of burst.

In conclusion, as a result of the modeling benchmark exercise completed in the CRP ACTOF, various fuel performance codes from IAEA Member States, widely used by research institutions and industry, have been (i) extended to the analysis of FeCrAl cladding, (ii) applied to simulations of integral fuel rod and separate-effects cladding problems covering normal LWR operation and loss of coolant accidental conditions, respectively, and (iii) compared systematically to each other for these calculations. The obtained results provided valuable information on FeCrAl cladding performance compared to traditional cladding alloys. Furthermore, from this work, some important areas for future research were identified. In particular, based on the modelling benchmark for FeCrAl, the following main recommendations for future research on FeCrAl cladding applications are derived:

- Future benchmark exercises should aim to investigate FeCrAl cladding behaviour for a broader range of conditions, such as realistic LWR base irradiation and LOCA cases that include temperature transients, oxidation, and integral fuel rod behaviour;
- Given the limited amount and spread of the available data for high temperature creep, and the observed sensitivity of burst failure predictions to the calculated creep rates, further experimental investigation of FeCrAl creep behaviour at temperatures beyond the normal operating temperatures is advisable in order to improve modelling for accidental conditions;
- Experimental investigation of oxidation behaviour of FeCrAl in steam at high temperature would be useful to extend the current oxidation models to accidental conditions;
- Future improvements of the corrosion models should also include dissolution of the metal besides oxide layer growth;
- Data are needed in order to include irradiation embrittlement of FeCrAl in calculations.

As a more general recommendation for future fuel performance codes development, it is advisable to investigate the fuel deformation behaviour under cladding external restraint during PCMI. In particular, this would include stress-dependent contributions to fuel deformation (creep, swelling) and the representation of fuel cracking, which affects calculated fuel stresses. This recommendation is motivated by the significant differences observed in the calculations for cladding mechanical behaviour after gap closure.

## 6. BENCHMARK ON THE QUENCH-19 BUNDLE TEST WITH ATHLET-CD AND SOCRAT CODES

### 6.1. INTRODUCTION

Iron-chromium-aluminium alloys (FeCrAl) belong to an alloy class typically used in industrial facilities where high temperature oxidation resistance is needed. As examples, the following alloys of the Kanthal Company could be mentioned: APM (73% Fe, 21.2% Cr, 5.8% Al) and APMT (70% Fe, 21% Cr, 5% Al, 3% Mo). The station blackout accident in March 2011 at the Fukushima Daiichi nuclear power plant served as the catalyst for the recent significant increase of interest in FeCrAl alloys for nuclear power applications. The accident that prompted considerable research devoted to identifying LWR fuel systems that tolerate severe accident scenarios (or beyond design basis accident, BDBA). The objective is to provide larger safety margins, i.e. delay the onset of severe core degradation by reducing the rate of hydrogen and heat generated by the rapid oxidation of Zr-based alloy cladding and increase the coping time after an accident.

Development of iron based wrought FeCrAl alloys has been initiated for LWR fuel cladding to serve as a substitute for Zr-based alloys with enhanced accident tolerance. The most systematic efforts have been focused on the development of wrought FeCrAl alloys which are to be considered *nuclear grade*, i.e. it should be an optimized material composition to perform in both operation and accident conditions. Especially the chromium content should be not higher than 13% to decrease the cladding hardening under irradiation. Many of these studies of wrought FeCrAl alloy relate to compositions developed by Oak Ridge National Laboratory (ORNL) including two different generations of alloys. Generation I alloys are simple systems with only Fe, Cr, Al, and Y used to form the alloy, while Generation II alloys are derived from Generation I alloys but include minor alloying additions to increase specific performance factors. Firstly, ORNL examined in detail the oxidative behavior of the Kanthal materials, which cannot be used in reactors due to too high Cr content [165–167]. In contrast to this, the B136Y alloy (13% Cr, 6.2%Al, 0.03% Y, Fe balance) developed by ORNL can be considered suitable for the nuclear applications [168–171]. Series of single effect tests were performed at different laboratories to study different properties of this material. However, such tests are performed under simplified laboratory conditions (e.g. [169, 170]) and not really prototypical for the reactor environment.

Only bundle tests can provide more realistic adiabatic conditions. The advantages of bundle tests can be described as follows: radiative heat exchange between the fuel rods, changing of coolant channel during cladding swelling, interactions of materials after fuel rod failures, influence of spacer grids. The data of the bundle tests gives important basis for code validation. Taking these considerations into account, it was decided to perform bundle test with B136Y claddings in the QUENCH facility of the Karlsruhe Institute of Technology (KIT). The QUENCH-19 bundle experiment with B136Y claddings and 4 Kanthal AF spacer grids as well as 7 KANTHAL APM corner rods and KANTHAL APM shroud was conducted at KIT on 29th August 2018 [172]. The test objective was to compare B136Y and ZIRLO claddings under similar electrical power and gas flow conditions. The electrical power supply was the same as in the reference test QUENCH-15 (ZIRLO) during the first two stages (pre oxidation and transient). The third stage with constant electrical power was performed to extend the temperature increase period. This artificial approach led to not prototypical decrease of the temperature growth rate but such an approach made it possible to observe a change in the evolution of hydrogen release in the “slow motion” mode. The test was terminated at peak cladding temperature of about 1460°C by water flooding similar to QUENCH-15. The test results are described in the corresponding chapter of Annex. Here it could be mentioned that the total hydrogen release was significantly lower in comparison to the QUENCH-15 test (9 g vs. 41 g). However, there were problems with the integrity of the FeCrAl cladding tubes: in the hottest bundle positions cylindrical tube parts with a length up to 20 mm were spalled. The reasons for these phenomena are still under investigation but are likely due to the crack initiation by melted thermocouples and increased thermal expansion coefficient of FeCrAl in comparison to Zr alloys.

The results of the QUENCH-19 bundle test were used for performance of post test benchmark. Two organizations provided results for first exercises on the modelling of bundle test with FeCrAl materials (detailed descriptions of corresponding simulations are given in the Annex):

- GRS (Germany), ATHLET-CD code [173];
- IBRAE (Russian Federation), SOCRAT code [174].

In both codes, the rod bundle was described by three concentric rings as shown in Fig. 170 and Table 46: an inner ring (ROD1) containing four central rods, a second ring containing eight rods (ROD2), and a third ring containing twelve rods (ROD3).

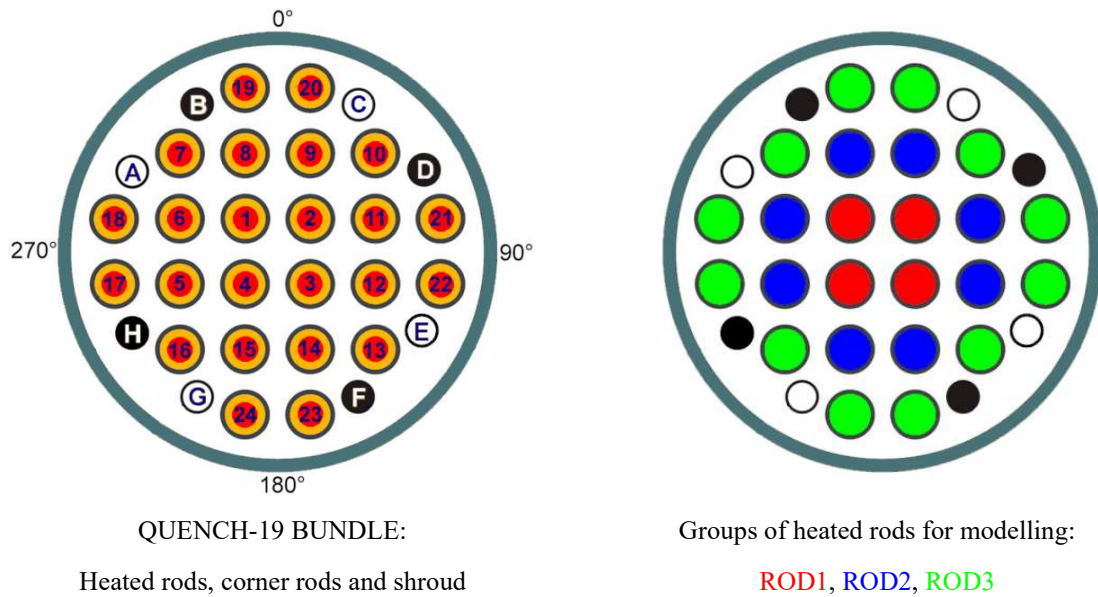


FIG. 170. QUENCH-19 bundle composition.

TABLE 46. QUENCH-19 HEATED ROD GROUPS FOR MODELLING

| Rod group in code | Composition                | Rod number                                    |
|-------------------|----------------------------|---|
| ROD1              | 4 central rods             | 1, 2, 3, 4                                    |
| ROD2              | 8 rods (intermediate ring) | 5, 6, 8, 9, 11, 12, 14, 15                    |
| ROD3              | 12 rods (outermost ring)   | 7, 10, 13, 16, 17, 18, 19, 20, 21, 22, 23, 24 |

The boundary conditions used for the calculations are given in the test description (see Annex). The reference time (0 s) was established for the beginning of the experiment. The reference bundle elevation (0 mm) corresponded to the bottom of the tungsten heaters in the rod simulator.

## 6.2. TEMPERATURE HISTORY OF QUENCH-19 FOR DIFFERENT BUNDLE ELEVATIONS

Figures 171–176 show calculated temperature distributions in the bundle elevations between 250 and 1350 mm in comparison with the experimental data.

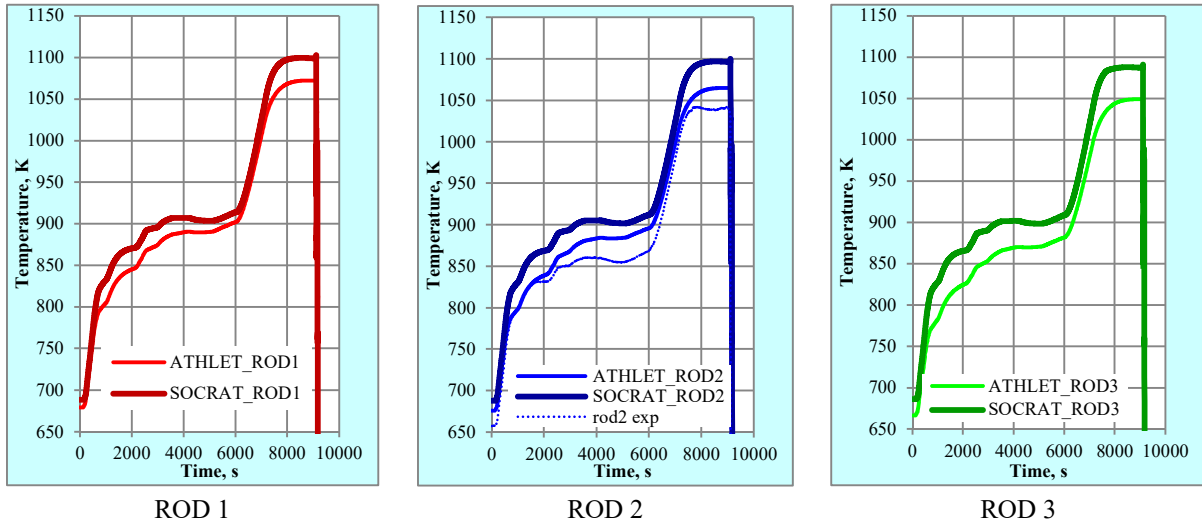


FIG. 171. ATHLET-CD and SOCRAT modeling of temperature progressing at elevation 250 mm.

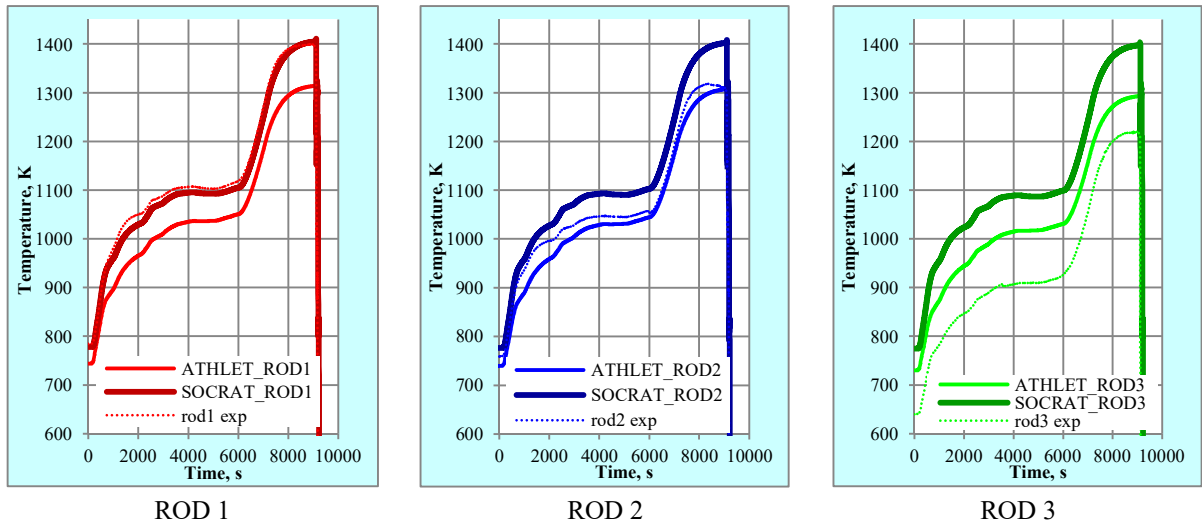


FIG. 172. ATHLET-CD and SOCRAT modeling of temperature progressing at elevation 550 mm.

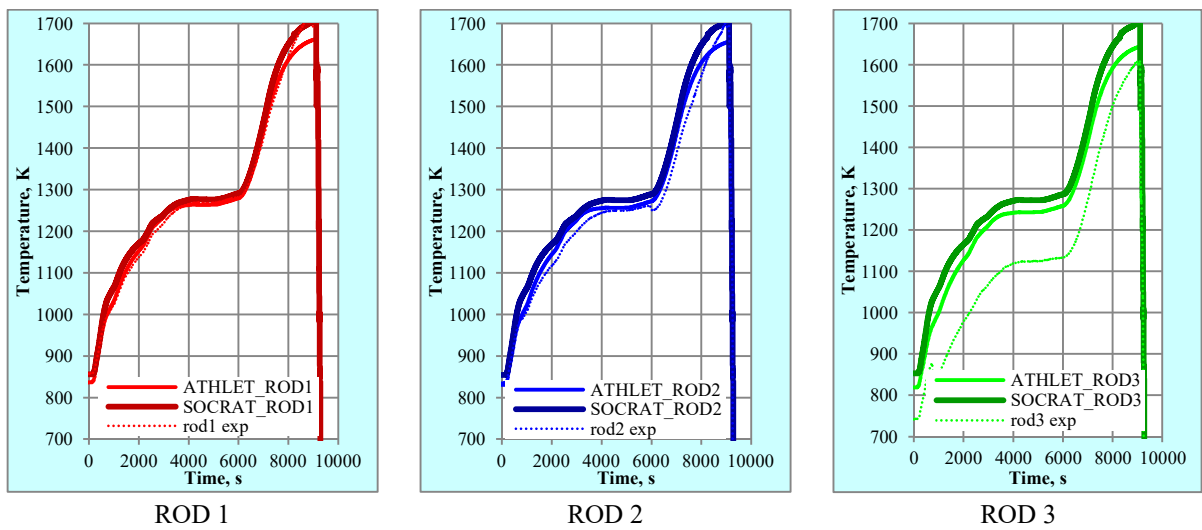


FIG. 173. ATHLET-CD and SOCRAT modeling of temperature progressing at elevation 850 mm.

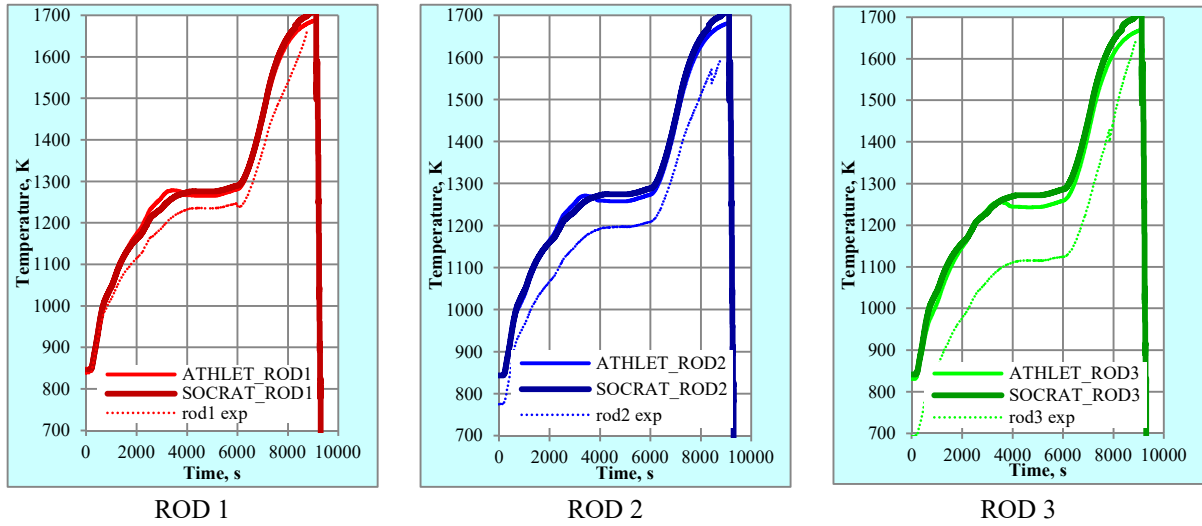


FIG. 174. ATHLET-CD and SOCRAT modeling of temperature progressing at elevation 950 mm.

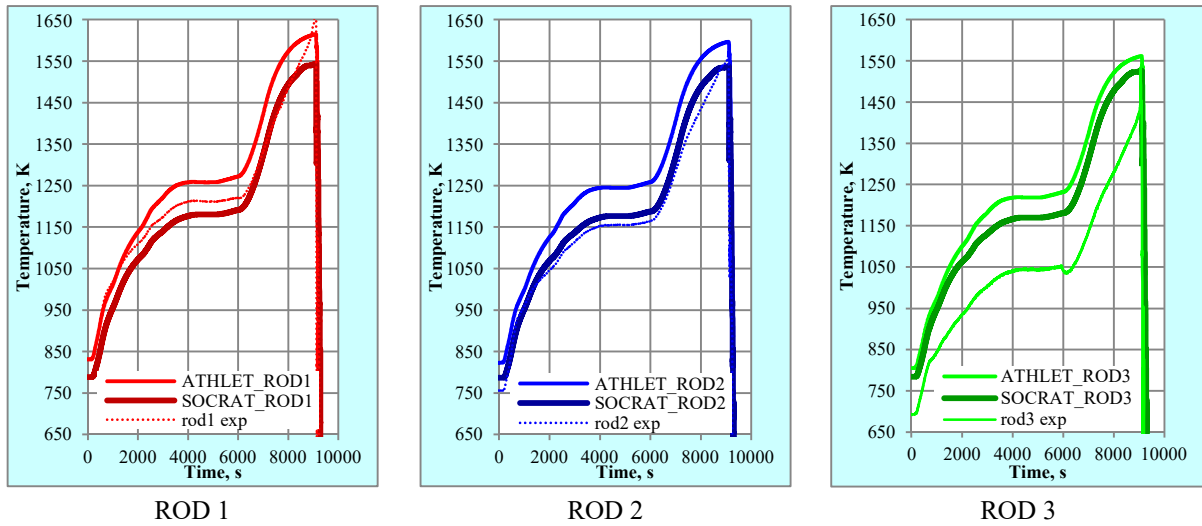


FIG. 175. ATHLET-CD and SOCRAT modeling of temperature progressing at elevation 1050 mm.

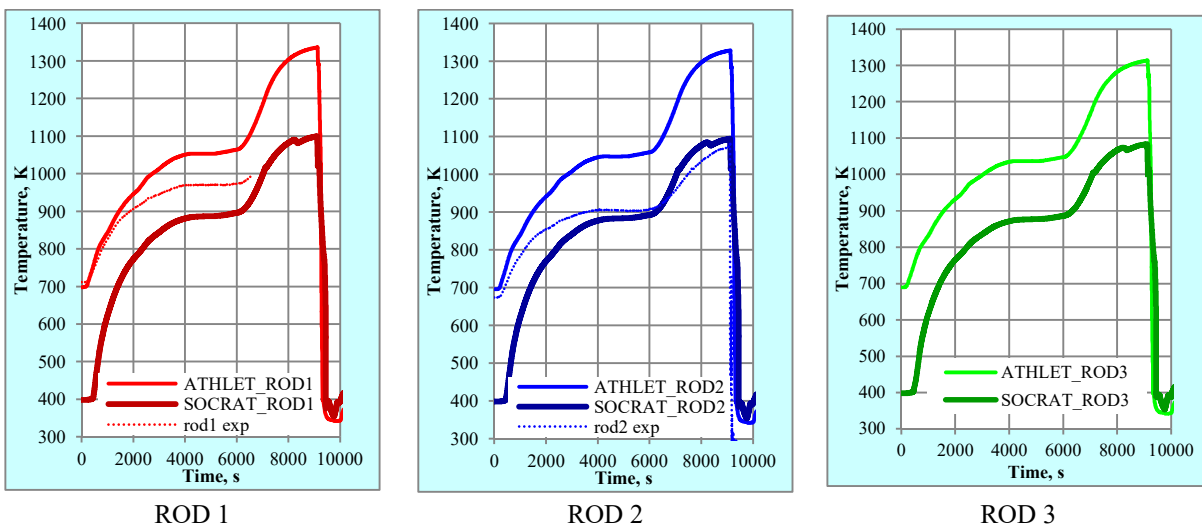


FIG. 176. ATHLET-CD and SOCRAT modeling of temperature progressing at elevation 1350 mm.

The bundle temperatures for inner rods (ROD1), intermediate rods (ROD2) are satisfactorily reproduced by the codes for the elevations up to 1050 mm, i.e. inside the bundle axial part surrounded by heat insulation. For the position of not insulated bundle at 1350 mm height the cladding temperatures of ROD1 and ROD2 were overestimated by ATHLET-CD and partially underestimated by SOCRAT. The cladding temperatures of the outer ring of rods ROD3 were overestimated by both codes. It should be mentioned that in the experiment there exists a pronounced radial gradient between inner and outer temperatures with a difference up to 200 K in the measured data (noticeable larger in comparison to QUENCH-15; the reasons are not yet completely understood), whereas the simulation yields a flat profile with a difference less of 50 K. The ATHLET-CD simulations show more distinctive radial temperature gradients than SOCRAT simulations.

In agreement with the measurement there is no temperature excursion in the simulations. The melting temperature of FeCrAl claddings (which is about 1783 K) was not reached either in experiment or in the simulations.

### 6.3. HYDROGEN RELEASE DURING QUENCH-19

The calculation of hydrogen release was based on the oxidation correlations for the KANTHAL APMT material derived by KIT for the ATHLET-CD and IBRAE models from the experiments performed by ORNL between 1323 and 1473 K [165] and between 1473 and 1750 K [166]. On the basis of these two data sets [167], the common kinetics for the APMT oxidation in the temperature region from 1323 to 1750 K was described by ORNL with the following Arrhenius coefficient for mass gain [168]:

$$K_1 = A_1 \exp\left(\frac{-E_a}{RT}\right) \quad (50)$$

where the activation energy  $E_a = 344$  kJ/mol and the pre-exponential constant  $A_1 = 7.84$  g<sup>2</sup>/cm<sup>4</sup>·s,  $R$  is the gas constant.

Unfortunately, no data for the high temperature oxidation of KANTHAL APMT (used for shroud and corner rods of QUENCH-19) are currently available.

Concerning the B136Y3 alloy (used for the claddings), there are only few experimental data. The first set of such data was achieved for transient conditions at ORNL [169]. During the modelling of these tests, the suggested activation energy was 344 kJ, i.e. the same as for APMT; only the pre exponential constant was varied with factors of 3–10 in comparison to APMT. The second series of tests under quasi isothermal conditions was performed at MIT in the temperature range, and the following correlations for B136Y3 were published [170]:

$$K_2 = \begin{cases} 9.62 \times 10^{-12} [\text{g}^2/\text{cm}^4\text{s}], & T \leq 1473 \text{ K} \\ A_2 \exp\left(\frac{-E_a}{RT}\right) & , 1473 < T < 1648 \text{ K} \end{cases} \quad (51)$$

where the activation energy  $E_a = 344$  kJ/mol and the pre-exponential constant  $A_2 = 15.18$  g<sup>2</sup>/cm<sup>4</sup>·s.

However, such approximation of the experimental data with application of the same activation energy as for the APMT material (containing only 5.0% Al and 21% Cr in comparison to 6.2% Al and 13% Cr for B136Y) significantly underestimates the oxidation of the experimental samples at  $T > 1550$  K. The fitting of the MIT experimental data with the quite high coefficient of determination ( $R^2 = 0.94$ ) gives following oxidation correlation for B136Y:

$$K_3 = A_3 \exp\left(\frac{-E_a}{RT}\right) \quad , 1473 < T < 1648 \text{ K} \quad (52)$$

where the activation energy  $E_a = 594.354$  kJ/mol and the pre-exponential constant  $A_3 = 3 \times 10^9$  g<sup>2</sup>/cm<sup>4</sup>·s,  $R$  is the gas constant.

According to the experimental data, at  $T > 1648$  K significant oxidation acceleration occurred. Probably, the protective Al<sub>2</sub>O<sub>3</sub> was disappeared either due to evaporation of Al(OH)<sub>3</sub> [171] or due to dissolution in the metallic matrix. This temperature boundary is depending on the experimental conditions because practically all tests showed that the steam velocity affected the oxidation behaviour.

For the first version of benchmark calculations, the APMT oxidation correlation was used. In ATHLET-CD the multiply factor 300 was used for all test temperature region. In the SOCRAT simulation, this correlation used up to 1723 K, thereafter a special intermediate correlation is implemented up to 1723 K to smooth transition to the melt oxidation. Oxidation of melt was simulated by correlation for steel oxidation above 1773 K according to referee [169].

The corresponding comparison of experiment and simulation for the hydrogen generation rate and the mass of total generated hydrogen (Fig. 177. and Fig. 178.) shows a strong underestimation of oxidation in the simulation.

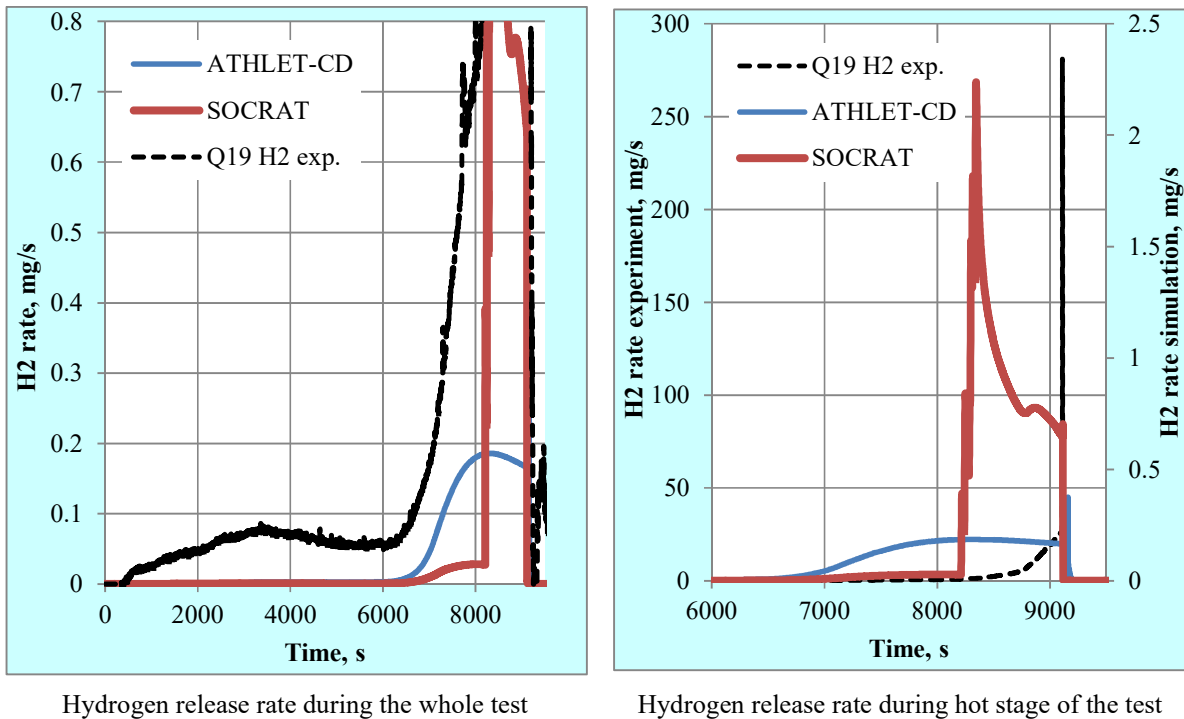


FIG. 177. Simulation (with APMT correlation) and experimental data for hydrogen release rate in QUENCH-19.

The hydrogen production in the test was comparable low up to the time when the calculated maximum cladding temperatures reached a level of about 1670 K at about 800 s before reflood (reflood initiation: 9116 s). The corresponding measured value is about 100 K lower because the surface TC measured an intermediate value between cladding surface temperature and steam temperature. A sharp increase in the hydrogen release rate was observed, which is probable due to the melting of steel thermocouple claddings and partial cladding dissolution by this melt. These phenomena were not considered in the models.

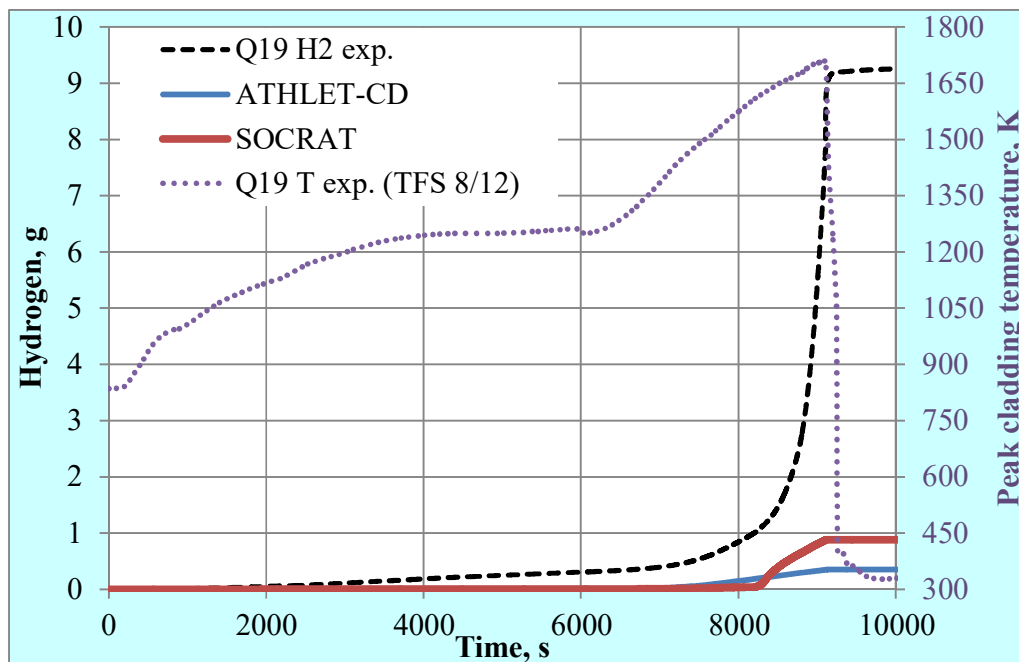


FIG. 178. Hydrogen integral release during QUENCH-19: comparison of simulations (APMT) with experiment.

In the second version of simulations based on the MIT data for the B136Y alloy, GRS has applied the Equations (51) and (52), wherein the dependence (52) was used up to the highest peak cladding temperature reached during QUENCH-19 ( $T_{\text{pct}}=1733$  K). As result, the simulated hydrogen generation is much lower than measured (0.07 g simulated vs. 9 g measured).

In this second series of simulations, IBRAE used the dependence (52) in the temperature range  $T \leq 1623$  K.

Above 1723 K (50 K below the melting temperature of FeCrAl), the following (modified) correlation (derived early for stainless steel oxidation [169]) was used for application in SOCRAT:

$$K_4 = A_4 \exp\left(\frac{-E_a}{RT}\right) \quad , \quad T > 1723 \text{ K} \quad (53)$$

where the activation energy  $E_a=352513$  J/mol and the pre-exponential constant  $A_4=4.57 \times 10^7$  g<sup>2</sup>/cm<sup>4</sup>s,  $R$  is the gas constant.

In the temperature range  $1623 \text{ K} \leq T \leq 1723 \text{ K}$  the the MIT experimental data were used by IBRAE to derive the transition correlation of the Arrhenius form (53) between formulas (52) and (53).

Results of corresponding SOCRAT calculations for the hydrogen release are given in Fig. 179. It can be seen that the calculated hydrogen release is underestimated also for the MIT correlation, even at lower temperatures. Concerning the total hydrogen release, the uncertainty analysis showed that the result is very sensitive to the temperature in the hot bundle region: an increase in temperature of only 20 K here gives an increase in the total mass of hydrogen to 12 g.

For a detailed evaluation of the calculated hydrogen generation it is necessary to use the final results of the post test examination of the bundle. Moreover, the oxidation kinetics needs to be updated for the ORNL cladding material B136Y3, which is the cladding material chosen for the QUENCH-19 bundle.

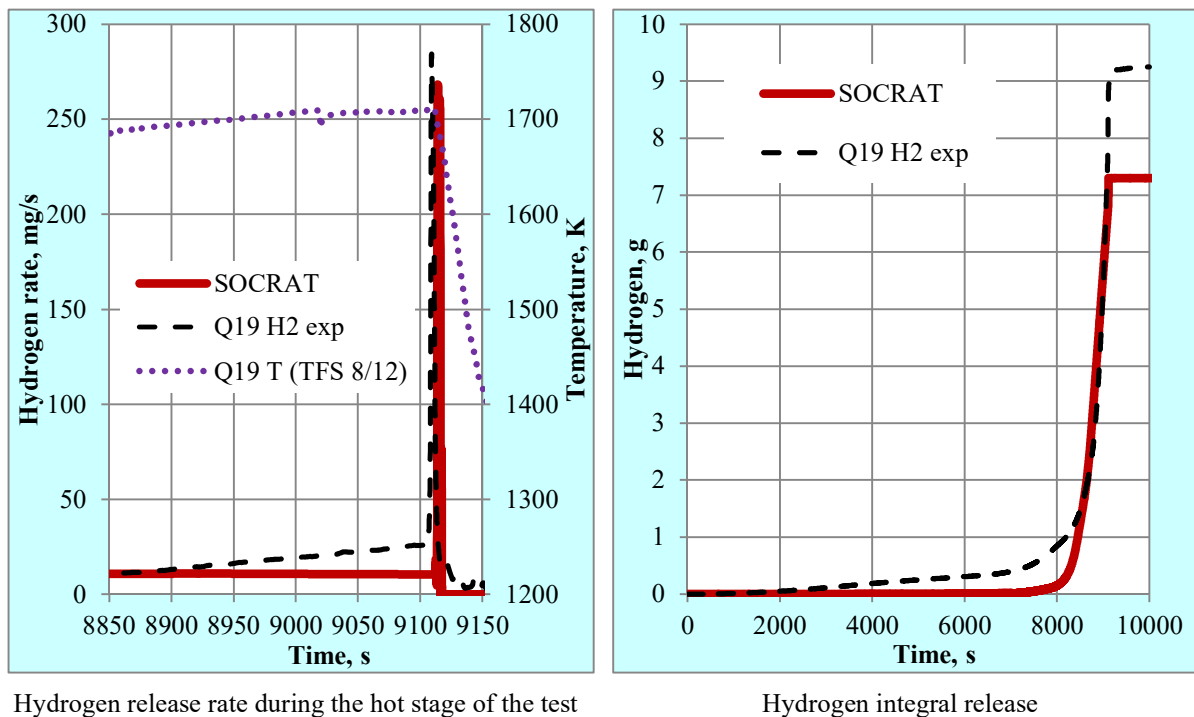


FIG. 179. Simulation (with MIT correlation) and experimental data for hydrogen release in QUENCH-19.

#### 6.4. CONCLUSIONS

The first bundle test performed with FeCrAl cladding tubes under severe accident conditions showed significant reduction of the hydrogen release in comparison to the bundle tests with Zr alloys. However, many tubes in the hot bundle zone were damaged and small pipe segments broke away from them. This degradation phenomenon is likely due to cracking induced by the molten thermocouples under axial stresses and the higher thermal expansion coefficient of FeCrAl alloys in comparison to Zr. It can be qualitatively concluded that FeCrAl shows longer coping time in QUENCH-19 in comparison with the reference test QUENCH-15. Quantitative assessments for reactor conditions should be made with care due to the artificial extension of transient before reflood.

The post test modelling was performed with two systems codes ATHLET-CD and SOCRAT. Both codes described quite well the thermal-hydraulic bundle behaviour. The calculated temperatures of the internal fuel rod simulators were in good agreement with the test results. On the other hand, there is a noticeable overestimation of cladding temperatures for outer rods. However, the radial temperature gradient in this test was significantly higher in comparison to early bundle tests with Zr alloys, which is not yet completely understood.

The second modelled phenomenon was oxidation of FeCrAl bundle materials in steam. The current oxidation kinetics model for FeCrAl led to strong underestimation of the hydrogen release rate during the whole test, and especially at high temperatures before the reflood initiation. Using the few SET experimental data obtained for the temperatures near to the melting point of FeCrAl in modelling simulation showed satisfactory results for the total hydrogen release. More single effect tests at high temperature are needed to obtain the oxidation kinetics for different FeCrAl alloys. In addition, further bundle tests with FeCrAl materials would be useful for severe accident codes benchmark, calibration, and verification.

## CONCLUSIONS AND FUTURE WORK

The overall coordinated research activities were executed successfully for the IAEA CRP on Analysis of Options and Experimental Examination of Fuels for Water-Cooled Reactors with Increased Accident Tolerance. For the coated cladding round robin autoclave testing, it was found that the Cr coating was effective to prevent the zirconium substrate from oxidation for long period of exposure up to 150 days. Future optimization for other coatings such as MAX phase and ZrSi-Cr and AISI 348 SS are needed. The autoclave corrosion test data are consistent in general among three different test labs: Czech Technical University/UJP Praha (CTU), Technical Research Centre of Finland (VTT) and Polish National Institute of Science and Technology (INCT). For high temperature steam oxidation tests, the Cr coating also showed the best protection for zirconium substrates. At 1200°C no oxidation was found for zirconium substrate. At higher temperatures such as 1300 and 1350°C, the zirconium substrate was oxidized and the extent of oxidation depended on the temperature and duration.

Benchmark modelling of the FeCrAl cladding with regular UO<sub>2</sub> fuel was performed using five different fuel performance codes from five different organizations. The calculations performed for normal operating conditions showed good consistency in predicting the cladding mechanical behaviour, especially in open gap conditions before PCMI was established. The BISON, FEMAXI-7 and TRANSURANUS codes showed good consistency in modelling cladding strains and stresses during PCMI. Calculations for fuel pellet behaviour such as centreline temperature, fission gas release, and swelling were less consistent among these codes. LOCA calculations performed using BISON, TRANSURANUS and FEMAXI-7 codes showed that the cladding strain behaviour during the transients to be qualitatively consistent. All calculations suggested that the FeCrAl cladding may be more resistant to ballooning and bursting than Zry-4.

The first severe accident QUENCH bundle test was performed for FeCrAl cladding at KIT, and the post test modelling was performed with two systems codes ATHLET-CD and SOCRAT. Both codes captured the thermohydraulic behaviour for the interior FeCrAl rods reasonably well but overestimated the cladding temperature for exterior rods. Using the current FeCrAl oxidation kinetics, the models underpredicted the hydrogen production significantly compared to the test results. More single effect tests for high temperature oxidation of different FeCrAl alloys are needed.

This CRP has provided significant values to the participating members. For a future CRP, it is recommended that the group focuses on one or two best performing coatings for further investigation. In particular, hydrogen pickup inside the coating and hydrogen transport mechanism through the coating into the substrates should be studied. The benchmark modelling can be extended to coated cladding and SiC, with an emphasis on uncertainty analysis. Modelling of the QUENCH-19 test should continue, with more severe accident codes participating, such as MAAP and MELCOR. The high temperature oxidation data are still needed for FeCrAl. Future QUENCH tests can be extended to coated cladding and SiC cladding.



## REFERENCES

- [1] TERRANI, K.A., ZINKLE, S.J., SNEAD, L.L., Advanced oxidation-resistant iron-based alloys for LWR fuel cladding, *Journal of Nuclear Materials* **448** (2014) 420.
- [2] PINT, B.A., TERRANI, K.A., YAMAMOTO, Y., SNEAD, L.L., Material selection for accident tolerant fuel cladding, *Metall. Mater. Trans. E* **2** (2015) 190.
- [3] TERRANI, K.A., PINT, B.A., UNOCIC, K.A., YANG, Y., SILVA C.M., MEYER, H.M., III, REBAK, R.B., Uniform corrosion of FeCrAl alloys in LWR coolant environments, *Journal of Nuclear Materials* **479** (2016) 36.
- [4] STACHOWSKI, R.E., REBAK, R.B., GASSMANN, W.P., WILLIAMS, J., "Progress of GE development of accident tolerant fuel FeCrAl cladding", *Proceedings of TopFuel*, Boise, ID, USA, 2016.
- [5] McMURRAY, J.W., HU, R., USHAKOV, S.V., SHIN, D., PINT, B.A., TERRANI, K.A., NAVROTSKY, A., Solid-liquid phase equilibria of Fe-Cr-Al alloys and spinels, *Journal of Nuclear Materials* **492** (2017) 128.
- [6] GEORGE, N.M., TERRANI, K.A., POWERS, J., WORRALL, A., MALDONADO, I., Neutronic analysis of candidate accident-tolerant cladding concepts in pressurized water reactors, *Annals of Nuclear Energy* **75** (2015) 703.
- [7] HU, X., TERRANI, K.A., WIRTH, B.D., SNEAD, L.L., Hydrogen permeation in FeCrAl alloys for LWR cladding application, *Journal of Nuclear Materials* **461** (2015) 282–291.
- [8] FIELD, K.G., HOWARD, R., YAMAMOTO, Y., Experimental plan and irradiation target design for FeCrAl embrittlement screening tests conducted using the high flux isotope reactor, *Technical Report ORNL/TM-2015/311*, Oak Ridge National Laboratory (2015).
- [9] YAMAMOTO, Y., PINT, B.A., TERRANI, K.A., FIELD, K.G., YANG, Y., SNEAD, L.L., Development and property evaluation of nuclear grade wrought FeCrAl fuel cladding for light water reactors, *Journal of Nuclear Materials* **467** (2015) 703.
- [10] THOMPSON, Z.T., TERRANI, K.A., YAMAMOTO, Y., Elastic Modulus Measurement of ORNL ATF FeCrAl Alloys, *Technical Report ORNL/TM-2015/632*, Oak Ridge National Laboratory (2015).
- [11] TERRANI, K.A., KARLSEN, T.M., YAMAMOTO, Y., Input correlations for irradiation creep of FeCrAl and SiC based on in-pile Halden test results, *Technical Report ORNL/TM-2016/191*, Oak Ridge National Laboratory, (May 2016).
- [12] MASSEY, C.P., TERRANI, K.A., DRYEPONDT, S.N., PINT, B.A., Cladding burst behavior of Fe-based alloys under LOCA, *Journal of Nuclear Materials* **470** (2016) 128.
- [13] FIELD, K.G., BARRETT, K., SUN, Z., YAMAMOTO, Y., Submission of FeCrAl feedstock for support of AFC ATR-2 irradiations, *Technical Report ORNL/TM-2016/426*, (2016)
- [14] GAMBLE, K.A., BARANI, T., PIZZOCRI, D., HALES, J.D., TERRANI, K.A., PASTORE, G., An investigation of FeCrAl cladding behavior under normal operating and loss of coolant conditions, *Journal of Nuclear Materials* **491** (2017) 55.
- [15] PASTORE, G., GAMBLE, K.A., HALES, J.D., Modeling Benchmark for FeCrAl Cladding in the IAEA CRP ACTOF: FeCrAl-C35M Material Models and Benchmark Cases Specifications, *Technical Report INL/EXT-17-43695*, Idaho National Laboratory (2017).
- [16] Kanthal APMT (Tube) Datasheet (2012), <http://kanthal.com/en/products/material-datasheets/tube/kanthal-apmt/>.
- [17] NIFFENEGGER, M., REICHLIN, K., The proper use of thermal expansion coefficients in finite element calculations, *Nuclear Engineering and Design* **243** (2012) 356.
- [18] YANO, Y., TANNO, T., SEKIO, Y., OKA, H., OHTSUKA, S., UWABA, T., KAITO, T., Tensile properties and hardness of two types of 11Cr-ferritic/martensitic steel after aging up to 45,000 h, *Nuclear Materials and Energy* **9** (2016) 324-330.
- [19] SAUNDERS, S.R.J., EVANS, H.E., LI, M., GOHIL, D.D., OSGERBY, S., Oxidation growth stresses in an alumina-forming ferritic steel measured by creep deflection, *Oxidation of Metals* **48** (1997)189.
- [20] FIELD, K.G., HU, X., LITRELL, K.C., YAMAMOTO, Y., SNEAD, L.L., Radiation tolerance of neutron-irradiated model Fe-Cr-Al alloys, *Journal of Nuclear Materials* **465** (2015) 746.
- [21] ERBACHER, F.J., NEITZEL, H.J., ROSINGER, H., SCHMIDT, H., WIEHR, K., "Burst criterion of Zircaloy fuel claddings in a loss-of-coolant accident", in: *Zirconium in the Nuclear Industry, Fifth Conference*, ASTM STP 754 (Franklin, D.G., Ed.), American Society for Testing and Materials (1982) 271–283.
- [22] WHITE, J.T., NELSON, A.T., DUNWOODY, J.T., BYLER, D.D., SAFARIK, D.J., McCLELLAN, K.J., Thermophysical properties of U<sub>3</sub>Si<sub>2</sub> to 1773K, *Journal of Nuclear Materials* **464** (2015) 275.
- [23] HARP, J.M., HE, L., HOGAN, R.E., WAGNER, A.R., "Corrosion and interdiffusion studies of U<sub>3</sub>Si<sub>2</sub>", in *Proceedings of TopFuel*, Boise, ID, USA, 2016.
- [24] WOOD, E.S., WHITE, J.T., BYLER, D.D., NELSON, A.T., "The synthesis and air oxidation behavior of U-Si-Al and U-Si-B compositions", in *Proceedings of TopFuel*, Boise, ID, USA, 2016.
- [25] WHITE, J.T., WOOD, E.S., DUNWOODY, J.T., NELSON, A.T., "State of knowledge and challenges of U-Si compounds for use in light water reactor accident tolerant fuel designs", in: *Proceedings of TopFuel*, Boise, ID, USA, 2016.
- [26] GODDARD, D.T., MATHERS, D.P., EAVES, D.G., XU, P., LAHODA, E.J., HARP, J.M., "Manufacturability of U<sub>3</sub>Si<sub>2</sub> and its high temperature oxidation behavior", in: *Proceedings of TopFuel*, Boise, ID, USA, 2016.
- [27] FINLAY, M.R., HOFMAN, G.L., SNELGROVE, J.L., Irradiation behaviour of uranium silicide compounds, *Journal of Nuclear Materials* **325** (2004) 118.
- [28] SHIMIZU, H., The properties and irradiation behavior of U<sub>3</sub>Si<sub>2</sub>, *Technical Report NAA-SR-10621*, Atomic International (1965).

- [29] BARANI, T., PASTORE, G., PIZZOCRI, D., ANDERSSON, D.A., MATTHEWS, C., ALFONSI, A., GAMBLE, K., VAN UFFELEN, P., LUZZI, L., HALES, J.D., Multiscale modeling of fission gas behavior in  $U_3Si_2$  under LWR conditions, *Journal of Nuclear Materials* (2019) (submitted).
- [30] HARP, J.M., CAPPIA, F., CAPRIOTTI, L., Postirradiation Examination of the ATF-1 Experiments – 2018 Status, Technical Report INL/EXT-18-51497, NTRD-FUEL-2018-000054 (2018).
- [31] Update to the  $U_3Si_2$  Property Handbook, Technical Report NTRD-M3NT-18LA020201033 LA-UR-18-28719, Los Alamos National Laboratory (2018).
- [32] KNACKE, O., KUBASCHEWSKI, O., HESSELMANN, K., "Thermochemical properties of inorganic substances", Berlin Heidelberg: Springer (1991) 1-2541 pp.
- [33] WHITE, J.T., NELSON, A.T., DUNWOODY, J.T., SAFARIK, D.J., McCLELLAN, K.J., Corrigendum to Thermophysical Properties of  $U_3Si_2$  to 1777 K, *Journal of Nuclear Materials* **484** (2017) 386.
- [34] MOHAMAD, A., OHISHI, Y., MUTA, H., KUROSAKI, K., YAMANAKA, S., Thermal and mechanical properties of polycrystalline  $U_3Si_2$  synthesized by spark plasma sintering, *Journal of Nuclear Science and Technology* **55** (2018) 1141.
- [35] ANTONIO, D., SHRESTHA, K., HARP, J., ADKINS, C., ZHANG, Y., CARMACK, J., GOFRYK, K., Thermal and transport properties of  $U_3Si_2$ , *Journal of Nuclear Material* **508** (2018) 154.
- [36] TAYLOR, K.M., McMURTRY, C.H., Synthesis and Fabrication of Refractory Uranium Compounds, Summary Report ORO-400 United States of America (1961).
- [37] CARVAJAL-NUNEZ, U., SALEH, T., WHITE, J., BAIOROV, B., NELSON, A., Determination of elastic properties of polycrystalline  $U_3Si_2$  using resonant ultrasound spectroscopy, *Journal of Nuclear Materials* **498** (2018) 438.
- [38] GAMBLE, K.A., HALES, J.D., PASTORE, G., Nuclear Energy Advanced Modeling and Simulation (NEAMS) Accident Tolerant Fuels High Impact Problem:  $U_3Si_2$  Modeling Capabilities, Technical Report INL/EXT-17-43117, Idaho National Laboratory, USA (2017).
- [39] HOFMAN, G.L., RYU, W. S., Detailed Analysis of Uranium Silicide Dispersion Fuel Swelling, Technical Report CONF-8909141-10, Argonne National Laboratory (1989).
- [40] MIAO, Y., GAMBLE, K.A., ANDERSSON, D., YE, B., MEI, Z., HOFMAN, G., YACOUT, A.M., Gaseous swelling of  $U_3Si_2$  during steady-state LWR operation: A rate theory investigation, *Nuclear Engineering and Design* **322** (2017) 336.
- [41] DECK, C.P., JACOBSEN, G.M., SHEEDER, J., GUTIERREZ, O., ZHANG, J., STONE, J., KHALIFA, H.E., BACK, C.A., Characterization of SiC-SiC composites for accident tolerant fuel cladding, *Journal of Nuclear Materials* **466** (2015) 667-681.
- [42] ZINKLE, S.J., TERRANI, K.A., GEHIN, J.C., OTT, L.J., SNEAD, L.L., Accident tolerant fuels for LWRs: A perspective, *Journal of Nuclear Materials* **448** (2014) 374-379.
- [43] KURATA, M., Research and Development Methodology for Practical Use of Accident Tolerant Fuel in Light Water Reactors, *Nuclear Engineering and Technology* **48** (2016) 26-32.
- [44] KIM, H.-G., YANG, J.-H., KIM, W.-J., KOO, Y.-H., Development Status of Accident-tolerant Fuel for Light Water Reactors in Korea, *Nuclear Engineering and Technology* **48** (2016) 1-15.
- [45] OTT, L.J., ROBB, K.R., WANG, D., Preliminary assessment of accident-tolerant fuels on LWR performance during normal operation and under DB and BDB accident conditions, *Journal of Nuclear Materials* **448** (2014) 520-533.
- [46] PINT, B.A., TERRANI, K.A., YAMAMOTO, Y., SNEAD, L.L., Material Selection for Accident Tolerant Fuel Cladding, *Metallurgical and Materials Transactions E* **2E** (2015).
- [47] DUAN, Z., YANG, H., SATOH, Y., MURAKAMI, K., KANO, S., ZHAO, Z., SHEN, J., ABE, H., Current status of materials development of nuclear fuel cladding tubes for light water reactors, *Nucl. Eng. Des.* **316** (2017) 131-150.
- [48] ASTM "Test Methods for Determining the Inclusion Content of Steel."
- [49] ASTM "Practice for Microetching Metals and Alloys."
- [50] ASTM "Practices for Detecting Susceptibility to Intergranular Attack in Austenitic Stainless Steels."
- [51] ASTM "Test Methods for Determining Average Grain Size."
- [52] KREJCI, J., SEVECEK, M., CVRCEK, L., Development of Chromium and Chromium Nitride Coated Cladding for VVER Reactors, WRFPM (2017).
- [53] TANG, C., et al., Deposition, characterization and high temperature steam oxidation behavior of single-phase  $Ti_2AlC$ -coated Zircaloy-4, *Corros. Sci.*, **135** (May 2018) 87-98,
- [54] KREJČÍ, J. et al., "Experimental behavior of Chromium-based coatings", Top Fuel 2018 - React. Fuel Perform., Paper A0233, Prague, Czech Republic (30.09.2018 - 4.10.2018).
- [55] KREJČÍ, J., ŠEVEČEK, M., CVRCEK, L., KABÁTOVÁ, J., MANOCH, F., "Chromium and Chromium Nitride Coated Cladding for Nuclear Reactor Fuel", in Proceedings of the 20th International Corrosion Congress, EUROCORR 2017, Prague, Czech Republic (2017).
- [56] TANG, C., et al., Synthesis and characterization of  $Ti_2AlC$  coatings by magnetron sputtering from three elemental targets and ex-situ annealing, *Surf. Coat. Technol* **309** (Jan. 2017) 445-455.
- [57] TANG, C., et al., Deposition, characterization and high temperature steam oxidation behavior of single-phase  $Ti_2AlC$ -coated Zircaloy-4, *Corros. Sci.* **135** (May 2018) 87-98.
- [58] EPRI NP-7077. PWR Primary Water Chemistry Guidelines: Revision 2. Palo Alto, CA: Electric Power Research Institute (1990).
- [59] ALLEN, T., BUSBY, J., MEYER, M., PETTI, D., Materials challenges for nuclear systems. *Materials Today* **13** 12 (2010) 14-23.

- [60] ALLEN, T.R., KONINGS, R.J.M., MOTTA, A.T., Corrosion of zirconium alloys (KONINGS, R.J.M., Ed.), Amsterdam Elsevier, Comprehensive nuclear materials **5**, (2012) 49-68.
- [61] BARSOUM, M.W., "MAX phases: Properties of machinable ternary carbides and nitrides." Weinheim, Germany, Wiley-VCH Verlag GmbH & KGaA (2013).
- [62] CHAIA, N., MATHIEU, S., ROUILLARD, F., VILASI, M., The ability of silicide coating to delay the catastrophic oxidation of vanadium under severe conditions. *J. Nucl. Mater.* **457** (2015) 124-129.
- [63] EPRI. PWR primary water chemistry guidelines. Revision 2. Palo Alto, CA, Electric Power Research Institute. Report EPRI NP-7077 (1990).
- [64] INTERNATIONAL ATOMIC ENERGY AGENCY, Accident tolerant fuel concepts for light water reactors (Proc. of a Technical Meeting held at Oak Ridge National Laboratories, USA, 13-16 October 2014.), IAEA-TECDOC-1797, IAEA, Vienna (2016).
- [65] KRZEŚNIAK, A., SARTOWSKA, B., STAROSTA, W., WALIŚ, L., SMOLIK, J., MIŁKOWSKA, M., Silicon concentration changes in Zry-2 coated with Zr-Si and ZrSi<sub>2</sub>-Cr during the autoclave oxidation tests (Proceedings of the 24th International Quench Workshop, Karlsruhe Institute of Technology KIT, Germany, 13-15.11.2018), (STEINBRUCK, M., Ed), Germany (2018).
- [66] LEE, Y.H., McKRELL, T., KAZIMI, M.S., Safety of light water reactor fuel with silicon carbide cladding. Massachusetts Institute of Technology. Advanced Nuclear Power Programme. MIT-ANP-TR-150 (2014).
- [67] MARIANI, R.D., MEDVEDEV, P., PORTER, D.L., HAYES, S.L., COLE, J.I., BAI, X.M., "Novel accident-tolerant fuel meat and cladding." In LWR Fuel Performance Meeting Top Fuel 2013 Charlotte, North Carolina, United States of America, 15-19 September 2013. Idaho Falls, Idaho, Idaho National Laboratory (2013) 763-770.
- [68] MASSALSKI, T.B., OKAMOTO, H., SUBRAMANIAN, P.R., KACPRZAK, L., Eds, "Binary alloy phase diagrams" 2nd edn, ASM International, Vol. 1 (1990). 3383-3385.
- [69] SARTOWSKA, B., STAROSTA, W., WALIŚ, L., MIŁKOWSKA, M., BARLAK, M., KOŁODZIEJCZAK, P., SMOLIK, J., RYDZEWSKI, M., TOMASSI, P., "Accident Tolerant Materials – Ideas and Research Directions", 23rd International QUENCH Workshop, 17-19 October 2017, Karlsruhe Institute of Technology, Karlsruhe, Germany (2017) 668-688.
- [70] SARTOWSKA, B., STAROSTA, W., WALIŚ, L., KRZEŚNIAK, A., SMOLIK, J., MIZERACKI, J., "Zirconium alloy coatings with Si based compounds - inct experiments", Proceedings of the 24th International Quench Workshop, Karlsruhe Institute of Technology KIT, Germany, 13-15.11.2018.
- [71] STAROSTA, W., BARLAK, M., BUCZKOWSKI, M., KOSIŃSKA, A., SARTOWSKA, B., WALIŚ, L., JANIĄK, T., Analiza mechanizmów tworzenia się oraz właściwości warstw tlenkowych powstających w wyniku rozkładu wody na powierzchni koszulek cyrkonowych oraz zbadanie wpływu modyfikacji struktury warstwy wierzchniej koszulek na procesy generacji wodoru. In: Analiza procesów generacji wodoru w reaktorze jądrowym w trakcie normalnej eksploatacji i w sytuacjach awaryjnych z propozycjami działań na rzecz podniesienia poziomu bezpieczeństwa jądrowego Warszawa, Instytut Chemii i Techniki Jądrowej (2015) 55-72.
- [72] STAROSTA, W., SEMINA, V.K., SMOLIK, J., WALIŚ, L., RYDZEWSKI, M., SARTOWSKA, B., Studies on magnetron-sputtered zirconium-silicide coatings deposited on zirconium alloy for the enhancement of their high temperature oxidation resistance, *Nukleonika* **63** 3 (2018) 73-79.
- [73] TANG, C., STUEBER, M., SEIFERT, H.J., STEINBRÜCK, M., Protective coatings on zirconium-based alloys as accident-tolerant fuel (ATF) claddings, *Corros. Rev.* **35** 3 (2017) 141-165.
- [74] TERRANI, K.A., ZINKLE, S.J., SNEAD, L.L., Advanced oxidation-resistant iron-based alloys for LWR fuel cladding, *J. Nucl. Mater.* **448** (2014) 420-435.
- [75] US DEPARTMENT OF ENERGY, Development of self-healing zirconium-silicide coatings for improved performance zirconium-alloy fuel cladding. Final report. Nuclear Energy University Programme grant No. DE-NE 0008300, (2018).
- [76] YEOM, H., LOCKHART, C., MARIANI, R., XU, P., CORRADINI, M., SRIDHARAN, K., Evaluation of steam corrosion and water quenching behavior of zirconium-silicide coated LWR fuel claddings, *J. Nucl. Mater.* **499** (2018) 256-267.
- [77] YUEH, K., TERRANI, K.A., Silicon carbide composite for light water reactor fuel assembly applications, *J. Nucl. Mater.* **448** (2014) 380-388.
- [78] ZINKLE, S.J., TERRANI, K.A., GEHIN, J.C., OTT, L.J., SNEAD, L.L., Accident tolerant fuels: a perspective, *J. Nucl. Mater.* **448** (2014) 374-379.
- [79] PAWEL, R.E., CATHCART, J.V., McKEE, R.A., The Kinetics of Oxidation of Zircaloy-4 in Steam at High Temperatures, *J. Electrochem. Soc.* **126** 7 (Jan. 1979) 1105-1111.
- [80] ŠEVEČEK, M., et al., Development of Cr cold spray-coated fuel cladding with enhanced accident tolerance, *Nucl. Eng. Technol.* **50** 2 (Mar. 2018) 229-236.
- [81] TANG, C., STEINBRÜCK, M., GROBE, M., Interlaboratory test in ACTOF project — High temperature steam oxidation test in KIT, Institute for Applied Materials (IAM), Karlsruhe Institute of Technology (KIT), D-76021 Karlsruhe, Germany.
- [82] PENTTILÄ, S., AUTIO, J.-M., LYDMAN, J., TAPPER, U., Performance of candidate ATF cladding materials in simulated high temperature steam and normal LWR conditions - Results of IAEA Coordinated Research Project "Analysis of Options and Experimental Examination of Fuels for Water Cooled Reactors with Increased Accident Tolerance" ACTOF.

- [83] KWON, Y., CORBET, J., The zirconium-tin system, with particular attention to the  $Zr_5Sn_3$ - $Zr_5Sn_4$  Region and  $Zr_4Sn$ , *Chemistry of Materials* **2** 1 (January 1990) 27-33.
- [84] BAYKOV, V., et al., Structural stability of intermetallic phases in the Zr-Sn system, *Scripta Materialia* **55** (2006) 485-488.
- [85] McPHERSON, D.J., HANSEN, M., The System Zirconium-Tin, *Transactions ASM* **45** (1953) 915-933.
- [86] GRAN, G., ANDERSSON, S., The Crystal Structures of  $Zr_5Sn_3$  and  $Zr_3Sn$ , *Acta Chemica Scandinavica* **14** (1960) 956.
- [87] LUO, H.L., VIELHABER, E., CORENZWIT, E., Occurrence of A-15 Phases, *Zeitschrift für Physik* **230** (1970) 443-448.
- [88] NAIK, V., BANERJEE, S., Precipitation in Dilute Zr-Sn Alloys, *Trans. Indian Institute of Metals* **31** (1978) 318.
- [89] KWON, Y.-U., CORBETT, J.D., Influence of Oxygen on the Stability of  $Zr_4Sn$ , *Chemistry of Materials* **4** (1992) 187.
- [90] ARIAS, D., ROBERTY, L., The solubility of tin in  $\alpha$  and  $\beta$  zirconium below 1000°C, *Journal of Nuclear Materials* **118** (1983) 143.
- [91] CARMACK, J., GOLDNER, F., BRAGG-SITTON, S. M., SNEAD, L. L., Top Fuel 2013, North Carolina, Charlotte (15.09.2013-19.09.2013) 734.
- [92] PINT, B. A., TERRANI, K. A., BRADY, M. P., CHENG, T., KEISER, J. R., *J. of Nuclear Materials* **440** (2013) 420.
- [93] TERRANI, K. A., ZINKEL, S. J., SNEAD, L. L., Advanced oxidation-resistant iron-based alloys for LWR fuel cladding, *J of Nuclear Materials* **448** 1-3 (2013) 420-435.
- [94] KIM, H. G., KIM, II-H., JUNG, Y-II., PARK, D. J., PARK, Y. Y., KOO, Y. H., Adhesion property and high temperature oxidation behavior of Cr-coated Zircaloy-4 cladding tube prepared by 3D laser coating, *J. of Nuclear Materials* **465** (October 2015) 531-539.
- [95] WANG, Y., ZHOU, W., WEN, Q., RUAN, X., LUO, F.A, BAI, G., QING, Y., ZHU, D., ZHANG, Y., LIU, T., LI, R., Behavior of plasma sprayed Cr coatings and FeCrAl coatings on Zr fuel cladding under loss-of-coolant accident conditions, *Surface & Coatings Technology* **344** (2018) 141-148.
- [96] HÓZER, Z., GYÖRI, C.S., MATUS, L., HORVÁTH, M., Ductile-to-brittle transition of oxidised Zircaloy-4 and E110 claddings, *Journal of Nuclear Materials* **373** (2008) 415-423.
- [97] KIRÁLY, M., KULACSY, K., HÓZER, Z., PEREZ-FERÓ, E., NOVOTNY, T., High temperature steam oxidation kinetics of the E110G cladding alloy, *Journal of Nuclear Materials*, **475** (2016) 27-36.
- [98] XU, P., Meeting Report of the 2nd Research Coordination Meeting related to the IAEA Coordinated Research Project T12030 on Analysis of Options and Experimental Examination of Fuels for Water cooled Reactors with Increased Accident Tolerance (ACTOF), Technical Report, IAEA, (2017).
- [99] YAMAMOTO, Y., PINT, B.A., TERRANI, K.A., FIELD, K.G., YANG, Y., SNEAD, L.L., Development and property evaluation of nuclear grade wrought FeCrAl fuel cladding for light water reactors, *Journal of Nuclear Materials* **467** (2015) 703.
- [100] THOMPSON, Z.T., TERRANI, K.A., YAMAMOTO, Y., Elastic Modulus Measurement of ORNL ATF FeCrAl Alloys, Technical Report ORNL/TM-2015/632, Oak Ridge National Laboratory (2015).
- [101] MASSEY, C.P., TERRANI, K.A., DRYEPONDT, S.N., PINT, B.A., Cladding burst behavior of Fe-based alloys under LOCA, *Journal of Nuclear Materials* **470** (2016) 128.
- [102] TERRANI, K.A., PINT, B.A., UNOCIC, K.A., YANG, Y., SILVA, C.M., MEYER, H.M., III, REBAK, R.B., Uniform corrosion of FeCrAl alloys in LWR coolant environments, *Journal of Nuclear Materials* **479** (2016) 36.
- [103] TERRANI, K.A., KARLSEN, T.M., YAMAMOTO, Y., Input correlations for irradiation creep of FeCrAl and SiC based on in-pile Halden test results, Technical Report ORNL/TM-2016/191, Oak Ridge National Laboratory (May 2016).
- [104] FIELD, K.G., HOWARD, R., YAMAMOTO, Y., Experimental plan and irradiation target design for FeCrAl embrittlement screening tests conducted using the high flux isotope reactor, Technical Report ORNL/TM-2015/311, Oak Ridge National Laboratory (2015).
- [105] GAMBLE, K.A., BARANI, T., PIZZOCRI, D., HALES, J.D., TERRANI, K.A., PASTORE, G., An investigation of FeCrAl cladding behavior under normal operating and loss of coolant conditions, *Journal of Nuclear Materials* **491** (2017) 55.
- [106] PASTORE, G., GAMBLE, K.A., HALES, J.D., Modeling Benchmark for FeCrAl Cladding in the IAEA CRP ACTOF: FeCrAl-C35M Material Models and Benchmark Cases Specifications, Technical Report INL/EXT-17-43695, Idaho National Laboratory, (2017).
- [107] GEORGE, N.M., TERRANI, K.A., POWERS, J., WORRALL, A., MALDONADO, I., Neutronic analysis of candidate accident-tolerant cladding concepts in pressurized water reactors, *Annals of Nuclear Energy* **75** (2015) 703.
- [108] PEREZ-FERÓ, E., HÓZER, Z., NOVOTNY, T., KRACZ, G., HORVÁTH, M., NAGY, I., VIMI, A., PINTÉR-CSORDÁS, A., GYÖRI C.S., MATUS, L., VASÁROS, L., WINDBERG, P., MARÓTI, L., Technical Report EK-FRL-2012-255-01/02, Center for Energy Research, Hungarian Academy of Sciences, Budapest, Hungary (2013).
- [109] INTERNATIONAL ATOMIC ENERGY AGENCY, Fuel Modelling in Accident Conditions (FUMAC), Final Report of a Coordinated Research Project – CRP T12028 (2014–2018), Technical Report IAEA-TECDOC-1889, IAEA, Vienna (2019).
- [110] WILLIAMSON, R.L., HALES, J.D., NOVASCONE, S. R., TONKS, M.R., GASTON, D.R., PERMANN C.J., ANDRS, D., MARTINEAU, R.C., Multidimensional multiphysics simulation of nuclear fuel behavior, *Journal of Nuclear Materials* **423** (2012) 149.
- [111] GASTON, D., NEWMAN, C., HANSEN, G., LEBRUN-GRANDIÉ, D., MOOSE: A parallel computational framework for coupled systems of nonlinear equations, *Nuclear Engineering and Design* **239** (2009) 1768.
- [112] RASHID, M.M., Incremental kinematics for finite element applications, *International Journal of Numerical Methods and Engineering* **36** (1993) 3937.

- [113] HALES, J.D., WILLIAMSON, R.L., NOVASCONE, S.R., PASTORE, G., SPENCER, B.W., STAFFORD, D.S., GAMBLE, K.A., PEREZ, D.M., GARDNER, R.J., LIU, W., GALLOWAY, J., MATTHEWS, C., UNAL, C., CARLSON, N., BISON theory manual: The equations behind nuclear fuel analysis, Technical Report INL/EXT-13-29930 Rev. 3, Idaho National Laboratory (2016).
- [114] PASTORE, G., SWILER, L.P., HALES, J.D., NOVASCONE, S.R., PEREZ, D.M., SPENCER, B.W., LUZZI, L., VAN UFFELEN, P., WILLIAMSON, R.L., Uncertainty and sensitivity analysis of fission gas behavior in engineering-scale fuel modeling, *Journal of Nuclear Materials* **465** (2015) 398.
- [115] WILLIAMSON, R.L., GAMBLE, K.A., PEREZ, D.M., NOVASCONE, S.R., PASTORE, G., GARDNER, R.J., HALES, J.D., LIU, W., MAI, A., Validating the BISON fuel performance code to integral LWR experiments, *Nuclear Engineering and Design* **301** (2016) 232.
- [116] Assessment of BISON: A Nuclear Fuel Performance Analysis Code. BISON Release 1.3, Technical Report INL/MIS-13-30314 Rev. 3, Idaho National Laboratory (2016).
- [117] PASTORE, G., NOVASCONE, S.R., WILLIAMSON, R.L., HALES, J.D., SPENCER, B.W., STAFFORD, D.S., "Modelling of fuel behaviour during loss-of-coolant accidents using the BISON code", in Proc. of the LWR Fuel Performance Meeting, Zurich, Switzerland, September 13–17, 2015.
- [118] PASTORE, G., WILLIAMSON, R.L., NOVASCONE, S.R., SPENCER, B.W., HALES, J.D., "Modelling of LOCA tests with the BISON fuel performance code", in Enlarged Halden Programme Group Meeting, Fornebu, Norway, May 8–13, 2016.
- [119] WILLIAMSON, R.L., FOLSOM, C.P., PASTORE, G., VEEARAGHAVAN, S., Reactivity insertion accident (RIA) capability status in the BISON fuel performance code, Technical Report CASL-X-2016-1104-000, Consortium for Advanced Simulation of LWRs (2016).
- [120] PASTORE, G., FOLSOM, C.P., WILLIAMSON, R.L., HALES, J.D., LUZZI, L., PIZZOCRI, D., BARANI, T., "Modelling fission gas behaviour with the BISON fuel performance code", in Enlarged Halden Programme Group Meeting, Lillehammer, Norway, September 24–29, 2017.
- [121] HALES, J.D., WILLIAMSON, R.L., NOVASCONE, S.R., PEREZ, D.M., SPENCER, B.W., PASTORE, G., Multidimensional Multiphysics Simulation of TRISO Particle Fuel, *Journal of Nuclear Materials* **443** (2013) 531.
- [122] LASSMANN, K., URANUS - A computer programme for the thermal and mechanical analysis of the fuel rods in a nuclear reactor, *Nuclear Engineering and Design* **45** (1978) 325.
- [123] LASSMANN, K., TRANSURANUS - A fuel rod analysis code ready for use, *Journal of Nuclear Materials* **188** (1992) 295.
- [124] LASSMANN, K., RONCHI, C., SMALL, G.J., The development of fuel performance models at the European Institute for Transuranium Elements, *Journal of Nuclear Materials* **166** (1989) 112.
- [125] LASSMANN, K., O'CARROL, C., VAN DE LAAR, J., WALKER, C. T., The radial distribution of plutonium in high burnup UO<sub>2</sub> fuels, *Journal of Nuclear Materials* **208** (1994) 223.
- [126] LASSMANN, K., WALKER, C.T., VAN DE LAAR, J., LINDSTRÖM, F., Modelling the high burnup UO<sub>2</sub> structure in LWR fuel, *Journal of Nuclear Materials* **226** (1995) 1.
- [127] LASSMANN, K., VAN DE LAAR, J., "The Transient TRANSURANUS version", Proceedings of IAEA RER/4/019, Licensing Fuel and Fuel Modelling Codes for WWER Reactors, Seminar "Implementation of the WWER version of the TRANSURANUS code and its application to safety criteria", Sofia, Bulgaria, 7-11 December 1998.
- [128] VAN UFFELEN, P., GYORI, C., SCHUBERT, A., VAN DE LAAR, J., HOZER, Z., SPYKMAN, G., Extending the application range of a fuel performance code from normal operating to design basis accident conditions, *Journal of Nuclear Materials* **383** (2008) 137.
- [129] GYORI, C., HÖZER, Z., LASSMANN, K., SCHUBERT, A., VAN DE LAAR, J., HATALA, B., CVAN, M., Extension of Transuranus code applicability with Niobium containing cladding models (EXTRA) , Final Report, EVOL-EXTRA-D5 / FIKS-CT2001-00173 (2004).
- [130] SPYKMAN, G., MÄRTENS, D., BOUR, D., KOCK, P., LASSMANN, K., SCHUBERT, A., VAN DE LAAR, J., "Implementation of a Cladding Failure Model for a Loss of Coolant Accident (LOCA)-Analysis in Transuranus", Proceedings of Enlarged Halden Programme Group Meeting on High Burn-up Fuel Performance, Safety and Reliability, Sandefjord, Norway, 9-14 May 2004.
- [131] DI MARCELLO, V., SCHUBERT, A., VAN DE LAAR, J., VAN UFFELEN, P., The TRANSURANUS mechanical model for large strain analysis, *Nuclear Engineering and Design* **276** (2014) 19.
- [132] PASTORE, G., LUZZI, L., DI MARCELLO, V., VAN UFFELEN, P., Physics-based modelling of fission gas swelling and release in UO<sub>2</sub> applied to integral fuel rod analysis, *Nuclear Engineering and Design* **256** (2013) 75.
- [133] DI MARCELLO, V., RONDINELLA, V., SCHUBERT, A., VAN DE LAAR, J., VAN UFFELEN, P., Modelling actinide redistribution in mixed oxide fuel for sodium fast reactors, *Progress in Nuclear Energy* **72** (2014) 83.
- [134] DI MARCELLO, V., SCHUBERT, A., VAN DE LAAR, J., VAN UFFELEN, P., Extension of the TRANSURANUS plutonium redistribution model for fast reactor performance analysis, *Nuclear Engineering and Design* **248** (2012) 149.
- [135] LASSMANN, K., HOHLEFELD, F., The revised URGAP model to describe the gap conductance between fuel and cladding, *Nuclear Engineering and Design* **103** (1987) 215.
- [136] SCHUBERT, A., VAN UFFELEN, P., VAN DE LAAR, J., WALKER, C.T., HAECK, W., Extension of the TRANSURANUS burn-up model, *Journal of Nuclear Materials* **376** (2008) 1.
- [137] ICHIKAWA, M., "On the theory of FEMAXI, an axisymmetric finite element programme for analysis of local deformations of operating fuel rods", HIR-93, 1978.
- [138] SUZUKI, M., SAITOU, H., UDAGAWA, Y., NAGASE, F., "Light Water Reactor Fuel Analysis Code FEMAXI-7; Model and Structure", JAEA-Data/Code 2013-005, July 2013.
- [139] SUZUKI, M., SAITOU, H., UDAGAWA, Y., NAGASE, F., "Input/Output Manual of Light Water Reactor Fuel Analysis Code FEMAXI-7 and Its Related Codes", JAEA-Data/Code, 2013-009 (October 2013).

- [140] TVERBERG, T., WIESENACK, W., "Thermal Performance of High Burnup Fuel – In-pile Temperature Data and Analysis–", in Proc. 2000 Int. Topical Mtg. on LWR Fuel, Park City, USA (2000).
- [141] "MATPRO-09, A Handbook of Materials Properties for Use in the Analysis of Light Water Reactor Fuel Rod Behavior", USNRC TREE NUREG-1005 (1976).
- [142] HAGRMAN, D.L., REYMANN, G.A., "MATPRO-Version11, A Handbook of Materials properties for use in the analysis of light water reactor fuel rod behavior", NUREG/CR-0497, TREE-1280, Rev.3 (1979).
- [143] TACHIBANA, T., FURUYA, H., KOIZUMI, M., Dependence on Strain Rate and Temperature Shown by Yield Stress of Uranium Dioxide, *J. Nucl. Sci. Technol.* **13** (1976) 497.
- [144] ITOH, K., IWASAKI, R., IWANO, Y., Finite Element Model for Analysis of Fission Gas Release from UO<sub>2</sub> Fuel, *J. Nucl. Sci. Technol.* **22** (1985) 129.
- [145] GEELHOOD, K., LUSCHER, W., RAYNAUD, P., PORTER, I., FRAPCON-4.0: A Computer Code for the Calculation of Steady-state, Thermal-Mechanical Behavior of Oxide Fuel Rods for High Burnup, Technical Report PNNL-19418, Vol. 1, Rev.2, Pacific Northwest National Laboratory, USA (2015).
- [146] MARINO, A.C., SAVINO, E.J., HARRIAGUE, S., BaCo (BARra COmbustible) Code Version 2.20: a thermo-mechanical description of a nuclear fuel rod, *Journal of Nuclear Materials* **229** (1996) 155.
- [147] MARINO, A.C., Starting Point, Keys and Milestones of a Computer Code for the Simulation of the Behaviour of a Nuclear Fuel Rod, *Science and Technology of Nuclear Installations* (2011).
- [148] SAH, D.N., VISWANATHAN, U.K., VISWANATHAN, C.S., UNNIKRISHNAN, K., RATH, B.N., Blind Prediction exercise on modelling of PHWR fuel at extended burnup, *Journal of Nuclear Materials* **383** (2008) 144.
- [149] ROSSITER, G., MASSARA, S., AMAYA, M., BOLDT F., COZZO, C., DENIS, A., DOSTAL, M., HE, X., HERRANZ, L., KOZLOWSKI, T., KRUPKIN, A., MARCHAND, O., MARELLE, V., MARINO, A., ORTEGO, P., POWERS J., PRUDIL, A., ROZZIA, D., SCHUBERT, A., VESHCHUNOV, M., WIESENACK, W., WILLIAMSON, R., ZHANG, J., OECD/NEA benchmark on pellet-clad mechanical interaction modelling with fuel performance codes, OECD/NEA Workshop on Pellet cladding Interaction (PCI) in Water cooled Reactors, Lucca, Italy (2016).
- [150] MARINO, A.C., "Computer simulation of the behaviour and performance of a CANDU fuel rod", in Proceedings of the 5th International Conference on CANDU Fuel, Toronto, Canada, September 1997.
- [151] MARINO, A.C., FLORIDO, P.C, High power ramping in commercial PHWR fuel at extended burnup, *Nuclear Engineering and Design* **236** 13 (2006) 1371.
- [152] BOADO MAGAN, H., et al., CAREM Projects Status, *Science and Technology of Nuclear Installations* (2011).
- [153] MARINO, A.C., ADELFIANG, P., PÉREZ E.E., Irradiation of Argentine MOX fuels. Post-irradiation results and experimental analysis with the BaCo code, *Journal of Nuclear Materials* **229** (1996) 169.
- [154] BRASNAROF, D.O., et al, A New Fuel Design for Two Different HW Type Reactors, *Science and Technology of Nuclear Installations* (2011).
- [155] MARINO, A.C., "Crack and dishing evolution models and PCI-SCC considerations for fuel pellets in a quasi-bidimensional environment", in Proceedings of the Les Journées de Cadarache 2004, International Seminar on Pellet-Clad Interaction in Water Reactor Fuels, Aix en Provence, France (2004).
- [156] DEMARCO, G.L., MARINO, A.C., 3D Finite Elements Modelling for Design and Performance Analysis of UO<sub>2</sub> Pellets, *Science and Technology of Nuclear Installations* (2011).
- [157] MARINO, A.C., et al., "Sensitivity analysis applied to nuclear fuel performance related to fabrication parameters and experiments", in Proceedings of the 14th International Conference on Structural Mechanics in Reactor Technology, Lyon, France, August 1997.
- [158] MARINO, A.C., "An overview of the dry storage of nuclear fuels with the BaCo code", Proceedings of the 8th International Conference on WWR Fuel Performance, Modelling and Experimental Support, Helena Resort near Burgas, Bulgaria, September 26-October 4, 2009.
- [159] BARANI, T., PIZZOCRI, D., PASTORE, G., LUZZI, L., HALES, J.D., Isotropic softening model for fuel cracking in BISON, *Nuclear Engineering and Design* **342** (2019) 257.
- [160] INTERNATIONAL ATOMIC ENERGY AGENCY, Waterside Corrosion of Zirconium Alloys in Nuclear Power Plants, IAEA-TECDOC-996, IAEA, Vienna (1998)
- [161] VITANZA, C., GRAZIANI, U., FORDESTROMMEN, N.T., VILPPONEN, K.O., "Fission Gas Release from in-pile Measurements", in Proceedings of Enlarged Halden Programme Group Meeting, Vol. HPR-221.10, OECD Halden Reactor Project, Loen, Norway, 1978.
- [162] WALKER, C.T., KNAPPIK, P., MOGENSEN, M., Concerning the development of grain face bubbles and fission gas release in UO<sub>2</sub> fuel, *Journal of Nuclear Materials* **160** (1988) 10.
- [163] PASTORE, G., PIZZOCRI, D., HALES, J. D., NOVASCONE, S.R., PEREZ, D.M., SPENCER, B.W, WILLIAMSON, R.L., VAN UFFELEN, P., LUZZI, L., "Modelling of Transient Fission Gas Behaviour in Oxide Fuel and Application to the BISON Code", in Proceedings of Enlarged Halden Programme Group Meeting, OECD Halden Reactor Project, Rorøs, Norway, 7-12 September 2014.
- [164] BARANI, T., BRUSCHI, E., PIZZOCRI, D., PASTORE, G., VAN UFFELEN, P., WILLIAMSON, R.L., Analysis of transient fission gas behaviour in oxide fuel using BISON and TRANSURANUS, *Journal of Nuclear Materials* **486** (2017) 96.
- [165] PINT, B.A., TERRANI, K.A., BRADY, M.P., CHENG, T., KEISER, J.R., High temperature oxidation of fuel cladding candidate materials in steam-hydrogen environments, *Journal of Nuclear Materials* **440** (2013) 420–427.
- [166] UNOCIC, K.A., YAMAMOTO, Y., PINT, B.A., Effect of Al and Cr Content on Air and Steam Oxidation of FeCrAl Alloys and Commercial APMT Alloy, *Oxidation of Metals* **87** (2017) 431–441.
- [167] PINT, B.A., TERRANI, K.A., YAMAMOTO, Y., SNEAD, L.L., Material Selection for Accident Tolerant Fuel Cladding, *Metallurgical and Materials Transactions E* **2** (2015) 190-196.

- [168] FIELD, K.G., SNEAD, M.A., YAMAMOTO, Y., TERRANI, K.A., Handbook on the Material Properties of FeCrAl Alloys for Nuclear Power Production Applications, Report ORNL/SPR-2018/905.
- [169] ROBB, K.R., HOWELL, M., OTT, L.J., Parametric and Experimentally Informed BWR Severe Accident Analysis Using FeCrAl, Report ORNL/SPR-2017/373.
- [170] GURGEN, A., SHIRVAN, K., Estimation of coping time in pressurized water reactors for near term accident tolerant fuel claddings, *Nuclear Engineering and Design* **337** (2018) 38-50.
- [171] PINT, B.A., Performance of FeCrAl for accident-tolerant fuel cladding in high temperature steam, *Corrosion Reviews* **35** 3 (2017) 167–175.
- [172] STUCKERT, J., GROßE, M., LAIER, J., MOCH, J., PETERS, U., STEGMAIER, U., STEINBRÜCK, M., TERRANI, K., "First results of the bundle test QUENCH-19 with FeCrAl claddings", Proceedings of 24th International Quench Workshop, 13.11.2018 – 15.11.2018, Karlsruhe (2018).
- [173] AUSTREGESILO, H., et al., ATHLET-CD 3.2 User's Manual, GRS Report, GRS-P-4 Vol. 1 (Dec. 2018) .
- [174] BOLSHOV, L.A., DOLGANOV, K.S., KISELEV, A.E., STRIZHOV, V.F., Results of SOCRAT code development, validation and applications for NPP safety assessment under severe accidents, *Nuclear Engineering and Design* **341** (2019) 326-345.
- [175] IVEKOVIĆ, A., et al., Current status and prospects of SiCf/SiC for fusion structural applications, *Journal of the European Ceramic Society* **33** 10 (2013) 1577-1589.
- [176] MERRILL, B.J., BRAGG-SITTON, S.M., HUMRICKHOUSE, P.W., Modification of MELCOR for severe accident analysis of candidate accident tolerant cladding materials. *Nuclear Engineering and Design* **315** (2017) 170-178.
- [177] CARPENTER D.M., et al., Assessment of innovative fuel designs for high performance light water reactor, Massachusetts Institute of Technology (2006).
- [178] TERRANI, K.A., Silicon Carbide Oxidation in Steam up to 2 MP, *Journal of the American Ceramic Society*, **97** 8 (2014) 2331-2352.
- [179] SNEAD, L.L., et al. Handbook of SiC properties for fuel performance modeling. *Journal of Nuclear Materials* **371**(2007) 329-377.
- [180] OZAWA, K., et al., Mechanical properties of advanced SiC/SiC composites of neutron irradiation, *Journal of Nuclear Materials* **367-370** (2007)713-718.
- [181] KATOH, Y., et al., Continuous SiC fiber, CVI SiC matrix composites for nuclear application: properties and irradiation effects, *Journal of Nuclear Materials* **448** 1-3(2004) 448-476.
- [182] KREJČÍ, J., et al., Development and testing of multicomponent fuel cladding with enhanced accidental performance, *Nuclear Engineering and Technology* (2019).



## ANNEX

The supplementary files for this publication can be found on the publication's individual web page at [www.iaea.org/publications](http://www.iaea.org/publications). These include:

|  |     |
|--|-----|
| A STARTING POINT OF THE ASSESSMENT OF ACCIDENT TOLERANT FUELS .....  | 1   |
| <i>A.C. Marino, L. Furlano, G.L. Demarco, A. Baruj, H. Mosca, S. Jaroszewicz,<br/>E.L. Losada, G. Bozzolo, A. Yawny, E. Dari</i>                         |     |
| PERFORMANCE OF ACCIDENT TOLERANT FUEL USING IRON-BASED<br>ALLOY AS CLADDING .....  | 24  |
| <i>C. Giovedi, T. Carluccio, M. R. Martins, A. Abe, A. T. Silva, R. O. R. Muniz</i>  |     |
| ANALYSIS AND ASSESSMENT OF SILICON CARBIDE CLADDING<br>PERFORMANCE UNDER ACCIDENT CONDITION IN PWR.....  | 42  |
| <i>T. Liu, M.T. Chen, Y.R. Xie, L. Li</i>  |     |
| PERFORMANCE MODELING OF FCM PELLET AND SiC CLADDING.....   | 54  |
| <i>P. Chen, S.C. Liu, Y. Zhou, S.X. Gao, W.J. Li, L. He, H.Y. Lu, S. Xing</i>  |     |
| PRELIMINARY MODELING AND SIMULATION OF FUEL ROD<br>WITH SiC <sub>F</sub> /SiC CLADDING FOR LWRS .....  | 72  |
| <i>X.Y. Shang, A.M. Zhang, S.Y. Zhang</i>  |     |
| DEVELOPMENT AND TESTING OF COATED FUEL CLADDING FOR<br>WWER REACTORS WITH ENHANCED ACCIDENT TOLERANCE .....  | 87  |
| <i>M. Ševeček, J. Krejčí, A. Chalupová, L. Cvrček, J. Kabátová, F. Manoch,<br/>J. Kočí, K. Shirvan, R.G. Ballinger, T. Novotny, E. P. Feró, Z. Hózer</i> |     |
| PERFORMANCE OF CANDIDATE ATF CLADDING MATERIALS IN<br>SIMULATED HIGH TEMPERATURE STEAM AND NORMAL LWR<br>CONDITIONS .....                                | 104 |
| <i>S. Penttilä, J-M. Autio, J. Lydman, U. Tapper</i>   |     |
| POST TEST SIMULATION OF QUENCH TEST 19 WITH ATHLET-CD.....   | 151 |
| <i>C. Bals, T. Hollands</i>  |     |
| FIRST RESULTS OF THE BUNDLE TEST QUENCH-19 WITH FeCrAl<br>CLADDINGS .....  | 160 |
| <i>J. Stuckert, M. Große</i>   |     |
| ROUND ROBIN HIGH TEMPERATURE OXIDATION TESTS AT KIT .....  | 170 |
| <i>C. Tang, M. Steinbrueck, M. Grosse</i>  |     |
| FABRICATION OF Cr <sub>2</sub> AlC COATINGS AT ZIRCALOY-4 AT KIT .....   | 188 |
| <i>C. Tang, M. Steinbrueck, M. Grosse, S. Ulrich, M. Stueber</i>   |     |
| SIMULATION OF FeCrAl CLADDED FUEL ROD .....  | 190 |
| <i>M. Cherubini</i>  |     |
| FEMAXI-7 ANALYSIS FOR MODELING BENCHMARK FOR FeCrAl .....  | 199 |
| <i>A. Yamaji, N. Susuki, Y. Kaji</i>   |     |

|  |     |
|--|-----|
| DEVELOPMENT AND IMPLEMENTATION IN THE FRAPCON CODE<br>OF ACCIDENT TOLERANT FUEL MODELS FOR COATED ZIRCALOY<br>CLADDING AND METALLIC MICROCELL UO <sub>2</sub> PELLET.....  | 210 |
| <i>C. Shin, H.C. Kim, Y.S. Yang, Y.H. Koo</i>  |     |
| SILICIDE/SILICATE COATINGS ON ZIRCONIUM ALLOYS FOR<br>IMPROVING THE HIGH TEMPERATURE CORROSION RESISTANCE .....  | 223 |
| <i>B. Sartowska, W. Starosta, L. Waliś, M. Miłkowska, A. Krześniak, E. Pańczyk,<br/>P. Kalbarczyk, K. Kulisa, M. Barlak, J. Smolik, M. Rydzewski, V.K. Semina, P. Tomassi,<br/>P. Kołodziejczak, J. Mizeracki, A. Presz, J. Maurin</i> |     |
| RESULTS OF SA MODELING AT A LWR WITH FeCrAl CLADDINGS.....   | 245 |
| <i>K. Dolganov, A. Kiselev, T. Yudina</i>  |     |
| NEW ATF CONCEPTS AND MATERIALS: EVALUATION AND INVESTIGATIONS .....  | 255 |
| <i>A.M. Savchenko, L.A. Karpyuk, V.V. Novikov, V.K. Orlov</i>  |     |
| MODELING FeCrAl CLADDING AND U <sub>3</sub> Si <sub>2</sub> FUEL USING THE BISON CODE.....   | 271 |
| <i>G. Pastore, K.A. Gamble, J.D. Hales</i>   |     |
| DEVELOPMENT OF ACCIDENT TOLERANT FUEL (ATF) FOR LWRS .....   | 282 |
| <i>P. Xu</i>   |     |

## ABBREVIATIONS

|        |  |
|--------|--|
| ATF    | accident tolerant fuel                                     |
| ATR    | advanced test reactor                                      |
| BEI    | backscattered electron images                              |
| BWR    | boiling water reactor                                      |
| CANDU  | Canada deuterium–uranium pressurized heavy water reactor   |
| CASL   | consortium for advanced simulation of light water reactors |
| CEM    | controlled evaporation and mixing                          |
| CIAE   | China Institute of Atomic Energy                           |
| CNEA   | Comisión Nacional de Energía Atómica (Argentina)           |
| CNPRI  | China Nuclear Power Technology Research Institute          |
| CRP    | coordinated research project                               |
| CTE    | coefficient of thermal expansion                           |
| CTU    | Czech Technical University                                 |
| DOE    | US Department of Energy                                    |
| EDS    | energy-dispersive X-ray spectroscopy                       |
| EDX    | energy dispersive X-ray microanalyser                      |
| HT     | high temperature   |
| IGF    | inert gas fusion   |
| INCT   | Institute of Nuclear Chemistry and Technology (Poland)     |
| INL    | Idaho National Laboratory (United States of America)       |
| ITS    | Institute for Sustainable Technologies (Radom, Poland)     |
| JAEA   | Japan Atomic Energy Agency (Japan)                         |
| JFNK   | Jacobian-Free Newton Krylov (method)                       |
| KIT    | Karlsruhe Institute of Technology (Germany)                |
| LOCA   | loss of coolant accident                                   |
| LWR    | light water reactor  |
| MOOSE  | multiphysics object oriented simulation environment        |
| MOX    | mixed oxide (fuel)   |
| MTA EK | Hungarian Academy of Sciences Centre for Energy Research   |
| NEAMS  | nuclear energy advanced modelling and simulation           |
| NINE   | Nuclear and Industrial Engineering (Italy)                 |
| NWC    | normal water chemistry                                     |
| ORNL   | Oak Ridge National Laboratory                              |

|         |  |
|---------|--|
| PHWR    | pressurized heavy water reactor                            |
| PNNL    | Pacific Northwest National Laboratory                      |
| PVD     | physical vapor deposition                                  |
| PWR     | pressurized water reactor                                  |
| RCA     | recrystallized alumina                                     |
| SA      | selected area  |
| SE      | secondary electron   |
| SEI     | secondary electron image                                   |
| SEM     | scanning electron microscope                               |
| TDO     | total dissolved oxygen                                     |
| TWG-FPT | Technical Working Group on Fuel Performance and Technology |
| UBM     | using unbalanced magnetron                                 |
| USP     | University of São Paulo (Brasil)                           |
| UTS     | ultimate tensile strength                                  |
| WWER    | water cooled, water moderated power reactor                |
| XRD     | X-ray diffraction  |
| YS      | yield stress   |

## LIST OF CHIEF SCIENTIFIC INVESTIGATORS

|                      |  |
|----------------------|--|
| Chen, P.             | Nuclear Power Institute of China,<br>China   |
| Cherubini, M.        | Nuclear and Industrial Engineering (NINE),<br>Italy  |
| Giovedi, C.          | Universidade de Sao Paulo (USP),<br>Brazil   |
| Grosse, M.           | Karlsruhe Institute of Technology,<br>Germany  |
| Kaji, Y.             | Japan Atomic Energy Agency,<br>Japan   |
| Kiselev, A.          | Nuclear Safety Institute, Russian Academy of Sciences (IBRAE),<br>Russian Federation   |
| Koo, Y.H.            | Korea Atomic Energy Research Institute,<br>Korea - Republic of   |
| Liu, T.              | China Nuclear Power Technology Research Institute (CNPRI)<br>China   |
| Marino, A.           | Comisión Nacional de Energía Atómica (CNEA),<br>Argentina  |
| Pastore, G.          | Idaho National Laboratory,<br>United States of America   |
| Sartowska, B.        | Institute of Nuclear Chemistry and Technology,<br>Poland   |
| Savchenko, A.        | Stock Company "A.A. Bochvar High-technology Research Institute<br>of Inorganic Materials" (SC "VNIINM"),<br>Russian Federation |
| Ševeček, M.          | Czech Technical University (CTU),<br>Czech Republic  |
| Sinha, S.            | Bhabha Atomic Research Centre (BARC),<br>India   |
| Toivonen, A.         | VTT Technical Research Centre of Finland,<br>Finland   |
| Xu, P.<br>(Chairman) | Westinghouse Electric Company,<br>United States of America   |
| Zhang, A.            | China Institute of Atomic Energy (CIAE),<br>China  |



## CONTRIBUTORS TO DRAFTING AND REVIEW

|                |   |
|----------------|---|
| Cherubini, M.  | Nuclear and Industrial Engineering, Italy           |
| Pastore, G.    | Idaho National Laboratory, United States of America |
| Penttilä, S.   | VTT Technical Research Centre, Finland              |
| Ševeček, M.    | Czech Technical University, Czech Republic          |
| Stuckert, J.   | Karlsruhe Institute of Technology, Germany          |
| Veshchunov, M. | International Atomic Energy Agency                  |
| Xu, P.         | Westinghouse Electric Co., United States of America |
| Zozulia, I.    | International Atomic Energy Agency                  |

### **The 1st Research Coordination Meeting**

Vienna, Austria: 2–4 November 2015

### **The 2nd Research Coordination Meeting**

Vienna, Austria: 20–22 June 2017

### **The 3rd Research Coordination Meeting**

Vienna, Austria: 26–29 November 2018

### **Consultants Meeting**

Vienna, Austria: 28 February – 1 March 2019





## ORDERING LOCALLY

IAEA priced publications may be purchased from the sources listed below or from major local booksellers.

Orders for unpriced publications should be made directly to the IAEA. The contact details are given at the end of this list.

### NORTH AMERICA

***Bernan / Rowman & Littlefield***

15250 NBN Way, Blue Ridge Summit, PA 17214, USA

Telephone: +1 800 462 6420 • Fax: +1 800 338 4550

Email: [orders@rowman.com](mailto:orders@rowman.com) • Web site: [www.rowman.com/bernan](http://www.rowman.com/bernan)

### REST OF WORLD

Please contact your preferred local supplier, or our lead distributor:

***Eurospan Group***

Gray's Inn House  
127 Clerkenwell Road  
London EC1R 5DB  
United Kingdom

***Trade orders and enquiries:***

Telephone: +44 (0)176 760 4972 • Fax: +44 (0)176 760 1640

Email: [eurospan@turpin-distribution.com](mailto:eurospan@turpin-distribution.com)

***Individual orders:***

[www.eurospanbookstore.com/iaea](http://www.eurospanbookstore.com/iaea)

***For further information:***

Telephone: +44 (0)207 240 0856 • Fax: +44 (0)207 379 0609

Email: [info@eurospangroup.com](mailto:info@eurospangroup.com) • Web site: [www.eurospangroup.com](http://www.eurospangroup.com)

### Orders for both priced and unpriced publications may be addressed directly to:

Marketing and Sales Unit

International Atomic Energy Agency

Vienna International Centre, PO Box 100, 1400 Vienna, Austria

Telephone: +43 1 2600 22529 or 22530 • Fax: +43 1 26007 22529

Email: [sales.publications@iaea.org](mailto:sales.publications@iaea.org) • Web site: [www.iaea.org/publications](http://www.iaea.org/publications)



**International Atomic Energy Agency  
Vienna**